Performance of the cosmic ray fluorescence detector EUSO-TA

Zur Erlangung des akademischen Grades eines
Doktors der Naturwissenschaften
bei der Fakultät für Physik
des Karlsruher Instituts für Technologie (KIT)

genehmigte
Dissertation

von
Francesca Bisconti
aus Rimini (Italien)

Abstract

Performance of the cosmic ray fluorescence detector EUSO-TA

The EUSO-TA detector is a down-scaled pathfinder experiment for JEM-EUSO (Extreme Universe Space Observatory on board the Japanese Experiment Module). It is located at the Telescope Array (TA) site in Utah, USA. Its main goal is to test the observation principle and the detector design of JEM-EUSO on ground. The detection principle is to detect Extensive Air Showers (EASs) induced by primary high-energy cosmic rays and developed through the atmosphere, by the consequent emission of fluorescence and Cherenkov light. The incoming light is detected by an array of Multi-Anode PhotoMultiplier Tubes (MAPMTs), sensors with single-photon counting capability. EUSO-TA can work in coincidence with a TA fluorescence detector, allowing cross-checks and improved reconstruction of the detected events.

This thesis is centered on the analysis of the data collected by EUSO-TA and on simulation studies to evaluate the detector capabilities.

Because of the high spatial resolution of EUSO-TA, it has been possible to evaluate the width of the tracks of the detected EAS, which gave an estimation of the shower lateral distributions between 0.6° and 1°, depending on the energy and the distance of the EAS from the detector. A study on the background showed that (close) EASs visible on just one time frame of 2.5 μs contribute significantly to the whole frame intensity, while (distant) EASs split on more frames contribute with the same magnitude as background fluctuations.

The Offline analysis and simulation framework has been adopted from the Pierre Auger Observatory experiment and adapted for JEM-EUSO and its pathfinders. In the context of this thesis, the contribution to the improvement of the software was to implement the detector response, including the sensor efficiency and the dead times. This allowed us to simulate the detected events and the results are in good agreement with the data. The detailed simulations gave the possibility to study the origin of the light arriving to the telescope, i.e. fluorescence, direct or scattered Cherenkov light. On a single event basis, most of the light was from fluorescence emission, between 65% and 80%, and direct Cherenkov light was more intense for EAS going towards the telescope. The transmission efficiency of the optical system is between 15% and 17%, while the overall efficiency of the telescope is between 4% and 5%. The simulation of the events which crossed the field of view of EUSO-TA but have not been detected provided the identification of additional candidate events. This study

allowed us also to determine the limitations of the detection capability of EUSO-TA. It has been also found that the detected and the candidate events have a total number of counts higher than 200, or about 30 counts per photomultiplier. Finally, a test considering Silicon PhotoMultiplier (SiPM) arrays instead of MAPMTs has been performed. The test revealed that the most recent model of SiPMs seems to be slightly more efficient than MAPMTs.

Zusammenfassung

Verhalten des Fluoreszenz-Teleskopes EUSO-TA bei der Messung kosmischer Strahlung

Der EUSO-TA Detektor ist ein Vorbereitungsexperiment von JEM-EUSO (Extreme Universe Space Observatory on board the Japanese Experiment Module) und befindet sich EUSO-TA auf dem Gelände des Telescope Array (TA) in Utah, USA. Das wesentliche Ziel des Experiments ist die Vermessung von durch hochenergetische kosmische Teilchen ausgelöste ausgedehnte Luftschauer (EAS) über die Detektion von im EAS emittierter Fluoreszenz- und Cherenkov-Strahlung. EUSO-TA arbeitet im Verbund mit einem Fluoreszenzdetektor von TA, was Vergleichsstudien und eine verbesserte Rekonstruktion der detektierten Ereignisse ermöglicht.
Diese Arbeit konzentriert sich auf die Analyse der durch EUSO-TA gesammelten Daten und auf Simulationsstudien zur Bewertung der Detektoreigenschaften.

Die hohe Winkelauflösung von EUSO-TA ermöglicht die Vermessung der Spurbreite des detektierten Luftschauers. Dies erlaubt Rückschlüsse auf die Herkunftsrichtung mit einer Präzision von 0.6° bis zu 1°, abhängig von der Energie des Primärteilchens und der Entfernung des Luftschauers zum Detektor. Eine Untersuchung des Untergrundes ergab, dass nahe Luftschauer, die nur während eines einzelnen Messintervalls von 2.5 μs erscheinen, signifikant zur absoluten Lichtintensität während des Messintervalls beitragen. Entfernte Luftschauer hingegen, die sich über mehrere Messintervalle erstrecken, tragen nur mit der gleichen Intensität wie Fluktuationen des Untergrundes zur Gesamtintensität bei.

Die Analyse- und Simulationssoftware Offline wurde vom Pierre-Auger Observatorium übernommen und an JEM-EUSO und dazugehörige Pfadfinderexperimente angepasst. Der Hauptbeitrag dieser Arbeit zur Verbesserung von Offline war die Implementierung der Detektoreigenschaften, die die Effizienz der Sensoren und Totzeiten beinhalten. Dies ermöglicht eine Simulation der detektierten Ereignisse. Die Resultate befinden sich in guter Übereinstimmung mit den gemessenen Daten. Mit den detaillierten Simulationen war es möglich, den Ursprung des vom Detektor detektierten Lichts zu bestimmen, das sich aus Licht von Fluoreszenz-Emission sowie direkter und gestreuter Cherenkov-Strahlung zusammensetzt. Der mit 65% bis 80% größte Anteil des während eines Luftschaues detektierten Lichts stammt von der Fluoreszenz-Emission. Der Anteil von direkter Cherenkov-Strahlung steigt für Luftschauer, die in Richtung des Detektors gerichtet sind. Für die Transmissionseffizienz des optischen Systems ergab sich ein Wert zwischen 15% und 17%. Die

Gesamteffizienz des Teleskops beträgt 4% bis 5%. Die Simulation von Luftschauern, die zwar das Sichtfeld von EUSO-TA kreuzen aber nicht detektiert werden, führte zur Identifikation von vier weiteren möglichen Ereignissen. Diese Studie ermöglichte auch eine Abschätzung der Detektionsgrenzen von EUSO-TA. Ein weiteres Ergebnis ist, dass die Anzahl der gemessenen Photonen für detektierte Ereignisse als auch für durch Simulationen gefundene Ereignisse höher als 200 ist. Dies entspricht etwa 30 gemessenen Photonen pro Photomultiplier. Abschließend wurde ein Vergleich von Multi-Kanal Silicon PhotoMultiplier (SiPM) und Multi-Anode Photomultiplier Tubes (MAPMTs) als Photosensoren für EUSO-TA durchgeführt. Es stellte sich heraus, dass das die neuste SiPM Generation leichte Vorteile in der Effizienz gegenüber MAPMTs bietet.

Contents

Introduction

Cosmic rays are energetic particles coming from space at a speed close to the speed of light, hitting the Earth, as well as any other astronomical object or artificial satellite, anywhere and anytime.

Nowadays, cosmic ray research is an active and challenging branch of astroparticle physics, starting with the cosmic ray discovery in 1912 by Victor Hess. In the following years, a wide variety of investigations confirmed that the primary cosmic rays, mostly protons, arrive from space at the top of the Earth's atmosphere and, interacting with it, generate secondary radiation composed primarily by electrons, photons and muons, which interact further with the atmosphere until they reach the ground level. Such interactions produce so called "extensive air showers". It has been found that the primary cosmic ray flux covers a wide range of energies, from 10^9 to 10^{20} eV or more. The study of cosmic rays helped in the development of particle physics, before accelerators which could reach adequate energies were built, leading to the discovery of particles like the positron (the first antiparticle detected), the muon and strange particles. Today, the energy involved in cosmic ray physics, in particular studying the highest energy cosmic rays, is still millions of times higher than that reachable in accelerators.

The cosmic ray spectrum decreases many orders of magnitude with the increase of the energy. Therefore, different methods are used for different energy ranges. Until 10^{15} eV direct measurements of primary cosmic rays are possible using detectors onboard stratospheric balloons or satellites. These cosmic rays have galactic origins, and are accelerated by phenomena like supernovae explosions. For higher energy particles of probably extragalactic origin ($E > 10^{18}$ eV), the flux is so low that huge detectors would be necessary to measure them directly, with obvious logistic problems. For this purpose, indirect detection methods have been developed, in which the target are the secondary cosmic rays, those produced by the interaction of primary cosmic rays with the molecules in the atmosphere. Very large detector arrays have been installed on ground, sized from hundreds to thousands of square kilometers, like the Pierre Auger Observatory or the Telescope Array (TA). Once the number of secondary cosmic ray per event is measured, it is possible to retrieve the primary cosmic ray flux using simulations. At energies above $5 \cdot 10^{19}$ eV the flux is highly suppressed by the so called GZK suppression, which is caused by the interaction of protons with such energies with the cosmic microwave background. The detection of cosmic rays with energy higher than 10^{20} eV of high statistics is of great importance, because this would lead to the identification of their sources

and to measure the sources' energy spectra, to constrain acceleration and emission mechanisms. Indeed, just particles with such energies are not deflected by magnetic fields in the interstellar medium, and their direction points to the sources.

Looking in particular to these Extreme Energy Cosmic Rays (EECRs), the Extreme Universe Space Observatory onboard Japanese Experiment Module (JEM-EUSO) mission was started. The JEM-EUSO project aims to install a cosmic ray fluorescence detector on the International Space Station (ISS) or as a free-flyer satellite. From there, it would look downward to the Earth's atmosphere, used as a huge calorimeter. Indeed, when cosmic rays enter the atmosphere, in the consequent air showers fluorescence light in the ultraviolet band is emitted. A detector with high spatial and temporal resolution and large field of view (FOV) at 400 km altitude would cover an area projected on ground of the order of $10^5 \, km^2$. This is much larger then the length of a cosmic ray air shower, which extends tens of kilometers, depending on its inclination. Moreover, such a detector would orbit around the Earth, providing an uniform coverage of both hemispheres, which means not having a preferential direction regarding the cosmic ray sources identification, and therefore the shower is fully visible during its development. In order to test the design and the detection principle of this new generation space-based detector, a few pathfinders have been developed: one of these is EUSO-TA.
EUSO-TA is a scaled version of the JEM-EUSO detector, installed at the Telescope Array site in front of one of its fluorescence detector stations. The advantage of being placed in front of the TA fluorescence detectors is that EUSO-TA can acquire data in coincidence with them, when cosmic ray air showers cross their FOV. Afterwards, the event information provided by the TA event reconstruction algorithms allow to analyze the events detected by EUSO-TA. A several data acquisition campaigns have been performed in 2015 and 2016, and a few coincident cosmic ray events have been detected.

In this thesis, the analysis on the detected cosmic ray events are described, as well as studies on stars, laser events and background. In Chapter 1 an overview of cosmic rays and extensive air showers will be given. Chapter 2 will present the JEM-EUSO mission with its baseline design, goals, and pathfinder experiments. Chapter 3 will describe the EUSO-TA pathfinder setup in greater detail. In Chapter 4 the data acquisition campaigns will be discussed, mentioning the conditions under which they are performed, and showing the detected cosmic ray events, stars and the laser. In Chapter 5 an analysis of the data is shown and the following topics will be discussed: a method to evaluate the cosmic ray air shower lateral distribution; an analysis of temporal parameters which characterize the events, as well as background variation over time. Chapter 6 will give an overview of the Offline simulation and reconstruction framework, used to perform simulations of cosmic ray events for EUSO-TA and which will be the main topic of discussions in the following chapters. In particular, the improvements to the software to perform the detector response will be discussed. In Chapter 7 the detected events are compared with the simulation results. In Chapter 8 a simulation study to evaluate the detection threshold of EUSO-TA, as well as other studies evaluating the expected number of detected

events will be presented. Finally, Chapter 9 will give an overview of new generation light sensors, the Silicon Photo-Multipliers (SiPMs), which might be used in future missions.

Chapter 1

Cosmic Rays and Extensive Air Showers

1.1 Cosmic rays

1.1.1 History

At the end of 18th century, C. A. de Coulomb discovered that an electroscope spontaneously discharges, which means that the air around it is charged. For more than one century many studies have been done on this topic, without a definitive explanation of the phenomena. At the beginning of 20th century it was found that radioactive matter was present in the terrestrial crustal plate, and this was considered for years as the explanation for the measured charges.

Around 1910, D. Pacini [1] developed experiments underwater which revealed that the radiation was coming from above and not from ground. In the same years A. Gockel [2] launched an electroscope onboard a balloon at an altitude of 4 km, which discharged faster in quote than at sea level. The experiment was repeated by V. Hess [3, 4], who confirmed the results and stated that the radiation could have an extraterrestrial origin, or atmospheric. Hess got the Nobel prize for being the pioneer in this field. W. Kolhorster [5] repeated again the experiment with an electroscope on a balloon, but this time at 9 km. The result was that the difference in the duration of the discharge of the electroscope was up to 10 times faster than on ground. Moreover, he observed that if the radiation was coming from space, it should be 5-10 times more penetrating than the most energetic γ rays, since they were traversing the whole atmosphere. In the 20s, after the first world war, similar experiments but at 16 km altitude were done by R. Millikan and I. Bowen [6], and it seemed that the discharge velocity was decreasing in the upper atmosphere, which supported the hypothesis of an atmospheric origin.

The research went ahead changing the method: measuring the electroscope discharge duration, at a few tens of meters under water. This was done first by Kolhorster in Germany and then by Millikan and G. Cameron [7] in the USA and others. The result was that the measured radiation was less ionizing underwater than above,

and was also more energetic than the known radiation, because it was penetrating layers of water corresponding to three times the whole atmosphere. In 1925 Millikan used the term "cosmic rays" for the first time, to indicate an extraterrestrial origin, although the atmospheric origin was still under discussion.

The following studies were concentrated on the determination of the nature and the energy of this radiation. The first study was done by Millikan and Anderson [8] using a Wilson cloud chamber, observing the penetration and the deviation of charged particles in presence of a strong magnetic field. The measured energies were of the order of 10^9 eV, while up to that time just particles with energies of $15 \cdot 10^6$ eV were known. The energy was so high that it was necessary to add a layer of lead 6 mm thick, in order to reduce the particle energy and see any trajectory deviation. This experiment led to the discover of the *positron*, announced in 1932 by C.D. Anderson and confirmed by following experiments.

Coming back to the origin of the radiation, it was noticed that the nature of the penetrating radiation was similar to that of the atomic disintegration products obtained meanwhile in laboratories. This brought, in the mid 30s, the idea that the measured radiation could have been a secondary product generated by interaction of primary radiation with the atmosphere. In the same years, again with the Wilson cloud chamber, a particle of mass between those of protons and electrons was discovered. A new particle was introduced by H. Yukawa [9], in Japan, with mass 300 times the mass of the electron, which could be positive and negative, and which could be exchanged between protons and neutrons during interactions, as well as charged particles exchange photons. Finally, this particle was named *meson*, and when another less massive meson has been found, the first become the *pion* and the second the *muon*. With the technological improvements, new particles were discovered.

The historical information reported has been taken from [10].

About the origin of the cosmic rays, questions are still open. In particular, there is a lack in the understanding of the possible sources and mechanisms which could produce and accelerate particles at extremely high energies. These and other topics are discussed next.

1.1.2   Cosmic ray spectrum

Cosmic rays are extraterrestrial particles, mainly fully ionized atomic nuclei, of which about 90% are hydrogen nuclei (protons), 9% are helium nuclei and the remaining 1% is composed of heavier nuclei and electrons. Their energy extends over a wide range, from about 10^9 to 10^{20} eV or more, and still are millions of times higher than the energies reachable in artificial accelerators. Over this energy range, the cosmic ray flux varies by many orders of magnitude, between 1 particle $\mathrm{m^{-2}\,s^{-1}}$ at low energies ($E \sim 10^9$ eV), 1 particle $\mathrm{m^{-2}\,yr^{-1}}$ at intermediate energies ($E \sim 10^{15}$ eV), 1 particle $\mathrm{km^{-2}\,yr^{-1}}$ at high energies ($E \sim 10^{19}$ eV) and 1 particle $\mathrm{km^{-2}}$ per century at extreme energies ($E \sim 10^{20}$ eV).

The cosmic ray flux follows the power law:

$$\frac{\mathrm{d}N}{\mathrm{d}E} \propto E^{-\gamma}, \tag{1.1}$$

with the number of particles N, the energy E of the primary cosmic ray, i.e. the incident nucleus, and the spectral index γ varying between 2.7 and 3.3.

Figure 1.1 shows the spectrum scaled by $E^{2.5}$. At energies $> 10^{11}$ eV (not in the plot), the main source of cosmic rays is the Sun, while increasing the energy, nuclei from the entire Galaxy are detected. Before $3 \cdot 10^{15}$ eV the spectral index is $\gamma = 2.7$, while at this energy a change of slope to $\gamma = 3$ characterizes the so-called *first knee*. At around $4 \cdot 10^{17}$ eV, a *second knee* occurs due to a steepening to $\gamma = 3.3$. These features are associated with the mass of the cosmic rays from the Galaxy and their acceleration and propagation mechanisms. The first knee is due to the decreasing of the light particle flux, and the second knee is for heavy particles, as explained in Section 1.1.2.

At higher energies, γ increases for a small energy interval between $3 \cdot 10^{18}$ eV and 10^{19} eV, before it decreases again. This energy region is the so-called *ankle*. The interpretation of this change strongly depends on the scenario considered for the transition between galactic and extragalactic cosmic rays.

Above $5 \cdot 10^{19}$ eV, a strong suppression is observed. At this energy, the Greisen-Zatsepin-Kuzmin suppression (GZK) [11, 12] was predicted, describing the energy loss due the interaction of protons with photons from the Cosmic Microwave Background (CMB). But also other effects are predicted at this energy, such as the photo-disintegration of the nuclei. Thus, the origin of this suppression is still debated. However, at these energies the cosmic rays come from extragalactic sources. Until 10^{15} eV cosmic rays can be observed directly with detectors mounted on balloons or space-based experiments. For higher energy particles, the flux is so low that huge detectors would be necessary to measure them directly. For this purpose, indirect detection methods have been developed, in which the secondary cosmic rays are the target, particles produced by the interaction of primary cosmic rays with the atmospheric molecules. In Section 1.3 a brief description of the different detection techniques is given.

Galactic cosmic rays

The cosmic ray flux below 10^{15} eV allows direct measurements of the mass, charge and energy of individual nuclei, with balloon or satellite experiments. At these energies the composition mimics the known solar system element abundance, except for some light elements (e.g., lithium, beryllium, and boron), and elements below iron and lead are more abundant in the cosmic ray composition due to spallation processes during their propagation [14]. Thus, cosmic rays are made of ordinary matter and accelerated in the Galaxy in this energy regime. For higher energies these direct measurements become insufficient, because the flux gets too low and detectors would have to become unreasonably big.
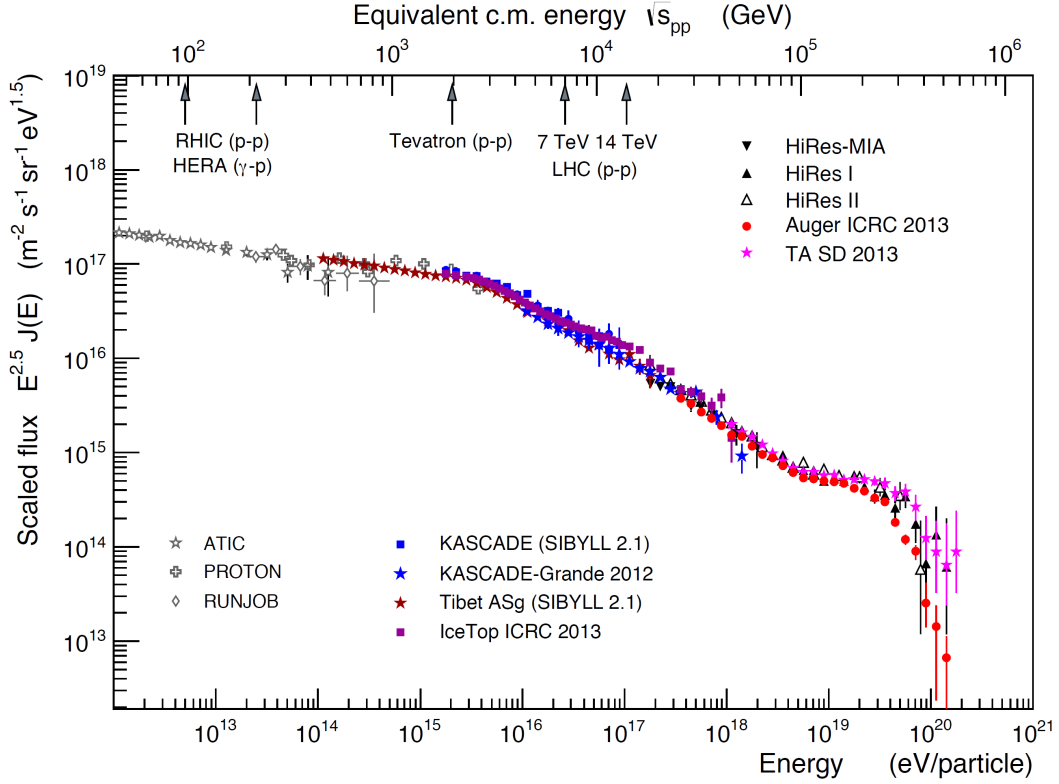
Figure 1.1: All-particle energy spectrum of the cosmic rays scaled by $E^{2.5}$. A steepening of the spectrum becomes visible at about $3 \cdot 10^{15}$ eV (*first knee*) and a second one at about $4 \cdot 10^{17}$ eV (*second knee*). A flattening appears at about $3 \cdot 10^{18}$ eV (*ankle*). Above $5 \cdot 10^{19}$ eV the flux is highly suppressed. Plot taken from [13].

To describe the observed energy spectrum, models of cosmic ray sources and particle propagation in the galaxy are developed (for example [15]). The most accredited theory is that in this range of energy cosmic rays are accelerated by Supernova Remnants (SNR) via the *Fermi acceleration mechanism* and confined by the galactic magnetic field as stated by the *leaky box* model [16]. The Fermi acceleration mechanism predicts that in a moving shock front with a strong magnetic field (conditions occurring for example in supernova remnants where the expanding shell of plasma forms the shock front, because its velocity is much larger than the velocity of sound in the interstellar medium), a particle can go in the opposite direction to the moving front with a stochastic process. Due to the magnetic field it can be reflected back through the shock with a resulting acceleration. If a similar process occurs again, the particle will gain even more energy. This multiple reflection leads to an increase of the particle energy. As the energy is increased, so does the probability to escape from the shock front since this is a "statistical acceleration" process. The lifetime of the shell ($\sim 10^5$ yr), its size and the magnetic field strength determine the maximum energy attainable.

The Fermi mechanism explains an energy spectrum with a power law $\propto E^{-2}$, while the observed ones is steeper, $\propto E^{-2.7}$. Another phenomenon has to be considered.

Once a particle leaves the acceleration site, it is deflected and confined in the Galaxy by the galactic magnetic field. The radius of the circular motion of a particle with atomic mass A, charge Ze (with Z atomic number of the particle and e electron charge) and energy E in a magnetic field B is the Larmor radius R_L:

$$R_L = \frac{E}{ZeB} \tag{1.2}$$

According to the leaky box model, particles are confined within the Galaxy by the galactic magnetic field, but have a certain probability to escape it, proportional to the energy. This explains the distortion of the energy spectrum and lead to an observed spectrum $\propto E^{-2.7}$ instead of $\propto E^{-2}$.

With a galactic magnetic field of $3\,\mu G$ and a thickness of the galactic plane of 300 pc, in our Galaxy it is expected that nuclei with energies below 10^{18} eV are confined by its magnetic fields. At higher energies, no known sources and acceleration mechanisms of cosmic rays within our galaxy exist.

The maximum energy for proton and iron primary particles predicted from this model are in agreement with the measurements of the knees from KASCADE-Grande [17]. The experiment measured the spectra separately for electron-rich and electron-poor showers.

The electron-rich showers are produced by protons and light elements. Their measurement estimates the energy of the first knee and it corresponds to the maximum energy estimated for protons or helium $\sim 10^{15}$ eV. The electron-poor showers are produced by heavy elements. The iron knee is estimated to be at $\sim 10^{17}$ eV. As consequence, the flux of the galactic cosmic rays is expected to disappear quickly after the iron knee, which gives origin to the second knee. The term High Energy Cosmic Rays (HECRs) is used from the first knee onwards to about the ankle.

Extragalactic cosmic rays

When a nucleus has enough energy, the corresponding Larmor radius is larger than the galactic disk and it is no longer confined. Since there are no sources and acceleration mechanisms found in our Galaxy, which could allow cosmic rays to reach energies higher than $\sim 10^{18}$ eV, the sources of these cosmic rays are presumably located outside of our Galaxy. Particles with such energies are called Ultra-High Energy Cosmic Rays (UHECRs). In Figure 1.2, the so called Hillas plot is shown [18]. Every kind of astrophysical source is shown as a function of the size of the acceleration region in the Fermi process (x axis) and the magnetic field in the source (y axis). The relation between the dimension L and the magnetic field B is:

$$BL > \frac{2E}{z\beta} \tag{1.3}$$

with L in pc, B in μG, the particle energy E in PeV, z the particle charge and $\beta = v/c$ with v the speed of the moving shock front (accelerating region) and c the speed of light.
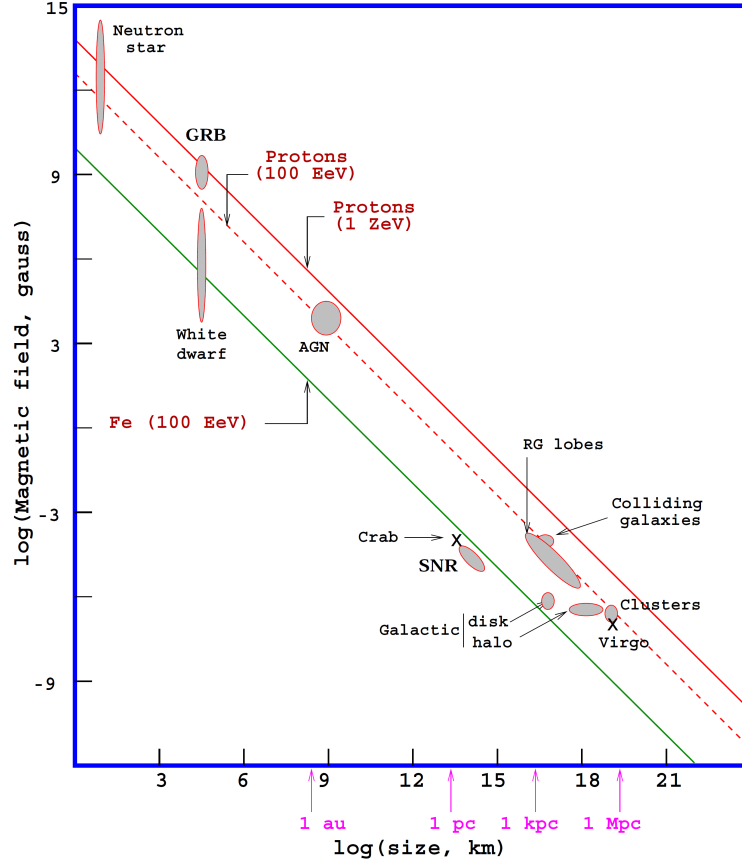
Figure 1.2: Hillas plot with the estimated magnetic field strength versus characteristic sizes of cosmic ray source candidates. Objects below the red dashed line are not capable of accelerating protons above 10^{20} eV (100 EeV). For iron nuclei the green line is the limit for the same energy. Plot taken from [18].

A proton accelerated to an energy of 10^{20} eV corresponds to the red dashed line in the Hillas plot. The red solid line indicates the limit for protons with energy of 10^{21} eV. The energy scales with the charge, thus heavier nuclei are represented by lines laying below the proton limits, as the iron accelerated to an energy of 10^{20} eV represented with the green line. Objects below the respective lines are not capable of accelerating protons or iron nuclei above that energy. Only a few sources remain as acceleration sites of protons up to such energies: Active Galactic Nuclei (AGN), Gamma Ray Bursts (GRB), radio lobes of radio galaxies and young neutron stars [19, 20].

A strong suppression of the particle flux is observed above $5 \cdot 10^{19}$ eV. This feature can be explained by the interaction of the protons and nuclei with the photons of the Cosmic Microwave Background (CMB). This effect is called Greisen-Zatsepin-Kuzmin (GZK) effect [11, 12]. Protons can interact via the process of *photo-pion*

production:

$$p + \gamma_{\text{CMB}} \to \Delta^+ \quad \to \quad p + \pi^0 \to p + \gamma\gamma \tag{1.4}$$

$$\to \quad n + \pi^+ \to n + \mu^+ + \nu_\mu \tag{1.5}$$

where the mass of the resonance Δ^+ is $m_{\Delta^+} = 1232$ MeV. The kinetic energy of protons is reduced by the energy needed to form the pion.

Heavier nuclei with atomic mass number A are fragmented into lighter nuclei (with n nucleons N) due to its excitation for giant dipole resonances at similar energies. This effect is named *photo-disintegration* and can occur both with the CMB and the Extragalactic Background Light (EBL):

$$A + \gamma_{\text{CMB,EBL}} \to (A - nN) + nN. \tag{1.6}$$

This effect can produce secondary protons that may lose energy with the GZK effect. While in case of a spectrum dominated by light nuclei (H, He), the GZK effect suppresses the cosmic ray flux, for heavier nuclei the photo-disintegration process is the dominant one. This leads to the assumption of a GZK horizon with a radius of about 100 Mpc. UHECRs of energies exceeding $5 \cdot 10^{19}$ eV have to originate from sources within the GZK horizon [21]. Particles that are near the limit of the GZK effect or beyond are called Extreme Energy Cosmic Rays (EECRs).

1.2 Extensive Air Showers

Primary cosmic rays coming from space arrive at the top of the Earth's atmosphere and penetrate it. During the path through the atmosphere, they interact with the molecules, via different mechanisms which lead to different interaction products:

- *Strong interaction*: interaction between quarks of the cosmic ray and the air nuclei;

- *Weak interaction* of the particles and *electromagnetic decay*;

- *Bremsstrahlung*: emission of radiation (photons) at the deceleration of the particles (mainly $e^\pm$);

- *Pair production*: photons split into a matter/antimatter pairs (mainly $e^\pm$). This can occur only if a photon has enough energy to create the particle masses;

- *Fluorescence light*: charged particles (mainly $e^\pm$) excite air molecules (mainly N_2) losing energy for ionization; when these excited states decay, photons in the UV range are emitted isotropically;

- *Cherenkov light*: when a charged particle travels a medium faster than the speed of light in the same medium, this light is emitted, directionally with the particle direction.

Through these interactions, a primary cosmic ray generates several new particles that can further interact with the atmosphere until they reach ground. These secondary particles form the so called extensive air shower (EAS).

An EAS consists of three components, depicted in Figure 1.3:

- The *hadronic component* directly originates from the interaction of the primary particle with air molecules. Through inelastic scattering and hadronic interactions, new hadronic particles are created. About 2/3 of the interactions end up with charged particles (mainly $\pi^{\pm}$), the remaining 1/3 with neutral particles (π^0): these are particles which afterwards introduce the other two components;

- The neutral pions π^0 decays quickly into photons inducing the *electromagnetic component* of the shower ($\pi^0 \to \gamma\gamma$). γ can produce $e^{\pm}$ pairs, also part of this component;

- The charged pions $\pi^{\pm}$ decay into muons and neutrinos ($\pi^+ \to \mu^+ + \nu_\mu$ or $\pi^- \to \mu^- + \bar{\nu}_\mu$) which form the *muonic component* of the air shower.

The electromagnetic component is the most abundant but it is also considered "soft", because $e^{\pm}$ and γ are easily absorbed by the atmosphere; the hadronic component is called "hard" because it is composed by $\mu^{\pm}$ and ν which, because of their small cross-section, are deeply penetrating.

A shower develops along its *shower axis*, the direction of the primary particle. The profile of the number of particles of this development as a function of atmospheric depth is called *longitudinal profile*. When the shower front reaches the ground, the *shower core* can be defined as the point where the shower axis hits the ground. From the core, the density perpendicular to the axis is called *lateral profile*. Distances traveled across the atmosphere are usually expressed in g/cm^2 as traversed column density. The depth X is defined as the integral over the path length in a given density profile $\rho(z)$ from infinity (space) to local height z_0:

$$X(z) = \int_{\infty}^{z_0} \rho(z) \cdot dz. \tag{1.7}$$

X_{max} is the depth at which the maximum number of particles is reached, afterwards it decreases through absorption processes in the atmosphere.

The *Heitler model* describes the growth of the EAS during the path in the atmosphere [23, 13].

When a nucleus enters the atmosphere a first hadronic interaction occurs, creating kaons, pions and several other hadrons, by which several other strong interactions start, generating the hadronic component. Pions and kaons will decay mostly in γ, μ and ν. Generated $e^{\pm}$ and γ will start also electromagnetic cascades and originate the emission of Cherenkov and fluorescence radiation. In the hadronic component, the initial energy is split among the secondary particles in the way sketched in Figure 1.4(a). The exact height of the first interaction $\hat{X}_h$ point is subject to a large
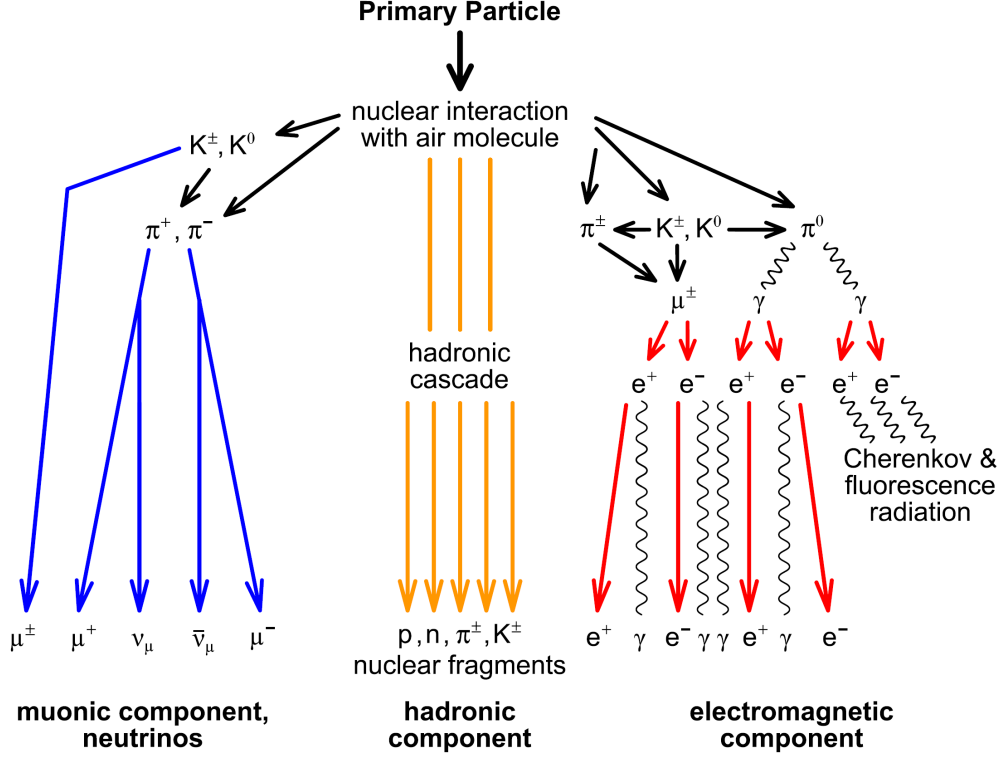
Figure 1.3: Schematic EAS development. The primary particle has a nuclear interaction with a molecule in the atmosphere and a hadronic shower is produced via inelastic scattering. Charged and neutral pions are produced through decay. The charged pions decay further to muons and neutrinos, generating the muonic component. The neutral pions start an electromagnetic cascade which emits radiation at various wavelengths. Image taken from [22].

fluctuation, because the air has a low density at those heights and the particle interaction is stochastic in nature.

In this simplified model, several assumptions are made. Only pions are produced as secondaries from a single nucleon as primary. The π^0 initiate electromagnetic cascades; the $\pi^\pm$ start the hadronic one. The hadronic interaction length $\hat{X}_h$ (about 120 g/cm^2 in air) takes into account the inelastic hadronic processes. A hadron as primary particle is split in n_{mult} secondaries, which is the secondaries multiplicity per interaction, each one the energy E_0/n_{mult}. One third are π^0 (dashed red lines in Figure 1.4(a)); two thirds are charged $\pi^\pm$ (solid black lines). In this approximation, at the n-th generation the energy is distributed as

$$E_{had} = \left(\frac{2}{3}\right)^n E_0, \qquad E_{em} = \left[1 - \left(\frac{2}{3}\right)^n\right] E_0. \qquad (1.8)$$

With $n = 6$, about 90% of the initial shower energy is carried by the electromagnetic particles and eventually deposited as ionization energy in the atmosphere. Another parameter is the energy at which $\pi^\pm$ decay length becomes comparable to the interaction length ($E_{crit}^{decay} \simeq 20$ GeV) or, in other words, the energy when the decay of pions starts to dominate on the interaction processes.

(a) Hadronic cascade   (b) Electromagnetic cascade
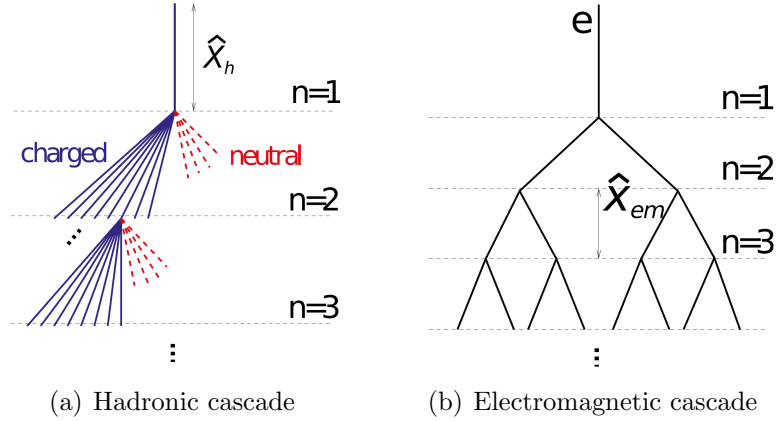
Figure 1.4: Heitler model for hadronic and electromagnetic cascades. Images taken from [13].

In the electromagnetic component, the number of particles doubles after each interaction, producing 2^n particles after n interactions, sketched in Figure 1.4(b). Every radiation length $\hat{X}_{em}$ (about 37 g/cm^2 in air), $e^{\pm}$ emit γ due to bremsstrahlung and γ produce $e^{\pm}$ due to pair production, until ionization energy losses exceed the radiative losses (at $E_{crit}^{ion} = 86$ MeV).

In this approximate model, a primary particle ($e^{\pm}$ or γ) with an initial energy E_0 will have secondaries ($e^{\pm}$ and γ) at the n-th step with an energy $E_n = E_0/2^n$. When the ionization energy losses start to exceed the radiative losses, at a depth X_{max}, absorption starts to dominate over particle creation and the particle number decreases with the longitudinal development.

Due to multiple Coulomb scattering of electrons with the atoms in the air, a lateral spread of the shower particles occurs [24].

In Figure 1.5 examples of longitudinal and lateral profiles of a simulated shower are shown. In (a) it is evident that the maximum of the shower profile is dominated by the electromagnetic component, while the muonic component and the hadronic component have roughly the same particle density, but are around 1% of the electromagnetic particle density. A shift of X_{max} in the order of 100 g cm^{-2} can be expected comparing proton and iron longitudinal distributions. This is the key feature for mass composition studies. The lateral profile of the hadronic cascade is broader than the electromagnetic one. Secondary hadrons are produced at a typical transverse momentum of $p_{\perp} \sim 350 - 400$ MeV, almost energy independent. Thus the low-energy hadrons are generated with a larger angle relative to the shower axis. In (b) an example of the particle density expected at the ground as a function of the distance from the shower core is shown.

(a) Average longitudinal shower profile.

(b) Average lateral shower profile.
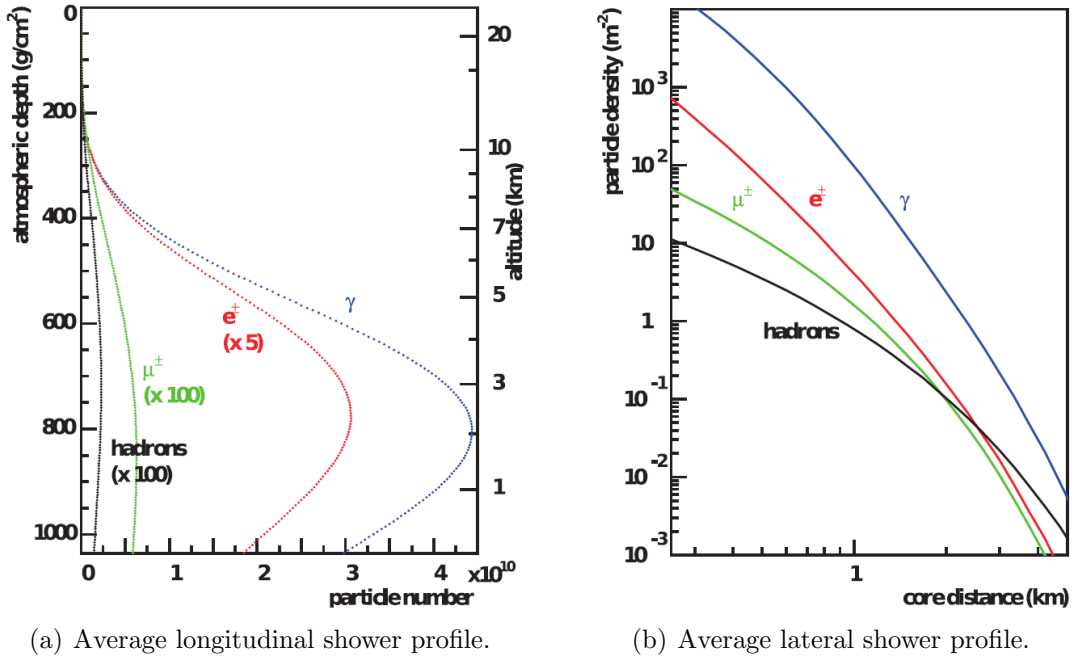
Figure 1.5: Longitudinal and lateral profiles of a simulated proton air showers of energy 10^{19} eV. Hadrons, $\mu^{\pm}$, $e^{\pm}$ and γ are shown separately. The lateral distribution of the particles at ground is calculated for 870 g/cm^2, the depth of the Pierre Auger Observatory [13].

1.3 Detection techniques

As mentioned already, the cosmic ray flux decreases with the increase of energy. The flux allows to measure them directly up to 10^{15} eV with detectors mounted on balloons or space-based experiments. For higher energy particles, the flux is so low that huge detectors would be necessary to measure them directly. Indirect detection methods have been developed in order to measure the secondary cosmic ray (or EAS) flux on ground and then, via Monte Carlo simulation, retrieve the primary cosmic ray flux.

The detection techniques for EAS can be divided into two groups: particle and radiation detectors.

The particle detectors can be Cherenkov water or scintillator detectors, distributed in arrays covering wide areas of the order of hundreds or thousands square kilometers, to measure the lateral particle distribution of the EAS on ground. Examples of this kind of detectors are the Pierre Auger Observatory surface detectors (water tanks) [25] which cover about 3000 km^2 and the Telescope Array surface detector (scintillators) [26] distributed over more than 700 km^2.

These detectors only see a developed state of the shower. In every station of an array, the shower footprint is sampled. Observables are the extrapolated total particle number, energy distributions, and arrival time profiles. These are used to infer the energy, mass, composition, and arrival direction of the primary particle. Their duty cycle is basically 100%.

The radiation detectors measure radiative emission caused by charged secondary particles in air, during the shower development. The associated emissions can be UV-light (fluorescence and Cherenkov light) detected for example by the Pierre Auger Observatory and Telescope Array fluorescence detectors [27, 28], radio emission (MHz range) detected with antennas for example by LOPES and Tunka-Rex [29, 30], and microwave emission (GHz range) [31]. Fluorescence telescopes detect
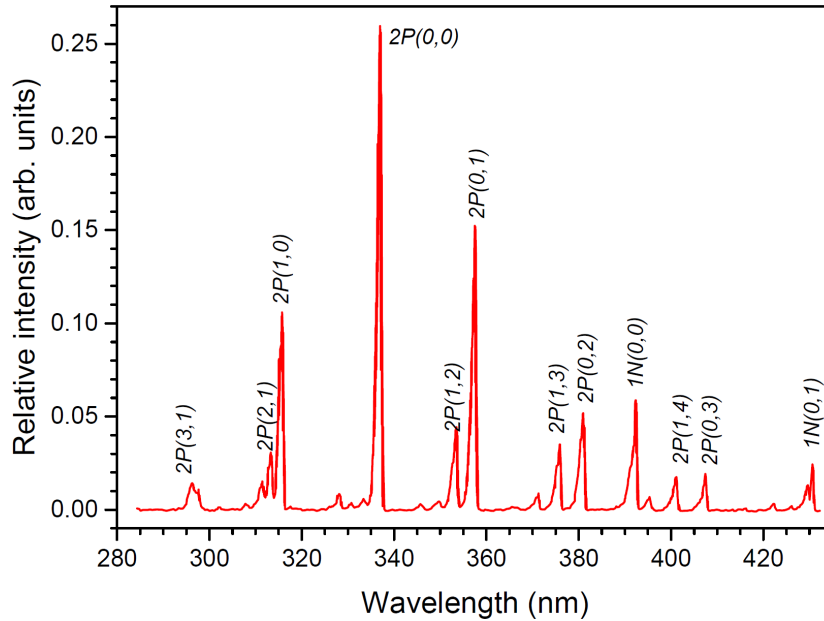
Figure 1.6: Air fluorescence spectrum of nitrogen relaxation in the UV band from 280 nm to 435 nm at 800 hPa (about 2 km) measured by the AIRFLY collaboration in the laboratory. The area is scaled to unity. This shows that 25% of the spectrum intensity is due to the main line at 337.1 nm. Plot taken from [32].

fluorescence and Cherenkov light along the development of an EAS in the atmosphere, allowing for a direct observation of the shower maximum and calorimetric measurement of the energy of the primary particle. Fluorescence telescopes can only be operated in night-time, with good weather conditions and in places with low artificial light background. A duty cycle of about 10-15% is expected for ground-based fluorescence detectors.

To get the advantages of both detection techniques, often they are used in hybrid mode, where fluorescence telescopes survey the volume above a surface detector array. Currently, the two most prominent experiments employing these techniques are the already mentioned Pierre Auger Observatory in Argentina [33] and the Telescope Array in Utah (USA) [34].

For this work the focus lies on the UV-light emission from EAS, since this will be the technique used by the JEM-EUSO project. The two most important processes for the UV-light emission from EAS are fluorescence and Cherenkov light:

- *Fluorescence light*: it is emitted by the relaxation of nitrogen molecules that

have been excited by the interaction with charged particles from an air shower, mainly $e^{\pm}$. Therefore, the energy deposit is proportional to the number of electrons and positrons in the air shower. Since the energy deposit is stored in different oscillation and rotation modes of the molecule, the spectrum presents lines at discrete wavelengths, in the range from 290 nm to 430 nm of the UV-band, with the most intense emission around 377.1 nm (Figure 1.6). The overall fluorescence emission along the shower development is isotropic [32].

- *Cherenkov light*: it is produced when charged particles move through a dielectric medium with a velocity that is higher than the phase velocity of light in that medium [35]. In that case, the particle ionizes the medium in its path, leaving a locally excited path behind. The following relaxation is done via the emission of light. Since the velocity of the particle was higher than the phase velocity of light, the interference of the electromagnetic waves is constructive and a cone-shaped wave front is generated. The opening angle of the cone depends on the refractive index of the medium and the speed of the particle. The emission spectrum of Cherenkov radiation is continuous and the photon yield is higher for shorter frequencies, i.e. it presents higher intensities for UV-light than for visible light.

Chapter 2

JEM-EUSO

As seen in Chapter 1, many questions are still open regarding UHECRs, in particular about their elemental composition, sources and acceleration mechanism. For deeper investigations, a significantly higher statistics is needed. Since the rate for cosmic rays at an energy of $E = 10^{20}$ eV is about 1 particle per km^2 per century, very large detector areas are needed to increase statistics, much more than the current largest cosmic ray detector array, the Pierre Auger Observatory [33], covering 3000 km^2. The JEM-EUSO mission would be one solution for creating a detector area of the order of 10^5 km^2. The idea of JEM-EUSO is to detect the fluorescence light emitted during the path of EASs through the Earth's atmosphere from space.

The idea of a cosmic ray fluorescence detector based in space was born in 1979 by Linsley. The major challenge was the faint light because of the distance to the shower and the optical imaging required for geometrical reconstruction and X_{max} observations. The initial project was called SOCRAS (Satellite Observatory of Cosmic Ray Showers) [36]. Y. Takahashi took up this idea in the 1990s and developed it further, with the Maximum-energy Auger air Shower Satellite (MASS) [37], then renamed to Orbiting Wide-angle Light-collectors (OWL) proposed in 1996, which used Fresnel optics to enlarge the field of view to $\pm30°$ yielding an observational area of 10^5 km^2. A following proposal have been done in 1999 by L. Scarsi for the Extreme Universe Space Observatory (EUSO) which would have been mounted on the Columbus module of the International Space Station (ISS). The next years were followed by ups and downs, mostly by the tragic space shuttle Columbia disaster on 1st February 2003 which put all plans on hold. EUSO was frozen by ESA in 2005 due to different difficulties.

The possibility to mount EUSO on the Japanese Experiment Module (JEM) of the ISS, offered a new window of opportunity, and the JEM-EUSO mission began in 2007.

The JEM-EUSO collaboration consists of 358 scientists in 95 institutes in 16 countries (Spring 2017). The major space agencies involved are European Space Agency (ESA), Japan Aerospace Exploration Agency (JAXA), National Aeronautics and Space Administration (NASA), and Russian Federal Space Agency (ROSCOSMOS). In this chapter the JEM-EUSO mission is introduced. The scientific goals, the de-

tector design and the pathfinder experiments are explained. Further details on JEM-EUSO and its pathfinder experiments can be found in [38, 39].

2.1   Scientific goals

The main objective of JEM-EUSO as a space-based fluorescence telescope is the increase of exposure to cosmic rays at energies exceeding $5 \cdot 10^{19}$ eV (GZK threshold). Only few known astrophysical objects are viable sources for UHECRs and they have to be within the GZK horizon, with a radius of about 100 Mpc. Until now no sources have been identified. Protons with energy above $8 \cdot 10^{19}$ eV could directly point back to their sources, since their deflection due to magnetic fields would be small. Therefore, the main goals of JEM-EUSO are:

- detection and high statistics measurements of trans-GZK cosmic rays,

- study of the anisotropy of their arrival directions,

- identification of sources,

- measurement of the individual sources' energy spectra.

The statistics needed to reach these goals are at least 10^3 events [40]. Figure 2.1 shows the exposure of JEM-EUSO compared with those of other large-scale cosmic-ray experiments. (a) shows that in the last decades, the exposure has been improved, increasing the size of the experiments. A further increase in size of ground-based detector arrays is unlikely. The figure shows that an exposure of one order of magnitude larger than the largest UHECR experiments could be reached by JEM-EUSO in less then 5 years of operation. Regarding the study of anisotropy in the arrival directions of EECR, as orbiting telescope, JEM-EUSO has the advantage that it could uniformly cover the celestial sphere over both the northern and southern hemispheres, as shown in (b). Studies on the anisotropy scenarios have been done in [41].

In addition to the main goals given before, the JEM-EUSO mission also has exploratory objectives:

- detection of extreme energy gamma rays,

- detection of extreme energy neutrinos,

- study of galactic and extra-galactic magnetic fields,

- atmospheric phenomena like nightglows, plasma discharges, and lightning and meteors.

The GZK effect and the interactions in the dense regions of the acceleration processes do not only place a limit on the propagation of charged nuclei, but continuously produce UHE neutrinos and γ-rays through pion decay. UHE neutrinos and γ-rays can

(a) Exposure comparison   (b) JEM-EUSO exposure distribution
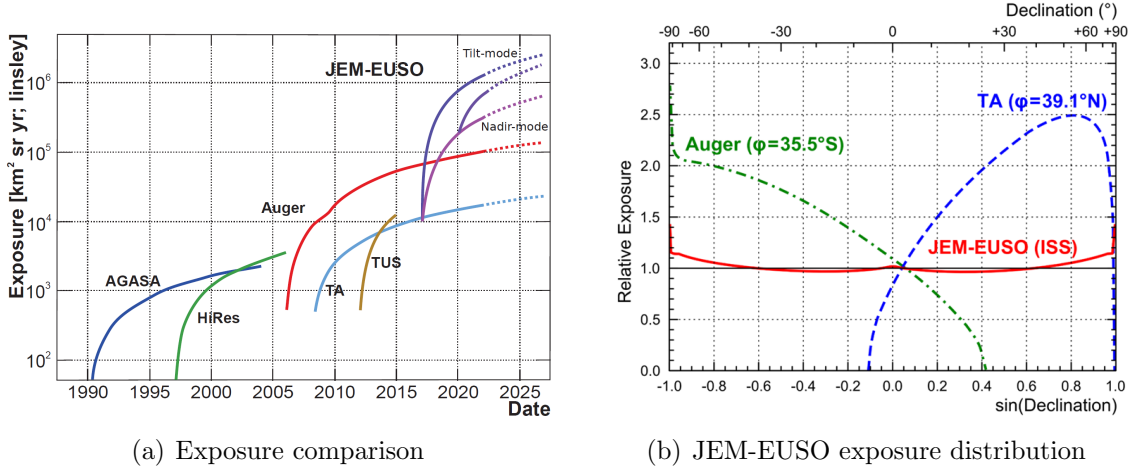
Figure 2.1: (a) Exposure versus time of cumulative exposure of JEM-EUSO, in km^2 sr yr (or Linsley units), compared to those of several UHECR observatories from 1990 to 2025. Exposures from 2011 onward are estimated for the Pierre Auger Observatory, Telescope Array and JEM-EUSO. This scenario is valid for a JEM-EUSO launch in 2017. Image adopted by [42] from [43]. (b) Relative deviation from uniformity of the expected JEM-EUSO exposure versus the declination of the celestial sky, compared with the exposure of the Pierre Auger Observatory and Telescope Array, covering the southern and northern hemisphere respectively. The line implies a uniform full sky coverage. Image adopted from [43].
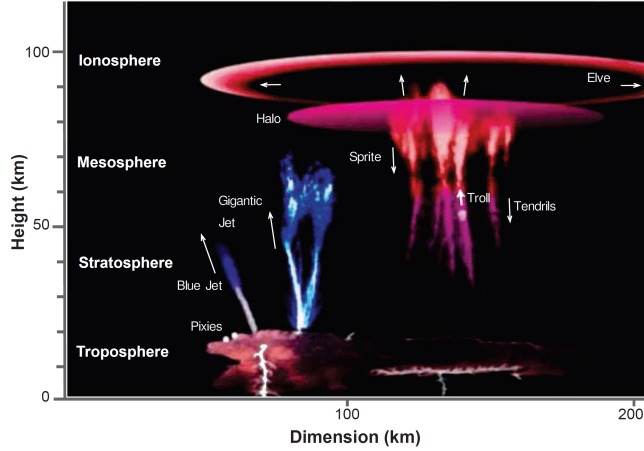
Figure 2.2: Artistic collection of various transient luminous events (TLE) by D. D. Sentmann (Univ. of Alaska in Fairbanks).

point back to their origin, since they interact rarely with the interstellar matter and are not deflected by magnetic fields, and can provide information on the physical processes of the source candidates. Some exotic dark matter theories predict a high γ-ray flux, which could be proven if this radiation is detected. With the high statistics measurements by JEM-EUSO, UHE neutrinos could be discriminated via the position of the first interaction and shower maximum, while UHE γ-rays can be identified by the sensitivity of the shower maximum to the geomagnetic field and

the early interaction in the atmosphere.

Also the magnetic fields can be studied with cosmic rays, because depending on their energy, different charged particles experience different deflection angles from magnetic fields. Therefore, if the particles' characteristics and their sources are known, galactic and extra-galactic magnetic fields can be determined.

Atmospheric phenomena would be studied too. Indeed, the strength of the fluorescent light and the Cherenkov signal received from EAS, as well as the reconstruction efficiency and errors, depend on the transparency of the atmosphere, the cloud coverage and the height of the cloud top. Therefore, JEM-EUSO will observe the conditions of the atmosphere in the FOV of the telescope making use of a state-of-art atmospheric monitoring system.

Transient Luminous Events (TLEs) occur in the upper atmosphere in association with thunderstorms. The spatial resolution of a few kilometers together with the time resolution of microseconds can provide important data for the understanding of the mechanisms of the formation of the filamentary structures of the plasma, especially in the "streamer beard" of the sprites. A graphical representation of the TLEs can be seen in Figure 2.2.

Meteors, meteorites and fireball observations are key to the derivation of both the inventory and physical characterization of small solar system bodies orbiting in the vicinity of the Earth. In comparison to the observation of extremely energetic cosmic ray events, meteoroid phenomena will appear very similar but in contrast are very slow, since their typical speeds are of the order of a few tens of km/s.

2.2 Detector design

The JEM-EUSO telescope consists of an optical system, with three Fresnel lenses and a focal surface made of Multi-Anode PtotoMultiplier Tubes (MAPMTs), plus the electronics and read out subsystems.

Optical system

The lenses have a diameter of 2.65 m and are made of Polymethyl-Metacrylate (PMMA), which has high UV transparency in the wavelength range from 330 nm to 400 nm [44]. The first and the third lens are curved double sided Fresnel focusing lenses, the second lens has a Fresnel surface on one side and a diffractive optical element (DOE) on the other. The optics are made with corrections for aberrations and have a focal point of roughly 2 mm in diameter at the focal surface. The diffractive system allows for a wide FOV of about $\pm 30°$ and an angular resolution of $0.07°$ (~ 550 m projected on ground). Figure 2.3 shows a scaled-down optical system of the one foreseen for JEM-EUSO.
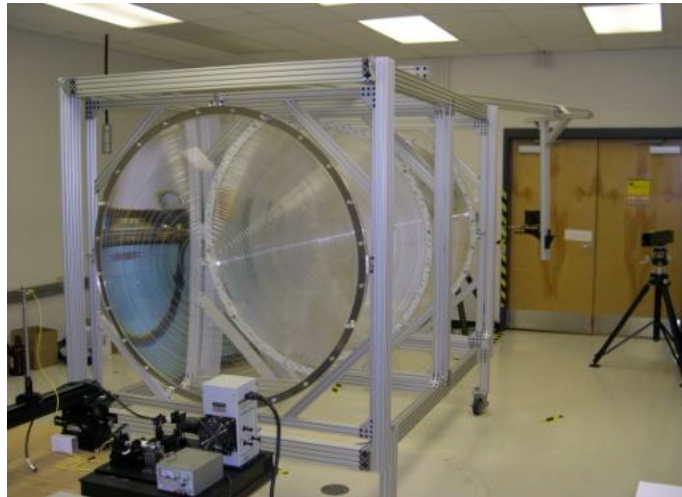
Figure 2.3: Three Fresnel lenses mounted on a support frame (smaller than those foreseen for JEM-EUSO).

Focal surface

The focal surface of JEM-EUSO consists of roughly 5000 MAPMTs which form an active area of about $2.3 \times 1.9\,\mathrm{m}^2$. The concave shape of the focal surface is the surface of a sphere with a radius of 2.5 m. Every MAPMT has 8×8 pixels and is glued with an UV-transmitting band pass filter *Schott BG3* for the range of 290 nm to 430 nm. 2×2 MAPMTs form one Elementary Cell (EC) and 3×3 ECs form one Photo-Detector Module (PDM). 137 PDMs form the complete JEM-EUSO focal surface. This "hierarchy" is depicted in Figure 2.4. All the pathfinders (described in Section 2.4) are equipped with only one PDM, and it is described more in detail

in Figure 2.5. Figure 2.6 shows the efficiency for light parallel to the optical axis, the band pass filter *Schott BG3* transmittance, the PMT efficiency and the total efficiency, as evaluated in [45]. The PMT efficiency is actually the Photo-Detection Efficiency $PDE = QE \cdot CE$, where QE is the PMT quantum efficiency and CE is the the PMT collection efficiency (generally 80%).
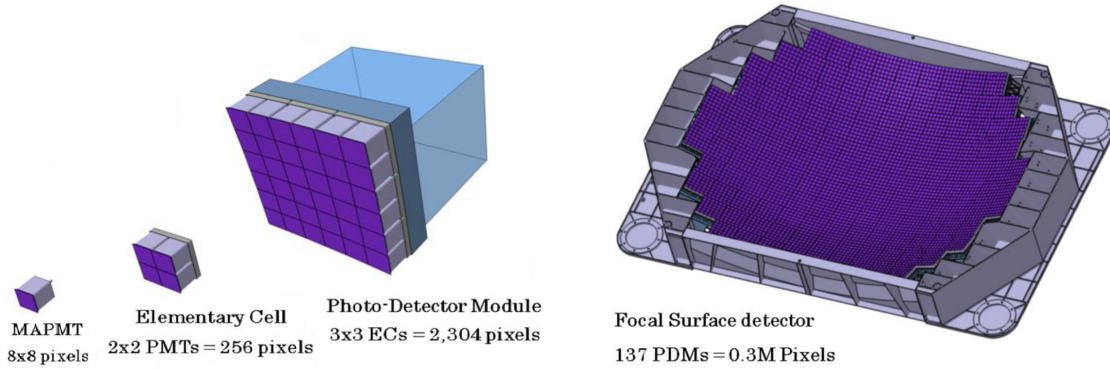
Figure 2.4: Modular "hierarchy" which goes from one MAPMT to the complete focal surface made of 137 MAPMTs.

Electronics

Because of the complex structure of the MAPMTs, special boards for power supply and signal measurements were designed. The front-end readout is done by custom made electronics using 64-channel Application Specific Integrated Circuits (ASICs), each one reading the signal of one 64-pixels MAPMT. They are called Spatial Photomultiplier Array Counting and Integrating Chip (SPACIROC) [45, 46]. They have built-in preamplifiers for single-photon counting and charge-to-time converters, to perform charge measurements for 10 to 1500 photoelectrons. To be able to use these ASICs in space, the power consumption was designed to be 1 mW per channel and radiation hardness is ensured.

After digitization of the triggered MAPMT-signals, the data of one PDM is transmitted to the Field-Programmable Gate Array (FPGA) board which controls the particular PDM. The first level trigger is also implemented into the FPGA boards. The data are sent to one of twenty Cluster Control Boards (CCBs), each one controlling a subset of FPGA boards. From there data are sent to the JEM-EUSO CPU for the storage.

The data transport from the ISS to Earth will be done via standard procedures, e. g. satellite down-link.
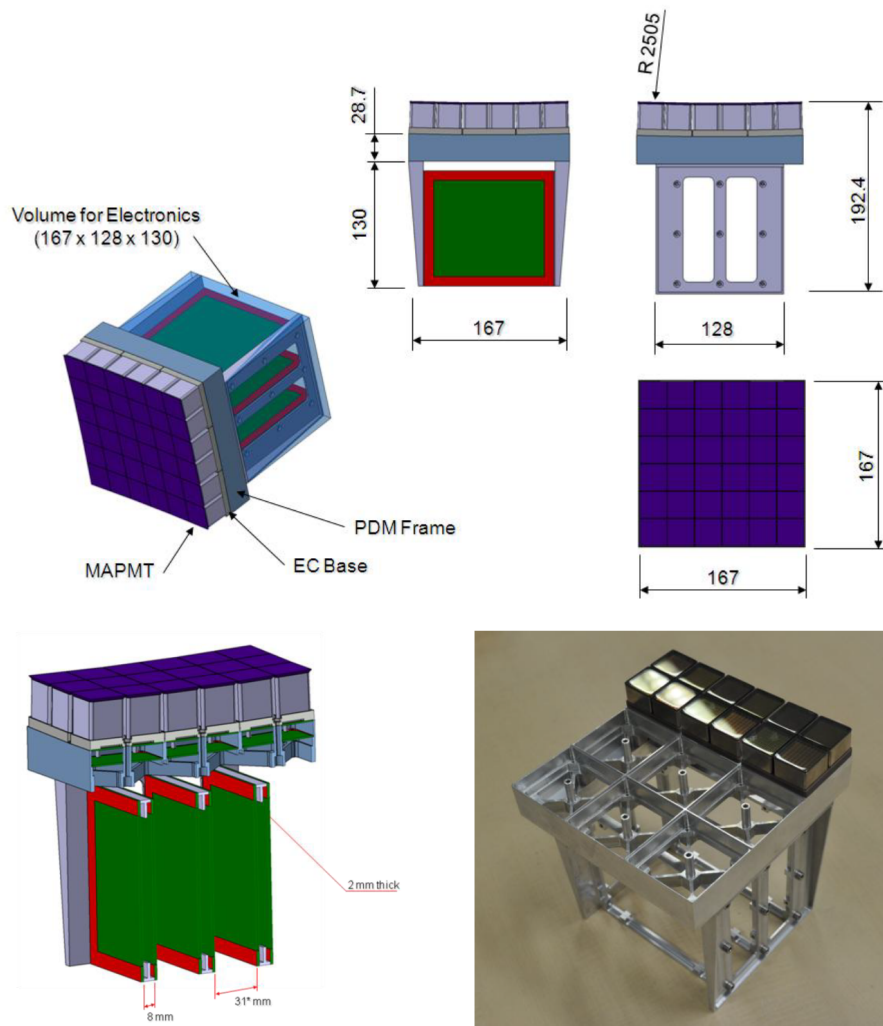
Figure 2.5: Design of the Photo-Detector Module (PDM) with lengths in mm. The frontal and lateral views are shown. The green blocks represent the Application Specific Integrated Circuits (ASICs) boards for the read-out of the signal. The picture in the bottom right shows the structure supporting the Elementary Cells (ECs) and three of them in a row. Each EC is an array of 2×2 Multi-Anode PhotoMultiplier Tubes (MAPMTs).
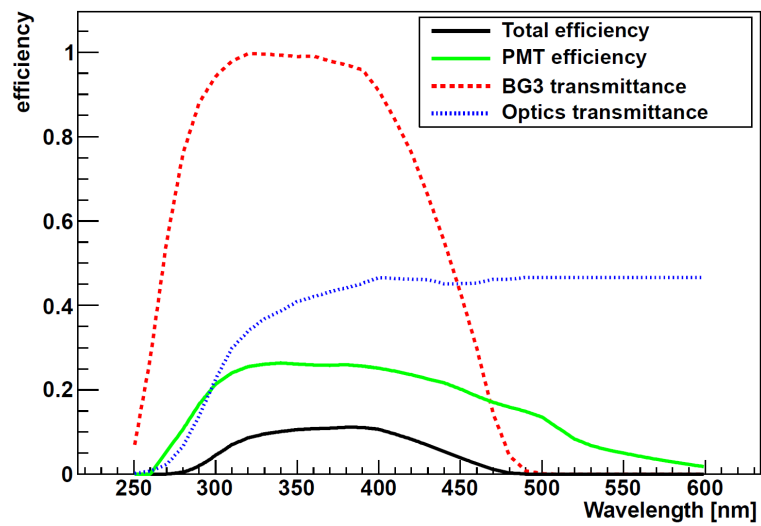
Figure 2.6: The optics efficiency for light parallel to the optical axis is plotted with a blue dotted line, the band pass filter *Schott BG3* transmittance with a red dotted line, PMT efficiency with a green solid line and the total efficiency with a black solid line. Image taken from [45].

2.3 Observation principle

JEM-EUSO will orbit the Earth on board the ISS with a mean altitude of 400 km and an orbit inclination of 51.2° with respect to the equatorial plane of the Earth. The ISS is occasionally lowered for docking maneuvers of transport vehicles by about 70 km or raised to reduce air friction. The duration of one orbit is about 90 minutes with about 36 minutes on the night-side of the Earth. The detection principle of JEM-EUSO is depicted in Figure 2.7 (a). The instantaneous observation area for JEM-EUSO onboard the ISS will be $1.4 \cdot 10^5 \, \text{km}^2$ in *nadir mode*. It will also be possible to operate the telescope in *tilt mode*, tilting the telescope by several degrees in order to increase the observable area. The detection of EASs will be done via UV light detection.

An EAS developing through the atmosphere produces fluorescence and Cherenkov light, and if this happens within the FOV of JEM-EUSO, the EAS can be detected. The fluorescence light is isotropically emitted and the Cherenkov light is emitted in forward direction of the EAS. Since JEM-EUSO will be above the atmosphere, Cherenkov light cannot be seen directly but has to be either scattered in the atmosphere or reflected on clouds or the ground. In Figure 2.7 (b), the characteristic light profile of a detected EAS is plotted as a function of the arrival time at the telescope aperture for a shower with a zenith angle of 60°. The direct fluorescence component is the main component of the signal, distributed over several GTUs*. The Cherenkov light arrives scattered, or reflected by clouds or ground. The latter appears as a peak well separated from the fluorescence contribution and the peak height is dependent on the abundance of clouds, the state of the atmosphere, and ground conditions.

JEM-EUSO aims to detect inclined extensive air showers, for which the length projected on the focal surface results to be longer than that of vertical showers. On the contrary, ground-based cosmic ray detectors are more efficient with vertical and low inclination showers since they develop through shorter distances in the atmosphere and, therefore, arrive on ground with more residual energy than the inclined ones, at a given energy. An example of how EASs detected with JEM-EUSO would appear is given in Figure 2.8. It is evident that the whole shower development would be observed by one or a few PDMs, depending on the shower inclination.

---

*One GTU is the time frame within which the signal is integrated, corresponding to the time resolution of the detector, lasting $2.5 \, \mu s$. It has been defined as the time in which a shower (or the light) crosses the FOV of one pixel
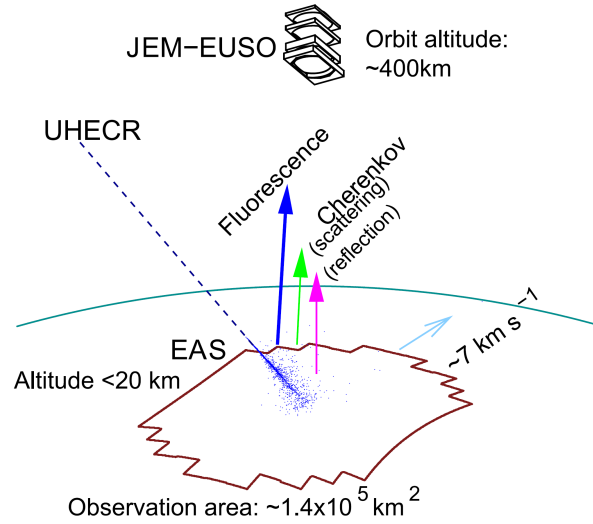
(a) JEM-EUSO observation principle.
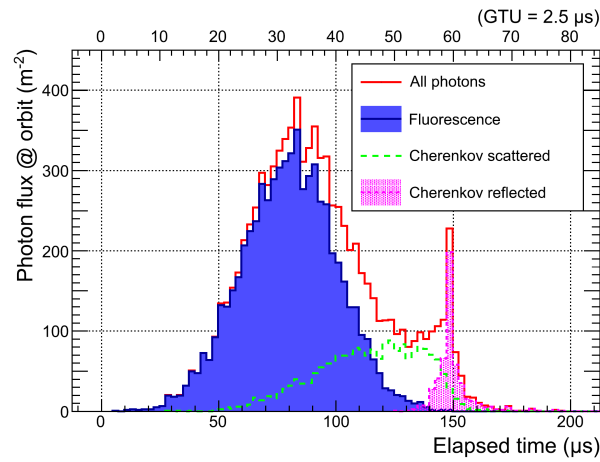
(b) Simulated photon flux at aperture.

Figure 2.7: Illustration of UHECR observation principle in the JEM-EUSO mission. For the telescope at $H_0 \sim 400$ km altitude, the main signals are fluorescence photons along the EAS track and Cherenkov photons diffusely reflected from the Earth's surface (a). Components of the photon signal at the entrance aperture for a standard EAS with $E = 10^{20}$ eV and $\theta = 60°$ as simulated by the EUSO Simulation and Analysis Framework (ESAF) (b). Images taken from [47].
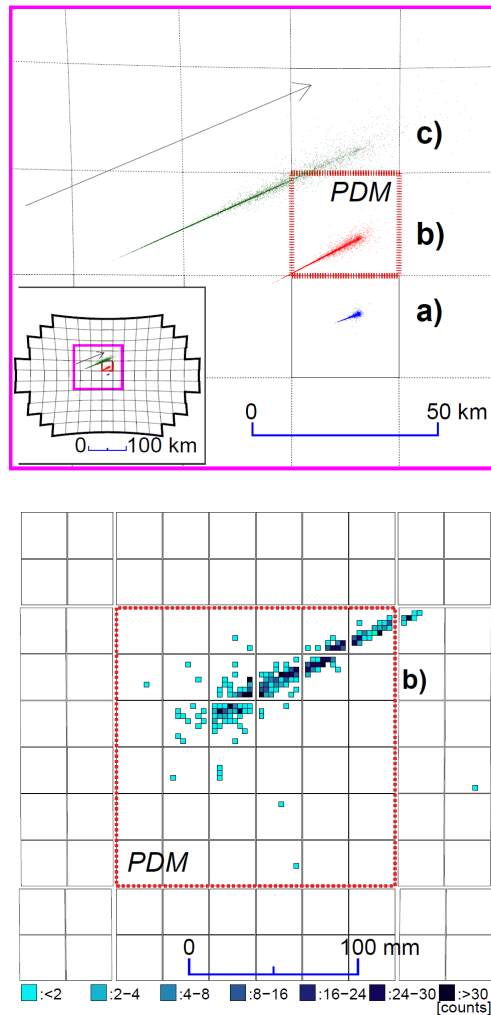
Figure 2.8: Top panel shows the projected tracks on the Earth's surface for EASs with $E = 10^{20}$ eV and zenith angles of a) $\theta = 30°$, b) $\theta = 60°$ and c) $\theta = 75°$, as simulated by the EUSO Simulation and Analysis Framework (ESAF). The dashed grid indicates the corresponding areas for the FOV of individual PDMs. In the sub-panel, the corresponding area of the plot is represented within the entire FOV. Bottom panel shows the image on the focal surface for the case b). Here the grid denotes the array of PMTs. The matrix of pixels is indicated with the integral number of counts in discrete scale. The regions enclosed by red dashed lines in both panels refer to the same PDM. Image taken from [47].

Since the atmospheric conditions have to be known at all times an EAS is recorded, JEM-EUSO will have an Atmospheric Monitoring System (AMS) installed. It consists of an infrared (IR) camera and a Light Detection and Ranging (LIDAR) system. With the IR camera clouds can be seen and the altitude of their top can be estimated. The LIDAR is used to get information about scattering of light in the atmosphere. Additional information about the atmospheric state can be drawn from Global Atmospheric Models (GAMs). The concept of the AMS is depicted in Figure 2.9.

The atmospheric information is important to reconstruct the energy and maximum of the EAS properly.
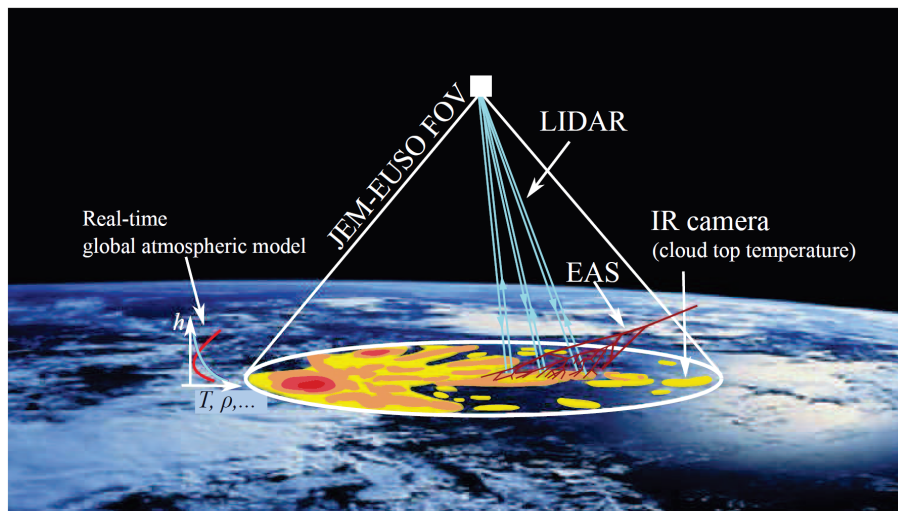
Figure 2.9: Conceptional sketch of the AMS of JEM-EUSO, with IR camera, LIDAR, and real-time GAMs data. Image taken from [42].

2.4 Prototype experiments and future missions

In order to test the design of JEM-EUSO and to do research and development with the apparatus, several prototype experiments have been designed and some of them are operative: EUSO-Balloon, EUSO-TA, EUSO-SPB and Mini-EUSO. Moreover, since the JEM-EUSO mission is at least temporarily suspended for fundings reasons, another option to launch and install a large-size cosmic ray fluorescence detector in space is considered, K-EUSO.

EUSO-Balloon

EUSO-Balloon is a pathfinder that looks downwards from a balloon, at 40 km altitude, to observe EAS and the UV night background [48]. It consists of one PDM with two Fresnel lenses, which allow a FOV of $\pm 5.5°$, as well as an IR camera prototype. The PDM uses the same electronics that are planned for JEM-EUSO. The IR camera is a smaller version of the one planned for JEM-EUSO. The instrument is accommodated inside a housing. The housing has crash pads and a flotation device to be safe for a land and water landing (Figure 2.10). In August 2014 the detector was launched from Timmins (Canada). During the flight of about 5 hours at an altitude of roughly 40 km, EUSO-Balloon measured the night sky background, laser shots and light pulses coming from a Xe-flasher, fired from a helicopter flying under the balloon. It also was used for testing the trigger algorithm of JEM-EUSO. Preliminary analysis of the data indicates an average night sky background of roughly 300 photons $\mathrm{m^{-2}\,sr^{-1}\,ns^{-1}}$ and shows the technical feasibility of the instrument.
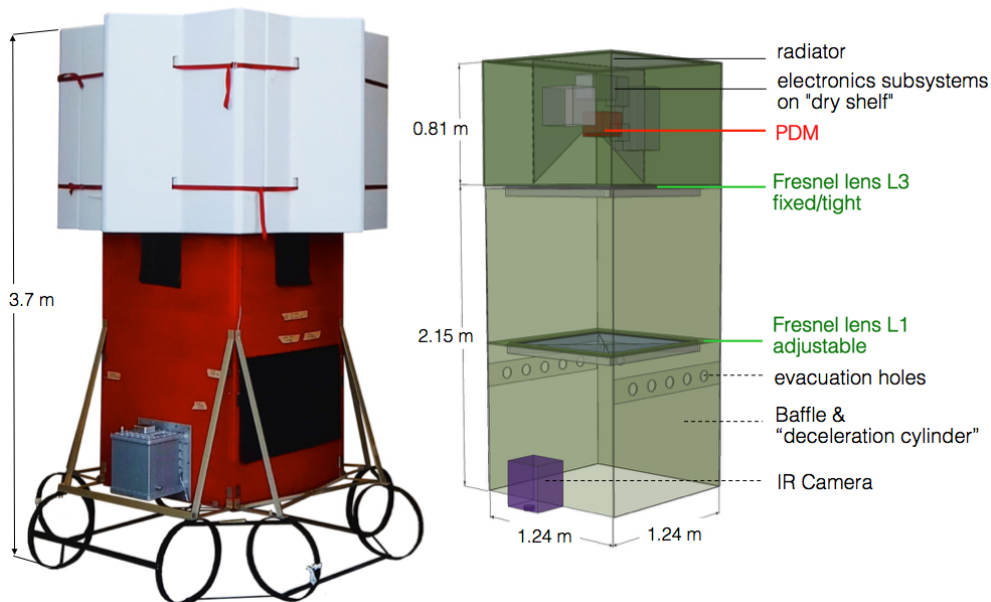
Figure 2.10: Picture of the EUSO-Balloon detector before the launch.

EUSO-SPB

EUSO-SPB is the successor experiment of EUSO-Balloon launched onboard a NASA Super Pressure Balloon (SPB) from New Zealand in Spring 2017 [49]. The detector structure is almost the same as the one of EUSO-Balloon (Figure 2.11).
It will perform long-duration flights of more than one month at an altitude of about 50 km and will look downwards towards the Earth with a FOV of $\pm 6°$. Next to the PDM of MAPMTs and behind two PMMA Fresnel lenses an additional, smaller camera made of SiPMs developed at KIT (SiECA) is installed. Its goal is to detect UHECRs and observe atmospheric phenomena for the first time from near space.
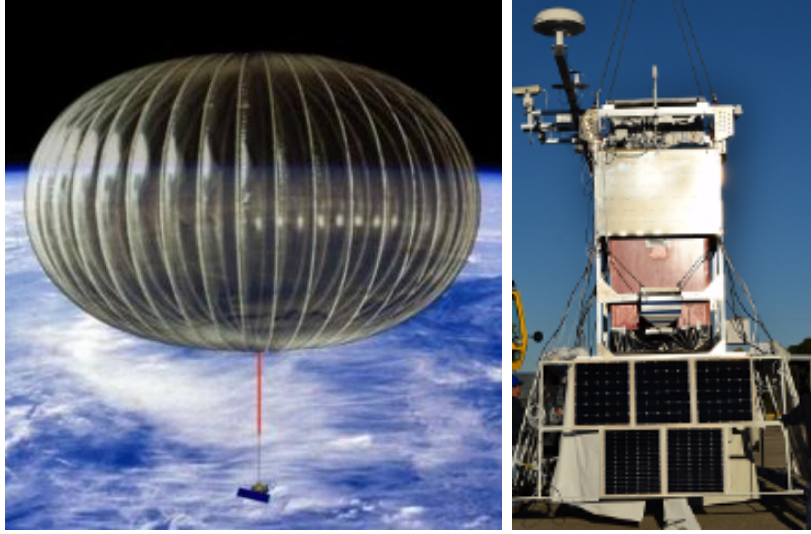
Figure 2.11: A NASA SPB (left [50]) and the EUSO-SPB at the first hang tests (right [51]).

EUSO-TA

EUSO-TA is a ground-based pathfinder experiment for JEM-EUSO [52, 53]. It is located at the TA site in Utah (USA), in front of one of the fluorescence detector stations of Telescope Array, which is used as an EAS trigger for EUSO-TA (Figure 2.12). The pathfinder consists of one PDM and two Fresnel lenses, which allow a FOV of $\pm 5.25°$. Since an Electron Light Source (ELS) as well as a LIDAR is located at TA site, this is a good location for a pathfinder experiment. The laser pulses and the induced showers from the ELS can be used for calibration purposes. Tests on the trigger algorithm foreseen for JEM-EUSO, and detection of EASs in coincidence with TA have been done. EUSO-TA was deployed at the TA site in March 2015. Several data acquisition campaigns have been performed and others are planned for the future. Further research and development with SiPMs instead of MAPMTs can be done.
This thesis focuses on EUSO-TA, therefore a more detailed description of the detector, the data acquisition, the data analysis and simulation studies are given in the following chapters.

Figure 2.12: Picture of the EUSO-TA detector in front of the TA fluorescence detectors station.

Mini-EUSO

Mini-EUSO will be installed inside the Russian module of the ISS behind an UV-transparent window, looking to the Earth in nadir position [54] with a FOV of $\pm 19°$. It will be launched in Autumn 2017 and be active for a few years orbiting around our planet. Its main goal is to define an almost global map of the UV background coming from the Earth during night time. It will also observe atmospheric phenomena, meteors and can even provide the first experimental evidence for the existence of Strange Quark Matter (SQM). It will be possible also to study the large-scale presence and evolution of the phenomenon of bioluminescence produced by algae, plankton and other such organisms to gain information and knowledge of the state of pollution of the oceans. Mini-EUSO also hosts a small SiPM-based camera, to test such sensors arrays in space for the first time. Present are also an IR camera, and a camera for visible light (Figure 2.13).
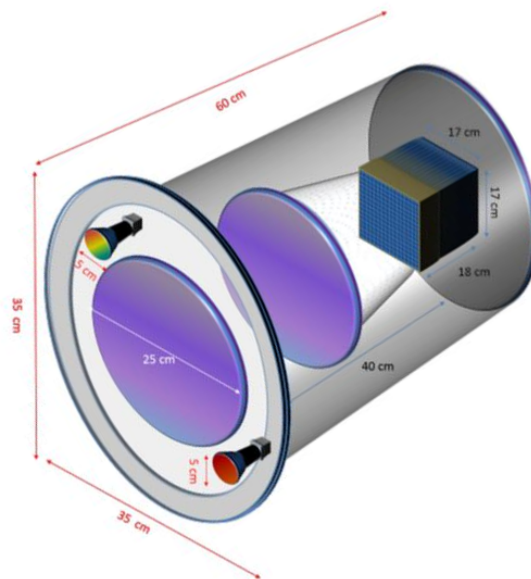
Figure 2.13: Design of the Mini-EUSO detector. Image taken from [54].

K-EUSO

The JEM-EUSO mission is currently suspended for financial problems. To succeed in the goal of detecting UHECRs with high statistics, another option developed in parallel is an improved version of the Russian KLYPVE mission, defined as K-EUSO. The KLYPVE project, included into the ROSCOSMOS long term program of experiments onboard the ISS, uses a compound mirror concentrator, instead of Fresnel lenses, reaching a better efficiency but a significantly smaller FOV (Figure 2.14). A prototype of the KLYPVE detector, the Transient Ultraviolet Setup (TUS) has been launched in 2016 as a pathfinder on the Russian satellite Mikhailo Lomonosov.
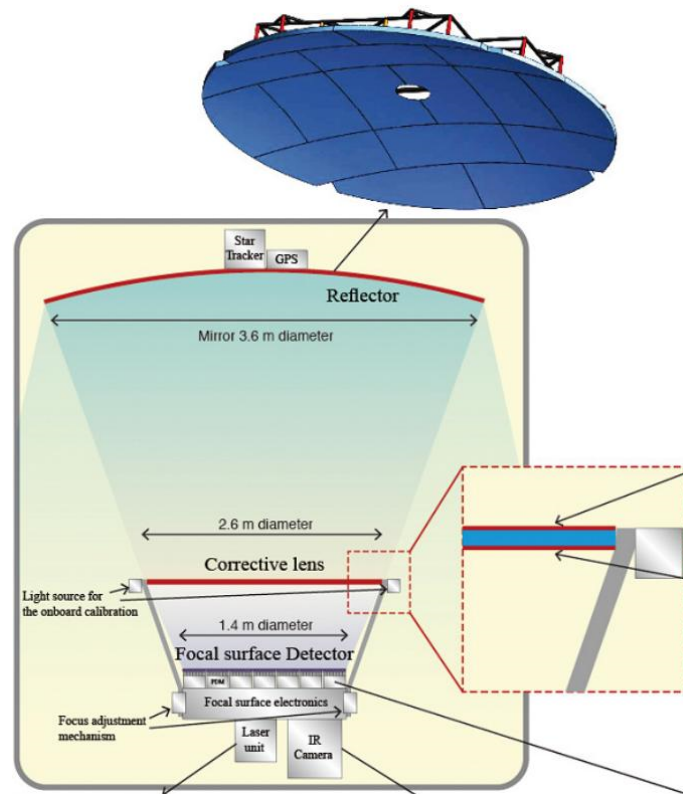
Figure 2.14: The KLYPVE detector on the MRM-1 module of the ISS. Image taken from [55]

To eliminate severe off-axis aberration and reduce the spot-size, a corrective Fresnel lens is included in the telescope system. The thickness of the lens is around 1 cm. In the current baseline system the diameter of the reflector and the lens-corrector are 3.4 m and 1.7 m respectively. In this configuration the field of view reaches up to $\pm14°$, with a granularity of $0.058°$, equivalent to a scale of 0.4 km on ground. The focal surface consists of 1900 MAPMTs, for a total of about 120,000 pixels. K-EUSO will be located on the external facility of the Russian MRM-1 module of the ISS. It will be delivered to the ISS by the Progress-TM vehicle, implying that the various components have to pass through a cylindrical lock of 70 cm diameter and 120 cm length. This requires segmentation of all the major components of the

system, including the lens, the mirror and the focal surface, and implies deployment and assembly in space. The annual exposure will be a factor of two that of the Pierre Auger Observatory, about 20% the one of JEM-EUSO. The threshold will be lower than that of JEM-EUSO thanks to the larger collection efficiency of the reflective optics. Details can be found in [56, 57, 58]. The mission is planned to be launched in 2020.

Chapter 3

EUSO-TA

3.1 Motivation and goal

EUSO-TA is a pathfinder detector of the JEM-EUSO project. The purpose of this experiment is to validate some aspects of the observation principle of JEM-EUSO and the detector design detecting EASs from ground. It is located at the Telescope Array (TA) [59] site in Utah (USA), in front of the Black Rock Mesa fluorescence detectors (BRM-FDs) station [28].

As all the fluorescence cosmic ray detectors, EUSO-TA works in night time. The best conditions are clear and moon-less sky, to reduce effects of atmospheric and cloud attenuation, and to not be affected by the strong background due to the light reflected by the Moon, respectively. The elevation of the instrument can be manually changed from 0° to 25°, whereas the azimuth is fixed to 53° from North counterclockwise.

One advantage of the EUSO-TA location is the possibility to use two facilities present at the TA site for calibration purposes: the Central Laser Facility (CLF) [60] and the Electron Light Source (ELS) [61]. These facilities will be described in Section 3.2.

The second advantage is to have the possibility to acquire data with external trigger, i.e. in coincidence with BRM-FDs. This is an important point since this acquisition mode allows to know which events crossed the EUSO-TA field of view (FOV) and then, from the event reconstruction made by the TA-group, the nature of the event (i.e. direction, distance, energy etc.) are known and usable for further analysis. Another acquisition mode consists in using an internal trigger, also called first level trigger (L1), implemented for the JEM-EUSO experiment and described in Section 3.4. The internal trigger has been tested during one of the EUSO-TA data acquisition campaigns.

EUSO-TA has a smaller FOV than BRM-FDs, so it is able to detect just a small portion of the cosmic ray air showers. However, due to its high spatial resolution (the FOV of one pixel is 0.19°), it can observe the cosmic ray air showers with much higher detail than TA, useful for example for the evaluation of their lateral distribution, as shown in Section 5.1.2.

3.2   Telescope Array site

The Telescope Array (TA) experiment is the largest cosmic-ray detector in the northern hemisphere. It is located in a desert area close to Delta, Utah, USA.
TA consists of 507 surface detectors (SDs) deployed on a square grid with 1.2 km spacing, covering an effective area of about 700 km^2 schematized in Figure 3.1 [26].
  The SD array is overlooked by three stations of fluorescence detectors (FDs or
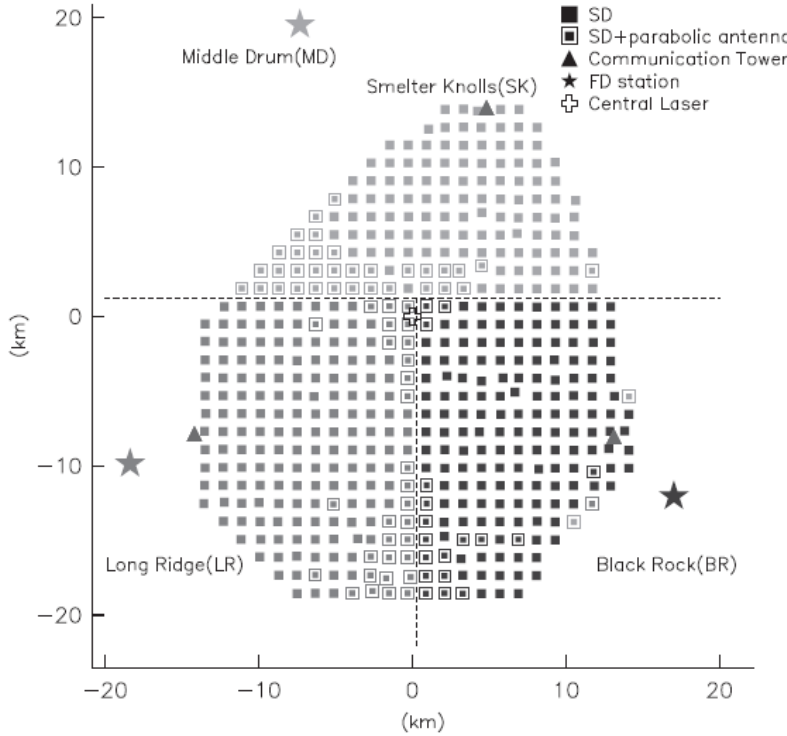
Figure 3.1: Layout of the Telescope Array in Utah, USA. Squares denote 507 Surface Detectors (SDs). There are three subarrays controlled by three communication towers denoted by triangles. The three star symbols denote the fluorescence detector (FD) stations. Image taken from [26].

TAFDs). One FD station, called *Middle Drum* (MD) and located northwest of the SD array, consists of 14 FDs previously used in the High Resolution Fly's Eye (HiRes) experiment [62]. Two other stations are located at the southeast and southwest ends of the SD array, respectively called *Black Rock Mesa* (BRM) and *Long Ridge* (LR), each of 12 newly designed FDs [28]. At each station, 12 FDs are arranged in two layers of six telescopes each. The upper-layer telescopes are oriented to view the sky at elevations from 3° to 18.5°, and the lower layer observes higher elevations, from 17.5° to 33°, for a combined elevation coverage between 3° and 33°. The combined azimuth coverage is 108° at each station, with BRM looking west and northwest, and LR looking east and northeast.
The BRM and LR FDs have spherical mirrors with a diameter of 3.3 m, which are composed of 18 hexagonal segments. The camera design of these FDs consists of 256

(a) The PMT camera of the TA Fluorescence Detector (TAFD)

(b) Black Rock Mesa FD station

Figure 3.2: (a) the PMT camera (photograph from a prototype) and (b) the spherical mirrors installed inside the Black Rock Mesa FD station. Images taken from [28].

hexagonal photo-multiplier tubes (PMTs) arranged in a 16×16 honeycomb array, installed at the focal plane of the spherical mirror (Figure 3.2).

In order to calibrate the atmospheric conditions and relative gains among the three FD stations, a Central Laser Facility (CLF) is installed at the center of the TA site, at a distance of 20.85 km from each station. A UV laser with a wavelength of 355 nm fires 300 vertical shots in 30 s every 30 min, with a frequency of 10 Hz [60]. The standard laser energy is 4 mJ, but can be adjusted; the light scattered from the beam is equivalent to that produced by an equally distant UHECR with energy of $10^{19.5}$ eV.

For measurements of the attenuation in atmosphere, TA has a laser system called LIght Detection And Ranging (LIDAR) [63] which is located 100 m away from the BRM station. The atmospheric attenuation is calculated from the amount of backscattered light measured by a PMT at the focus of a telescope mounted in parallel with the laser beam (355 nm wavelength, 4 mJ power and 1 Hz frequency). The attenuation variation at ground level is measured by making horizontal shots and its variation with altitude by firing vertical shots. The LIDAR is operated before the beginning and after the end of an FD observation, twice a night.

The Electron Light Source (ELS) is a compact linear accelerator located 100 m away in front of the BRM station. It can fire an upward going electron beam with an output of 10^9 electrons per pulse with an energy of 40 MeV at a frequency of 0.5 Hz. The fluorescence light generated by the interaction of electrons with Nitrogen molecules in the atmosphere corresponds to photons emitted from 10^{20} eV shower injected 20 km away from BRM. Since the fluorescence photons induced by electron beams are produced by the identical phenomena that produce photons from EAS, it can be used for end-to-end absolute energy calibration at BRM [61]. During the measuring time of EUSO-TA relevant for this thesis, unfortunately no coincident

operation of the ELS and EUSO-TA was possible.

Figure 3.3 shows the satellite (a) and the front (b) view of EUSO-TA at the BRM station. Both FOVs are directed towards the CLF and the ELS (visible in the image (a)).

(a) BRM site

(b) EUSO-TA at BRM site
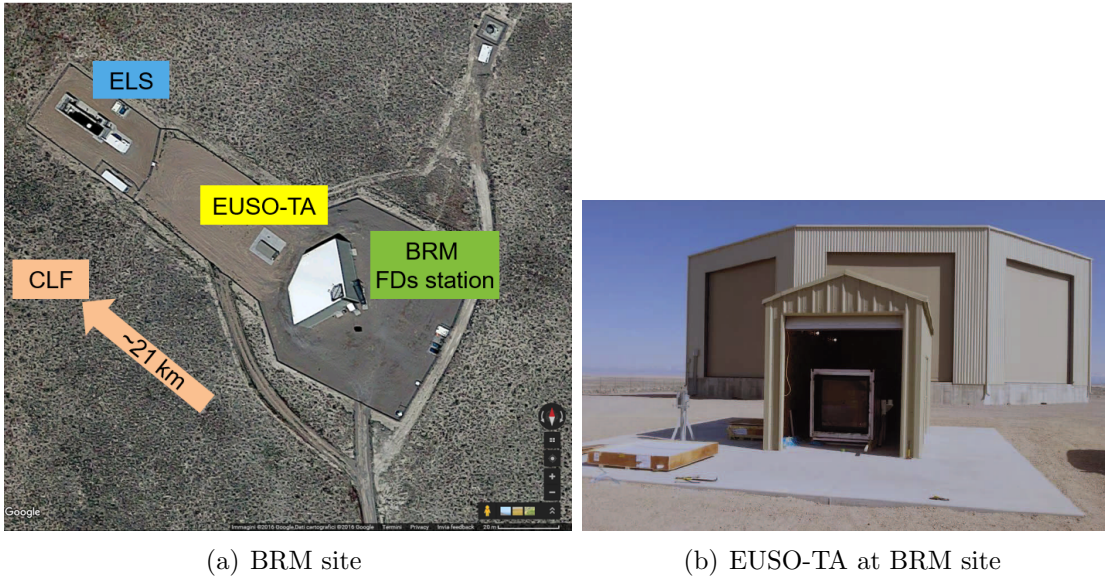
Figure 3.3: Black Rock Mesa site from Google Maps (a) and EUSO-TA dome in front of BRM-TAFDs station (b).

3.3   EUSO-TA design

EUSO-TA is a ground telescope, prototype of the JEM-EUSO detector and consists of an optical system with two Fresnel lenses focusing the light on a Photo-Detector Module (PDM) composed by 36 Multi-Anode Photomultiplier Tubes (MAPMTs), both shown in Figure 3.5. The detector is sensitive in the 300-400 nm UV range, corresponding to the wavelength of fluorescence light emitted by EAS through the atmosphere. The optical system defines the FOV of the detector. From direct measurements, using LEDs at different angles in front of EUSO-TA, the FOV resulted to be $10.5° \times 10.5°$ ($0.19°$ per pixel). The FOV can be extended by adding more PDMs. Although EUSO-TA has a small FOV compared to the BRM FDs one (about 1/30), its resolution is much higher because of the small pixel size of the MAPMTs, as shown in Figure 3.4. The elevation of the instrument can be manually changed from 0° to 25°, whereas the azimuth is fixed to 307° from North clockwise, being the telescope pointing to the CLF direction.
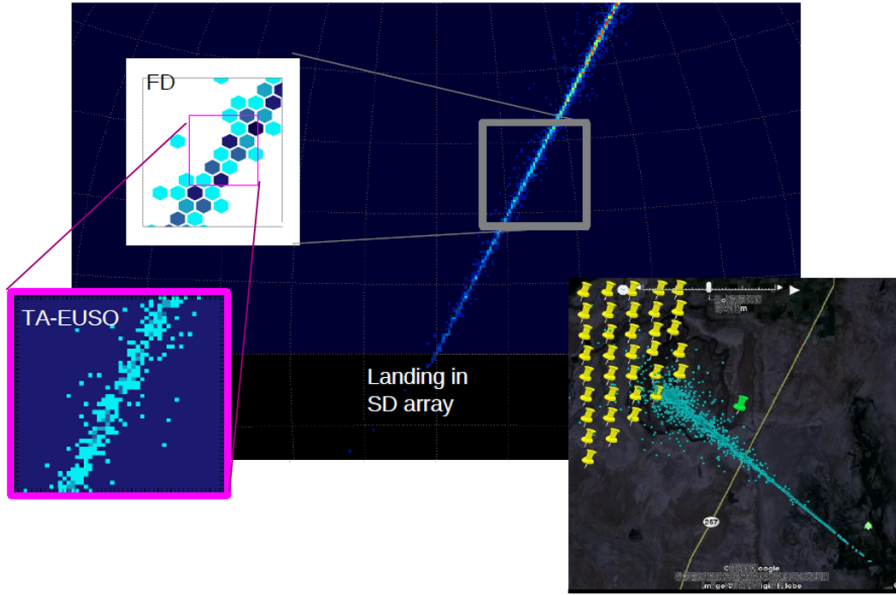
Figure 3.4: Simulation of a shower with energy 10^{18} eV trough the FOV of EUSO-TA. The white frame shows the shower as seen by one of the TAFDs; the pink frame shows the FOV of EUSO-TA, smaller than the TA one, but with higher spatial resolution. Image taken from [64].

3.3.1 Optical system

EUSO-TA has the same optical system used also in the EUSO-Balloon and EUSO-SPB telescopes. The front and rear lenses are quadratic, 8 mm thick and measure $1 \times 1 \, \mathrm{m}^2$. The front side of the front lens and the back side of the rear lens have a plane surface, which is useful for EUSO-TA in order to clean the dust easily, since it is placed in a desert area. The back side of the front lens and the front side of the rear lens have a circular Fresnel structure. Figure 3.6 shows the conceptual development of a Fresnel lens. The light-bending accomplished by lenses takes place only at the surface, when the rays enter and leave the glass. The angle of the glass surface determines how much each ray bends. The interior of the lens does not really serve a function. Therefore, it is possible to get rid of the bulk interior of the glass, and just have the surface curvature of the glass preserved in small segments. This allows to have the refractive performances of usual lenses, with a significant reduction of the weight, that is of great importance for space-based experiments.

They are made of UV grade polymethyl-methacrylate (PMMA)* and details about their manufacture can be found in [66]. The surface roughness of the lenses should be smaller than 20 nm RMS. This is the most important requirement to meet the observation performance. In fact, the surface roughness has a direct impact on the overall transmission.

Since in the desert the temperature varies between -30 ℃ and $+40$ ℃ due to seasonal and daily variation, studies on the material behavior under different thermal conditions have been made. The refractive index in the near UV region for

---

*Manufactured at the Institute of Physical and Chemical Research (RIKEN) in Wako, Japan.

(a) Optical system   (b) PDM
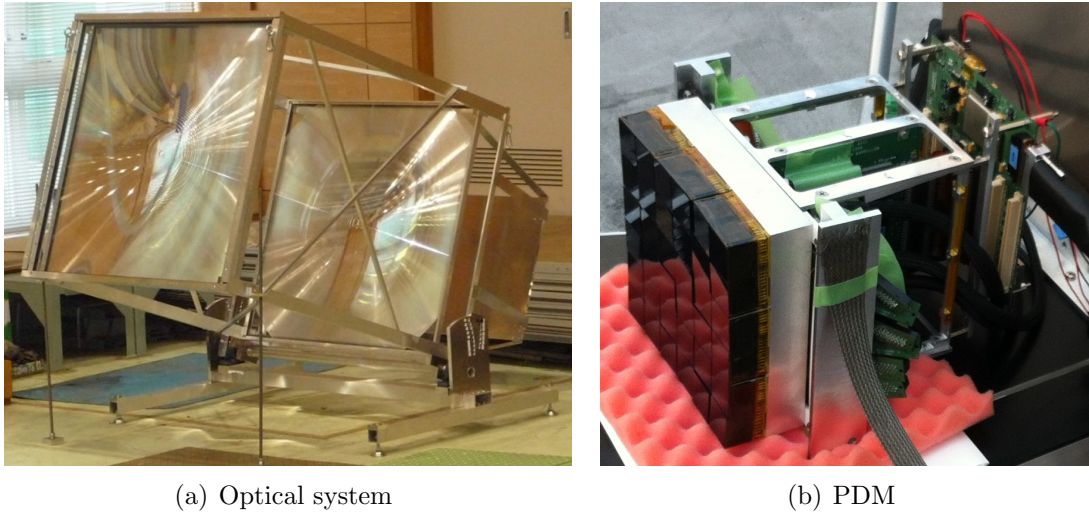
Figure 3.5: EUSO-TA optical system (a) and PDM (b).

three different temperatures (-40 ℃, $+20$ ℃ and $+40$ ℃) is shown in Figure 3.7(a). The PMMA transmittance with 8 mm thickness in near UV region is shown in Figure 3.7(b).

Another requirement is that the angular resolution has to be better than the one of TAFD. The FOV of a TAFD pixel is 1°. It corresponds to 9.6×9.6 pixels of EUSO-TA. The RMS spot size of EUSO-TA should therefore be smaller than 9.6×9.6 pixels to resolve a TAFD pixel. The best design developed is shown in Figure 3.8, where tracks for off-axis angles between 0° and 8° are visible. This design results in a spot size of 9 mm RMS, which corresponds to 3×3 pixels of EUSO-TA [67]. In this study a EUSO-TA configuration with two PDMs has been considered, for a full estimated FOV of $8° \times 8°$. Simulated spot diagrams for incident angles between 0° and 8° in respect to the telescope axis are shown in Figure 3.9. The design was implemented for temperatures of front and rear lenses of 20 ℃. This optics is insensitive to changes of temperature between 0 ℃ and 40 ℃.
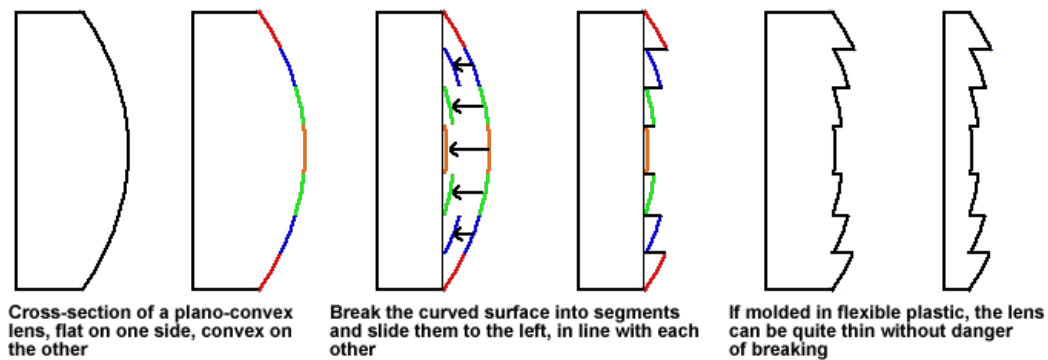
Figure 3.6: Conceptual development of a Fresnel lens. Image adopted from [65].
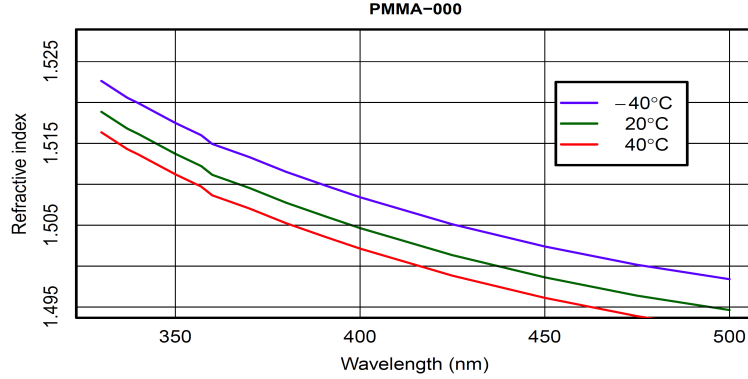
(a) PMMA-000 refractive index.
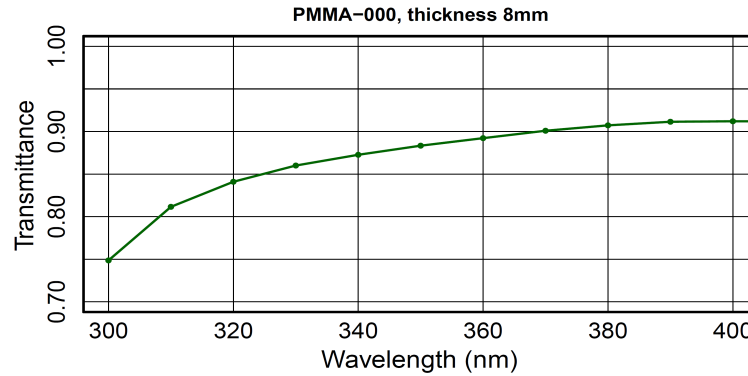
(b) The 8 mm PMMA transmittance.

Figure 3.7: PMMA refractive index in the near UV region with different temperatures (-40 °C, $+20$ °C and $+40$ °C) (a) and the 8 mm PMMA transmittance in the near UV region (b). Plots taken from [67].

3.3.2 Focal Surface

The EUSO-TA focal surface consists of one PDM, i.e. a 17×17 cm active surface composed by an array of 6×6 Hamamatsu R11265-M64 MAPMTs. Groups of 2×2 MAPMTs make the Elementary Cells (ECs).

Each MAPMT is a matrix of 8×8 pixels with a size of 2.88×2.88 mm^2, for a total of 2304 pixels of the PDM. Each pixel is associated to an anode generating a charge or a current in output. Their sensitivity is as low as a few tenths of a photon and their dynamic range can extend up to few thousands photons per μs when working at their nominal high gain, 10^6. The total photon detection efficiency is 35% at maximum, with a cross-talk of less than 1% in the UV wavelength range of 290-430 nm. Figure 3.10 shows a sketch of the "single photoelectron spectrum" obtained in one channel of a MAPMT, showing a clear separation of the single photoelectron response given by the right bump from the peak due to the dark noise, corresponding to no signal from a photoelectron registered at the anode of the PMT. This peak is also called *pedestal*. The area under the one photoelectron peak gives the number of detected photons, from which it is possible to calculate the photo detection efficiency.
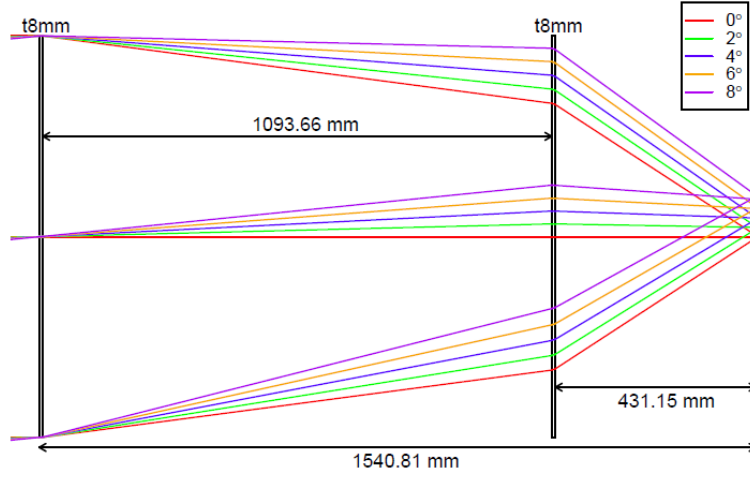
Figure 3.8: The optics design of EUSO-TA. Image taken from [67].
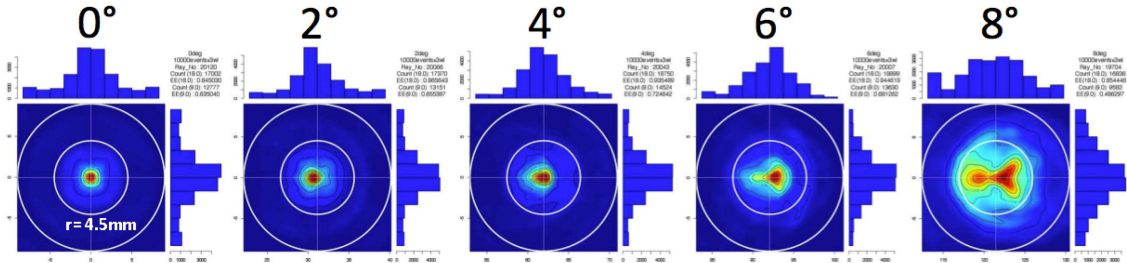
Figure 3.9: Frames showing the deformation of a light spot on the focal surface, for incident angles between 0° and 8° in respect to the telescope axis. The inner circle radius is 4.5 mm and the outer circle radius is 9 mm. The histograms show the distributions of the sum of the counts over the horizontal and the vertical side of the frames. Images taken from [67].

From this histogram it is possible to estimate the gain of the MAPMT by the distance between the photoelectron bump mean and the mean of the dark noise. Both parameters, the gain and the detection efficiency, are determined experimentally for each channel and are crucial parameters for the absolute calibration of the detection chain allowing to convert the measured photoelectron counts into the number of photons on the photocathode.

High voltage is necessary to achieve the required gain of 10^6. High voltage power supplies (Cockcroft-Walton) provide the typical voltage of -900 V. Fast switches responsive at μs time-scale, adapt the voltage values to tune the MAPMT gain according to the intensity of the (background) photon flux.
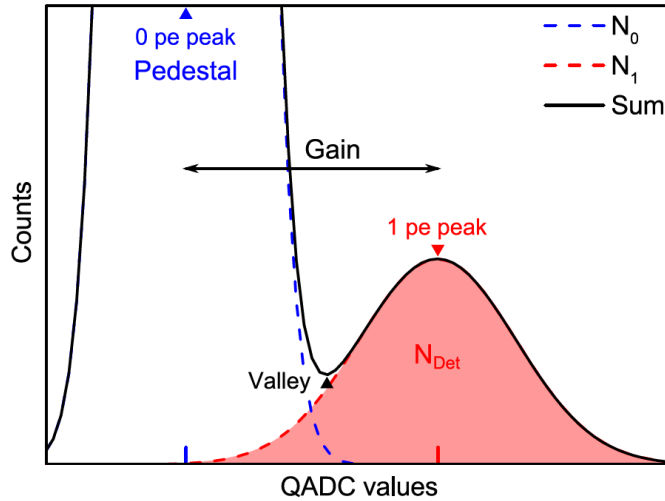
Figure 3.10: Schematic sketch of a "single photoelectron (pe) spectrum" with two Gaussian distributions for the 0 pe and 1 pe peak. The separation of both peaks gives the gain of the PMT. The area under the 1 pe peak gives the number of detected photons. Image taken from [68].

3.4 EUSO-TA data acquisition

Once the MAPMTs detects photons, the number of signals has to be reduced via a series of triggers from 1 Gbyte/s to 10-100 Gbyte/day which can be stored for offline analysis. 36 SPACIROC Application Specific Integrated Circuits (ASICs) [69] are used to perform measurement and digitization of the MAPMT signals, with 64 channels each, and integrate the counts in time intervals of Gate Time Units (GTU), which corresponds to $2.5\,\mu s^{\dagger}$. They process the 64 analog signals in parallel in two modes: *photoelectron counting mode*, in a range from 1/3-100 photoelectrons, by discriminating each of the channels over a programmable threshold; *integrating mode*, in which an eight-anode current sum is estimated from a time-over-threshold determination, in a range from 20 pC to 200 pC (12.5-1250 photoelectrons). The 64 analog channels are balanced in order to correct for the non-uniformity of the 64 MAPMT anodes by gain adjustment. There is no data buffering on the ASIC. The data are transferred, for each GTU, to the Field Programmable Gate Array (FPGA, Xilinks Virtex 6) of the PDM board integrated in the PDM at 40 MHz.

There are two trigger modes with which the detector starts to acquire data: an internal and and external trigger.
The internal trigger is called *first level trigger* (L1) [70] and is implemented in the FPGA of the PDM board. The PDM board reads out the data from the 36 ASICs (that means at PDM level) into its internal memory (the event buffer) per each GTU, to compute the L1 trigger, reducing the rate of triggers (mainly due to UV-background) to about 1 Hz/EC. The L1 counts an excess of signals over the UV-background in groups of 3×3 pixels lasting more than a preset time. The UV-

---

†The actual sensitive time window is $2.3\,\mu s$, because at the beginning of each GTU there is a dead time of $0.2\,\mu s$

background rate is monitored continuously to adjust the trigger threshold in real-time, keeping the L1 trigger rate compatible with the DAQ recording rate (a few Hz). Since the trigger algorithm has been implemented for the JEM-EUSO experiment, in which the detection of air showers may extend over 100 GTUs, this trigger has the buffering capability over packets of 128 consecutive GTUs. To reduce the dead-time induced by event readout, the event buffer temporarily saves two packets of 128 consecutive GTUs. The L1 trigger has been tested, but the current FPGA allows the implementation of the trigger logic only for a few ECs.

The second trigger mode is a reaction to an *external trigger*, which can be used for working in coincidence with TAFDs at Black Rock Mesa (BRM). In this way, when BRM-TAFDs detect an event inside the FOV (108° in azimuth and 30° in elevation), they send a trigger signal to EUSO-TA, which starts the data acquisition. Since the self triggering capabilities would be limited not just because currently the L1 trigger can be implemented for a partial focal surface, but also due to the small EUSO-TA FOV ($10.5° \times 10.5°$), the external trigger is advisable for this prototype. Moreover, it allows to make cross check of the events which crossed both the FOVs of the EUSO-TA and TA detectors, and to get the shower parameters from the reconstruction of the event performed by the TA group. But, being triggered by TAFDs, which has a larger FOV than EUSO-TA, leads EUSO-TA to acquire and save more data than those actually containing signal inside its FOV. In the current configuration the external trigger is received by a time synchronization subsystem called Clock Board.
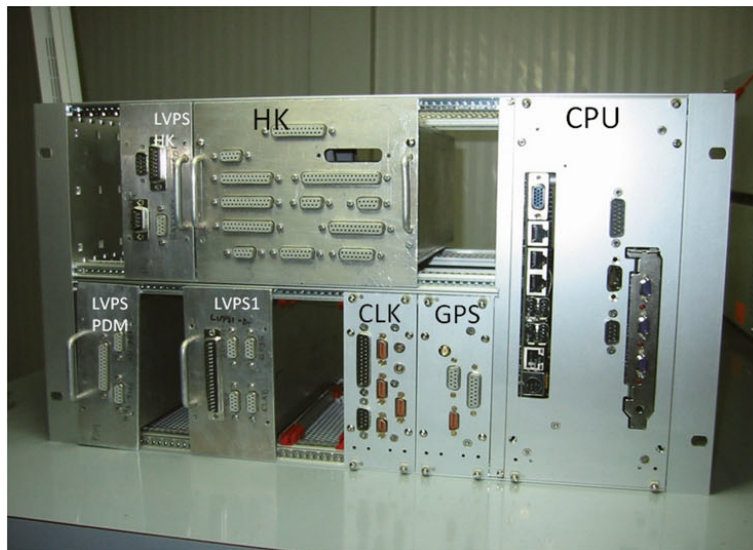
Figure 3.11: DP with the second level trigger board, CPU board, Clock board (CLK), GPS board, house keeping board (HK) and low voltage power supply (LVPS).

The PDM is controlled by the Data Processor (DP) shown in Figure 3.11. The DP consists of a Cluster Control Board (CCB) [71], CPU board, clock board (CLK), GPS board, house keeping board and Low Voltage Power Supply (LVPS). The CCB collects the data from the PDM board, processes and classifies the received data, and

can perform a second level trigger (L2) filtering (developed but not used yet during data acquisition with EUSO-TA). The DP then tags the events with their arrival time (in UTC) and payload position (GPS). It also manages the data storage, measures the operating- and dead-time of the instrument, performs housekeeping monitoring, and handles the interface with the telecommand/telemetry system. Most of the data passed through the L1 (and L2) trigger is intended for offline analysis. An event selected by both triggers represents roughly 330 kB of data. Data acquisition and status of the apparatus can be monitored remotely, and if needed reset, from a PC in the BRM control room, in order to avoid direct access to the EUSO-TA container during data acquisition in case of malfunction. In case of excessive photon flux (10^3 photons per GTU per pixel) generating an anode current above 100 μA, it would destroy the PMTs. To avoid this, an automatic control system can even switch off the voltage. The switching decision logic is implemented in the FPGA board which reads out the ASICs. In the PDM there are nine independent high voltage power supplies with their individual nine fast switches, each one controlling one of the nine ECs high voltages independently (1 PDM = 3×3 ECs = 6×6 MAPMTs). Given that the EUSO-TA container is located just in front of the BRM FDs station, it is important to prevent any inconvenience with light sources during TAFDs data acquisition. Even movements on the back side of the station have to be careful and always supported by red light, far from the UV range the telescopes are sensitive to.
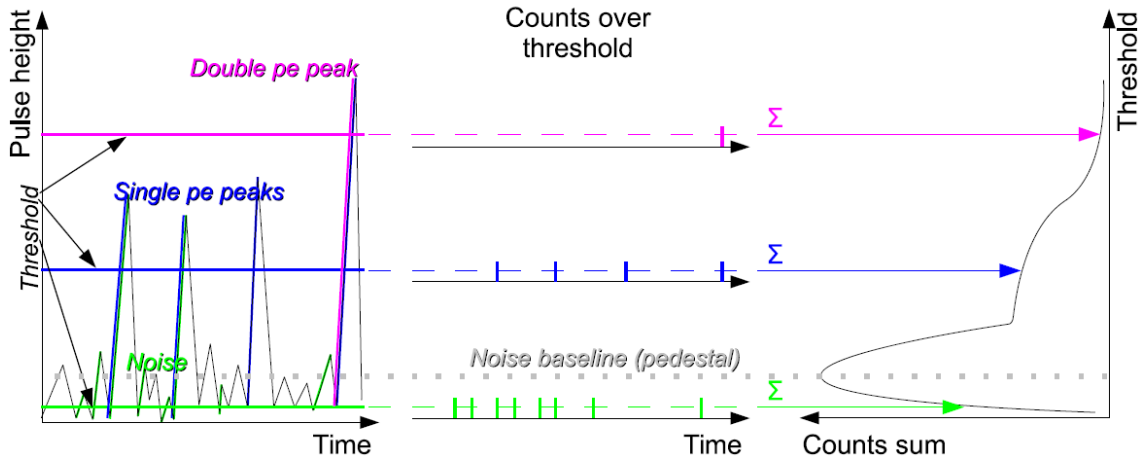
Figure 3.12: A schematic dependency of signal measurement and S-curve. The left image shows a signal change with time, where small fluctuations are due to electronic noise, big peaks are single photoelectron signals, and the biggest peak is the contribution of a double photoelectrons. Setting different thresholds, denoted by colored lines, just peaks above them originate signals. The middle image shows the counts detection of pulses exceeding the thresholds. The right image shows a schematic S-curve. Image taken from [72].
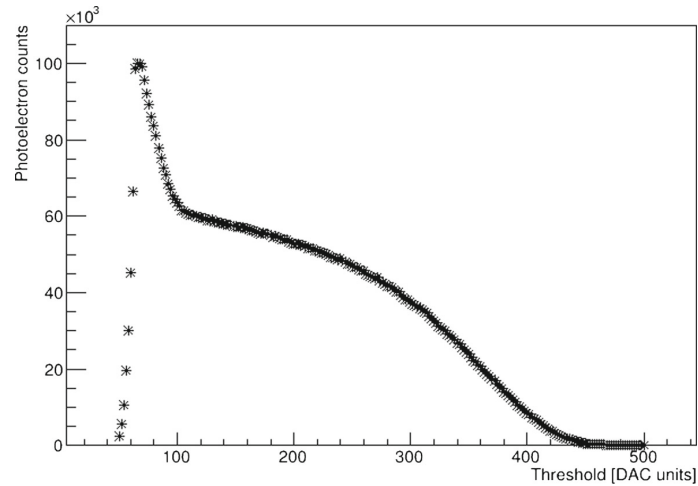
(a) S-curve
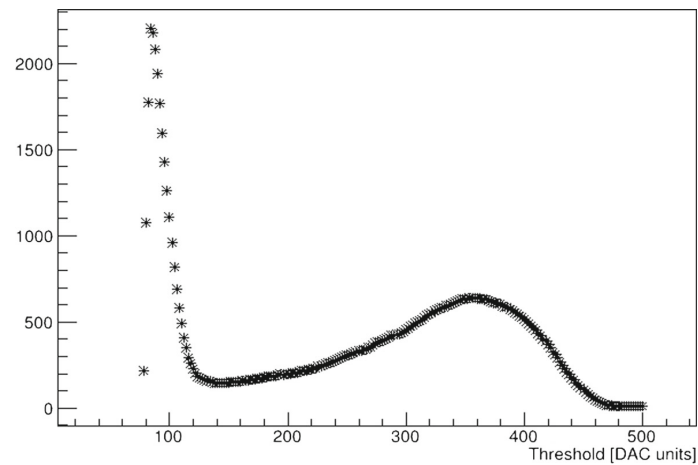
(b) Single pixel "single photoelectron spectrum"

Figure 3.13: A sample S-curve (sum of photon counts for specific number of measurements over the threshold for single photoelectron detection) in DAC units (a). A sample single pixel "single photoelectron spectrum" measured in laboratory, for threshold levels represented in DAC units (b). The noise peak on the left and single photoelectron peak on the right are clearly visible. The distance between peaks is determined by the total pixel gain. The minimum between the peaks is the single photoelectron valley - the optimal position of threshold for single photoelectron detection. Images taken from [72].

3.5 Detector calibration

An absolute calibration [73] is necessary to retrieve the number of photons hitting a pixel from the number of registered counts. This *offline calibration*, because of its complexity and time requirements, has been performed just once[‡] before the assembly of the detector.

Furthermore, an *online calibration* [74] is repeated in-situ between the measurements, to obtain similar overall performance for the single photon detection of all the pixels. In this way the noise from PMT and EC-ASIC electronics are rejected and more intense signals coming from a single photons accepted. This requires analysis of the so called S-curves, sum of photon counts for specific number of measurements over the threshold. An S-curve contains the signal in Digital-to-Analog Converter (DAC) units over threshold for single photoelectron detection. To obtain it, measurements of a high number of data frames[§] for different threshold setting are required, to minimize statistical fluctuations[¶]. In Figure 3.12 it is shown how a S-curve is created.

If the threshold is lower than the noise peaks' height (left), the S-curve (right) shows non-zero counts due to dark current and offset in readout electronics (pedestal). Increasing the threshold above the pedestal quickly cuts off the noise. If the threshold value is above the noise but below the typical single photoelectron signal value, the slope of the S-curve is very gentle, showing single photoelectron peaks. It steepens when the threshold crosses the typical single photoelectron signal, showing the rare double photoelectron peaks, and approaches zero for high threshold values, above which there is nearly no signal. A sample S-curve can be seen in Figure 3.13(a) and the "single photoelectron spectrum" in Figure 3.13(b) is the derivative of the S-curve. It shows separated peaks for the electronics noise and single photoelectron bump.

However a single threshold must be set for all pixels of a single MAPMT. Therefore, the calibration procedure must determine an optimal amplifier gain for all pixels to have the same total gain, which roughly corresponds to obtaining a similar shape of the "single photoelectron spectrum". For this task, the algorithm calculates the median position of the single photoelectron peak for all pixels and adjusts the gain of all pixels to move the peak to the median position. After the adjustment the measurement and median calculation is repeated to determine if the similarity of efficiency is satisfactory. If not, adjustment values are calculated and utilized again, until satisfactory performance is obtained.

[‡]Performed at the Institute for Cosmic Ray Research (ICRR) in Tokyo, Japan.

[§]A "frame" is data collected within one GTU and visible on a 2D histogram representing the PDM with a 48×48 matrix of pixels. One GTU is $2.5\,\mu s$ long. A packet of frames is composed of 128 frames (GTUs).

[¶]The actual number of frames requested for each threshold level has yet to be determined, but initial measurements show that the single photoelectron signal should be around 0.1%-1% of the maximal signal, requiring order of 10^4-10^5 GTUs.

Chapter 4

Data acquisition campaigns

4.1   Data acquisition

The best condition for the data acquisition with EUSO-TA is a clear and moonless night. Also in partially cloudy or cloudy nights it is possible to collect data, but in these cases low elevation of the EUSO-TA axis is preferred, to have the clouds in the FOV only at longer distances.

As discussed in Section 3.4, there are two acquisition modes: with *internal* and *external trigger*. During some nights, the internal trigger has been used, mainly in order to test its algorithm, but most of the data have been collected with external trigger by TAFD. The external trigger mode does not allow EUSO-TA to work independently from TA, but on the other hand the TA consolidated trigger guarantees to not lose events in the EUSO-TA FOV.

The detected events in EUSO-TA data have been identified in two ways. One way consists of using first algorithms of the quick-view and quick-analysis ETOS software (described in Appendix A) to find frames of data with possible events and, in a second step, asking the TA group for confirmation, given the time stamp of the candidate event. In case of positive response, the TA group shares the information about the event reconstruction parameters. The second way consists in looking first in the TA data for events crossing the EUSO-TA FOV (given the elevation angle of the telescope). Simulating them and studying the expected signal to background ratio, one can evaluate if it is visible in the data and then, if it is visible, check the data at the corresponding time stamp given by TA.

Independently of the trigger used, one of the important reasons why EUSO-TA is located in front of the Black Rock Mesa (BRM) TA fluorescence detectors (TAFDs) is that the EUSO-TA research group can benefit from the TA monocular (just using BRM-TAFDs) reconstruction of the events. The event reconstruction gives the parameters of the CR shower: energy of the primary particle, zenith and azimuth angle of the shower axis, position of the impact point of the shower axis on ground (*core*), minimum distance of the telescope from the shower axis (*impact parameter* R_p), inclination Ψ of the shower axis in the shower-detector plane (SDP) defined as the plane containing the detector center and the axis of the shower. Most of

these parameters are shown in Figure 4.1. To know them is fundamental in order to perform the simulations of the cosmic ray events and then compare the results with the data, as discussed in more detail in Chapter 7.
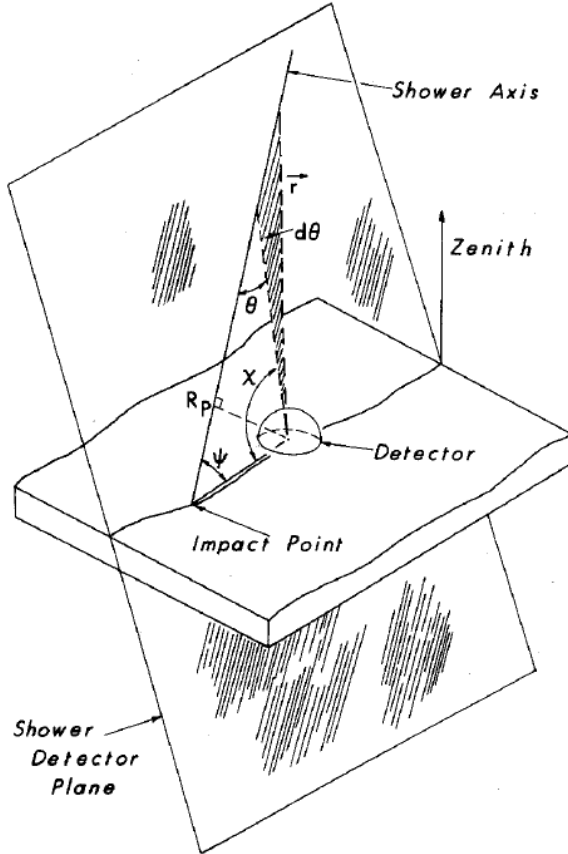
Figure 4.1: Shower detector plane and the reconstruction parameters characterizing each shower reconstruction. Image taken from [75].

4.2   Dataset statistics

Since March 2015, when the EUSO-TA installation was completed, the data acquisition campaigns started and four cosmic ray events have been detected. Another four events are considered "candidate events", because they are faint or irregular and there is the possibility that they were generated by noise instead of real cosmic ray air showers. As will be discussed in Section 8.3, studies for the estimation of the expected number of detected events say that between 8 and 15 events could have been detected, depending on the assumptions made in the analysis.

Table 4.1 summaries the data acquisition campaigns with *external trigger* by TA. The table includes the events which crossed the EUSO-TA FOV, evaluated from the analysis of TA data, in 2015 (5 campaigns, the first one was for the installation

of the detector and testing, and did not work with *external trigger* by TA) and 2016 (1 campaign). The total observation time corresponds to 143.6 hours, of which 122.8 hours in 2015. More campaigns were not possible due to missing person power and other priorities by the members of the JEM-EUSO Collaboration.

Period	Days	Observation time (s)	Packets	CRs	Detected
March 2015	8	491	2082	0	-
May 2015	13	84575	163396	24	1 (+1)
September 2015	11	97043	234904	23	2 (+2)
October 2015	11	88354	200841	20	0 (+1)
November 2015	12	171651	470487	43	1 (+0)
Total 2015	55	442114 (122.8 hours)	1071710	110	4 (+4)
October 2016	5	74828	177258	23	0 (+0)
Total 2015/16	60	516942 (143.6 hours)	1248968	133	4 (+4)

Table 4.1: Summary of the data acquisition campaigns in the year 2015 and 2016. For each campaign (month) the number of days of data acquisition, the actual total observation time (evaluated as sum of the difference between the CPU time of the last GTU and the first GTU in each file), total number of packets (1 packet = 128 GTUs), the number of cosmic rays that crossed EUSO-TA FOV (estimated by the TA group), the number of detected events and, within brackets, the number of candidate events are reported.

The graphs in Figure 4.2 show the energy, impact parameter R_p, zenith and azimuth distributions of the events in the EUSO-TA FOV (following the TA shower reconstruction), for the year 2015 and both 2015/16. The energy distribution ranges between 10^{17} eV and $10^{18.7}$ eV, with a maximum at $10^{17.7}$ eV. The limit at the lowest energies comes from the detection limit of TA for events that would look too faint to be detected; at the highest energies the limit is due to the smaller probability of having high energy events, and the small FOV of EUSO-TA, as well as the limited observation time play a role too. The R_p distribution goes from 0 to $\sim$ 17 km with a maximum between 2 and 3 km. The zenith angle is distributed between 5° and 65°, with an average of 33°. The azimuth angle has a distribution spread out on 360°, with 0 at North direction (the azimuthal orientation of EUSO-TA and BRM-TAFD is $-53°$).

Only the data of 2015 are analyzed in this thesis. Data from the 2016 campaign are shown only for cross-checks. The impact parameter R_p and the energy of each event of 2015 are plotted in Figure 4.3, where the green stars represent detected and candidate events of EUSO-TA and red crosses the not detected ones. It seems the detected and the candidate events lie in the region of the plot with $E \geq 10^{17.7}$ eV and $E \leq 10^{18.7}$ eV with $R_p \geq 2.5$ km and $R_p \leq 9$ km respectively. Further studies are used to define a detection threshold for the EUSO-TA detector and are discussed in Chapter 8.

(a) Energy

(b) R_p
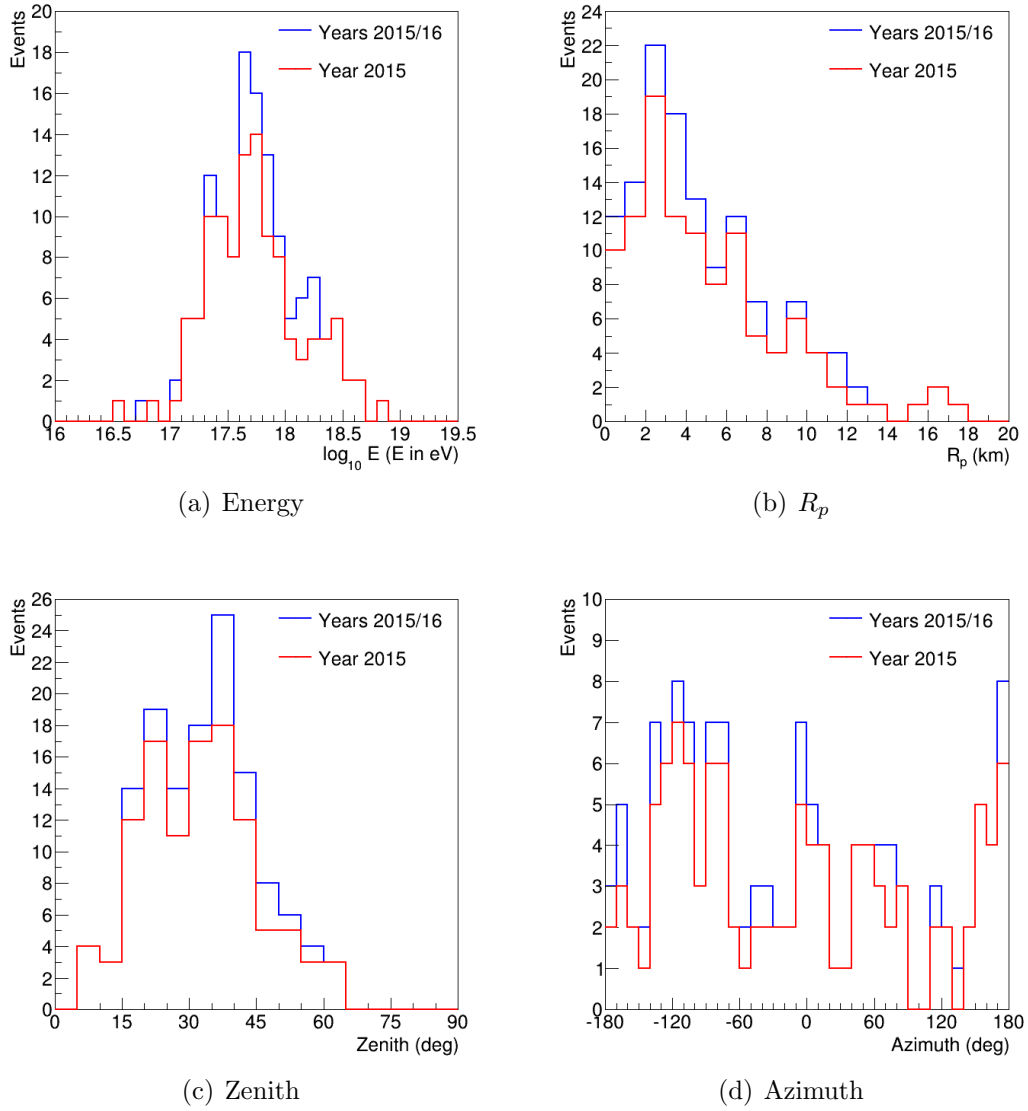
(c) Zenith

(d) Azimuth

Figure 4.2: Event distributions of energy, R_p, zenith and azimuth angles of the cosmic ray events which crossed EUSO-TA FOV.
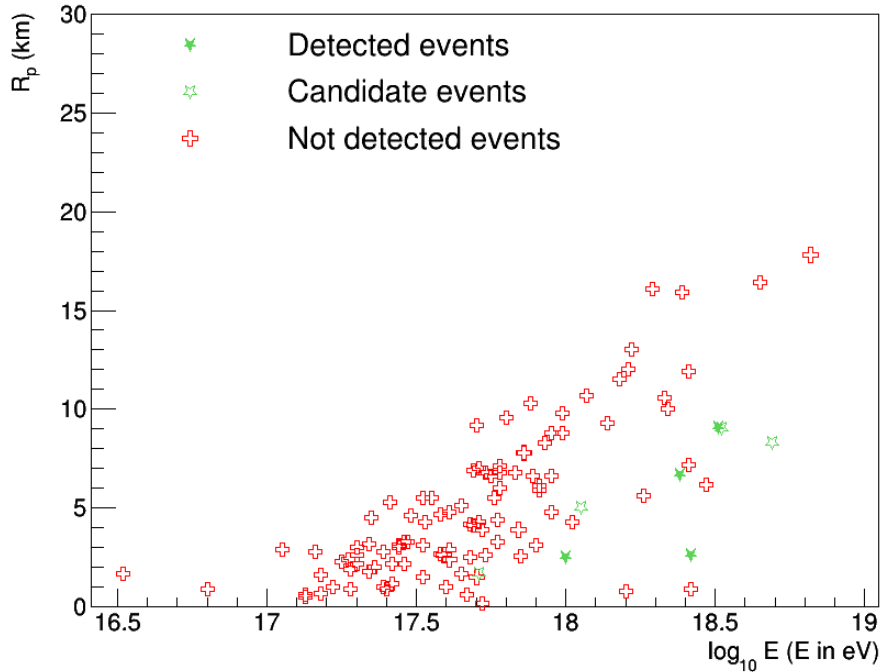
Figure 4.3: Energy and impact parameter as reconstructed by TA for the 110 events which crossed the EUSO-TA FOV during the data acquisition campaigns made in 2015. Green full stars show the detected events, the empty green stars represent the candidate events (see Section 4.3), and red crosses are the not detected events.

4.3 Detected cosmic ray events

In this section the four detected cosmic ray events are discussed. For each event, the images showing the data frames with the event track are taken with the quick-view and quick-analysis software ETOS, described in Appendix A. The images include information about the data file name (in the bottom), the sequence number of the frame in the file (GTU) and the sequence number of the frame in a packet of 128 frames (GTU in pkt), together with the UTC and local times (in the top). The event frames present blocks of pixels, most of the times 8×8 pixels corresponding to one PMT, with zero-counts. This is because a few PMTs and a few more pixels were not working or not working properly during the data acquisitions, and they have been masked. Information about the events are listed in tables, together with the reconstruction parameters. Each event as detected by BRM-TAFDs is also shown, with the FOV of the TAFDs extended to 108° in azimuth and 30° in elevation, and the FOV $10.5° \times 10.5°$ of EUSO-TA is overlaid. In these images, the EUSO-TA azimuthal orientation is 307° from North clockwise. TA integrates the signal in time windows of $51.2\,\mu\mathrm{s}$, while EUSO-TA does that in $2.5\,\mu\mathrm{s}$. For this reason, while TA events appear in one frame, EUSO-TA events are split in more than one frame, when the cosmic ray air shower distance to the telescope increases. It is evident

that, although EUSO-TA has a limited FOV with respect to BRM-TAFDs (about 30 times smaller), the spatial resolution of the EUSO system is much higher than the TA one, the FOV of a EUSO-TA pixel being 0.19° and the one of a TAFD pixel 1°.

Event of 13th May 2015

This is an event from a cosmic ray air shower crossing the EUSO-TA FOV almost through the diagonal at a short distance from EUSO-TA, with $R_p = 2.5$ km. It goes slightly toward the detector during its development through the atmosphere, since the zenith angle is 35° and azimuth angle 7° (from North clockwise) and given that the telescope axis is orientated at an azimuth of -53°.

The detected event lasts one GTU, since the shower was close, and is shown in Figure 4.4: in (a) as seen by TAFDs with EUSO-TA FOV overlaid; in (b) as seen by EUSO-TA, going through the PDM from top-right to bottom-left is presented. The reconstruction parameters received from TA and information on the EUSO-TA event are collected in Table 4.2. The comparison between data and simulation of this event is discussed in Chapter 7.

TA reconstruction	
Zenith	34.5°
Azimuth	7.2° (+ from N clockwise)
Energy	10^{18} eV
R_p	2.5 km
Ψ	100.7°
Core coord. w.r.t. CLF	(14.8 km, -10.9 km)
TAFD timestamp	8:26:49.3559 (in UTC)
EUSO-TA	
Elevation	15°
Number of GTUs	1
GPS timestamp	8:26:53.3762 (in UTC)

Table 4.2: Parameters of the event recorded on the 13th May 2015
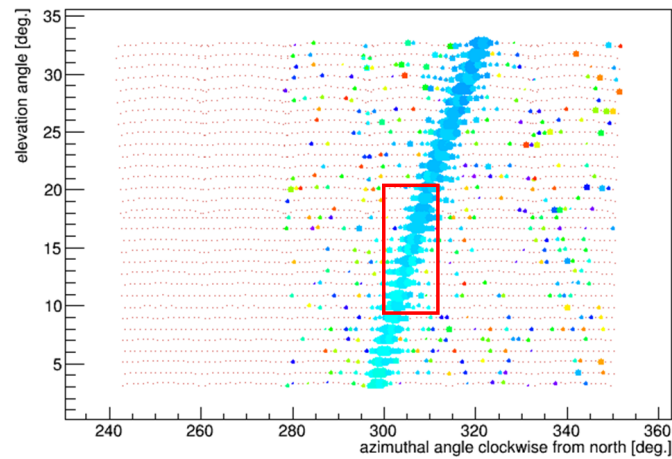
(a) TAFDs event with EUSO-TA FOV overlaid. The size of the point means signal strength and color means timing. Larger point size means stronger signal, and red points mean later than blue points. Image from [76].
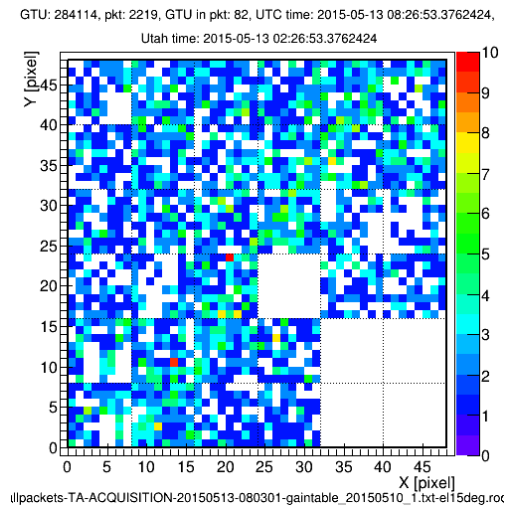
(b) EUSO-TA event, GTU 1

Figure 4.4: Event recorded on the 13th May 2015 by TAFDs (a) and EUSO-TA (b).

Event of 18th September 2015

This event has been found with the mentioned indirect approach, starting from the event displayed in TA data and simulating it. Then, since it was visible in the simulation, it was expected that it could be visible in the EUSO-TA data too and, looking at the time stamp given by TA, it has been found.

This is the case of a relatively distant cosmic ray air shower, with $R_p \simeq 9$ km, going toward the telescope, since the zenith angle is 60.4° and azimuth angle -79.3° (positive values from North clockwise) and being the telescope axis orientated at azimuth -53°.

The Figure 4.5 shows the event in TA (a) and in EUSO-TA (b,c,d), going from middle-left to bottom-right of the PDM data. In the data, the event is visible in just one GTU (c), but from the simulation and the distance of the cosmic ray air shower, it is reasonable to think that the event is distributed through three GTUs, and that the first segment of the event track is faint and the third one is not visible anyway because on not working PMTs. In Table 4.3 the reconstruction parameters and information of the EUSO-TA event are presented. The comparison between data and simulation of this event is available in Chapter 7.

TA reconstruction	
Zenith	60.4°
Azimuth	-79.3° (+ from N clockwise)
Energy	$10^{18.51}$ eV
R_p	9.1 km
Ψ	125.9°
Core coord. w.r.t. CLF	(11.2 km, -2.5 km)
TAFD timestamp	5:40:19.9036 (in UTC)
EUSO-TA	
Elevation	20°
Number of GTUs	3
GPS timestamp	5:40:21.9049 (in UTC)

Table 4.3: Parameters of the event recorded on the 18th September 2015.
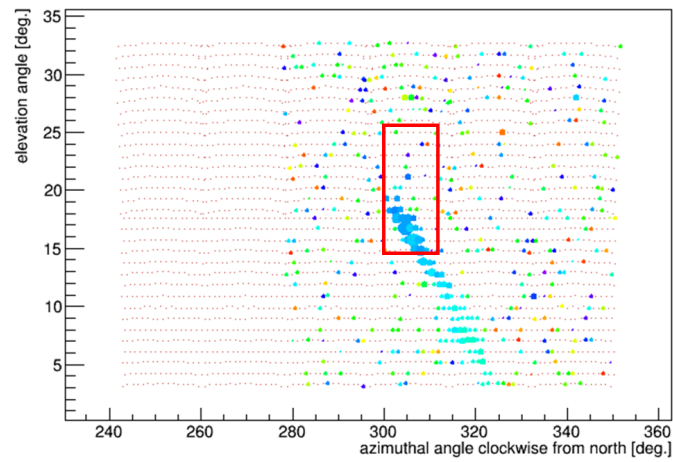
(a) TAFDs event with EUSO-TA FOV overlaid. The size of the point means signal strength and color means timing. Larger point size means stronger signal, and red points mean later than blue points. Image from [76].
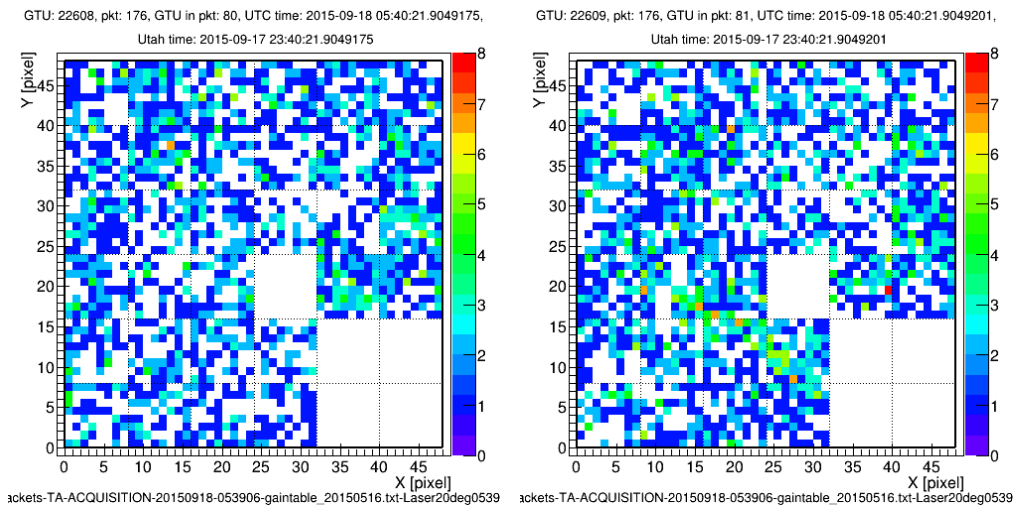
(b) EUSO-TA event, GTU 1
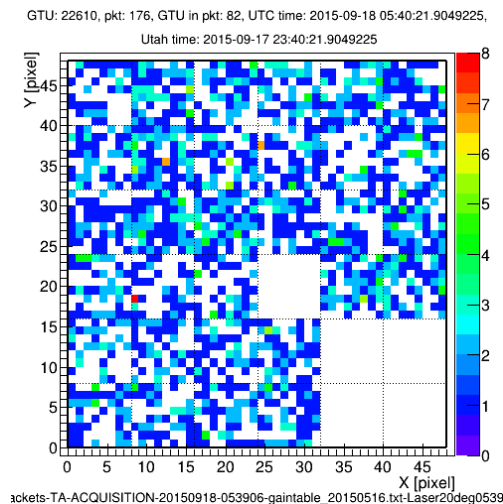
(c) EUSO-TA event, GTU 2

(d) EUSO-TA event, GTU 3

Figure 4.5: Event recorded on the 18th September 2015 by TAFDs (a) and EUSO-TA (b-d).

Event of 20th September 2015

It is a middle distance cosmic ray air shower with $R_p = 6.7$ km and goes slightly toward the telescope, since the zenith angle is about 41° and azimuth angle −24.8°. The detected event crosses the EUSO-TA FOV in the top left corner in two GTUs. In Figure 4.6 the event is shown as seen by TAFDs (a) and by EUSO-TA (b,c), going from the middle-top to the left of the frame. In Table 4.4 the reconstruction parameters and information on the EUSO-TA event are reported. The comparison between data and simulation of this event is available in Chapter 7.

TA reconstruction	
Zenith	41.2°
Azimuth	−24.8° (+ from N clockwise)
Energy	$10^{18.38}$ eV
R_p	6.7 km
Ψ	121.6°
Core coord. w.r.t. CLF	(10 km, −8.4 km)
TAFD timestamp	10:59:19.3094 (in UTC)
EUSO-TA	
Elevation	10°
Number of GTUs	2
GPS timestamp	11:00:43.3117 (in UTC)

Table 4.4: Parameters of the event recorded on the 20th September 2015.
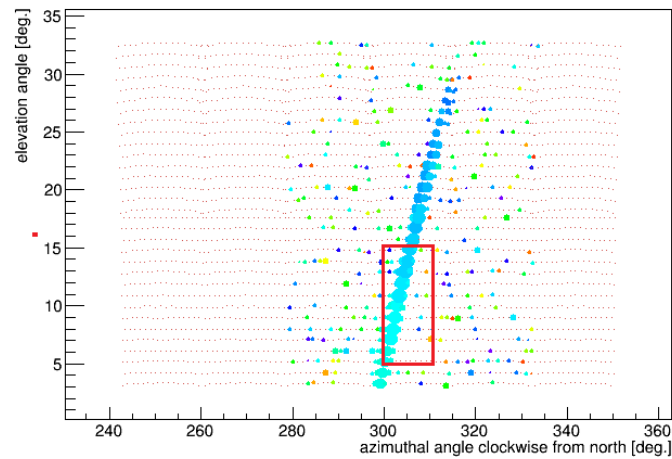
(a) TAFDs event with EUSO-TA FOV overlaid. The size of the point means signal strength and color means timing. Larger point size means stronger signal, and red points mean later than blue points. Image from [76].
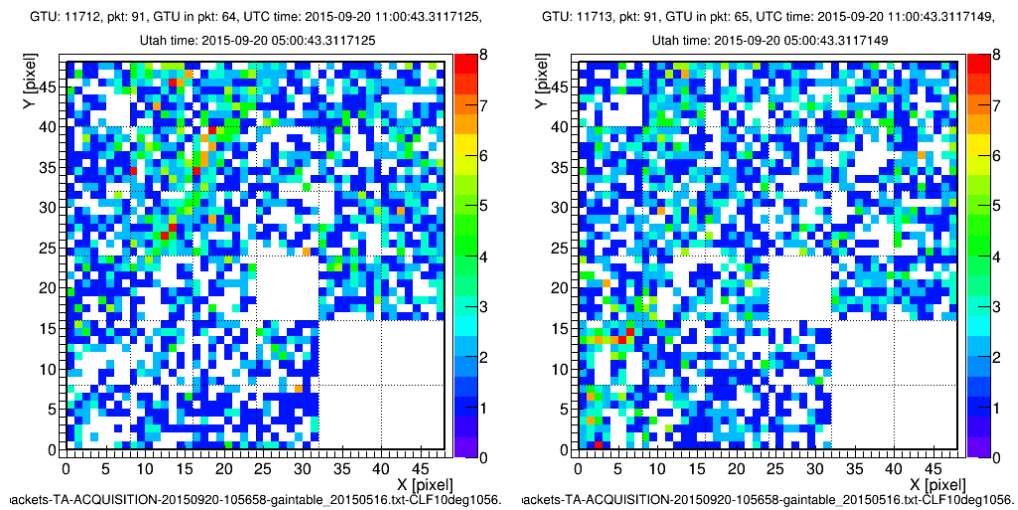
(b) EUSO-TA event, GTU 1

(c) EUSO-TA event, GTU 2

Figure 4.6: Event recorded on the 20th September 2015 by TAFDs (a) and EUSO-TA (b,c).

Event of 7th November 2015

This cosmic ray air shower is close, with $R_p = 2.6$ km, and going slightly towards the telescope, although being close to vertical since the small zenith angle of about 8° and azimuth angle about 82°.

It is the brightest of the detected events, due to the combination of high energy and short distance of the shower compared to the other ones. It is a one frame event looking almost vertical in the left hand side of the frame, as shown in Figure 4.7 for TAFDs (a) and EUSO-TA (b), where in the right hand side a noisy area is visible too. In Table 4.5 its reconstruction parameters and information on the EUSO-TA event are listed. The comparison between data and simulation of this event is available in Chapter 7.

TA reconstruction	
Zenith	8.1°
Azimuth	82° (+ from N clockwise)
Energy	$10^{18.42}$ eV
R_p	2.6 km
Ψ	84°
Core coord. w.r.t. CLF	(14.8 km, −10.6 km)
TAFD timestamp	9:15:06.7325 (in UTC)
EUSO-TA	
Elevation	15°
Number of GTUs	1
GPS timestamp	no active GPS

Table 4.5: Parameters of the event recorded on the 7th November 2015.
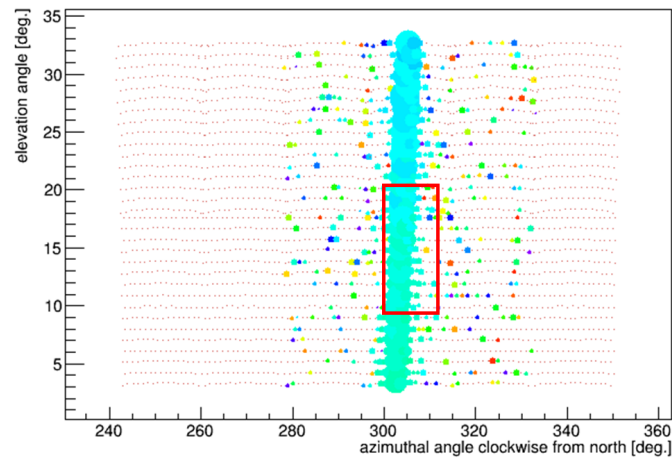
(a) TAFDs event with EUSO-TA FOV overlaid. The size of the point means signal strength and color means timing. Larger point size means stronger signal, and red points mean later than blue points. Image from [76].
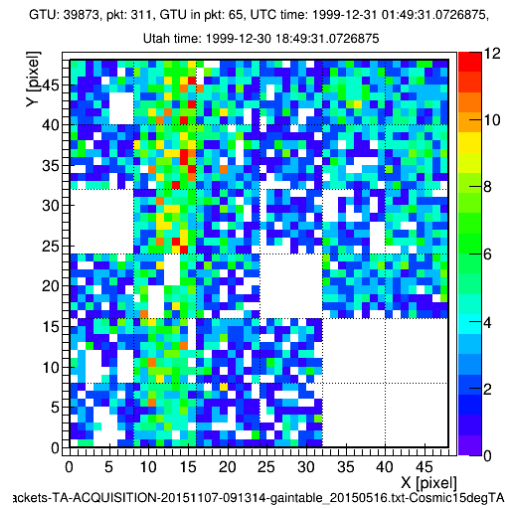
(b) EUSO-TA event, GTU 1

Figure 4.7: Event recorded on the 7th November 2015 by TAFDs (a) and EUSO-TA (b).

4.4   Candidate events

As mentioned before, the cosmic ray events which crossed the EUSO-TA FOV are known from a search of such events in TA data. The identification of events in EUSO-TA data is not unambiguous, especially when the signal is faint and even more if it is split in more than one GTU. The simulation of the events that crossed EUSO-TA FOV has been a helpful tool. Indeed, once the simulations of the detected events have been proved with the comparison of their results with the data, one can trust them also regarding the events not yet detected, and expecting a similar event in the data. With this "inverse" procedure, the detected event on the 18th September 2015 and a few other *candidate events* have been identified. However, the latter cannot be considered *detected events* because they are faint and with irregular tracks and, moreover, the variable and non-uniform background (see Section 5.3), mainly due to some noisy PMTs, could be the cause of such signals.

An additional analysis has been done to understand if these events can be cosmic ray events or generated by noise, and it is discussed in Section 5.1.3. It is based on the GTU sequence number (GTU#=0-127) of the frames containing the candidate event within the packet (1 packet=128 GTUs), which has to be within a certain fixed range. This is due to the cables which introduce a short time delay between the beginning of the data saving and the receiving of the trigger, i.e. the triggered event appears in a EUSO-TA frame which is not the first one of the packet. Anyway, once a trigger is received, the current whole packet is saved, so this delay does not lead to a loss of data. On the contrary, since TAFDs have a 30 times bigger FOV, even more EUSO-TA data than those really containing events are saved. Moreover, a search for frames looking similar to the candidate events within a large number of frames around it (9 packets, for a total of 1152 GTUs) has been performed: if similar frames are found, it reduces the probability that the candidate event is a detected event but instead could be due to noise, otherwise the probability is increased.

The simulation of the candidate events and their comparison with the data is discussed in Section 8.1.1.

Candidate event of 12th May 2015

This is, according to the simulation, a 4 GTUs event. It is the case of a relatively far cosmic ray air shower, with $R_p = 8.3$ km, going farther the telescope. In Table 4.6 the event reconstruction parameters and information on the EUSO-TA event are listed. Figure 4.8 shows the event for TAFDs coming from right to left (a) and the candidate event for EUSO-TA (b). In the data possible event track segments are visible just in GTU 3 (d) and GTU 4 (e) in the bottom part of the frames. As well as in (a) the first part of the track is not detected, probably due to the geometry of the cosmic ray air shower coming with a relatively high zenith angle toward the telescope, or to the presence of clouds in the upper part of the FOV. The track in the frames is weak and diffuse, and the PMT with the possible signal in GTU 3 is noisy from time to time, so the event cannot be considered detected without doubt.

TA reconstruction	
Zenith	56.9°
Azimuth	74.3° (+ from N clockwise)
Energy	$10^{18.69}$ eV
R_p	8.3 km
Ψ	44.8°
Core coord. w.r.t. CLF	(5.6 km, -8.7 km)
TAFD timestamp	8:26:45.4039 (in UTC)
EUSO-TA	
Elevation	25°
Number of GTUs	4
GPS timestamp	8:26:48.4158 (in UTC)

Table 4.6: Parameters of the candidate event recorded on the 12th May 2015.

As discussed in Section 5.1.3, the expected range of GTU# in the packet of data is 90-94. However, the most probable candidate is observed in GTU# 82. A similar difference between the expected range of GTU# and the actual one is also there for one of the detected events (on the 18th September 2015), so it can be preliminarily accepted. However, looking for similar frames, a few have been found, although the GTU# was too different from the expected one, so they cannot be in turn candidate events.
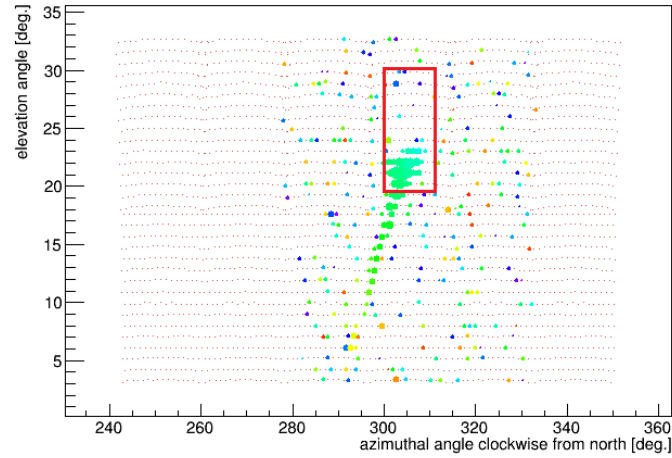
(a) TAFDs event with EUSO-TA FOV overlaid. The size of the point means signal strength and color means timing. Larger point size means stronger signal, and red points mean later than blue points. Image from [76].
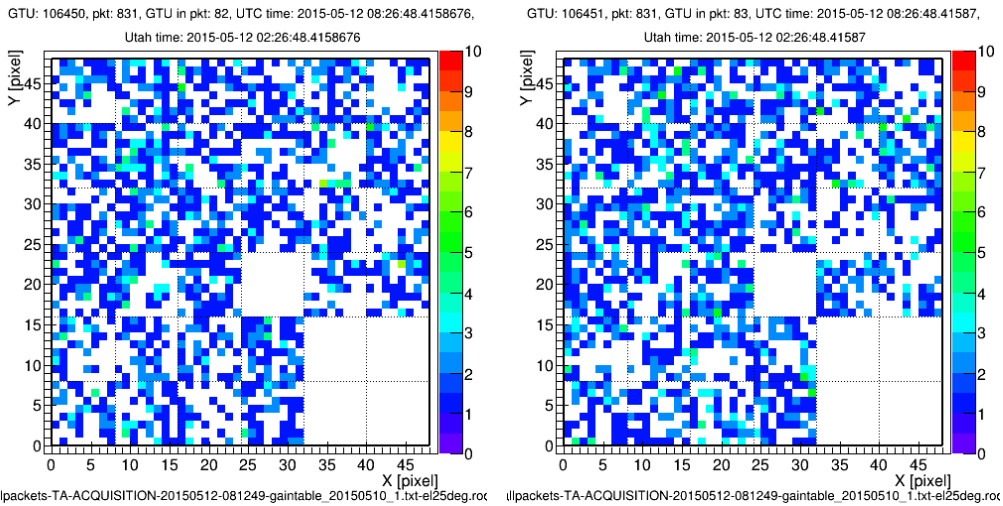
(b) EUSO-TA event, GTU 1
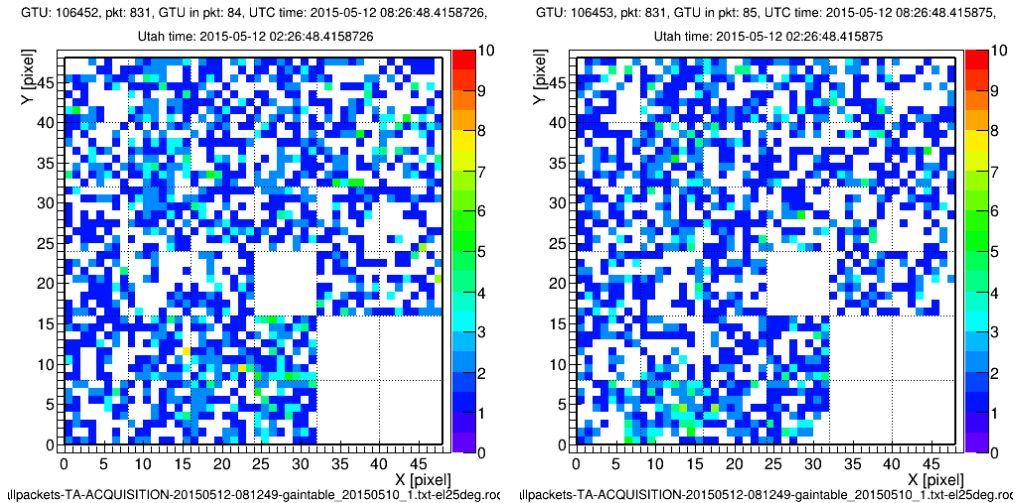
(c) EUSO-TA event, GTU 2

(d) EUSO-TA event, GTU 3

(e) EUSO-TA event, GTU 4

Figure 4.8: Candidate event recorded on the 12th May 2015 by TAFDs (a) and EUSO-TA (b-e).

Candidate event of 12th September 2015

According to the simulation, this event is a 2 GTUs event. It is a mid-distance cosmic ray air shower, with $R_p = 5.0$ km, going slightly away from the telescope. In Table 4.7 the event reconstruction parameters and information on the EUSO-TA event are listed.

In this case, the search for candidate events in the data has two positive results, compatible in terms of time stamp (they are in the same packet) and of GTU#. As shown in Figure 4.9 (a) for TAFDs it goes from left to right and in (b,c) and (d,e) the corresponding EUSO-TA candidate event #1 and #2 respectively are visible. The signal in GTU 1 is mainly on two PMTs often noisy, although the track seems to reflect the geometry of the shower.

TA reconstruction	
Zenith	29.5°
Azimuth	−164.9° (+ from N clockwise)
Energy	$10^{18.05}$ eV
R_p	5.0 km
Ψ	74.7°
Core coord. w.r.t. CLF	(13.5 km, -8.1 km)
TAFD timestamp	4:00:11.3779 (in UTC)
EUSO-TA	
Elevation	21°
Number of GTUs	2
GPS timestamp #1	4:00:13.3582275 (in UTC)
GPS timestamp #2	4:00:13.3582449 (in UTC)

Table 4.7: Parameters of the candidate event recorded on the 12th September 2015.

The expected GTU# range is 88-92 (see Section 5.1.3) and the candidate event #1 has the first frame with GTU# 83 and the #2 has GTU# 90. Considering that the expected GTU# range might be slightly larger, both the candidate events could be the actual detected event, as well as both can be just noise.
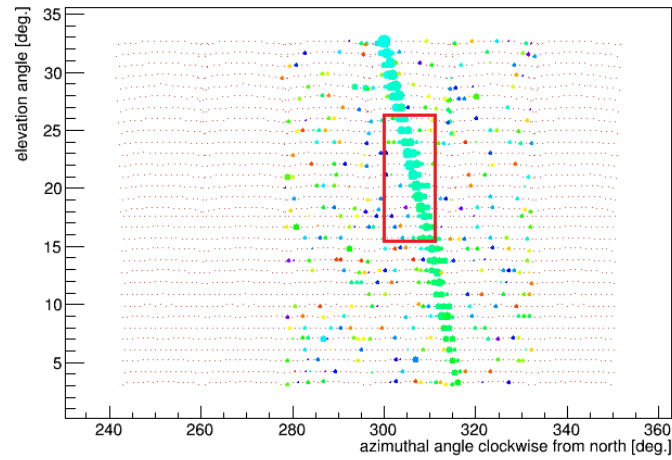
(a) TAFDs event with EUSO-TA FOV overlaid. The size of the point means signal strength and color means timing. Larger point size means stronger signal, and red points mean later than blue points. Image from [76].
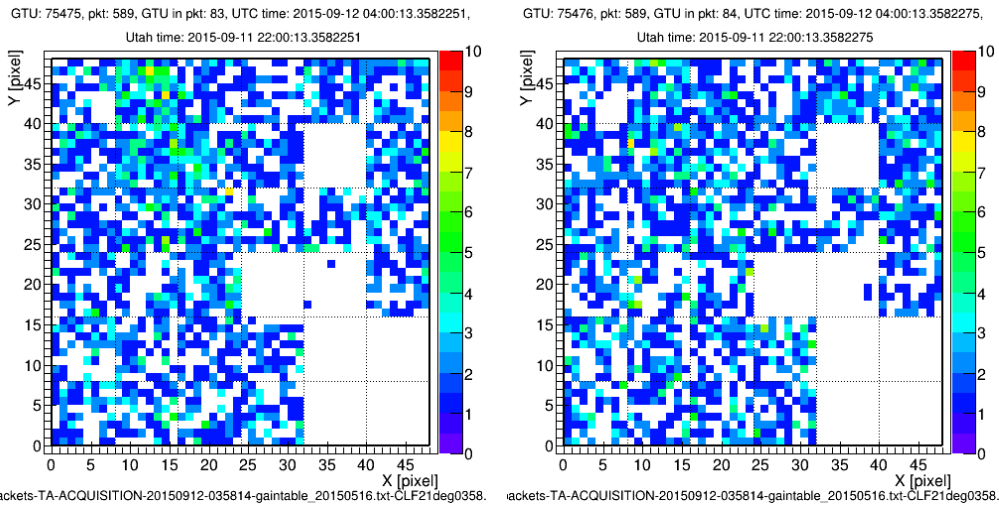
(b) EUSO-TA event #1, GTU 1

(c) EUSO-TA event #1, GTU 2
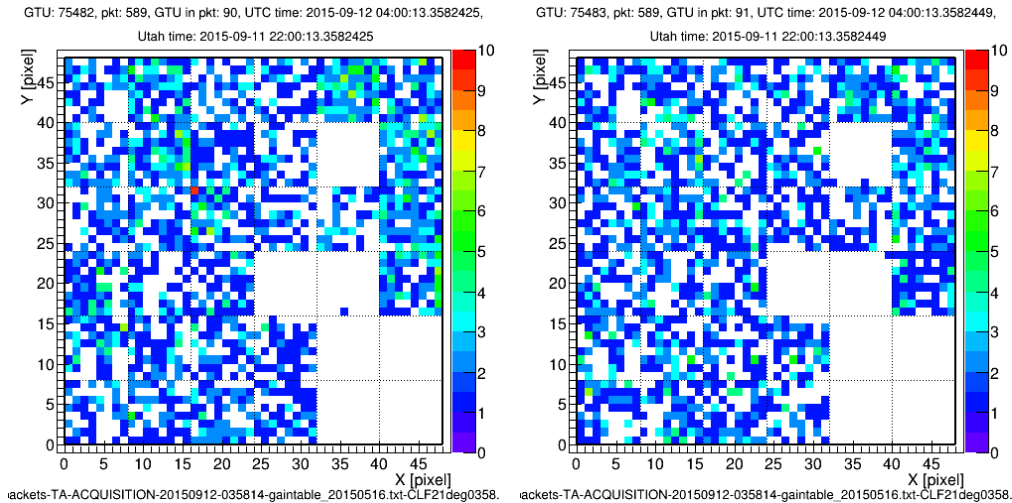
(d) EUSO-TA event #2, GTU 1

(e) EUSO-TA event #2, GTU 2

Figure 4.9: Two possible candidate events recorded on the 12th September 2015 by TAFDs (a) and EUSO-TA (b,c) and (d,e).

Candidate event of 15th October 2015

The simulation of this event shows it on 3 GTUs. It is a distant cosmic ray air shower, with $R_p = 9.0$ km, which travels almost in the plane parallel to the telescope lenses. In Table 4.8 the reconstruction parameters and the information on the EUSO-TA event are listed. Figure 4.10 shows the event for TAFDs (a) going from left to right and the relative candidate for EUSO-TA (b,c,d). The signal segments seem to be visible in GTU 1 and mainly in GTU 2, although the track seems not continuous but two separated spots.

TA reconstruction	
Zenith	40.6°
Azimuth	$-120.5°$ (+ from N clockwise)
Energy	$10^{18.52}$ eV
R_p	9.0 km
Ψ	99.5°
Core coord. w.r.t. CLF	(10.6 km, -5.6 km)
TAFD timestamp	9:26:28.5743 (in UTC)
EUSO-TA	
Elevation	15°
Number of GTUs	3
GPS timestamp	9:26:36.2988 (in UTC)

Table 4.8: Parameters of the candidate event recorded on the 15th October 2015.

The expected range of GTU# in the packet of data is 66-70 (see Section 5.1.3). For this event it is 68, and it seems to be acceptable. Also the search for similar frames has a negative result. However, the irregular track leaves the event among the candidate events, although it is highly possible that it is the case of a detected event.
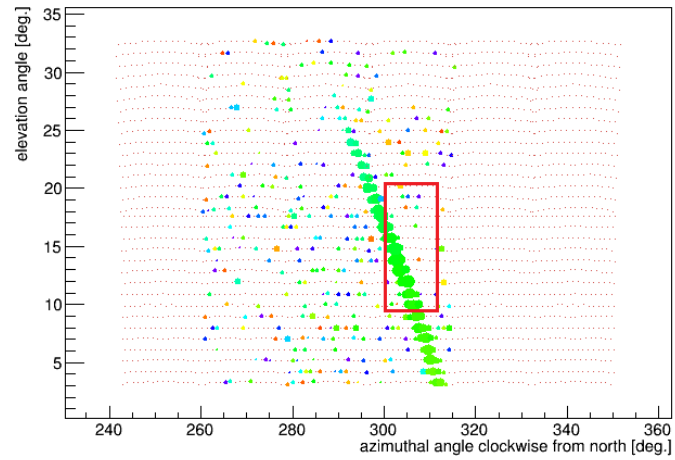
(a) TAFDs event with EUSO-TA FOV overlaid. The size of the
point means signal strength and color means timing. Larger point
size means stronger signal, and red point means later than blue
point. Image from [76].
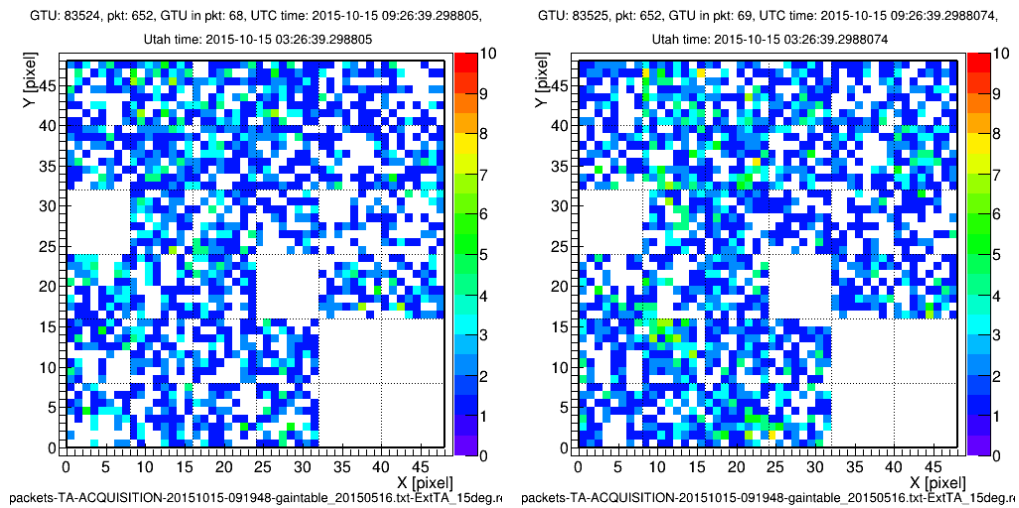
(b) EUSO-TA event, GTU 1
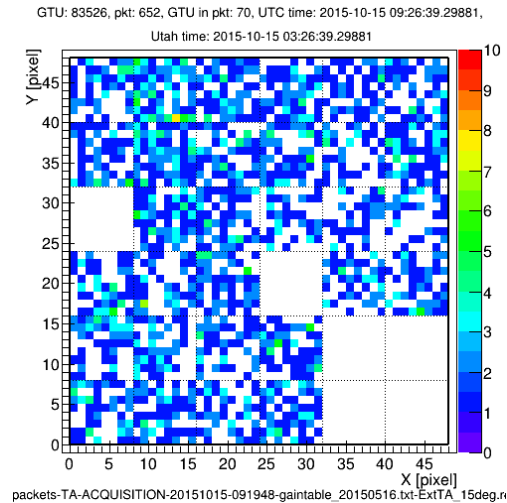
(c) EUSO-TA event, GTU 2

(d) EUSO-TA event, GTU 3

Figure 4.10: Candidate event recorded on the 15th October 2015 by TAFDs (a) and EUSO-TA
(b-d).

Candidate event of 16th October 2015

This cosmic ray event lasts just one GTU since the cosmic ray air shower is close, with $R_p = 1.7$ km, and goes slightly towards the telescope. Figure 4.11 shows the event for TAFDs (a), almost vertical in the middle-right part of the frame, and the only candidate event found for EUSO-TA (b), which crosses also a not active PMT.

TA reconstruction	
Zenith	10.6°
Azimuth	−40.5° (+ from N clockwise)
Energy	$10^{17.71}$ eV
R_p	1.7 km
Ψ	100.6°
Core coord. w.r.t. CLF	(15.6 km, −11.0 km)
TAFD timestamp	9:08:11.6085 (in UTC)
EUSO-TA	
Elevation	10°
Number of GTUs	1
GPS timestamp	9:08:16.6218 (in UTC)

Table 4.9: Parameters of the candidate event recorded on the 16th October 2015.

The expected range of GTU# in the packet of data is 63-68 (see Section 5.1.3). For this event it is 67, and it seems to be acceptable. But, being faint since the low energy of the cosmic ray, it remains classified as a candidate event, although most probably it is a detected event.
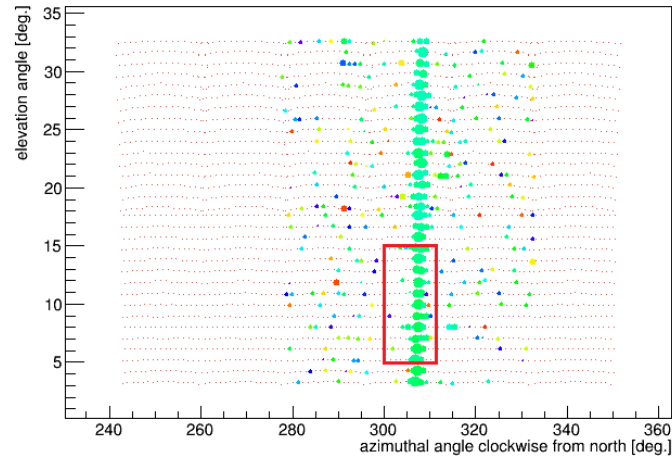
(a) TAFDs event with EUSO-TA FOV overlaid. The size of the point means signal strength and color means timing. Larger point size means stronger signal, and red points mean later than blue points. Image from [76].
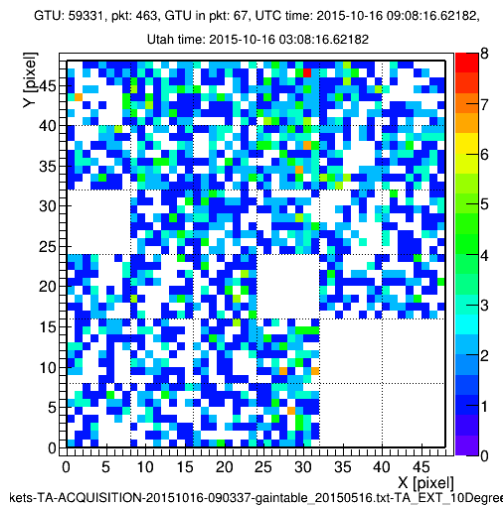
(b) EUSO-TA event, GTU 1

Figure 4.11: Candidate event recorded on the 16th October 2015 event by TAFDs (a) and EUSO-TA (b).

4.5 Laser from the Central Laser Facility

In order to monitor the atmospheric conditions, the Central Laser Facility (CLF) has been placed in the center of the TA site. It is located at a distance of 20.85 km from each of the three FD stations. It shoots a vertical pulsed laser with an energy of 2 mJ every 30 min. In every run, 300 laser pulses are shot in 30 s, with a frequency of 10 Hz. Figure 4.12 shows the laser from the CLF as seen by TA and Figure 4.13 as seen by EUSO-TA. The TA event is integrated in $51.2\,\mu$s time window, while the EUSO-TA one is shown in six frames (6 GTUs). Note that the GTU was defined for the cosmic ray air showers detection by JEM-EUSO, as the time in which the light crosses the FOV of one pixel from the ISS. EUSO-TA, because of the different distance of the light source and the different optical system, sees a laser pulse a few pixels long and wide.
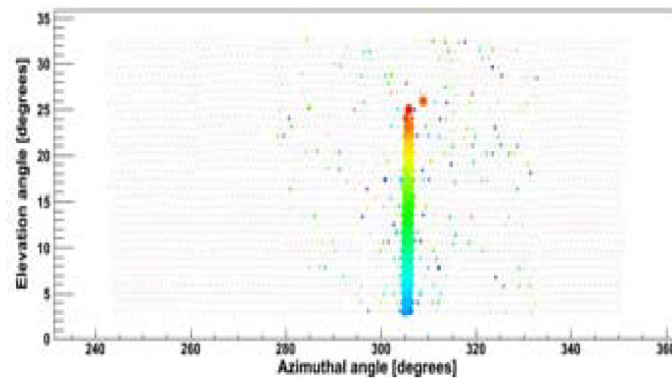
Figure 4.12: Event display of the CLF laser of TA. The size of the point means signal strength and color means timing. Larger point size means stronger signal, and red points mean later than blue points. Image taken from [77].

(a) Frame 1

(b) Frame 2

(c) Frame 3

(d) Frame 4

(e) Frame 5

(f) Frame 6
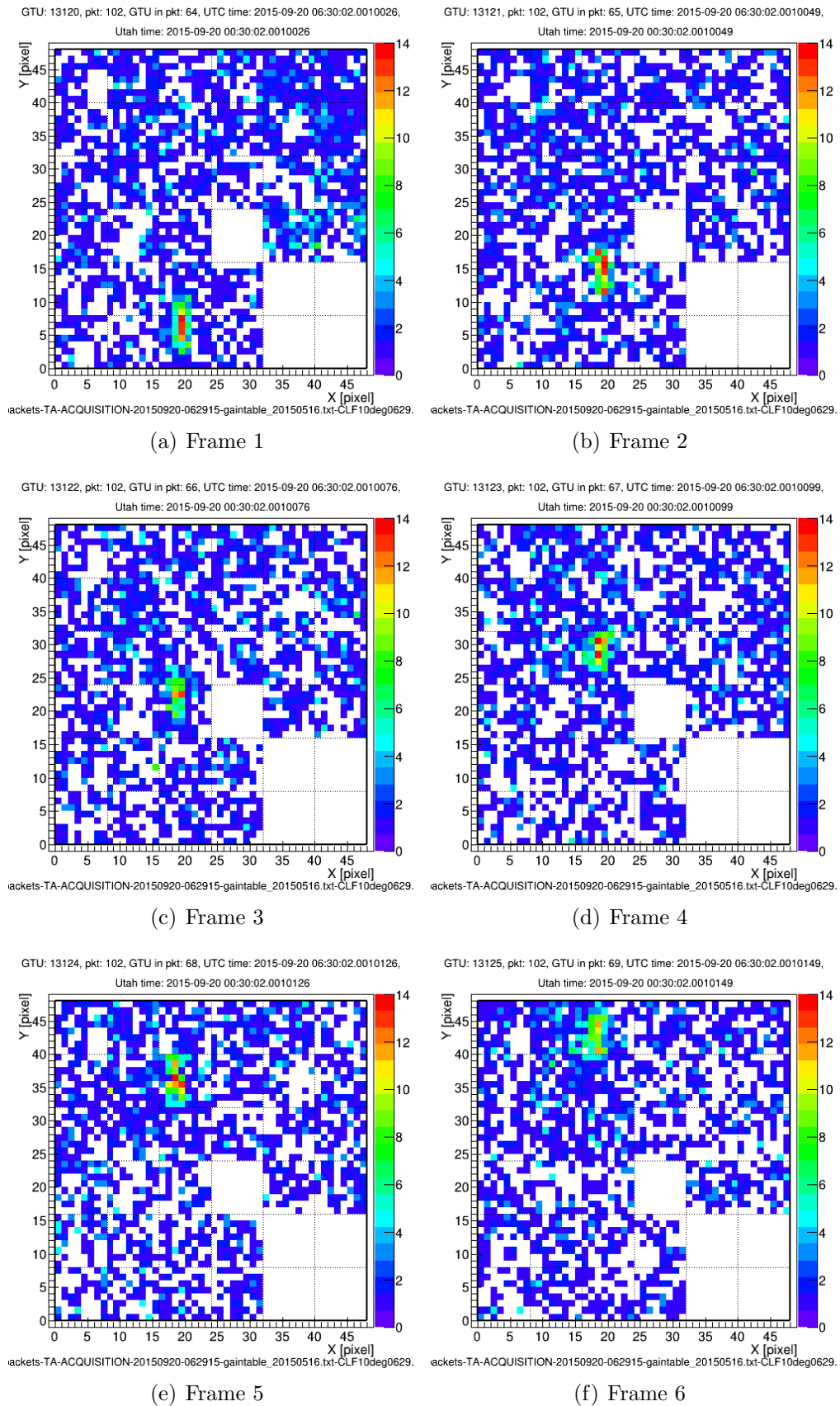
Figure 4.13: A sequence of a laser shot from CLF through the EUSO-TA FOV, detected on the 20th September 2015 with a telescope elevation of 10°.

4.6 Stars

Although stars represent a background signal for a fluorescence telescope, their detection is interesting. First of all, star signals give information on the "health" of the detector. Since the star positions in the sky are well known, given the location and time, it is possible to check if the telescope is able to see them. If yes, the point spread function* of the star images can be used to evaluate the status of the focus of the telescope. In Figure 4.14, β Persei (Algol) (a) with an absolute magnitude $M_B = 2.09$† and Vega (b) with $M_B = +0.03$ are clearly visible in the top left corner of the frames, with a few other fainter stars with $M_B < 5$. The sequences of both the stars through the PDM are available in Appendix C).

(a) β Persei (Algol)   (b) Vega
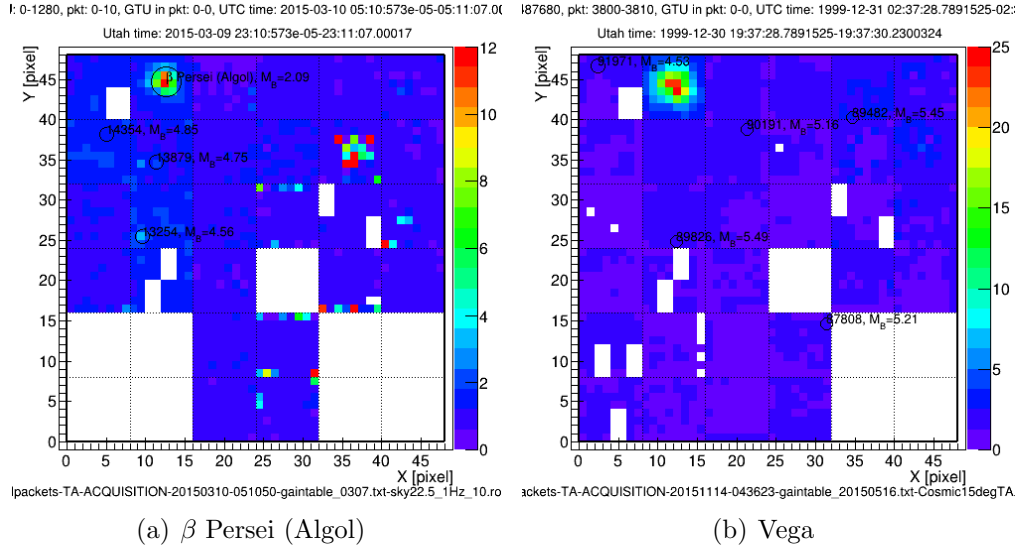
Figure 4.14: Frames showing β Persei (Algol) (a) and Vega (b), together with a few other fainter stars. Every frame shows the average of 1280 GTUs. The Algol image was taken on the 10th March 2015 and Vega on the 14th November 2015. The Hipparcos catalogue [78] is superimposed on the frames using the ETOS software, as well as the star absolute magnitudes M_B, and the circle size is proportional to the star luminosity. The sequences of both the stars through the frame are available in Appendix C.

As seen in Section 3.3.1, luminous spots can be asymmetrical in lateral regions of the frames, far from the optical axis, due to aberrations such as coma. A preliminary evaluation of such deformation is discussed in Section 5.2.

---

*The point spread function (PSF) describes the response of an imaging system to a point source or point object.

†In astronomy the "magnitude" is a measure of the luminosity of a star. Low magnitudes correspond to bright stars, with the brightest objects reaching negative values. M_B is the absolute magnitude of the star at the blue (B) wavelength (440 nm).

Chapter 5

Data analysis

5.1 Cosmic ray event analysis

5.1.1 Fit algorithms

Two fit algorithms have been developed for two purposes: the comparison between the track inclination of detected and simulated events (Section 7.2.2), and the evaluation of the lateral distribution of the showers (Section 5.1.2).

Linear fit

The linear fit algorithm finds the line which fits the cosmic ray air shower track best and Figure 5.1 shows its four main steps. Since the event tracks are displayed on discrete arrays of 48×48 pixels, some preparatory operations have to be performed, before the linear fit. First, straight lines $y = m \cdot x + q$ with different m and q parameters within intervals specified by the user are generated (a). Second, for each line 11 pixels are taken on both the sides of line along X per each row of pixels (i.e. per each pixel along Y) (b). The decision of considering a certain number of pixels around the line comes from the fact that, considering the whole rows of pixels, variation of the background could eventually compromise the fit; the choice of 11 pixels per side comes from tests which revealed 11 as the best value to get good performances of the fit algorithm. Each of the 48 rows of pixels is fitted with a Gaussian (c). Finally, the means of the Gaussians, which lie on the event track, are fitted with the method of least squares. Of all the generated lines, the fitting line is the one which minimizes the error.
The linear fit gives the value of the m and q parameters. Than, the angle α of the straight line with respect to the vertical, depending just on m, can be calculated as $\alpha = \mathrm{arccot}(m)$. α is related to the combination of the zenith and azimuth angles of the cosmic ray air showers, projected on the focal surface.
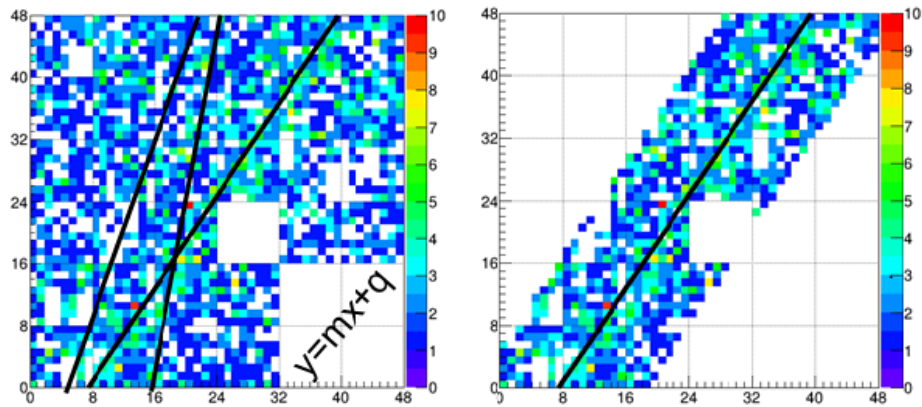
(a) Step 1: Definition of different lines with different m and q parameters.

(b) Step 2: For each line, consideration of 11 pixels on both the sides of it.
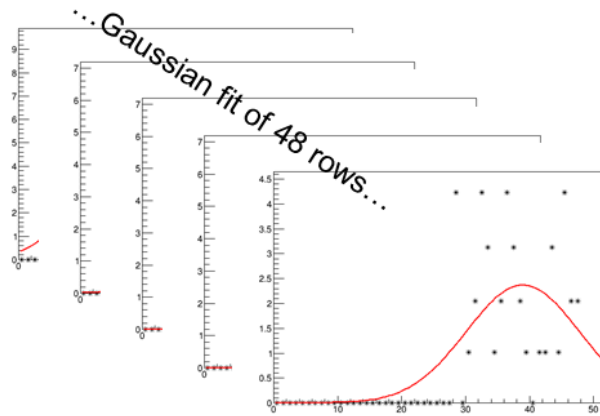
(c) Step 3: Gaussian fit per each row of pixels.
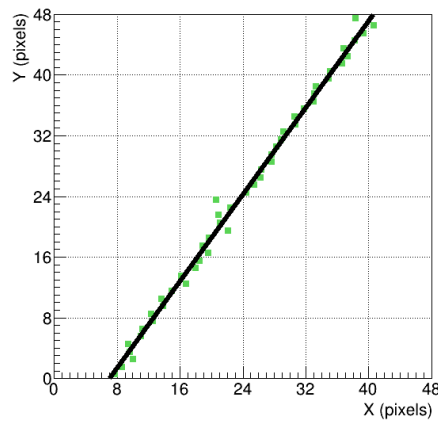
(d) Step 4: Linear fit with the method of least squares.

Figure 5.1: Sketch of the algorithm of the linear fit to evaluate the inclination of the track.

Gaussian fit

The cosmic ray air showers have an inner, most energetic part along the axis which appears as the brightest in fluorescence telescopes. With the distance from the shower axis, the number of photons decreases, due to scattering.

To evaluate the lateral distribution of the cosmic ray air showers, a Gaussian fit perpendicular to the shower axis is done, once the linear fit described in Section 5.1.1 gives the m and q parameters of the straight line fitting the shower axis. The Gaussian is the most simple first approximation fit. With more statistics and more stable measurements this can be refined and also theoretically investigated.

To perform Gaussian fits perpendicular to the shower axis, a grid with the x'-axis along the perpendicular to the shower axis (transverse direction) and y'-axis along the shower axis (longitudinal direction) is created, see Figure 5.2. The term "pixel" refers now to the original pixels of the focal surface, and "cell" to the gaps of the new "rotated" grid. Indeed, in the reference of the grid the shower track looks vertical. The cells are smaller than the pixels, in order to redistribute the original pixel content in the cells distorting the image as less as possible.

The grid is created as follows. Every half a pixel of the 48×48 pixels frame, a horizontal line is traced intersecting the line fitting the shower axis. From these intersection points, perpendicular lines to the shower axis are defined. Dividing the transverse line in segments of half a pixel size and drawing longitudinal lines from their edges, the grid is created, with bins sized half a pixel on the x'-axis and slightly longer on the y'-axis, depending on the inclination of the shower track. The grid's size is of 25×95 cells: 12 cells on both the sides of the shower axis, the central one along the shower axis; 95 cells along the y' axis. In each cell, the corresponding content of the pixel of the 48×48 array divided by four is set. Indeed, in average, the content of each pixel is split in four cells and, assigning to each cell 1/4 of the pixel content, allows to keep the total number of counts.

Afterwards, the average for each of the 25 columns of cells is calculated and displayed
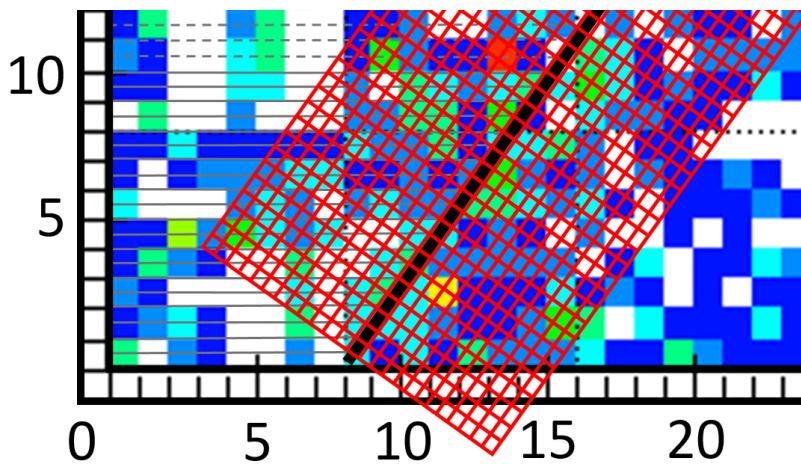
Figure 5.2: Sketch of the algorithm of the Gaussian fit to evaluate the width of the track.

as average distribution of the cells' content along the x'-axis. A Gaussian fit of the average distribution is then performed and the Full Width at Half Maximum (FWHM) of the Gaussian, in units of cells, is calculated. The FWHM can be determined from the standard deviation σ by

$$\text{FWHM} = 2.355 \cdot \sigma. \tag{5.1}$$

To have the final estimation of the track width, the FWHM has to be doubled to have the result in terms of pixels of the focal surface of the detector and, knowing the FOV of each pixel, the corresponding value in angular units can be calculated too. Section 5.1.2 describes the evaluation of the lateral distributions for the detected events.

5.1.2   Lateral distribution

The high spatial resolution of the EUSO detectors, with pixels with FOV of 0.19°, allows to study the structure of the cosmic ray air showers. Indeed, as shown in Figure 4.4, EUSO-TA has a much higher spatial resolution than the TA fluorescence detectors, which have pixels with FOV of 1°. In this section the calculation of the lateral distribution of the detected events is discussed. Per each event, the array of 25×95 cells is shown, together with the average over the columns of cells. The equation of the fitting line resulting from the linear fit $y = m \cdot x + q$ and the corresponding track inclination $\alpha = \text{arccot}(m)$ are reported, together with the FWHM from the Gaussian fit of the average distribution, which represents the width of the track. These parameters are accompanied with their uncertainties, calculated as explained in Appendix B.2. The results are also summarized in Table 5.1.

Parameters	Events (2015)			
	13 May	18 Sep.	20 Sep.	7 Nov.
E (eV)	10^{18}	$10^{18.51}$	$10^{18.38}$	$10^{18.42}$
R_p (km)	2.5	9.1	6.7	2.6
m	1.45 ± 0.01	-0.849 ± 0.005	2.04 ± 0.02	19.00 ± 1.49
q	-11.0 ± 0.3	33.01 ± 0.06	-1.7 ± 0.3	-220 ± 19
Width (pixels)	3.36 ± 4.21	3.63 ± 4.31	3.59 ± 4.58	5.27 ± 6.45
Width (°)	0.64 ± 0.80	0.69 ± 0.82	0.68 ± 0.87	1.00 ± 1.23

Table 5.1: Summary of the track widths for the detected events, with statistical uncertainties.

It is evident that the statistical uncertainties are larger than the estimated value of the track width, of about 20-25%. This is due to the low number of photons involved in the measurements, in particular to the low number of photons from the

shower, once the background is subtracted.

A higher number of detected events would allow a higher statistics of high energy events and, possibly, events with signal coming from the X_{max} of the shower. In both conditions, a higher number of photons would be detected and this would lead to more precise calculations.

Event of 13th May 2015

This is a close cosmic ray air shower with $R_p = 2.5$ km and energy 10^{18} eV. Figure 5.3 (a) shows the event track in the longitudinal perspective, with cells sized as half the actual pixels. To perform the average over the columns of cells, the rows with no counts because they are located beyond the edge of the frame of 48×48 pixels ($y' < 5$ and $y' > 90$) or because of non-active pixels ($35 < y' < 55$) have not been considered, to reduce asymmetries between one or the other side of the track and improve the Gaussian fit. In (b) the average distribution is shown, with the Gaussian fit superimposed, performed for $5 < x' < 20$ and constant number of background counts per cell of ~ 0.4 counts. The Gaussian fit allows to calculate the FWHM in units of actual pixels and degrees, considering the FOV of one pixel $0.19°$, as follows:

$$\begin{aligned} \mathrm{FWHM_{cells}} &= 6.72 \pm 8.41 \, \mathrm{cells} & (5.2) \\ \mathrm{FWHM_{pixels}} &= \mathrm{FWHM_{cells}}/2 \simeq 3.36 \pm 4.21 \, \mathrm{pixels} \rightarrow 0.64° \pm 0.80° \end{aligned}$$
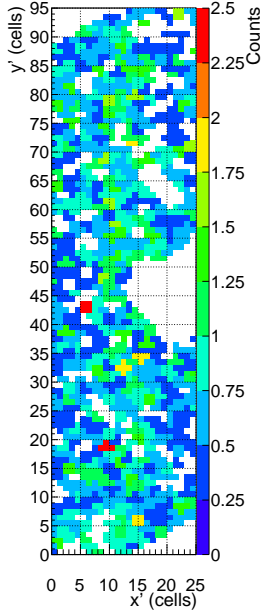
(a) 25×95 array of cells centered with the event track axis. The size of one bin along x'-axis is half an actual pixel.
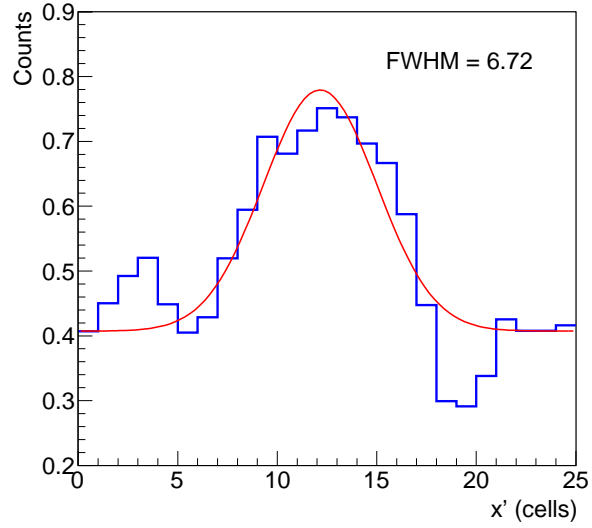
(b) Distribution of the average of the columns of cells. The rows of cells with $y' < 5$, $35 < y' < 55$ and $y' > 90$ are not considered in the average, to reduce asymmetries in the distribution. The Gaussian fit, performed for $5 < x' < 20$ and constant number of background counts per cell of ~ 0.4 counts, gives the FWHM reported on the plot, in units of cells.

Figure 5.3: Event of 13th May 2015. Event track along the longitudinal direction (a) and distribution of the average of the columns of cells (b).

Event of 18th September 2015

This is a distant cosmic ray air shower with $R_p = 9.1$ km, and energy $10^{18.51}$ eV. The event is split over three frames, because of the distance and its geometry. Figure 5.4 (a) shows the sum of the two frames in the longitudinal prospective along the track (in the last frame, a possible track would have been on the non-active EC in the right hand side), with binning sized as half the actual pixels. To perform the average over the columns of cells, the rows with no counts ($y' < 20$ and $y' > 51$) have not been considered. In (b) the average distribution is shown with the result of the Gaussian fit, performed for $5 < x' < 20$ and with a constant number of background counts per cell of ~ 0.4 counts. The FWHM in units of actual pixels and degrees is calculated as:

$$\text{FWHM}_{\text{cells}} = 7.26 \pm 8.62 \, \text{cells} \tag{5.3}$$
$$\text{FWHM}_{\text{pixels}} = \text{FWHM}_{\text{cells}}/2 \simeq 3.63 \pm 4.31 \, \text{pixels} \rightarrow 0.69° \pm 0.82°$$

(a) 25×95 array of cells centered with the event track axis. The size of one bin along x'-axis is half an actual pixel.
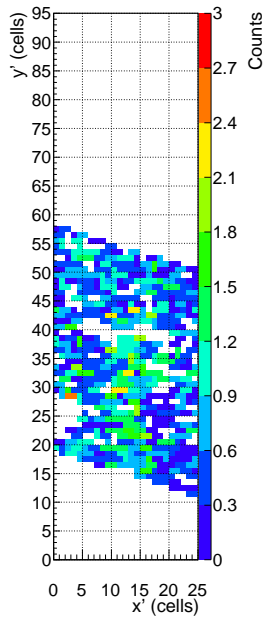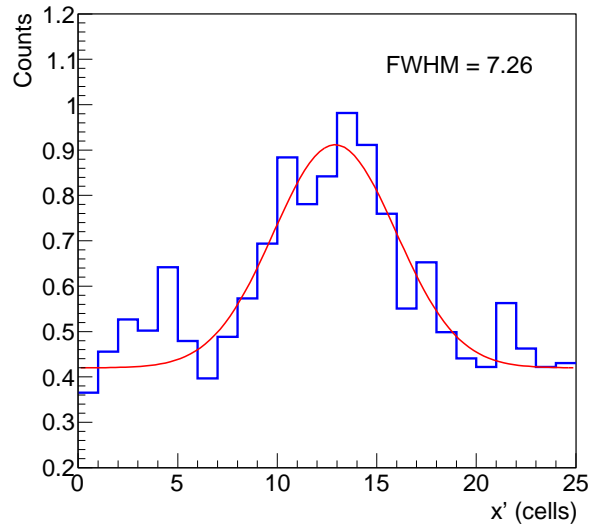
(b) Distribution of the average of the columns of cells. The rows of cells with $y < 20$ and $y > 51$ are not considered in the average. The Gaussian fit, performed for $5 < x' < 20$ and with a constant number of background counts per cell of ~ 0.4 counts, gives the FWHM reported on the plot, in units of cells.

Figure 5.4: Event of 18th September 2015. Event track along the longitudinal direction (a) and distribution of the average of the columns of cells (b).

Event of 20th September 2015

This is a distant cosmic ray air shower with $R_p = 6.7$ km, and energy $10^{18.38}$ eV. The event is split over two frames, because of the distance and its geometry. Figure 5.5 (a) shows the sum of the two track segments in the longitudinal prospective, with binning sized as half the actual pixels. To perform the average over the columns of bins, the rows with no counts because of being beyond the edge of the frame of 48×48 pixels ($y' < 25$ and $y' > 90$) have not been considered. In (b) the average distribution is shown with the Gaussian fit in the range $5 < x' < 20$ and with a constant number of background counts per cell of ~ 0.65 counts. The FWHM of the Gaussian fit, in units of pixels and degrees, has been calculated as:

$$
\begin{aligned}
\text{FWHM}_{\text{cells}} &= 7.18 \pm 9.16 \, \text{cells} \\
\text{FWHM}_{\text{pixels}} &= \text{FWHM}_{\text{cells}}/2 \simeq 3.59 \pm 4.58 \, \text{pixels} \rightarrow 0.68° \pm 0.87°
\end{aligned}
\tag{5.4}
$$
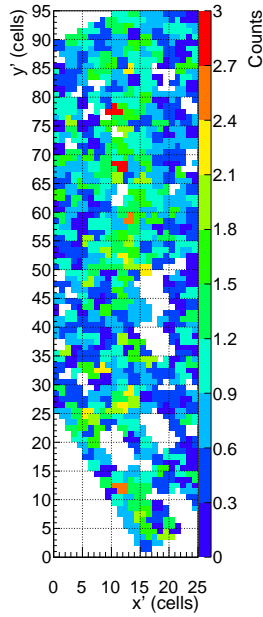
(a) 25×95 array of cells centered with the event track axis. The size of one bin along x'-axis is half an actual pixel.
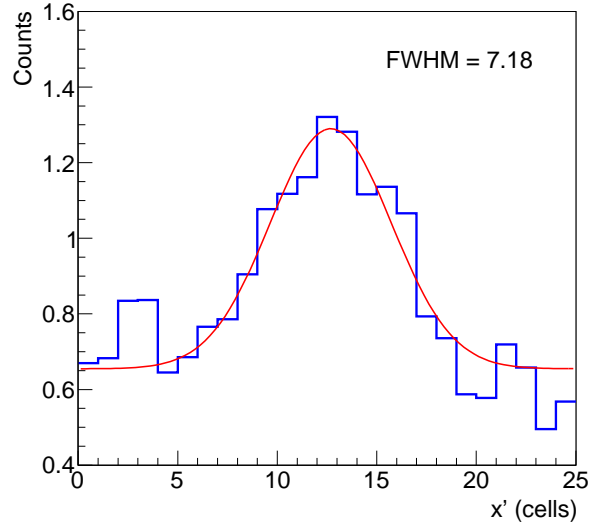
(b) Distribution of the average of the columns of cells. The rows of cells with $y < 25$ and $y > 90$ are not considered in the average. The Gaussian fit, performed for $5 < x' < 20$ and with a constant number of background counts per cell of ~ 0.65 counts, gives the FWHM reported on the plot, in units of cells.

Figure 5.5: Event of 20th September 2015. Event track along the longitudinal direction (a) and distribution of the average of the columns of cells (b).

Event of 7th November 2015

This is a close cosmic ray air shower with $R_p = 2.6$ km, and energy $10^{18.42}$ eV. Figure 5.6 (a) shows the event track in the longitudinal prospective, with binning sized as half the actual pixels. In this event, no cuts of rows of bins beyond the edge of the frame or on non-working pixels have been necessary. In (b) the average distribution is shown with the Gaussian fit in the range $5 < x' < 20$ and with a constant number of background counts per cell parameter of ~ 0.7 counts. The FWHM in units of pixels and degrees has been calculated as follows:

$$\text{FWHM}_{\text{cells}} = 10.54 \pm 12.91 \, \text{cells} \tag{5.5}$$

$$\text{FWHM}_{\text{pixels}} = \text{FWHM}_{\text{cells}}/2 \simeq 5.27 \pm 6.45 \, \text{pixels} \rightarrow 1.00° \pm 1.23° \tag{5.6}$$
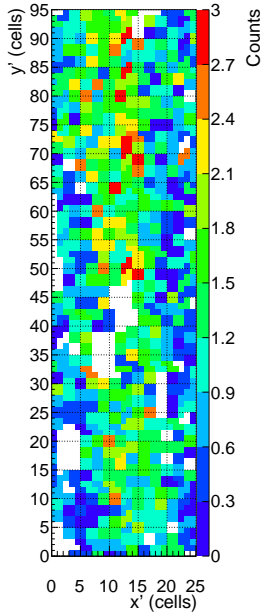
(a) 25×95 array of cells centered with the event track axis. The size of one bin along x'-axis is half an actual pixel.
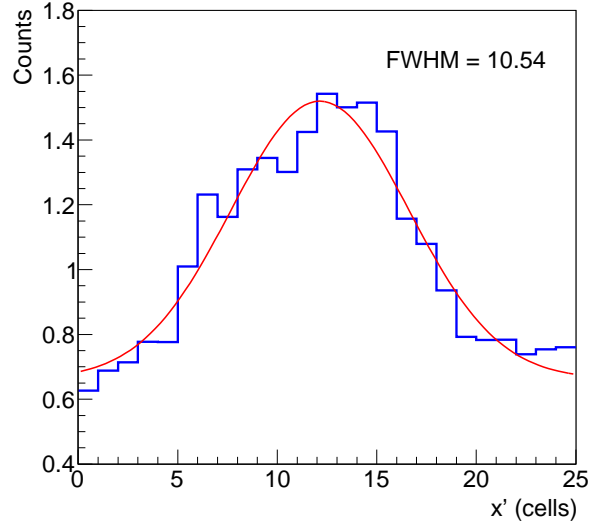
(b) Distribution of the average of the columns of cell. The Gaussian fit,, performed for $5 < x' < 20$ and with a constant number of background counts per cell of ~ 0.7 counts, gives the FWHM reported on the plot, in units of cells.

Figure 5.6: Event of 7th November 2015. Event track along the longitudinal direction (a) and distribution of the average of the columns of cells (b).

In general, one would expect that the track width is larger for close and for more energetic showers and thinner for distant and less energetic showers. Although the statistics is low, this is what seems to be for these four events. The 13th May event and the 7th November event are close to the detector (although the geometry is different) but the second one is more energetic than the first, and the track width follows the expected trend. Comparing the event of the 18th September with the one of the 13th May, they have similar track width, due to the combination of the higher energy and longer distance from the detector of the first. The 20th September event looks like an intermediate case, although summing the two frames the geometry of the track seems slightly irregular, and this might affect the result. Involved there are also the precision of the linear fit algorithm which gives the angular parameter m, on which the performance of the Gaussian fit then depends.
A larger number of detected events would also allow to evaluate the track width when X_{max} is inside the detector FOV, which is not the case for the events detected up to now.

5.1.3   Analysis of the event timestamps

As discussed in Chapter 4, most of the data acquisition of EUSO-TA happens in coincidence with TA, which sends a trigger signal to when a cosmic ray air shower crosses its large FOV. This acquisition mode is efficient for EUSO-TA, because it is possible to take advantage of the TA trigger and cosmic ray event reconstruction algorithms proved over the years and allows to identify the detected cosmic ray events and to get the reconstruction parameters for further independent analysis.
Important parameters that give the possibility to define a detected (or candidate) event are the timestamp of the event, which relates the TA and EUSO-TA counterparts, and the sequential number of the GTU (GTU#) inside the packet containing the event. These parameters for the detected and the candidate cosmic ray events are listed in Table 5.2.
The difference between the EUSO-TA and the TA timestamps is always of the order of a few seconds. This is caused in part by a systematic time shift of about 1 s between the time of the first trigger of a data acquisition run of EUSO-TA (creating a new data file) and the time corresponding to the first frame (GTU#0) of the data file; moreover, the difference might be related to a synchronization issue between the two detectors.
Regarding the GTU# in the packet, it is related to an almost regular offset between the time in which an event enters the EUSO-TA and the time corresponding to the beginning of the packet (GTU#0 in the packet), for example due to the length of the cables transmitting the signals. When a trigger signal is received, the current whole packet of 128 GTUs is saved. Some settings have been changed between the 18th and the 20th of September, and for this the GTU# in the packet for the events changes from ~ 85 to ~ 65. To have a reference of the expected GTU# in the packet for an event, the laser events from the CLF have been investigated.

Event (2015)	TA time (UTC)	EUSO-TA time (UTC)	Difference (s)	GTU# in pkt (CR)	GTU# in pkt (CLF)	Elevation (deg)
Detected Events						
13 May	08:26:49.3559	08:26:53.3762424	4.0203424	82	83-88	15
18 September	05:40:19.9036	05:40:21.9049175	2.0013175	80	86-90	20
20 September	10:59:19.3094	11:00:43.3117125	84.0023125	64	63-67	10
7 November	09:15:06.7325	n.a.	n.a.	65	65-70	15
Candidate Events						
12 May	08:26:45.4039	08:26:48.4158676	3.0120676	82	90-92	25
12 September I	04:00:11.3779	04:00:13.3582275	1.9803275	83	88-92	21
.... II	04:00:11.3779	04:00:13.3582449	1.9803449	90	88-92	21
15 October	09:26:28.5743	09:26:36.2988050	7.7245805	68	66-70	15
16 October	09:08:11.6085	09:08:16.6218200	5.013382	67	63-68	10

Table 5.2: Timestamps of EUSO-TA detected and candidate events and the corresponding TA events. The difference between the timestamps is reported too, as well as the GTU# in the packet for the cosmic ray events and for the CLF laser pulses from the same day of data acquisition.

Indeed every 30 minutes a run of laser shooting takes place for 30 s, and it is easy to find the frame in which the laser shot appears, since it happens regularly at a almost constant GTU# in all the packets. To check the expected GTU# in the packet with the laser event, a few data files have been taken into account, and in each file a few packets have been checked. The result is reported in the table as a range of GTU# in the packet, which is not actually constant due to fluctuations. Also the elevation of the EUSO-TA telescope may slightly influence the expected GTU# in the packet with the triggered event. Indeed, changing the elevation angle changes the relative position between the TA FOV and the EUSO-TA FOV, and so a difference between the time an event enters the two of them.

In this analysis the detected and the candidate events have the GTU# in the packet close to the GTU# in the packet of the laser events. However, some differences are visible. Probably this is in part due to the limited number of laser events checked. Moreover, the cosmic ray air showers enter both FOV from above, while the laser shots come from below. Depending on the elevation angle of EUSO-TA, the path traveled inside the TA FOV before entering the EUSO-TA FOV can be different for down going or upward going events, and this may play a role in the difference encountered. For the 12 September event, both the candidate events are reported, and although candidate I has a "better" GTU# in the packet respect to candidate II, from the comparison with the laser event, both can be accepted.

Considering these constrains, a quick consistency check on the data collected in the October 2016 campaign has been done. Knowing the event which crossed EUSO-TA FOV (from previous TA analysis), a check of the packets within a range of time consistent with the TA event timestamps and considering the time offset discussed before has been done. In each packet the frames around the expected GTU# in the packet have been observed, but no potential candidate events have been found.

5.2   Spot size of stars

(a) Frame 1   (b) Frame 14
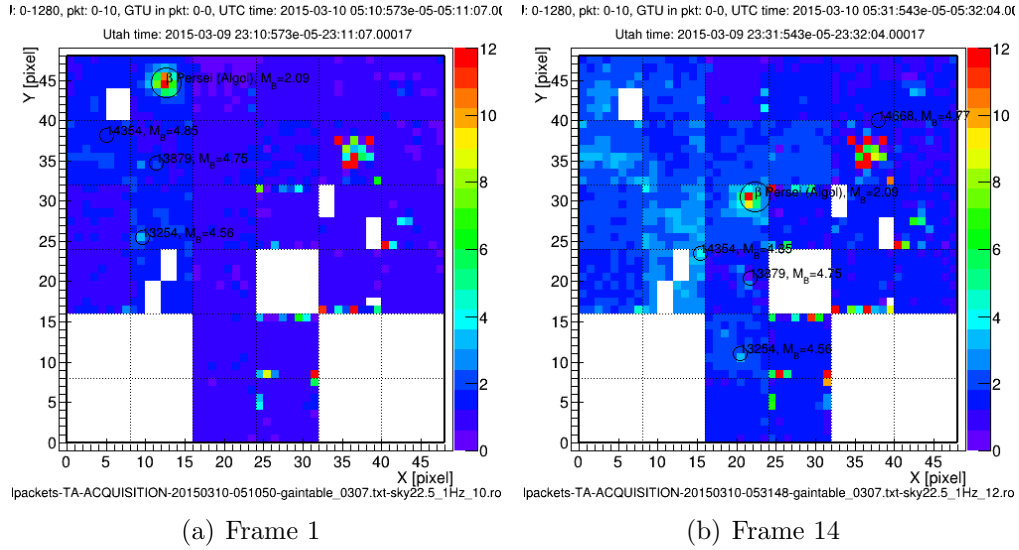
Figure 5.7: Algol image in two frames where the star spot is as much as possible in the center of a PMT, in order to evaluate its change in size while moving from the edge to the center of the PDM.

The stars can be used as point sources to analyze the Point Spread Function (PSF) of EUSO-TA. The wide field of view and the optics used result in the PSF to be asymmetrical in regions of the frame far from the optical axis, most likely due to the influence of aberrations such as coma or astigmatism. A proper analysis of the detector PSF is not performed in this thesis, but a basic evaluation of the deformation of the star spot on the focal surface is done. As seen in Section 4.6, EUSO-TA is capable to clearly detect stars, whose size appears more or less wide depending on their brightness. Very bright stars can be seen on single frames, while they become fainter, an averaging over, for example, 1280 frames (about 3.2 ms observation time), is necessary to get a good signal to noise ratio, with negligible star movement on the sky compared to the angular size of a pixel. Figure 5.7 presents the frame 1 and the frame 14 of the sequence in Appendix C.1, showing β Persei (Algol) moving through the FOV. The Hipparcos catalogue [78] is superimposed on the frame as well as the star magnitudes in the Johnson B filter (the circle size is proportional to the star luminosity). The choice of the two frames is not accidental, indeed in frame 1 Algol is in the external region of the frame (incident angle about 5° from the telescope axis, considering the measured EUSO-TA FOV of $\pm 5.25°$) and in frame 14 in the internal one (incident angle about 1.5°). Frame 14 is an intermediate state between the first and the second frame shown in Figure 3.9, from [67], (arrival direction of 0° an 2°, respectively), while frame 1 is between the third and the fourth ones (4° and 6° from the optical axis, respectively). The image of
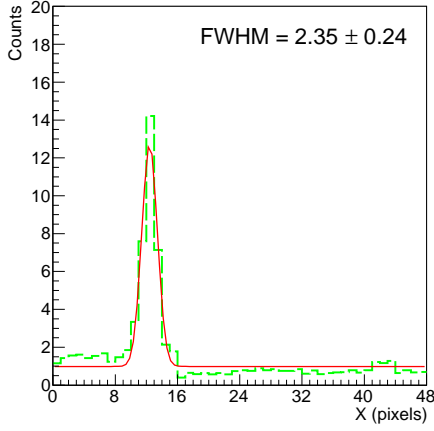
(a) Frame 1, Gaussian fit of the row of pixels with $Y = Y_M^1$.
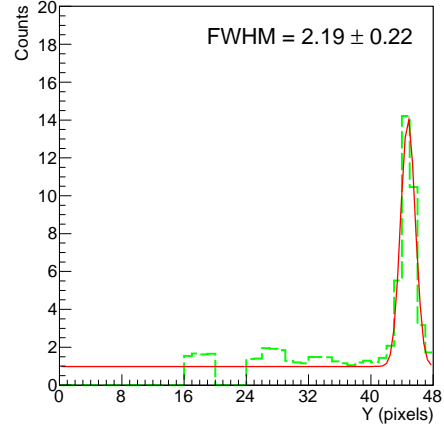
(b) Frame 1, Gaussian fit of the column of pixels with $X = X_M^1$.
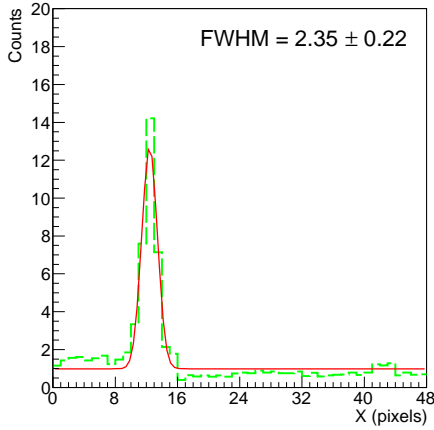
(c) Frame 14, Gaussian fit of the row of pixels with $Y = Y_M^{14}$
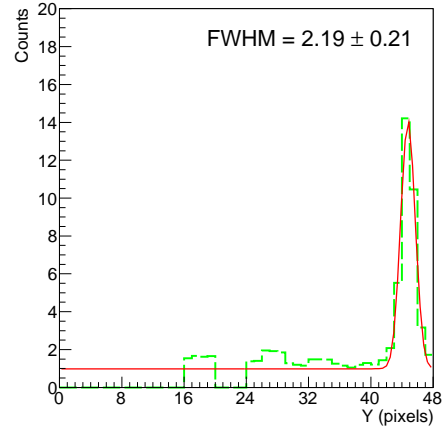
(d) Frame 14, Gaussian fit of the column of pixels with $X = X_M^{14}$

Figure 5.8: Gaussian fit over the the row of pixels with $Y = Y_M$ and the column of pixels with $X = X_M$, after having set a threshold of 1 count in order to remove the background. The FWHM value in units of pixels of each Gaussian is also given.

Algol (absolute magnitude* $M_B = +2.09$, 92.82 ly distant) is smaller than the one of Vega ($M_B = +0.03$, 25.04 ly), and allows to have almost the whole spot in one PMT. Indeed, while a star crosses the gap between one PMT and the adjacent one (4.7 mm), there is a loss of detection, since the gap is larger than the pixel size (2.88 mm). Of both the frames, the pixel with the maximum of the star image is measured with coordinate (X_M, Y_M) in the array of 48×48 PMTs. Then, the Gaussian fit over the row of pixels with $Y = Y_M$ and the column of pixels with $X = X_M$ is made, with a constant number of background counts per cell set at

---

*M_B is the absolute magnitude of the star at the blue (B) wavelength (440 nm).

1 count in frame 1 and 1.7 count in frame 14 for the background, and making the Gaussian fit in the range ±5 pixels around the spots' maximum, see Figure 5.8. From the standard deviation σ of the Gaussian, the FWHM of the Gaussian can be determined as FWHM $= 2.355 \cdot \sigma$, and it represents the width of the spot image. It is visible that the spot size decreases going from the edge of the frame toward the center. The average FWHM is, for

- Frame 1: $\text{FWHM}_1 \sim 2.27 \pm 0.50$ pixels$= 0.43° \pm 0.10°$

- Frame 14: $\text{FWHM}_{14} \sim 1.65 \pm 0.36$ pixels$= 0.31° \pm 0.07°$

with a decrease of $\sim 30\%$ going to the central area. The uncertainties are calculated as explained in Appendix B.2. An error could be introduced by the fact that the star image in frame 14 is close to the gap between two pixels, which leads to a loss of photons. Anyway, no data with star spots in better positions have been found.

In [67] no comparable values are available for the FWHM of the star spots at the arrival direction angle of those in frame 1 and frame 14. However, the trend of the variation of the spot size in this analysis is similar. Moreover, the requirement for EUSO-TA to have an angular resolution better than the one of TAFDs, which is 1°, i.e. ~ 5.3 pixels of EUSO-TA (with a FOV of one pixel 0.19°), is satisfied.

5.3   Background analysis

The background in the EUSO-TA data is not just due to fluctuations of a constant background. It consists also of natural and artificial sources like stars, meteors and planes, as well as of some parasitic noise present in some PMTs, in particular in the latest data acquisition periods. A frame showing such noise (at the right hand side) is shown in Figure 5.9.

A study of the background has been performed to judge if the presence of a cosmic ray event signal influences the mean of the pixels content of a whole frame and of a selected box of 2×2 PMTs containing the event in an evident manner (see Figure 5.10). It would be interesting to see if the event signal plays a significant role or if it can be confused with the noise. The selected box allows to have fewer pixels with low-counts when the event crosses it, and hence to increase the probability that the event is recognizable over the background.

For this purpose, 128 frames corresponding to the packet containing each of the detected cosmic ray events and a laser event from the CLF, have been collected. For each frame and for each selected box, the mean value of the pixel content has been calculated and the 128 mean values plotted on a graph to have an overview of their behavior. Figures 5.11-5.16 show the sequence of 128 mean values for the detected events, in red for the whole frame and in blue for the selected box. A line of the relative color shows the mean over all the 128 frames (baseline). The baseline of the selected box is lower than that of the whole frame, since the noisy areas are excluded. This occurs for three of the four detected events. The uncertainties are calculated as described in Appendix B.1.
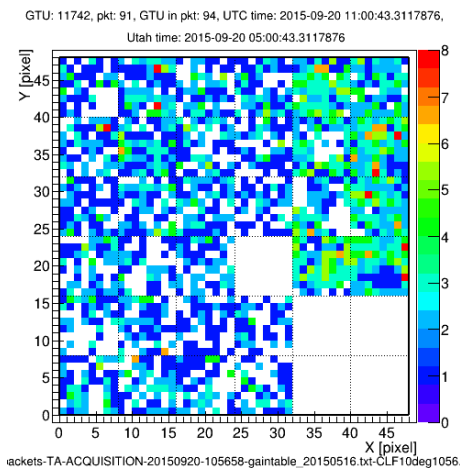
Figure 5.9: Example of a frame with a noisy area (at the right hand side), taken from the packet containing the 20th September 2015 event.
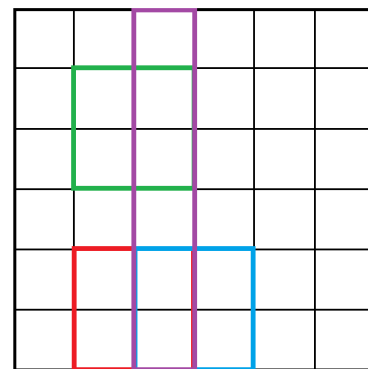
Figure 5.10: Selected boxes: red box used for the events of 13th May and 7th November; blue box for the event of 18th September; green box for the event of 20th September; violet box for the laser event.

5.3.1 Detected cosmic ray events

13th May 2015: background

Figure 5.11 shows the sequence relative to the 13th May 2015 event. This is a 1 GTU event (frame number 83 in the graph). It is evident that the contribution of the CR event is easily visible over the baseline of the background, considering the whole frame and the selected box as well.

18th September 2015: background

Figure 5.12 shows the sequence relative to the 18th September 2015 event. It is a 3 GTUs event (frame number 81-82-83 in the graph). Over the whole frame, the contribution of the CR event signal is not evident, but completely blended by the noise. Considering just the selected box, the event is recognizable over the baseline, although in a few frames the box has a similar mean value per pixel due to noise.

20th September 2015: background

Figure 5.13 shows the sequence relative to the 20th September 2015 event. It is a 2 GTUs event (frame number 65-66 in the graph). Also in this case, the presence of the CR event is not obvious in the whole frame, while it is in the selected box. For this event, the baseline background in the selected box is higher than that for the whole frame. This is because the selected box is over a slightly noisy area, but such selection was necessary in order to include the CR event.
Using the software *Stellarium*† it is visible that at the time of this cosmic ray event, the Milky Way was right in the EUSO-TA FOV. In order to check if and how this can influence the mean background on the whole frame, three packets of data with Milky Way (at about 10:56 UTC time, 4:56 Utah local time) in the FOV, including the packet with the cosmic ray event, and three without it (at about 06:02 UTC time, 00:02 Utah local time). The comparison is visible in Figure 5.14. The mean values of the packets in presence of the Milky Way (reddish lines) are slightly higher than those without (bluish lines), by about 19% on average. Here, the uncertainties have not been taken into account, focusing just on the variation of the baseline in the two conditions.

7th November 2015: background

Figure 5.15 shows the sequence relative to the 7th November 2015 event. It is a 1 GTU event (frame number 66 in the graph). Here the signature of the cosmic ray event is quite clear considering the whole frame and the selected box as well, since it is a bright event. As seen in Figure 4.7 (b), the data frame presents also a noisy area, which contributes significantly to the mean of the frame. In this case, the Milky Way is close but not right in the EUSO-TA FOV, so no calculation has

---

†http://www.stellarium.org/it/

been done do evaluate its contribution. Anyway, probably it influences the mean background slightly, but not at the level to explain the evident increase of the mean background in this packet with respect to the packets containing the other events. Most of the difference might be caused by electronic noise.
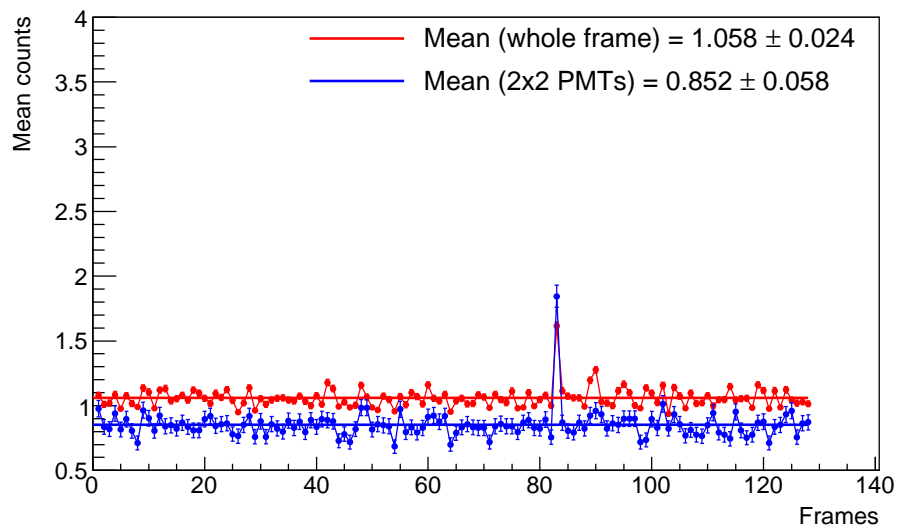
Figure 5.11: Packet of 128 frames containing the event detected on the 13th May 2015, considering the whole frame (red) and the selected box (blue). The value of the mean background over all the frames is reported, together with the mean of the uncertainties for both the cases.
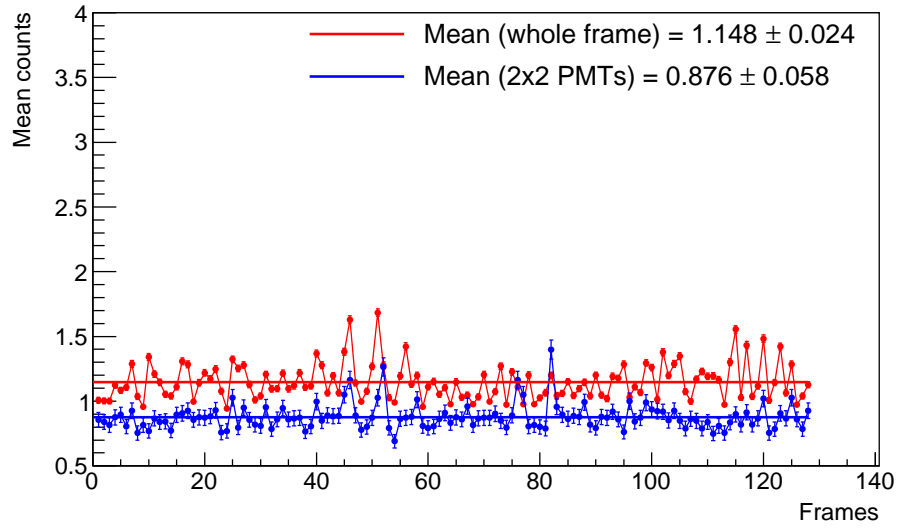
Figure 5.12: Packet of 128 frames containing the event detected on the 18th September 2015, considering the whole frame (red) and the selected box (blue). The value of the mean background over all the frames is reported, together with the mean of the uncertainties for both the cases.
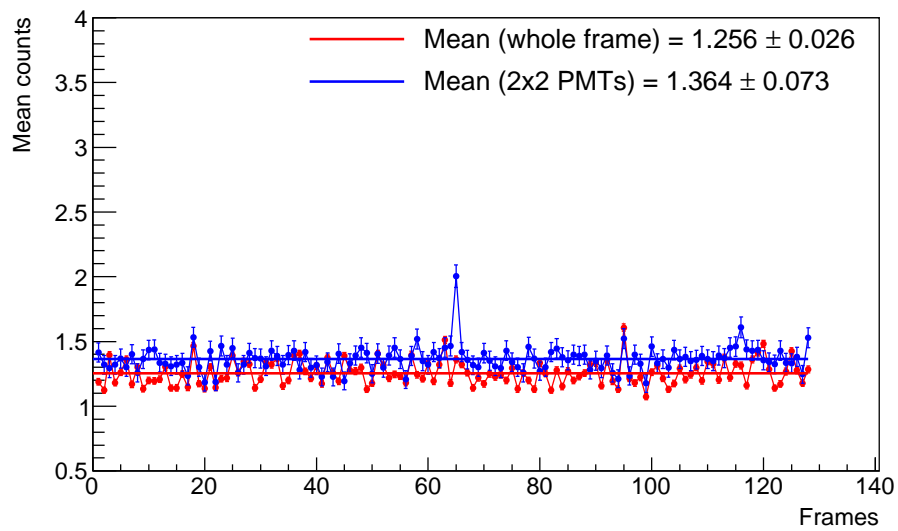
Figure 5.13: Packet of 128 frames containing the event detected on the 20th September 2015, considering the whole frame (red) and the selected box (blue). The value of the mean background over all the frames is reported, together with the mean of the uncertainties for both the cases.
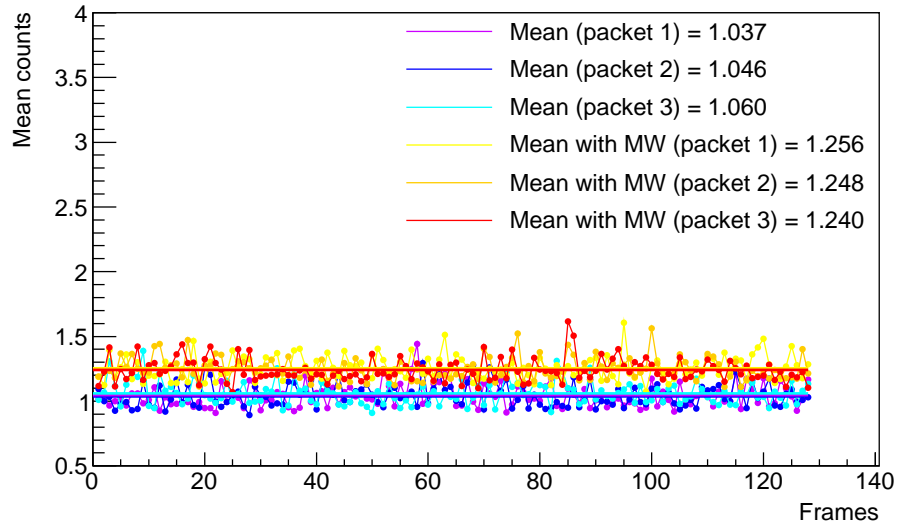
Figure 5.14: Three packets of 128 frames in presence (reddish lines) and three packets of 128 frames in absence (bluish lines) of the Milky Way in the FOV of EUSO-TA, detected on the 20th September 2015.
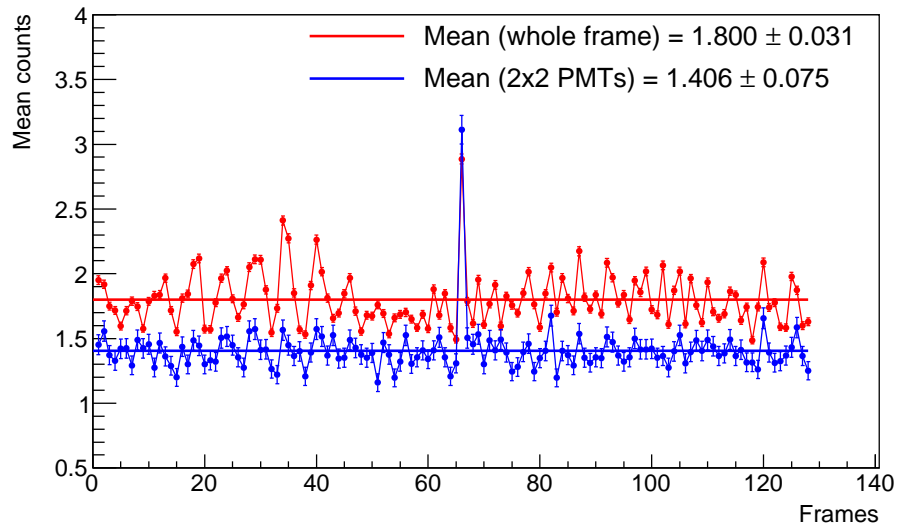
Figure 5.15: Packet of 128 frames containing the event detected on the 7th November 2015, considering the whole frame (red) and the selected box (blue). The value of the mean background over all the frames is reported, together with the mean of the uncertainties for both the cases.

5.3.2 Laser from the Central Laser Facility

The same study performed to evaluate if the cosmic ray event tracks give a significant contribution to the intensity of the whole frame, compared to the frames containing just background, is also done for a laser event from the CLF. In this case, as selected box, a column of 1×6 PMT where the laser pulse goes through has been considered. Figure 5.16 shows the sequence of 128 frames containing a laser pulse going through the EUSO-TA FOV, detected on the 20th September 2015 (see also Figure 4.13). The laser pulse crosses the frame in 6 GTUs (frame numbers 65-70 in the graph). The presence of the laser event is visible as a "long-lasting" event in the graph, since the mean value of five out of six frames containing the pulse is above the baseline considering the whole frame. Considering the selected box, all the values are above the baseline; this includes the frame number 64, in which just a small portion of the laser pulse enters the FOV.
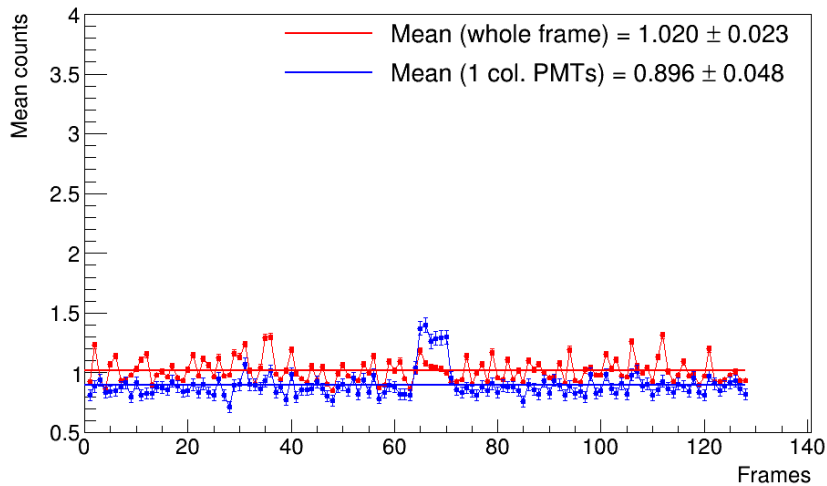
Figure 5.16: Packet of 128 frames containing a laser pulse emitted from the CLF on the 20th September 2015, considering the whole frame (red) and the selected box (blue). The value of the mean background over all the frames is reported, together with the mean of the uncertainties for both the cases.

The overall impression is that for events lasting just one GTU, i.e. close events, their contribute to the average value of the pixels content over the whole frame is visible, while for events split on more than one GTU, they affect the average in the same way as the background fluctuations and the parasitic noise do. However, considering a selected area which includes the CR event, but reduces the number of low-counts pixels, the CR events are recognizable over the baseline in all the cases. It is also to be noticed that the baseline of the background increases with time, starting being low in May and higher and more variable in November, when the background was up to the 70% more intense than in May. Furthermore, on the 13th of May different gain and threshold mappings have been used respect to the other
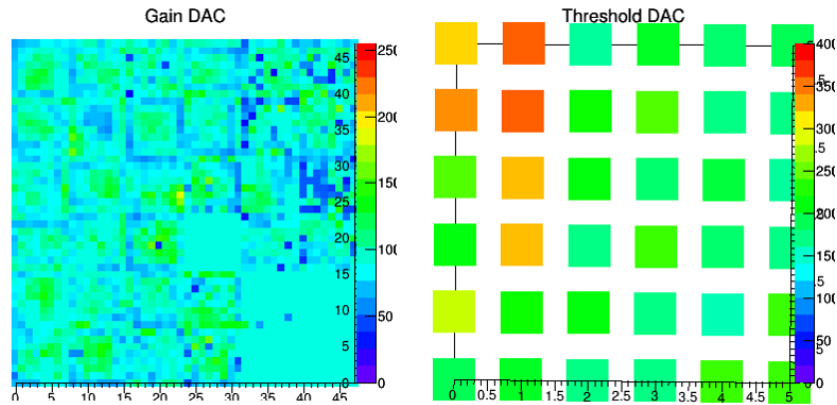
(a) Gain (left) and threshold (right) mappings used up to the 16th May 2015.
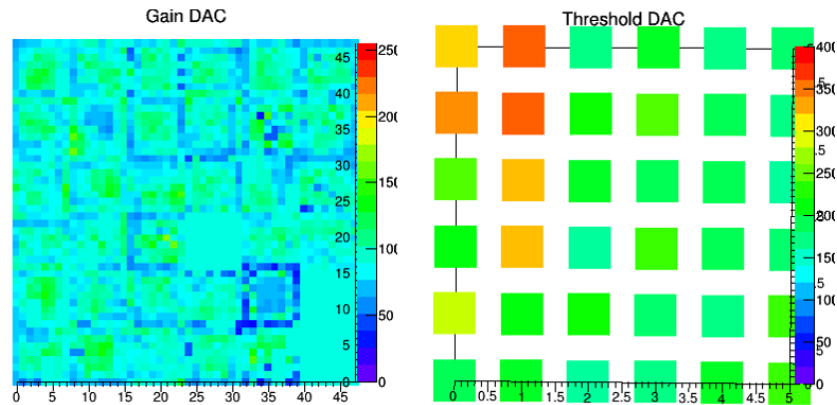
(b) Gain (left) and threshold (right) mappings used after the 16th May 2015.

Figure 5.17:   Gain and threshold mapping of the 6×6 PMTs composing the focal surface, produced on the 10th and on the 16th May 2015. The first ones has been used up to and including the 16th of May 2015, while the second ones have been used afterwards. Images from [76].

days. In Figure 5.17 the gain and threshold mappings used up to the 16th of May and the ones used afterwards are displayed. The difference is quite small, and the effect on the variation of the background baseline should not be affected by this.

5.4 Summary and discussion

The high spatial resolution of EUSO-TA, allows to evaluate the width of the cosmic ray event tracks on the focal surface. This analysis indicates that the width is proportional to the energy and to the inverse of the distance of the cosmic ray air shower. To do this, a fit algorithm which measures the track inclination has been developed and then a Gaussian fit along the direction perpendicular to the track axis have been performed to evaluate the track width.

To consider the reliability of the detected and of the candidate events, consistency checks have been done on parameters such as the timestamps of the events and the sequence number of the frame containing an event inside a packet, which has to be within a certain range. These checks demonstrated that all the detected and the candidate events most probably are real cosmic ray events. The candidate events are considered so because they are faint and their contribution to the frame brightness is of the same magnitude of some parasitic noise present on some areas of the frames, or because their tracks are not continuous and well defined.

The deformation of a star spot size depending on the incident angle in the FOV has been studied. The variation is about 30% between an incident angle of about 5° and one of about 1.5° from the telescope axis. Moreover, the requirement for EUSO-TA to have a higher angular resolution than the one of TAFDs, which is of 1°, i.e. ~ 5.3 pixels, is satisfied.

Analyzing the background within the packets (of 128 data frames) containing the detected events, the contribution given by a cosmic ray event track to the intensity of the whole frame/frames is evaluable in case of events lasting just one GTU, for which the mean intensity of the frame is higher than that for frames containing just background. It is of the same order of the noise fluctuations in the cases of events lasting more GTUs, for which each segment of the track on one frame is short. However, reducing the area selecting just a few PMTs including the CR events, i.e. reducing the number of low-counts pixels, then they are recognizable above the baseline. It seems that the variability as well as the baseline of the background increase from May to November 2015, up to 70%. Moreover, it seems that the detector is sensitive to the brightness of the Milky Way plane, when it is in its FOV, increasing the baseline of about 19%.

The overall conclusion of these analyses is that with the current tools it is tricky to find events in the data, mainly because of parasitic noisy areas present on the data frames, connected to electronic issues. This makes it difficult to identify of the events based on the intensity variation of the whole frame, in particular when the segment of the track is short. Some event identification algorithms under development by the EUSO-TA group, look for tracks or moving spots in the frames with counts above a threshold, and the parasitic noise is responsible of "false-triggers". The understanding of the problem might help solving the issue. Moreover, the foreseen replacement of the non-active PMTs (masked in the frames shown), will help having a larger active area and then it could be considered to mask the noisy PMTs instead,

for having a more stable background but still a reasonable active area.

Also the difference between the TA and EUSO-TA timestamps makes the research and the analysis of the events difficult.

However, the high spatial resolution of EUSO-TA with respect to the TAFDs one, as well those of the other cosmic ray fluorescence detectors, allows to see the details of the showers and to measure the track widths. Such a high spatial resolution is necessary for the observation of cosmic ray air showers from space, but also enables new kinds of studies in a ground-based detector.

Chapter 6

Offline simulation software

The EUSO-Offline framework [79] has its origin in the Auger-Offline [80], developed for simulation, shower reconstruction, and analysis of fluorescence and surface detector data of the Pierre Auger Observatory [33]. In March 2013 the adaptation to the new version of the framework has been started, to carry out simulations of a space based observatory such as JEM-EUSO [45], as well as its prototypes. The Offline framework is written in C++, making use of the fast computing capabilities of C++, and benefits from object oriented software design. Any user can easily run or modify simulation and reconstruction applications.

6.1 Framework structure

Simulation and reconstruction tasks in the Offline framework are performed by algorithms contained in modules run in sequence. This modular design facilitates comparison of algorithms and building a variety of applications by combining modules in various sequences. Control of module sequences is implemented with a *Run Controller*, which directs module execution according to a set of user provided instructions, written in an XML-based language. This approach has proved sufficiently flexible and simple to use.

Offline includes parallel hierarchies for accessing data: the *Detector Description* for retrieving information about the detector geometry, the calibration constants and the atmospheric conditions; an *Event Data Model* for reading and writing information for each event; a *Central Config* which directs the modules and framework components to their configuration data:

- The *Detector Description* provides an interface to retrieve the information via a registry of so-called managers, each of which is capable of extracting a particular sort of information from various data sources. The general structure of the detector description machinery is illustrated in Figure 6.1.

- The *Event Data Model* contains raw, calibrated, reconstructed and Monte Carlo information, and serves as the backbone for communication between
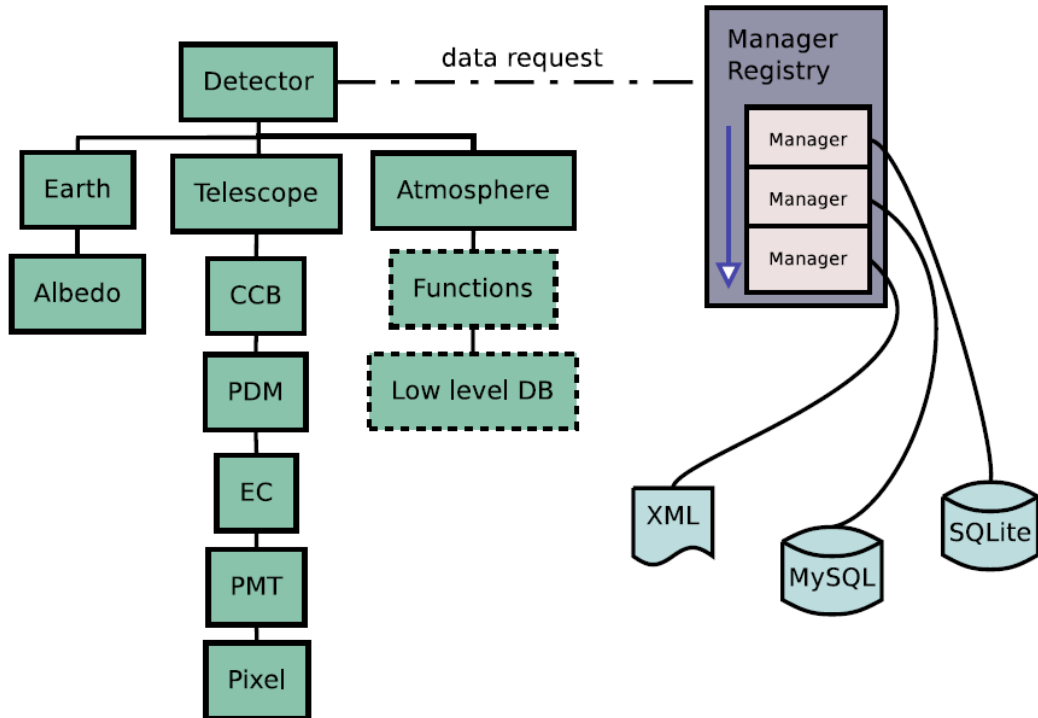
Figure 6.1: Simplified depiction of the machinery of the detector description. The user interface (left) comprises a hierarchy of objects describing the various components of the detector, where the atmosphere and the Earth surface or intervening clouds (which reflect Cherenkov light) are considered to be part of the detector. The objects shown below the Telescope are arranged with the hierarchy characteristics of the focal surface: the focal surface comprises 18 Cluster Control Boards (CCBs), each of which gathers signals from 8 Photo Detector Modules (PDMs). Each PDM is subdivided into 9 Elementary Cells (ECs), each of which contains 4 Multi-Anode Photomultiplier Tubes (PMTs), each of which in turn contains 64 pixels. At each level in the hierarchy, detector characteristics can be requested.

modules. The event contains a protocol allowing modules to discover its constituents at any point in during the simulation or reconstruction, and thereby determine whether the input data required to carry out the desired processing are available. Offline is also equipped to read formats employed by the most popular air shower simulation packages like Conex [81] or CORSIKA [82].

• The *Central Config* configuration tool points modules and framework components to the location of their configuration data. Syntax and content checking of the configuration files is implemented using W3C XML Schema validation [83]. XML Schema validation is used not only for internal configuration prepared by framework developers, but also to check the contents of physics module configuration files.

6.2 Modules for shower and laser simulation

As mentioned before, the Offline framework has a clear modular structure. Every step of the simulation is performed by an algorithm developed in modules written in C++ which call the respective configuration files written in XML containing all the necessary information. Many such modules are interchangeable, although they have to respect the correct order. This order is set in a module sequence written in XML where each module is called by name enframed by XML tags, and accompanied by a short designation of the working group*.

An example of module sequence for shower simulations for JEM-EUSO and its prototypes looks like the following:

```
<module> EventFileReaderOG              </module>
<module> EventGeneratorOG               </module>
<module> FdSimEventCheckerOG            </module>
<module> ShowerLightSimulatorKG         </module>
<module> LightAtDiaphragmSimulatorKG    </module>
<module> ShowerPhotonGeneratorOG        </module>
<module> GroundReflectionSimulatorJG    </module>
<module> UserModuleShower               </module>
<module> TelescopeSimulatorJG           </module>
<module> FdBackgroundSimulatorJG        </module>
<module> ElectronicsSimulatorOG         </module>
<module> UserModulePDM                  </module>
```

where

EventFileReaderOG reads the shower profile and energy deposit data from an EAS simulation program like Conex or CORSIKA.

EventGeneratorOG generates an event time and core location. The shower is considered a one-dimensional object here and in a few following modules.

FdSimEventCheckerOG is the starting point of every simulation. It determines whether the generated event satisfies the constrains of the detector, e.g., the time stamp of the simulated event shall be within the range of the effective detector run-time.

ShowerLightSimulatorKG simulates fluorescence and Cherenkov photons produced along the track of the EAS. Light production is calculated along the shower axis in steps of length $dl = c \cdot 2500$ ns. 2500 ns is the length of the signal trace in EUSO detectors, i.e. the GTU. In each step, only that part of the

---

*OG - Offline Group; JG - JEM-EUSO Group; KG - Karlsruhe Group; NA - Naples Group, where the author of this thesis is responsible for the KG, and contributed significantly to the modules developed by OG and JG.

shower can be taken into account, where all needed atmospheric properties like aerosols, temperature, density and refractive index are defined by the atmosphere models.

LightAtDiaphragmSimulatorKG calculates the fluorescence light, Cherenkov light, scattered Cherenkov light, or laser UV light reaching the telescope. To assure a constant quality of the simulation along the shower axis, the light flux reaching the telescopes is calculated with a time resolution dt, which is a fixed fraction of the final signal sampling time (GTU=2.5 μs). To have the desired time resolution of 10 ns/bin (the same used in the Auger-Offline), the corresponding binning parameter is 250. In Figure 6.2 it is visible how a wrong choice of the binning produces a wrong space-time development of the shower. Indeed, with a not optimized binning of 10 (standard parameter ofthe Auger-Offline, which is not fine tuned for the EUSO detectors), "bumps" are visible in the longitudinal distribution of the shower as well as in the photon distribution with the time. With a binning of 250 the same distributions are smoother.
The geometric check whether a shower is inside the FOV is done in this module too. The FOV is approximated by a cone along the telescope axis. The effective FOV angle of any EUSO telescope is slightly larger than the actual one, to not lose multi-scattered photons which could come from a direction outside the actual FOV. In Figure 6.3 the intersection of a one-dimensional shower with the FOV cone is represented. The entering and leaving time have to be calculated in order to evaluate the persistence of the shower in the FOV and the consequent light transportation to the telescope.

ShowerPhotonGeneratorOG gives the shower a three-dimensional aspect, simulating the lateral distribution of the shower. This leads to a broadening of the angular and timing distributions of the arriving photons, see Figure 6.4.

GroundReflectionSimulatorJG simulates the photons reflected back by the ground. This module is used just for telescopes at high altitude, like JEM-EUSO and EUSO-Balloon.

UserModuleShower is an optional module used by the user to visualize the photons at the telescope aperture.

TelescopeSimulatorJG simulates the optics of the telescope and generates photon traces and photoelectron traces for the PMTs, using GEANT4. It will be explained in more detail in Section 6.2.1

FdBackgroundSimulatorJG simulates the UV-background photons and adds it to the photoelectron traces.

ElectronicsSimulatorOG simulates the electronics creating signal traces, explained in more detail in Section 6.2.2.

`UserModulePDM` is an optional module used by the user to visualize the detector response, i.e. the output of the simulation directly comparable with the data, when possible (like it is currently for EUSO-Balloon and EUSO-TA).
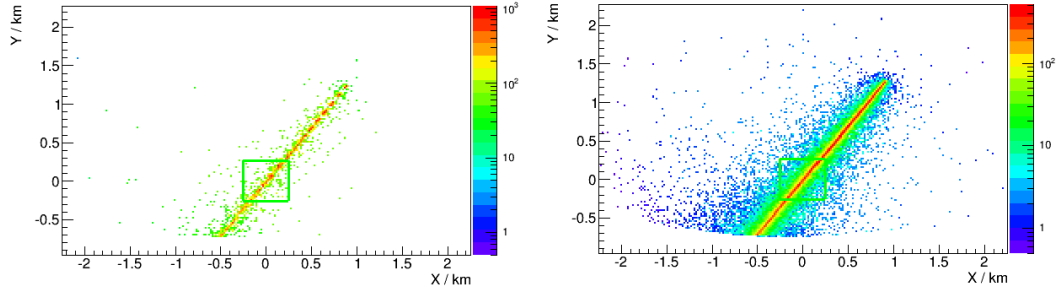
(a) Projection of the shower development in the X-Y plane using binning parameter 10 (left) and 250 (right).
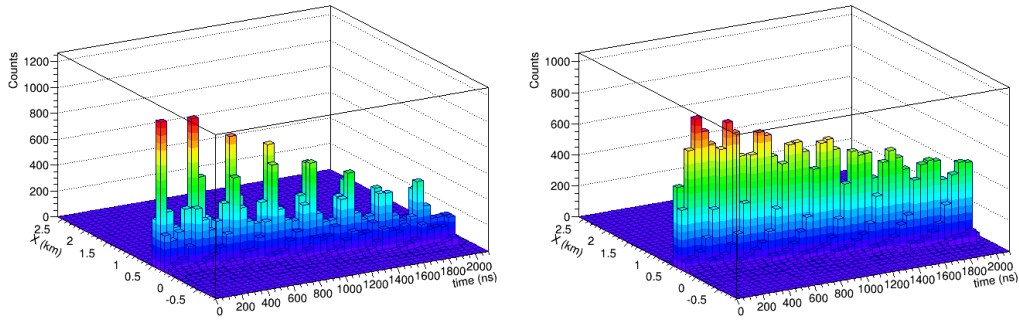
(b) X-to-time shower development using binning parameter 10 (left) and 250 (right).
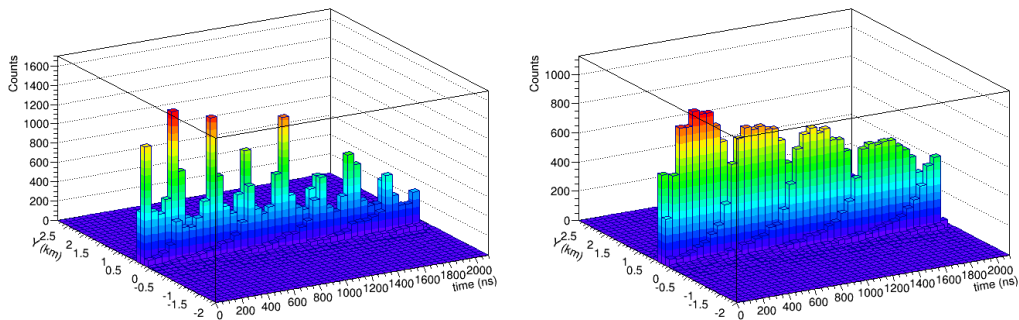
(c) Y-to-time shower development using binning parameter 10 (left) and 250 (right).

Figure 6.2: Difference in using a wrong binning parameter 10 (left) and a correct one 250 (right) in the `LightAtDiaphragmSimulatorKG` module. A non-optimized binning introduces "bumps" in the projection of the shower development in the X-Y plane (parallel to the telescope lenses) and a reduction of the shower lateral distribution (a). The same behavior is visible also in the X-to-time and Y-to-time distributions (b) and (c), respectively.
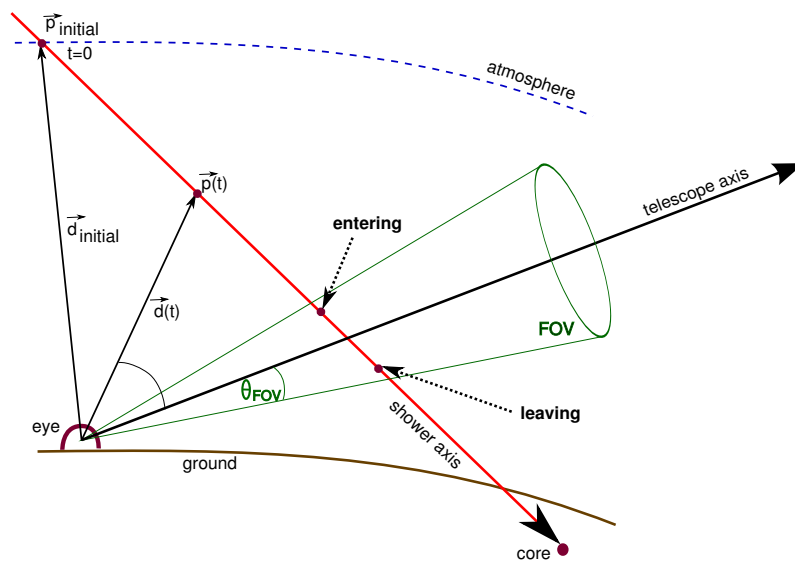
Figure 6.3: Geometry evaluation of a shower entering and leaving the FOV of a telescope. This task is performed by `LightAtDiaphragmSimulatorKG`.
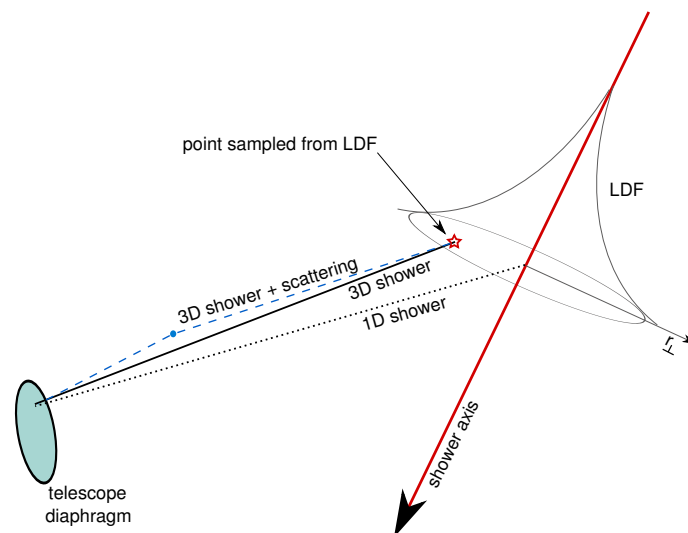
Figure 6.4:   The three dimensional structure of an air shower performed by `ShowerPhotonGeneratorOG`.

Also laser simulations are implemented in Offline. This is especially important for EUSO-TA and EUSO-Balloon simulations, since in both the laser is and has been commonly used for testing the detectors. By default the laser characteristics are those of the CLF at TA site, but it can be easily modified to simulate other kinds of portable lasers actually used for testing.

An example of a module sequence for a laser simulation is given below:

```
<module> LaserGeneratorNA              </module>
<module> EventGeneratorOG              </module>
<module> FdSimEventCheckerOG           </module>
<module> LaserLightSimulatorNA         </module>
<module> LightAtDiaphragmSimulatorKG   </module>
<module> ShowerPhotonGeneratorOG       </module>
<module> UserModuleShower              </module>
<module> TelescopeSimulatorJG          </module>
<module> FdBackgroundSimulatorJG       </module>
<module> ElectronicsSimulatorJG        </module>
<module> UserModulePDM                 </module>
```

where many of the modules are also used for the shower simulation and already described. The modules dedicated to the laser simulations are

`LaserGeneratorNA` sets direction (zenith and azimuth angles), energy and wavelength of the laser, via `LaserGeneratorNA.xml` as the corresponding configuration file.

`LaserLightSimulatorNA` contains the code for the propagation of the laser light along the beam, equivalent to the module for showers (`ShowerLightSimulator`) that calculates the production of Cherenkov and Fluorescence light. The starting number of photons N_0^γ is calculated from the energy set in the *LaserGenerator.xml* configuration file:

$$N_0^\gamma = \frac{\text{Energy[J]}}{hc/\lambda}$$

where h is Planck's constant, c the speed of light and λ is the laser's wavelength. The attenuation by the atmosphere is taken into account multiplying the number of photons by the transmission factors that account for Rayleigh and Mie scattering. Then the propagation of photons through the atmosphere from the source to the FD telescopes is performed by the module `LightAtDiaphragmSimulatorKG` in the usual way.

6.2.1 Telescope simulation

Once the photons are generated on the telescope diaphragm, they are traced through its optics. This is done with the `TelescopeSimulatorJG` module. This module gets

all the necessary information about the simulated EUSO telescope design (number of lenses, relative position lens/lens and lens/PDM, PDM curvature, size of all the components, etc.) from configuration files and performs the photon traces development inside the telescope using Geant4.

Before explaining the implementation of the PMT functionality in Offline, a reminder of the PMTs working principle is given in the following.
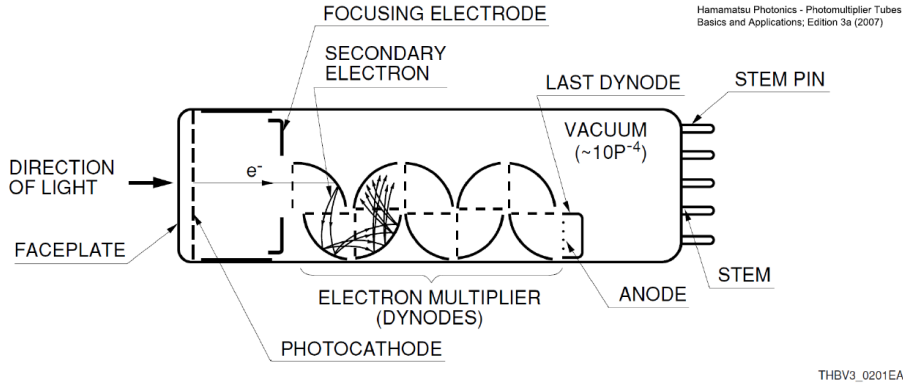
Figure 6.5: Sketch of a typical PMT showing its inner structure [84].

The following explanation for PMTs is summarized from [84]. Figure 6.5 shows the sketch of the inner structure of a typical PMT, a vacuum tube with a photocathode, a focusing electrode, several dynodes and an anode. It relies on the external photoelectric effect at the photocathode, where an incoming photon is absorbed and the excitation energy is transferred onto an electron, being able to leave the photocathode. This electron is called a photoelectron. The emitted electron is then focused by a focusing electrode and accelerated by an electric field onto the first dynode. The electron multiplier mechanism of a PMT is designed considering the electron trajectories so that electrons are efficiently multiplied at each dynode stage. However, some electrons may deviate from their favorable trajectories, not contributing to the multiplication. The probability that photoelectrons will land on the effective area of the first dynode is called *collection efficiency* and for the MAPMTs of the EUSO projects the collection efficiency is 80%. While hitting the first dynode, the photoelectron excites further electrons that can in return leave the dynode. They are then accelerated to the next dynode, and the process is repeated. At the anode, the secondary electrons are collected. With this kind of cascaded dynode chain an amplification of the initial photoelectron is realized and a measurable current pulse at the anode is the result. The multiplication factor by the dynode chain is called the gain of a PMT. The probability to detect a current pulse at the anode from one photon incident at the photocathode is called *photo-detection efficiency* (PDE) of the PMT and it is the product of the *quantum efficiency* (QE) and the *collection efficiency* (CE): $PDE = QE \cdot CE$.

The `TelescopeSimulatorJG` module creates the photon traces that, passing through the telescope, hit the photocathode of the MAPMTs and may produce

photoelectrons via the photoelectric effect. The randomness of the photoelectric effect can only produce photoelectrons randomly. Therefore, the creation of a photoelectron is virtually a truly random event. In this way, the module performs the photoelectron traces from the photon traces applying the PDE, drawing random booleans according to the MAPMTs quantum efficiency and collection efficiency, to decide whether to keep the hitting photon and convert it to photoelectrons or not.

While the photon traces are created with time bins large as one GTU ($2.5\,\mu s$), the photoelectron traces have bins of $\sim 30\,\mathrm{ns}$ for EUSO-Balloon and EUSO-TA and $\sim 10\,\mathrm{ns}$ for EUSO-SPB and Mini-EUSO. These values are the dead time of a detector channel following a hit on a pixel and depends on the model of ASIC board mounted on the detector (SPACIROC-1 for EUSO-Balloon and EUSO-TA and the newer model SPACIROC-3 for EUSO-SPB and Mini-EUSO, see Section 3.4). The dead time is implemented in `ElectronicsSimulatorJG` and discussed in Section 6.2.2.
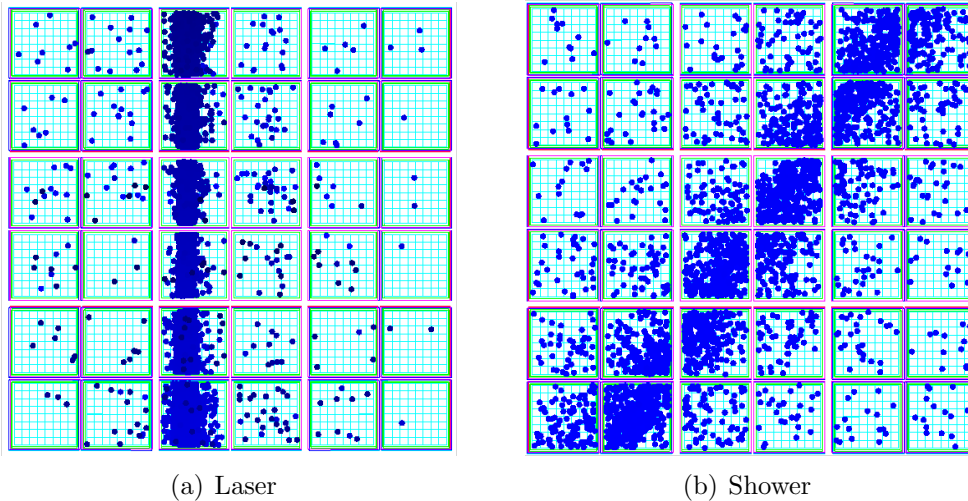
(a) Laser (b) Shower

Figure 6.6: Geant4 output image for photons at the focal surface of EUSO-TA, of a laser event (a) and a shower event (b). The darkness of the blue marks indicates the time of the hit (early - light blue; late - dark blue).

Ray tracing of photons in the telescope optics takes care of reflections and refraction, and transmission and reflectivity of all materials are properly considered. Reflections include the reflection by the Fresnel lenses, reflection of photons impinging on the optical interface at an angle larger than the critical angle and reflection computed by rough surfaces, to describe the effects of both geometrical and physical optics over a wide range of wavelengths and surface roughness.The `TelescopeSimulatorJG.xml` configuration file allows to switch on and off reflections inside the telescope.

In particular it is useful to have tools available to uncover possible optical artifacts in simulations of the EUSO optics. In fact, in the case of the Auger Observatory Fluorescence Telescopes, it turned out that reflections inside the optical system led to initially unexpected artifacts in the signal at the focal surface, including a faint

optical spot moving in the opposite direction to the shower spot (a *ghost*) as well as a *halo* of light extended across the optical surface [85].

At the time of writing, two rendering schemes are available for the visualization of the telescope simulation, that the user can define in the `TelescopeSimulatorJG.xml` configuration file: DAWN and VRML. The DAWN (Drawer for Academic WritiNgs) event display was created in coordination with the Geant4 collaboration, and produces 3D but static vector postscript images, see Figure 6.7. VRML (Virtual Reality Modeling Language) is an industry standard language for describing 3D graphical information, which produces a scene that one can interactively handle with rotations, translations, zoom in, zoom out. Both are useful for testing the detector design and the photon traces' behavior.
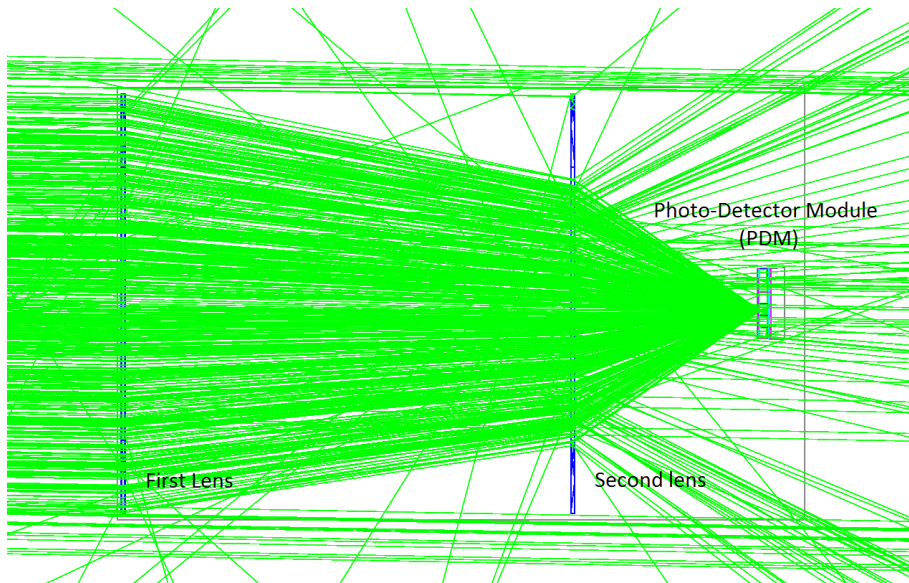
Figure 6.7: Photon traces coming from the aperture of the telescope, passing through the optical system and finally reaching the focal surface, shown via the DAWN event display.

6.2.2   Electronics simulation

With the photoelectron traces the detector response is still not completely simulated. After one photon hits a pixel of the light sensors, the detector becomes insensitive to further incoming photons for a certain period of time, causing the so called *pile-up*. This time length depends on the ASIC used to perform the conversion from photon counts to digital signal. Each photon count is converted in a square wave of fixed width. For the "first generation" telescopes EUSO-TA and EUSO-Balloon SPACIROC-1 boards are used and the square waves width is fixed at 30 ns. In the "new generation" telescopes developed afterwards (EUSO-SPB, Mini-EUSO and probably JEM-EUSO), SPACIROC-3 boards use 10 ns wide square

waves. This means that after a photon hits a pixel, the dead time for the first generation telescopes is larger than for the new ones. Therefore, the pile-up effect, which let the systems lose photons counts, has more influence on the first than the newer ones. The `ElectronicsSimulator` simulates the pile-up effect. It gets the photoelectron traces (photon traces with the photo-detection efficiency applied) created by `TelescopeSimulatorJG` with binning adapted to the dead time length of the ASIC board (relative to the simulated detector) PEs_{PDE}, and if more than one photoelectron belong to the same pixel within the same time bin, just one is kept. The selected photoelectrons are then summed up again within bins of one GTU and these new traces represent the signal traces PEs_{signal}, directly comparable with the real data. Figure 6.8 shows the effect of the pile-up, as behavior of the PEs_{signal}/PEs_{PDE} ratio as a function of the shower energy and distance of the shower core from EUSO-TA. For this study, vertical showers with same geometry (zenith 0° and azimuth 0°) but different energy, in the range $10^{17} - 10^{20}$ eV, are simulated at distances in the range of 2-20 km. The PEs_{signal}/PEs_{PDE} ratio for different energies as a function of the distance is shown in (a). It is possible to deduce that for showers of low energy, the pile-up has a weak effect on the detected counts that increase with the energy. The same ratio for showers at different distances as a function of the energy is shown in (b). Here it is possible to see how the ratio decreases with increasing energy. At high energies, it seems that the ratio slightly increases. In general, for high energies and close showers, the pile-up has a relevant influence and let EUSO-TA lose up to the 30% of the photoelectrons. This depends on the fact that high energy showers and close showers emit a high flux of photons and the probability to have more than one photon hitting the same pixel within a fixed time window is higher than for low energy showers and distant showers. Some combinations of close and high energy showers were impossible to simulate with Offline. This issue is still under study.

Furthermore `ElectronicsSimulator` simulates another dead time. At the beginning of each GTU there is a dead time of 200 ns for SPACIROC-1 and 50 ns for SPACIROC-3. For the first, the dead time is higher because of noise on the analogue part due to a signal just after the GTU rising edge: with the threshold corresponding to single photonelectron there was always a signal (noise) also without a signal in input. Since it was impossible to remove this fake trigger in the analogue part, the acquisition window has been reduced to mask the fake trigger, but this leads to an increased dead time. With SPACIROC-3 the startbit has been removed. Because of this dead time, while one GTU lasts 2.5 μs, the actual acquisition window is 2.3 μs for SPACIROC-1 and 2.45 μs for SPACIROC-3.
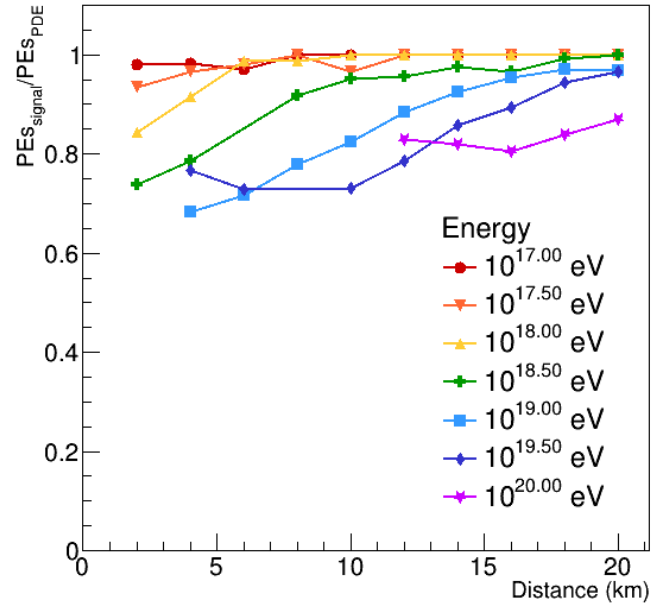
(a) PEs_{signal}/PEs_{PDE} ratio for showers with different energies as a function of the distance.
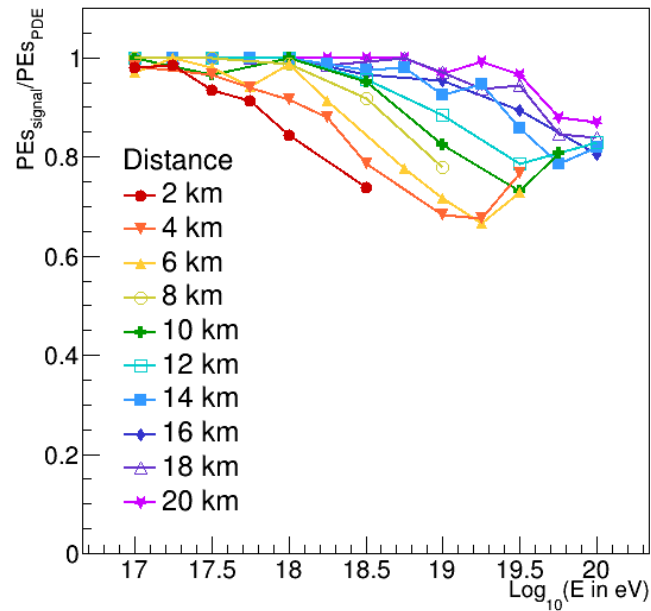
(b) PEs_{signal}/PEs_{PDE} ratio for showers at different distances as a function of the energy.

Figure 6.8: Effect of the pile-up, as behavior of the PEs_{signal}/PEs_{PDE} ratio as a function of the shower energy and distance of the shower core from EUSO-TA.

6.3 Earth shape approximation and coordinate systems

For a telescope orbiting the Earth, the curvature of the Earth cannot be neglected. For this reason, the shape of the Earth is approximated by a geocentric, oblate spheroid, standardized as WGS84, and displayed in Figure 6.9(a); the 3D Cartesian coordinate system with respect to the cardinal points is shown in (b).
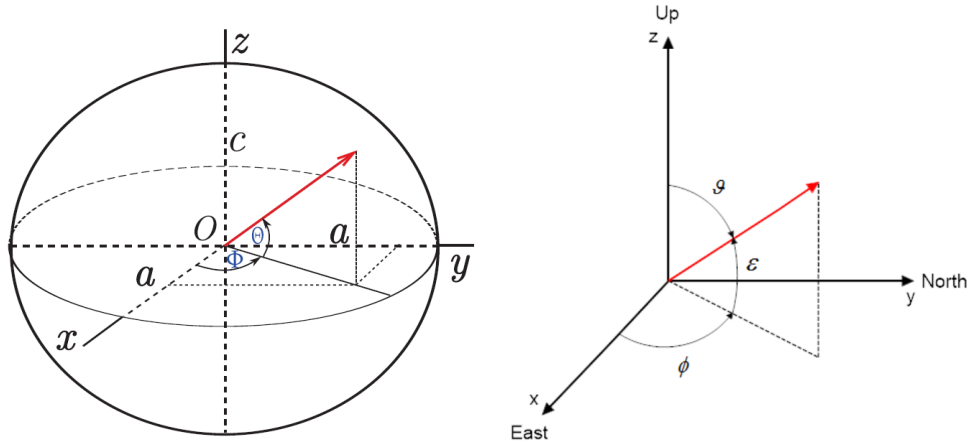
(a) Reference Ellipsoid (WGS84) of the Earth's surface. Semi-major axis or equatorial radius a and semi-minor axis or polar radius c, latitude Θ and longitude Φ.

(b) Cartesian system with zenith angle θ, elevation angle ϵ and azimuthal angle ϕ of a point (x, y, z).

Figure 6.9: Earth shape approximation (a) and coordinate systems (b).

The longitudinal curvature at the equator is about $1.57 \cdot 10^{-4}\,\mathrm{km^{-1}}$, compared to $2.55 \cdot 10^{-4}\,\mathrm{km^{-1}}$ at a latitude of 52°, which can be translated into a ground distance of about $111\,\mathrm{km/°}$ and about $68.4\,\mathrm{km/°}$ respectively. The Earth curvature plays an important role in particular for the simulation of horizontal showers ($\theta \geq 70°$) for whose their projections on ground are a few tens kilometers long. This is taken into account in Offline via a computation of inclined atmospheric profiles following [42]. In the case of flat Earth approximation, the local height z^{vert} can be calculated from the slant depth z^{slant} and the zenith angle θ of a shower axis at a local point z as:

$$z^{vert}(\theta) = z^{slant} \cdot \cos(\theta) \tag{6.1}$$

(see Figure 6.10 (a)). In the realistic case of a spheroidal Earth's surface, the atmosphere is described with several layers of concentric ellipsoids with a local height z_i^{vert} with respect to the surface of WGS84. Due to the Earth curvature, the z_i^{vert} will slightly deviate from the flat Earth approximation, as will the local zenith angle θ_i with respect to the normal vector of the tangential plane (see Figure 6.10 (b)). Starting with z_0^{vert} at about 100 km at the top of the atmosphere, the atmospheric

depth is computed iteratively in steps of $\Delta z_i^{slant} = 10 \, \mathrm{g \, cm^{-2}}$ along the shower axis, until the surface. For each Δz_i^{slant}, a corresponding vertical depth is calculated:

$$\Delta z_i^{vert}(\theta_i) = \Delta z_i^{slant} \cdot \cos(\theta_i). \tag{6.2}$$

(a) Flat   (b) Spheroidal
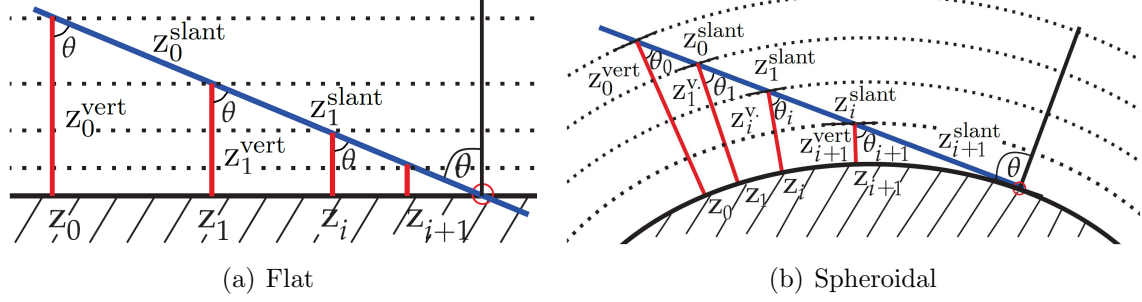
Figure 6.10: Reference surfaces for computation of inclined atmospheric profiles. (a) The atmospheric depth is computed from a vertical atmospheric depth profile using Equation 6.1. (b) The atmosphere is build by ellipsoids concentric to WGS84 with the height z_i^{vert}. The zenith angle θ of an EAS refers to the impact point on ground (empty circle), while θ_i are angles between the direction of the shower axis and the local normal vectors. Figures adapted from [42].

Different coordinate systems are useful for different purposes: the surveying of the detector utilizes Universal Transverse Mercator (UTM) coordinates with the WGS84 ellipsoid; physics analysis are made using Cartesian coordinates.

The UTM system is commonly used by geographers when assigning coordinates in maps on the spherical Earth surface. The surface of the Earth is divided into 60 zones, each 6° wide, bounded by meridians between 80°S and 84°N of latitude and labeled from 1 to 60, starting from the International Date Line in the Pacific Ocean. Parallels define bands, again 6° wide, labeled with letters starting from "C" at 80°S, increasing up the English alphabet until "X", omitting the letters "I" and "O" (because of their similarity to the numerals one and zero). Latitude bands "A" and "B" as well as "X" and "Y" bands cover the western and eastern side of the Antarctic and Arctic region respectively. For example, the coordinates of EUSO-TA in UTM system are (352138 mE, 4339087 mN), where "mE" means "meters towards East" and "nN" means "meters towards North", in the "S" band and "12" zone. The Geometry package present in the Offline framework provides abstract geometrical objects like planes, lines, points, and vectors. It can perform intersections, point and cross-products. In particular it provides an UTMPoint class for dealing with positions given in UTM, in particular for the conversion to and from Cartesian coordinates. This class also handles the geodetic conventions, which define the latitude based on the local vertical as opposed to the angle $90° - \mu$, where μ is the zenith angle in spherical coordinates.

The Cartesian system is easier to handle and therefore used in the analysis, with x, y and z in a right-handed configuration, see Figure 6.9(b). The x-axis is pointing

eastward, the y-axis northward and the z-axis upward. The line connecting the point (x, y, z) to the origin $(0, 0, 0)$ has zenith angle θ with the z-axis or elevation angle ϵ with the plane xy. The projection of the line on the plane xy has the azimuthal angle ϕ with the x-axis, increasing counter-clockwise.

6.4   Summary

Offline is a simulation and reconstruction framework of cosmic ray air showers. It has been proven for years in the contest of the Pierre Auger Observatory, and has been adapted for the EUSO experiments. It performs the propagation of the fluorescence and Cherenkov light from the shower (or laser) to the detector.

One of the changes made is related to the time resolution with which the photons are injected toward the telescope, which is related to the time resolution of the data acquisition. Indeed, with not optimized values of such parameters the cosmic ray air showers appear with bumps of high counts along the axis and appears to be thin in the outer part, while with a time resolution of 10 ns/bin the showers look more realistic and with a continuous central core.

Most of the modifications are about the detector description and response. In particular, aspects related to the MAPMTs, i.e. the quantum efficiency and the collection efficiency, and the electronics, i.e. the dead time at the beginning of each GTU of data (of the order of hundreds of ns) and the so called pile-up effect (dead time of tens of ns which occur after a photon is detected), have been implemented. The studies of the pile-up effect shows that there is an influence of up to 30% possible on the number of detected counts for close and energetic events.

The good level of simulation reached allows to perform consistent analysis, being able to compare the simulation results with the data.

Chapter 7

Detected events: simulation study and comparison with measurements

In Chapter 4 the *detected* and the *candidate events* have been introduced. The candidate events have very faint or irregular tracks and for this detailed analysis would be difficult. In this chapter, analysis of the simulations of the detected events and the comparison with the measurements are discussed. In Section 8.1.1 the comparison between the simulations and the measurements of the candidate events will be given.

7.1 Exploratory studies

In order to have simulations properly working and to ensure valuable comparison with the data, some preparatory work is performed. In particular, Offline requires the shower core position on ground as input. It has been found that a correction of the position of the core is necessary in order to represent the data. Moreover, for a quantitative comparison a method to "imitate" the background in the data has been developed, which is finally added to the pure shower simulations.

7.1.1 Shower core position

The TA group, together with the cosmic ray air shower reconstruction parameters, provides the EUSO-TA group of the images of the (detected, candidate and non-detected) events crossing the FOV of EUSO-TA, exported from BRM-TAFDs data. In this way, it is possible to know in which position the event is expected to be on the EUSO-TA data frames. For the shower core position on ground, it has to be noted that, to have the simulated events in the expected position, a shift of the core is always necessary. The reason for this issue has been investigated but the cause is still not completely clear. Indeed, the size of the shift is not proportional to the distance of the shower core, and it is not always in the same direction. This means

that it should not be related to a systematic uncertainty present in the simulation, such as the telescope orientation or the PDM position inside the telescope. The possible source of this discrepancy between data and simulation could be related to the uncertainty on the reconstruction parameters in monocular mode of the TA stand-alone reconstruction (using just the TAFD at Black Rock Mesa, as done for these events). The geometrical resolution of the arrival direction of the photons is 7.4°, which may lead to reconstruction of showers at a different angle, i.e. position, respect to the telescope axis. In Appendix E, the resolutions of all the reconstruction parameters are reported, taken from [86].
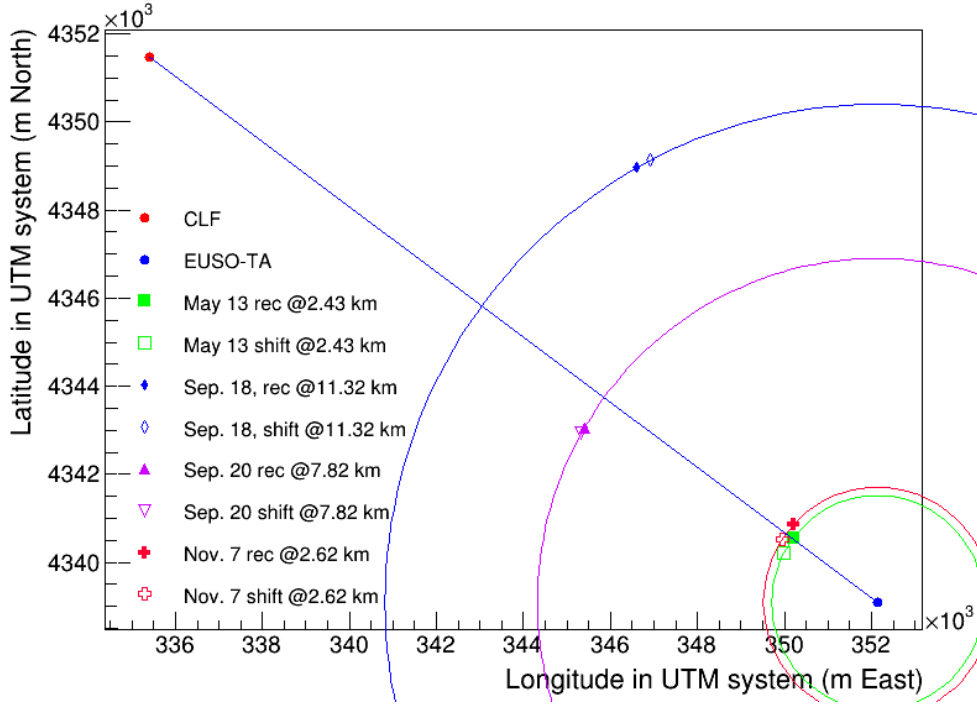
Figure 7.1: Plane in UTM coordinate system with the position of the CLF and EUSO-TA. The shower core positions obtained from the TA reconstruction and the new position after the shift are drawn too. The distance reported per event in the legend is the R_p parameter, i.e. the distance of closest approach between TA fluorescence detectors at Black Rock Mesa and each shower's axis.

Figure 7.1 shows a plane in UTM coordinate system with the position of the CLF (335405 mE, 4351462 mN) and EUSO-TA (352138 mE, 4339087 mN) (in the "S" band and "12" zone). EUSO-TA looks to the North-West direction towards the CLF. On this plane, the position of the showers' core obtained from the TA reconstruction as well as its position after the shift are drawn. Such a shift has been made keeping the distance of the shower core respect to the EUSO-TA constant, that means the cores are shifted on circles of radius equal to the distance between the reconstructed shower core position and EUSO-TA. The distance between EUSO-TA and BRM-TAFDs has been neglected, since it is about 20 m, while the closest shower core is at about 2.5 km. This method could slightly change the R_p parameter, i.e. the distance of closest approach between each shower's axis and TA fluorescence detectors at

Black Rock Mesa. Anyway, the method appears to be the most useful since for simulations with Offline the core position has to be set as input, while it is not the case for the R_p parameter.

7.1.2 Background "imitation"

In Offline, two background simulators are under development. However, for the comparison between data and simulations, it has been preferred to use background taken from the data around the event instead of a simulated one, taking into account its irregularity due to some noisy PMTs and the time variation of the noise baseline (see Section 5.3).
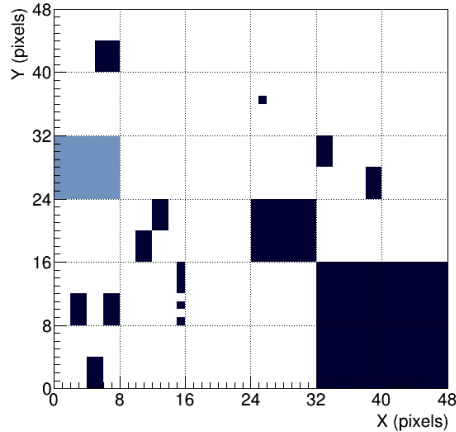
Figure 7.2: Mask to be applied to the simulation in order to not consider the defective PMTs and pixels. The light-blue PMT is masked for the events of October and November 2015.

In the simulations the defective PMTs are considered. In this way, the 2D histograms displaying the data on the PDM are masked, and the counts coming from the masked pixels are not considered in the quantitative analysis. The mask used is drawn in Figure 7.2. Some tests adding simply one frame of background, revealed that the difference between data and simulations varies depending on the chosen frame of background. For this reason, a kind of "imitation" of the real background has been developed. For every detected event, nine frames of background in the same packet of frames have been selected. In particular, if the frame with the detected event shows some noise in the usual noisy PMTs, nine frames of background with the same kind of noise have been chosen. In Figure 7.3 such nine frames of background are shown, selected for the event detected on the 13th May 2015. In this section the procedure is described using just the background for this event, but in Appendix D the figures for the background applied to the other events can be found. For each frame, the distribution of the pixels' counts is evaluated and the nine histograms are shown in Figure 7.4. For each histogram, the mean value is displayed, and just those frames with similar distributions and mean value, differing at most a few hundreds have been taken into account. If one frame was revealing a higher difference from the
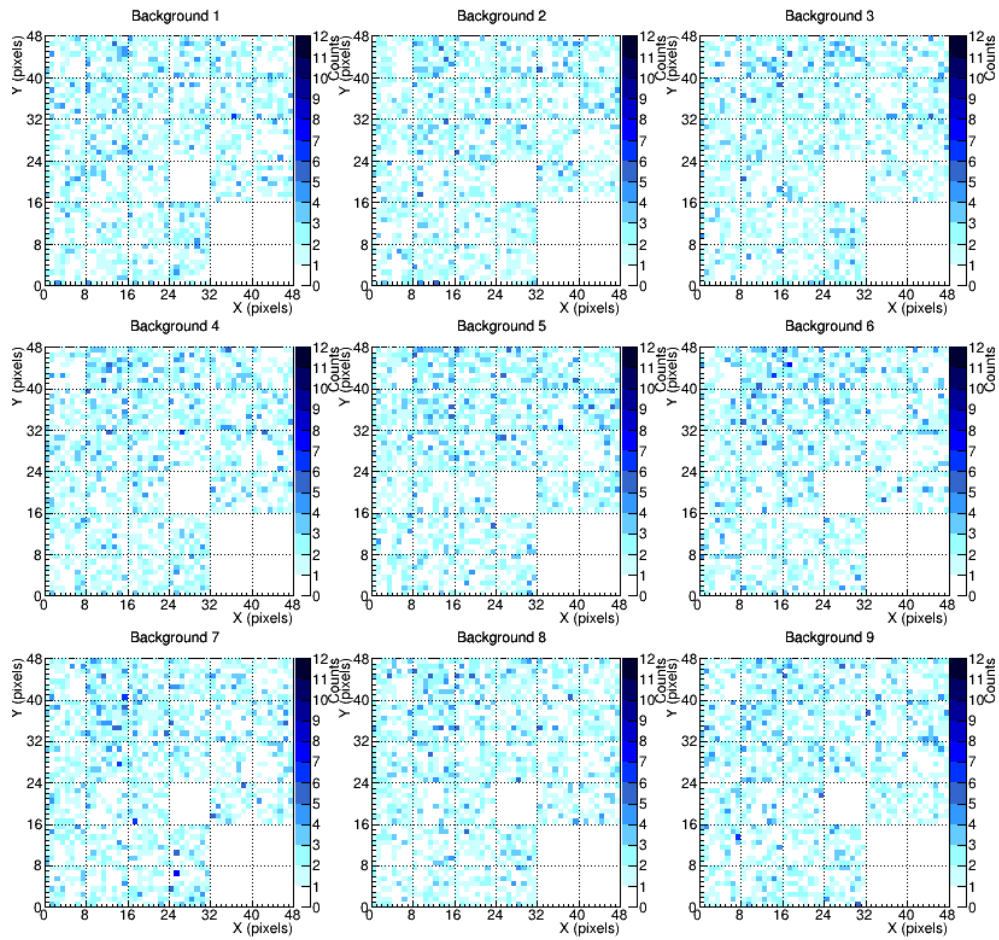
Figure 7.3: Nine frames of background for the detected event on 13th May 2015.

others, another frame in the same packet was selected and the procedure repeated. An average of the nine distributions it then calculated, visible in Figure 7.5. Given the latter distribution, the counts are then distributed randomly on a 2D histogram representing finally the mean frame of background to be added to the simulation of the event itself, visible in Figure 7.6. This procedure allows to make a more consistent comparison of data and simulations than just adding single frames of background taken from the data.
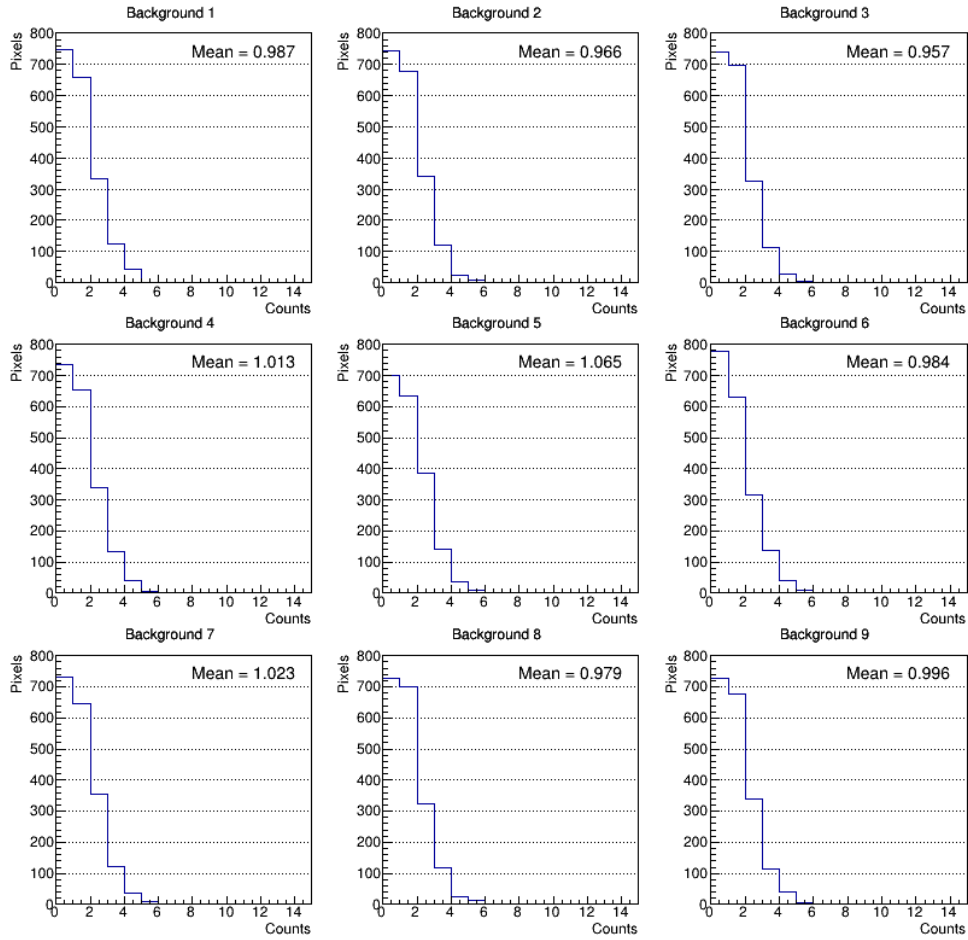
Figure 7.4: Distribution of counts of the nine frames of background for the detected event on 13th May 2015.
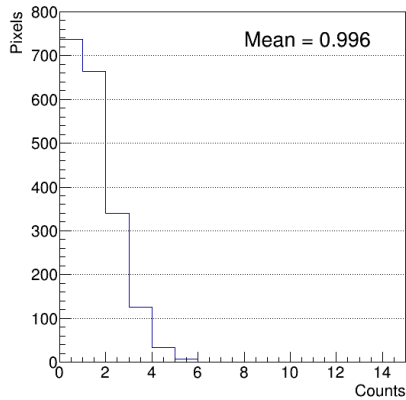
Figure 7.5: Mean distribution of counts for the detected event on 13th May 2015.
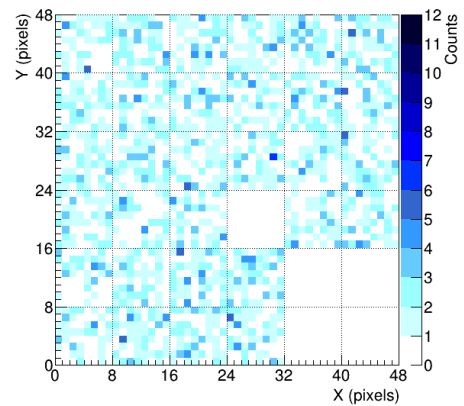
Figure 7.6: Mean frame of background for the detected event on 13th May 2015.

7.2   Simulations and comparison with measurements

In this section a series of analyses on the simulation of the four detected events (see Section 4.3 for details) is discussed and, when possible, a comparison with the data is performed.

For each event, a comparison between simulation and data is possible from a visual point of view and comparing the counts distribution, see Section 7.2.1. Another possibility is to compare the inclination of the event tracks on the simulated frames and data frames, which is the projection of the shower axis on the focal surface, combination of zenith and azimuth angles: this is discussed in the Section 7.2.2. Finally, the simulation results, which give information not available from the data, are explained in the Section 7.2.3.

7.2.1   Qualitative and quantitative comparison

After the overview of the events detected with EUSO-TA in the past data taking campaigns given in Section 4.3, and the improvements in Offline regarding the telescope and electronics simulators discussed in Sections 6.2.1 and 6.2.2, now the comparison between data and simulations is discussed.

All these events have been detected by EUSO-TA receiving the trigger from TA, and the TA-group provided the reconstruction parameters that characterize the events. Such parameters are available in Appendix F, including the shift of the shower core and the EUSO-TA elevation angle. In general, the parameters required as input in the simulations are listed below:

- Zenith angle

- Azimuth angle (positive going clockwise from North)

- Energy of the primary particle

- Coordinate of the shower core on ground (in UTM coordinates; "E" means East, "N" means North)

- Elevation of EUSO-TA axis.

Background frames constructed as explained in Section 7.1.2 are added to the simulation results. The background frames per individual event are available in Appendix D.

In the following, event by event and frame by frame, the comparison of the measurements with the simulations is shown. A further comparison from a geometric point of view is discussed in Section 7.2.2.

The event of 13th May is shown in Figure 7.7, where the comparison looks good in terms of signal intensity and geometry.
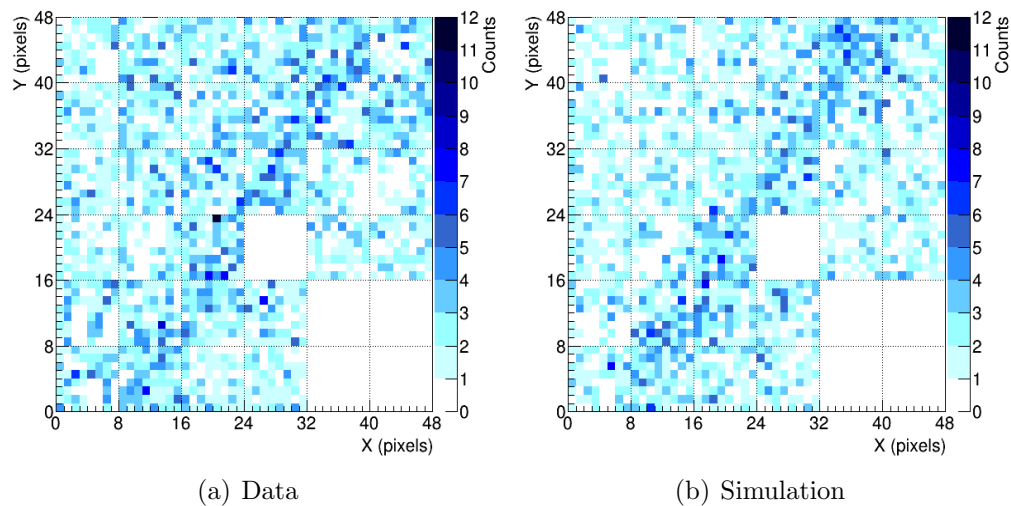
(a) Data   (b) Simulation

Figure 7.7: Event detected on the 13th May 2015. Comparison between frames of data (a) and simulation (b).
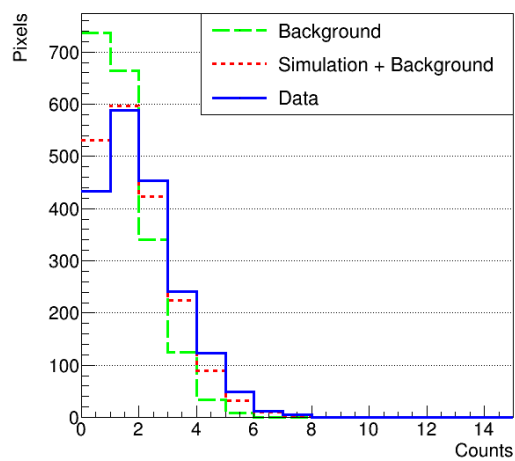
Figure 7.8: Event detected on the 13th May 2015. Comparison between the counts distributions of data, sum of simulation and background and background itself.

For this event, the comparison between the count distributions of data, sum of simulation and background and background itself is shown too, as example, in Figure 7.8. For each of the other three detected events, frame by frame, the comparison is available in Appendix F.2. These comparisons confirm the good agreement between measurements and simulations. The distributions are Poisson distributions, since the low average value of counts per pixel. The defective PMTs and single pixels are not considered in the analysis (see Figure 7.2). The distributions of data and simulation differ slightly. The difference probably comes, at least in part, from the impossibility to reproduce the exact background frame existing at the moment of the data taking of the frame with the event. But it is interesting to see how both distributions start to show an excess with respect to the background for counts ≥ 2 in both data and simulation.

The comparison between data and simulation for the event of 18th September is shown in Figure 7.9. This is one event which has been found in the data with an "inverse" approach. Indeed, it was known that such an event could have been in the data since it was present in TA data in the section of sky covered by the EUSO-TA FOV. First, the simulation of the event has been done and secondly it has been searched in the data at the corresponding time stamp given by TA. The simulation shows an event spread on three GTUs. In the data, just the frame at the GTU 2 shows a segment of the track; in the simulation a first segment is barely visible at GTU 1, while the last one cannot be detected because of the dead zone. Focusing on the frame at GTU 2, the agreement is quite good. The comparison of the count distributions for the three frames is available in Figure F.1. In general, the same trend as for the event of 13th May is observed, with an excess of counts in the data and the simulation distributions with respect to that of the background, for counts ≥ 2.

For the event of 20th September the comparison is shown in Figure 7.10. Visually, there is a slight difference in the length of the two segments of track in the frames, but their inclinations are in agreement. The comparison of the count distributions for the two frames is available in Figure F.2, with a trend similar to those of the two previous events.

Finally, data and simulation for the event of 7th November are shown in Figure 7.11. The event is bright and in both the frames counts are up to 12. The data frame shows a background with noisy PMTs on the right hand side. While creating the background to add to the simulation, similar background frames have been chosen. The procedure which makes background frames (Section 7.1.2), foresees the redistribution of pixel counts on the frame. So, the excess of noisy pixels is present also in the background frame added to the simulation, although it is not located on the PMTs on the right hand side. The comparison of the count distributions is available in Figure F.3. In this case, the signature of the event is visible for counts ≥ 3, because the background intensity for this event is higher than the other ones (see also Section 5.3).

(a) Data GTU 1

(b) Simulation GTU 1

(c) Data GTU 2

(d) Simulation GTU 2

(e) Data GTU 3

(f) Simulation GTU 3
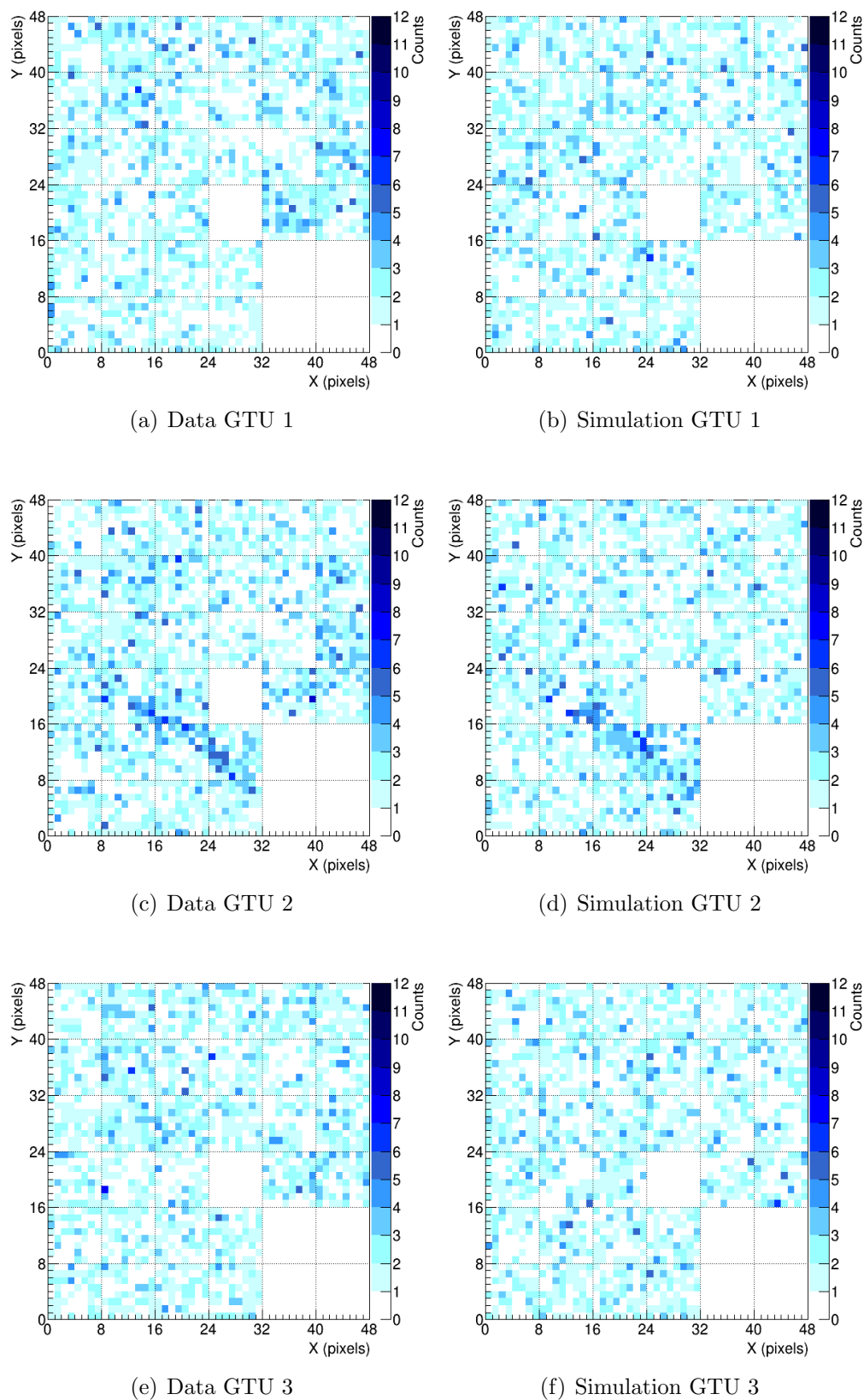
Figure 7.9: Event detected on the 18th September 2015. Comparison between frames of data (a, c, e) and simulation (b, d, f) for the three GTUs event.

(a) Data GTU 1

(b) Simulation GTU 1

(c) Data GTU 2
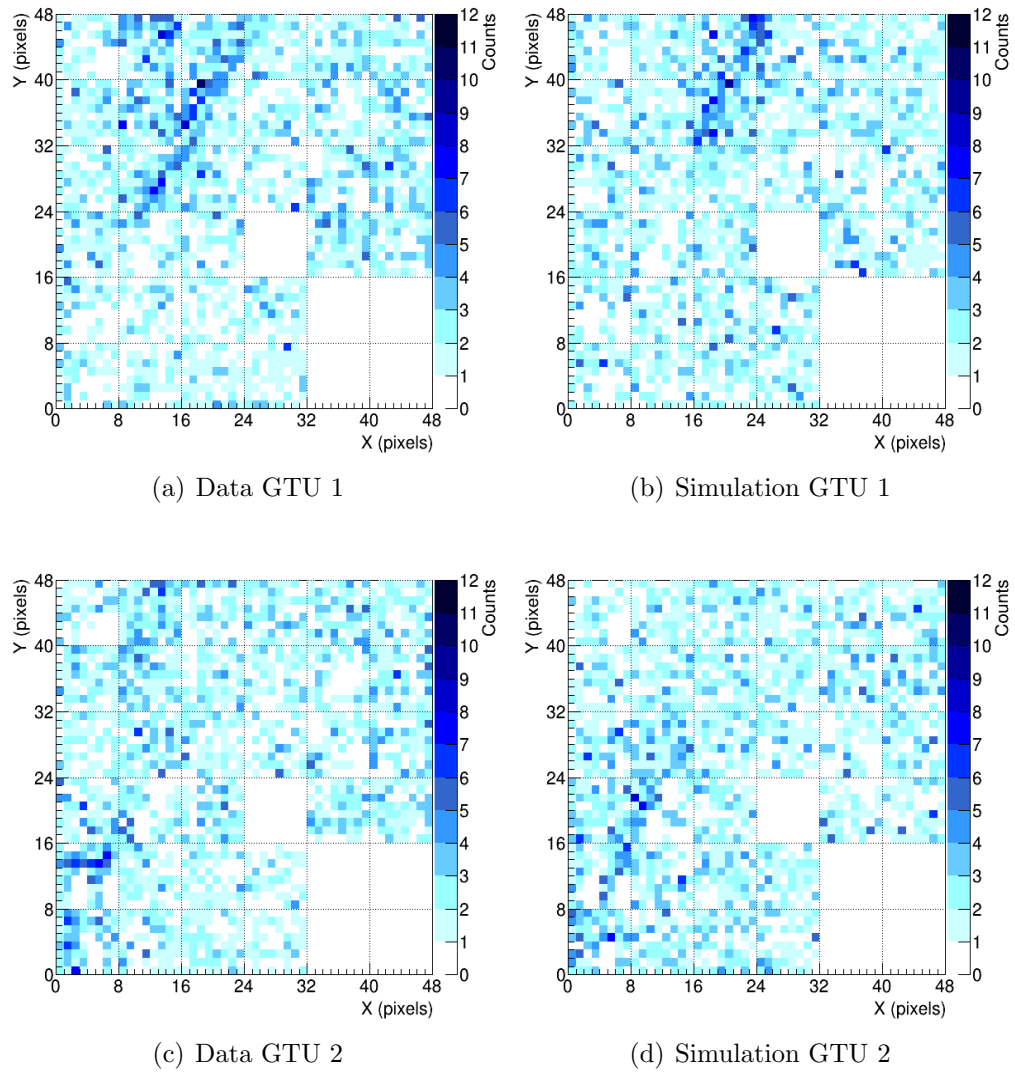
(d) Simulation GTU 2

Figure 7.10: Event detected on the 20th September 2015. Comparison between frames of data (a, c) and simulation (b, d) for the two GTUs event.

(a) Data
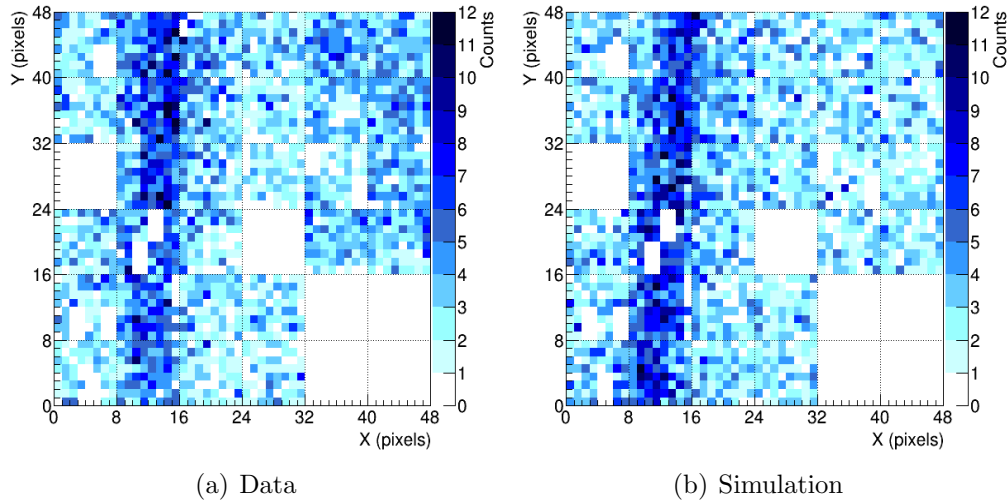
(b) Simulation

Figure 7.11: Event detected on the 7th November 2015. Comparison between frames of data (a) and simulation (b).

7.2.2 Geometric comparison

An analysis of the geometry of the shower track in the frames can be done, to compare simulated and detected events. With reference to Section 5.1.1 where the fit algorithm is described, the shower tracks have been fitted with a line, which is the linear fit of the mean values of Gaussians fitting of each row of pixels. The Gaussian means lie on the shower track. In the cases of events lasting more than one GTU, the frames have been summed, and then the fit on the sum of frames has been made. The linear fit gives the parameters m and q of the fitting line, given the general equation of a line:

$$y = m \cdot x + q \tag{7.1}$$

From the slope m, the inclination α of the line in the image to the vertical can be derived from the relation:

$$\alpha = \operatorname{arccot}(m) \tag{7.2}$$

In the following, the evaluation of the track inclination of the event of 13th May 2015 is described, while for the other events, the details are available in Appendix F.3. The inclination of the shower track on the PDM of the 13th May 2015 event is evaluated with the fit algorithm, comparing the result for data, simulation with background and simulation alone. Figure 7.12 displays the frames with the fitting line superimposed, while in Figure 7.13 the same line fits the means of the Gaussians (green markers) fitting every row of pixels.

(a) Data   (b) Sim. plus bkg.   (c) Simulation
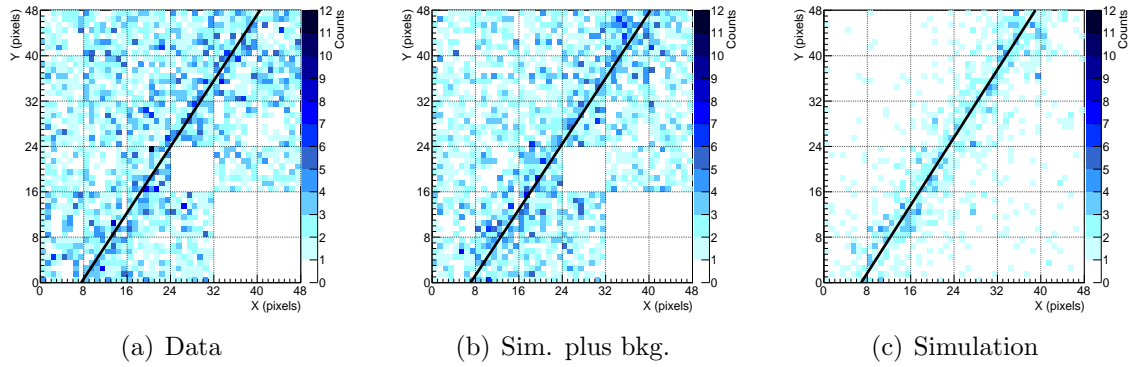
Figure 7.12: Event detected on the 13th May 2015. Linear fit of the shower track for data (a) simulation plus background (b) and simulation (c).

(a) Data   (b) Sim. plus bkg.   (c) Simulation
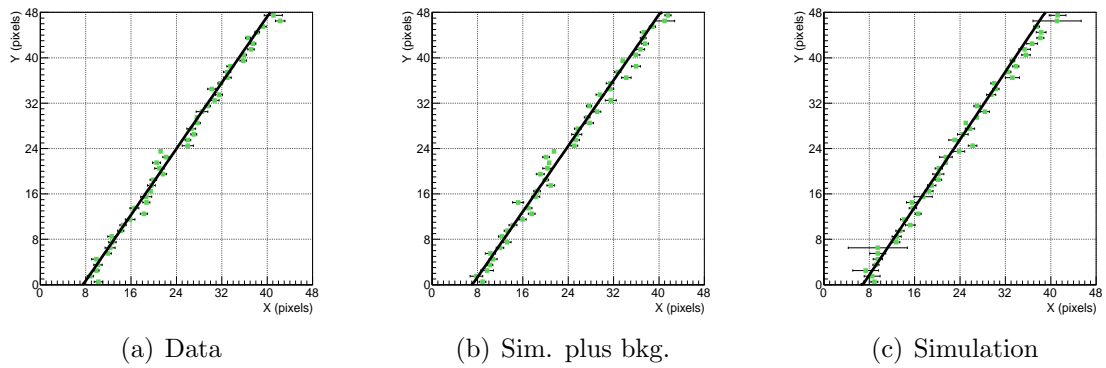
Figure 7.13: Event detected on the 13th May 2015. Linear fit of the mean (green markers) of the Gaussian fits of every row of pixels for data (a), simulation plus background (b) and simulation (c). The means lie on the shower track.

13 May 2015

	Data	Sim.+Bkg.	Sim.
$m \pm \delta m$	1.45 ± 0.01	1.45 ± 0.01	1.49 ± 0.02
$q \pm \delta q$	-11.0 ± 0.3	-10.3 ± 0.3	-10.3 ± 0.4
$\alpha \pm \delta\alpha$ (°)	34.592 ± 0.003	34.592 ± 0.003	33.867 ± 0.006

18 September 2015

	Data	Sim.+Bkg.	Sim.
$m \pm \delta m$	-0.849 ± 0.005	-0.841 ± 0.009	-0.725 ± 0.003
$q \pm \delta q$	33.01 ± 0.06	33.0 ± 0.2	28.95 ± 0.04
$\alpha \pm \delta\alpha$ (°)	130.331 ± 0.003	130.064 ± 0.005	125.942 ± 0.002

20 September 2015

	Data	Sim.+Bkg	Sim.
$m \pm \delta m$	2.04 ± 0.02	2.00 ± 0.02	1.90 ± 0.01
$q \pm \delta q$	-1.7 ± 0.3	-1.7 ± 0.4	0.3 ± 0.2
$\alpha \pm \delta\alpha$ (°)	26.114 ± 0.004	26.565 ± 0.004	27.759 ± 0.002

7 November 2015

	Data	Sim.+Bkg.	Sim.
$m \pm \delta m$	19.00 ± 1.49	12.7 ± 0.6	11.1 ± 0.5
$q \pm \delta q$	-220 ± 19	-138 ± 8	-117 ± 7
$\alpha \pm \delta\alpha$ (°)	3.013 ± 0.004	4.502 ± 0.004	5.148 ± 0.004

Table 7.1: Fit parameters m and q of the linear fit of the four detected events shower tracks, for data, simulation plus background and simulation. The resulting inclination of the track with respect to the vertical is shown too.

In Table 7.1 the comparison between the linear fit of the event tracks from data, simulations with background and simulation without background is shown. The statistical uncertainties of the x-coordinate of the points representing the mean of the Gaussians fitting the shower track in each row of pixels have been provided by the Gaussian fit as the uncertainty on the mean value. The propagation of the uncertainty to the angle α is explained in Appendix B.3.
Considering the uncertainties, it can be evaluated if the difference in the inclinations of the tracks is significant or not. The resulting difference between data and simulation with background is significant in most of the cases, apart the event of 13th May. Since the statistical uncertainties are small and make the inclinations are significantly different, the cause of this depends on systematics effect, in particular on the irregular background. Indeed, also the difference between the inclination of

the simulation with background and the simulation without background is generally significant. This means that adding the background, the fit result can be strongly perturbed.

For the event of 18th September, the first two of the three frames have been summed (not the third one because the segment of the track lies on non-active PMTs), and the two frames of the event of 20th September hae been summed too. This leads to an even more nonuniform background than usual. In the case of the event of 7th November the difference in the inclinations rely also on the uncertainty of the TA reconstruction parameters, see Appendix E.

7.2.3 Analysis of the simulation results

When a cosmic ray air shower travels through the atmosphere, fluorescence and Cherenkov light is emitted and, directly or after consecutive scattering, reaches the telescope. Then photons move through the optical system and are focused on the focal surface of the detector. At this point the photons are converted in photoelectrons. The electronics which receives the photoelectrons has some particular dead time and taking the dead time into account, the final detector response is available. This happens in reality and as well inside a simulation process, which performs all these steps.

The advantage of using a simulation framework like Offline is that not just information at the end-level of the detector response are available, as happens with a real detector, when data are collected. Indeed, with the simulations it is possible to retrieve information also of the photons in front of the detector (before they enter the telescope), of the photons at the focal surface, the photoelectrons produced just considering the sensors efficiency, and finally the photoelectrons considering also the dead times, those directly comparable with the data.

For each detected event, the information at different levels of the simulation process are discussed. Light from three main sources is detectable by EUSO-TA:

- Fluorescence light is emitted isotropically during the path of the cosmic ray air shower through the atmosphere, which is the main component.

- Direct Cherenkov light propagates along the direction of the cosmic ray air shower axis and, depending on the relative geometry between shower and telescope, it can be detected or not.

- Scattered light in air arrives to the EUSO-TA, although the initial direction was not pointing to the telescope. The scattering is named *Rayleigh* if the it happens by molecules much smaller than the incident wavelength, or *Mie* if made by particles larger than the incident wavelength.

Once it is proved the possibility to well reproduce the detected events with the simulations, this analysis allows to retrieve the expected characteristics of the real cosmic ray air showers detected, like the origin of the detected light.

As example, in the following the results relative to the event off 13th May are shown, while those for the other detected events are in Appendix F.4.

In Figure 7.14, the photons at the aperture of the telescope are plotted as a function of the number of GTUs, and on the top axis the corresponding elapsed time is reported too. Different components of the light arriving at the telescope are displayed separately, with their contributions to the total amount. Most of the light is fluorescence light, as expected. Because of the geometry of the cosmic ray air shower, just slightly going towards the detector, the direct Cherenkov light is a small percentage. Anyway, the total amount of scattered Cherenkov light is more than one third.
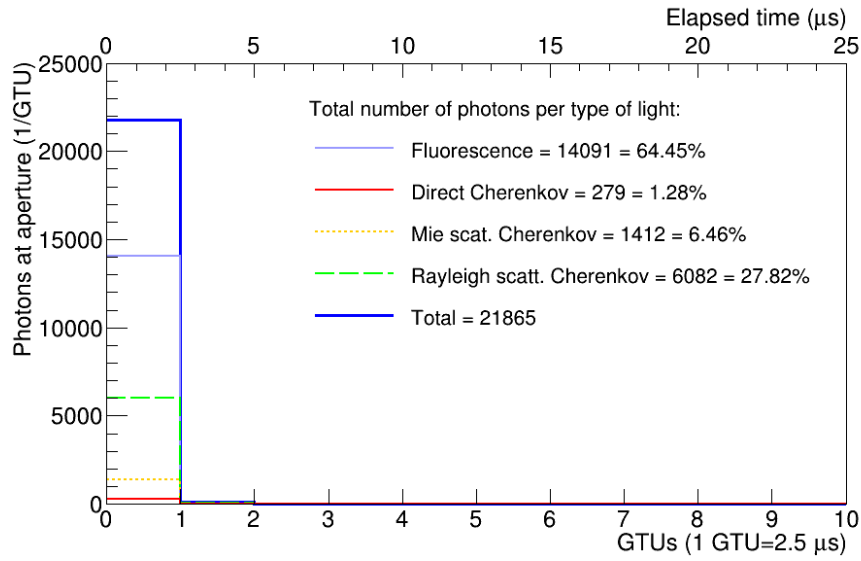
Figure 7.14: Event detected on the 13th May 2015. Different types of photons at the aperture in function of the time.

In Figure 7.15 the photons at the focal surface ($Photons_{FS}$) and the photoelectrons (PEs_{signal}) are shown respect to the total number of photons at the aperture ($Photons_{aperture}$) of the telescope. PEs_{PDE} indicates the photoelectrons produced just considering the photo-detection efficiency, and not considering the dead time. It shows that about 15% of the photons arrive at the focal surface, and the overall efficiency is about 4%.

Figure 7.16 (a-c) shows the photons at the focal surface $Photons_{FS}$, photoelectrons considering just the photo-detection efficiency PEs_{PDE} and also the dead times PEs_{signal}, for comparison. The ratios between the three quantities are reported in the plot in (d). About 27% of the photons at the focal surface contributes finally to the signal.

Table 7.2 shows the result of the analysis of the four detected events. It lists the main parameters of the cosmic ray air showers, because the results are connected to energy, distance and geometry of the showers; the kinds of light which contribute to the signal; the efficiencies of the overall detector and its subsystems.

In general, the fluorescence light is the main component of the signal. Depending on whether the shower goes towards the telescope or not, the fraction of direct
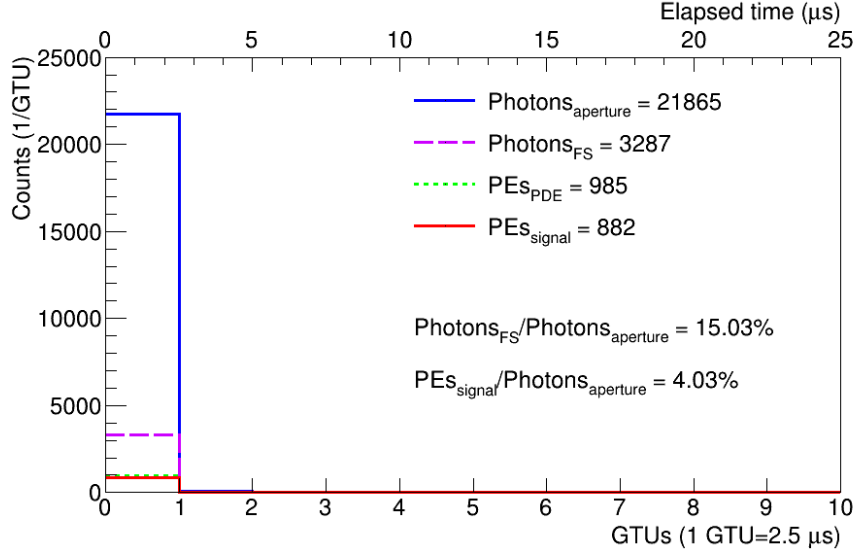
Figure 7.15: Event detected on the 13th May 2015. Photons at the aperture $Photons_{aperture}$, photons at the focal surface $Photons_{FS}$, photoelectrons considering just the photo-detection efficiency PEs_{PDE} and those considering also the dead times PEs_{signal}, as a function of time. The ratio $Photons_{FS}/Photons_{aperture}$ represents the transmission efficiency of the optical system and the ratio $PEs_{signal}/Photons_{aperture}$ represents the overall efficiency of the detector.

Cherenkov light, coming directly from the Cherenkov cone co-directional with the shower axis, gives a relatively high or low contribution, respectively. The direction of the shower can be evaluated from the zenith and azimuth angles of the showers and considering that the azimuth of the EUSO-TA axis is $-53°$: the events of 13th May and 20th September go slightly towards the detector, the one of the 18th September goes towards the detector, while the one of 7th November is almost vertical.
The transmission efficiency of the optical system is between 15% and 17% and the detector efficiency between 25% and 27.5%. The detection efficiency depends on the energy and the distance of the shower to the detector. Indeed, because of the dead time of a pixel after a photon hits it (lasting 30 ns), with high flux of photons, i.e. for close showers and energetic showers, there is a higher loss of photons than for distant and less energetic showers, for the so-called *pile-up* effect (see also Section 6.8). The pile-up effect is represented by the ratio between the photoelectrons of the signal, considering the photon-detection efficiency and the dead time, and photoelectrons produced just considering the photon-detection efficiency. It is possible to see that, although the events of 13th May and 7th November are both close to the detector, the percentage of photons contributing to the signal is less for the latter, since it is more energetic than the first one. For the events of 18th September and 20th September, split on three and two GTUs respectively, the average value of the pile-up effect is here reported. But, as visible in Figure F.12-F.14 (18th September) and Figure F.17-F.18 (20th September) the pile-up plays a stronger role in the last GTU than in the first one, since the showers approach the detector, so the distance to the detector gets shorter during the development inside the FOV.

(a) $Photons_{FS}$

(b) PEs_{PDE}

(c) PEs_{signal}

(d) Rates of the different quantities. The 0-counts bin has been cut to highlight the difference between the quantities.
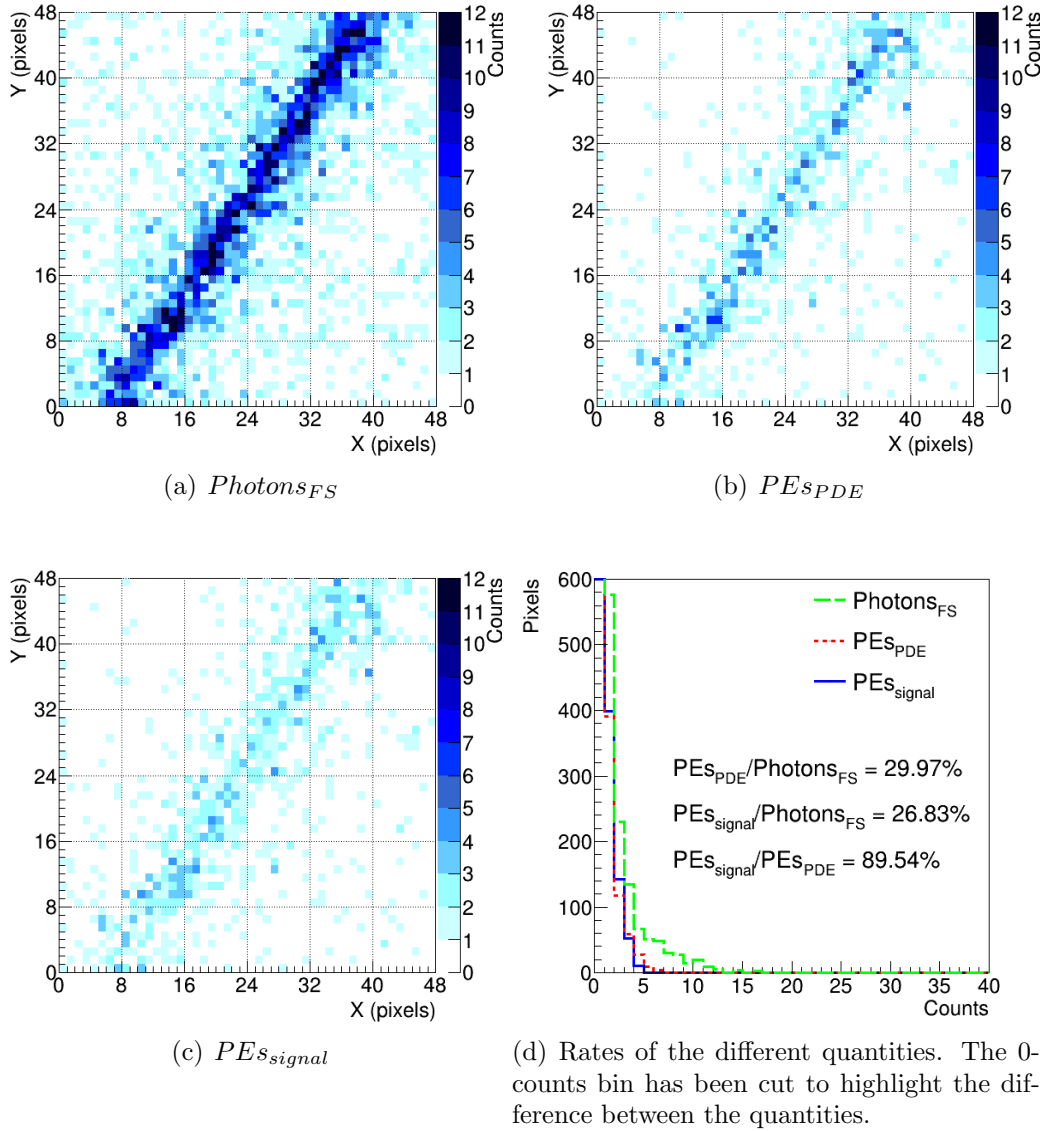
Figure 7.16: Event detected on the 13th May 2015. Distributions of the photons at the focal surface $Photons_{FS}$, the photoelectrons considering just the photo-detection efficiency PEs_{PDE} and those considering also the dead times PEs_{signal}.

	Events (2015)			
	13 May	18 Sep.	20 Sep.	7 Nov.
Parameters				
E (eV)	10^{18}	$10^{18.51}$	$10^{18.38}$	$10^{18.42}$
R_p (km)	2.5	9.1	6.7	2.6
Zenith (°)	34.5	60.4	41.2	8.1
Azimuth (°)	7.2	-79.3	-24.8	82
Light				
Fluorescence (%)	65.5	77.8	65.9	79.5
Direct Cherenkov (%)	1.3	9.6	2.4	0.6
Scattered Cherenkov (%)	34.3	12.6	31.7	19.9
Efficiencies				
Optical transmission (%)	15.0	16.7	16.9	16.1
Detector (%)	26.8	27.0	27.4	25.0
Pile-up effect (%)	89.5	79.5	85.6	78.4
Overall (%)	4.0	4.8	4.6	4.0

Table 7.2: Summary of the simulation results of the detected events. The contributions of the different kinds of light (fluorescence and direct and scattered Cherenkov) to the total amount arriving at the telescope is reported for each event. As well, the efficiencies related to the single subsystems of the detector and the overall efficiency are shown.

7.3 Summary and discussion

Given the good quality of the simulation, the measured events are compared with the detailed simulation. To the event simulation results, background frames taken from the data are added. There is good agreement between data and simulations with background, evaluated with a visual comparison of the frames and comparing the counts distributions per each frame. At about 2, 3 counts the contribution of the event to the frame brightness over the background appears.

A fit algorithm has been used to compare the the track inclination of data and simulations. Differences of up to about 4° has been found, but different factors may influence such results. The fit algorithm revealed different results if applied to simulation with or without background. Assuming that it works in the best way in the case of just simulation, the addition of background makes the surrounding of the track irregular and this influences the fit result. This is even more evident for events split on two or more frames, because the sum of the frames is made prior the fit. The different inclination may rely on the uncertainties of the TA reconstruction parameters. The geometrical resolution of the open angle is 7.4° for reconstruction in the monocular mode (just using the fluorescence detectors at Black Rock Mesa), which may reconstruct a shower at a different angle, i.e. position, respect to the telescope axis (Appendix E). But there is also the possibility that some inconsistencies between the actual relative position of the PDM and the optical axis in EUSO-TA and the one in Offline, contribute to the deformation of the track, for example close to the edge of the frames, where optical distorting effects are present.

A study on the simulation results has been performed for each detected event. The simulations make available the ratios between the different type of light detected: Fluorescence, direct Cherenkov and scattered Cherenkov. The ratios are consistent with what was expected considering the geometry of the cosmic ray air showers. For example, for showers coming toward the telescope, the fraction of direct Cherenkov light is higher than for other showers, since it propagates along the shower axis direction.

Finally, knowing the number of photons at the different steps of the simulation, i.e. at the aperture of the EUSO-TA (in front of the front lens), at the focal surface, the photoelectrons before and after considering the dead times, the ratios of the different quantities have been calculated. The transmission efficiency of the optical system resulted to be between 15% and 17%, while the overall efficiency of the telescope is between 4% and 5%. In [67], the transmission efficiency of the optical system, called photon collection efficiency (PCE) is about 40%, while informal communications reported the expected overall efficiency of the telescope as 3.5%. Unfortunately, no direct measurements have been done for this purpose. So, for the moment these results are taken into account.

Summing up the results, the events detected with EUSO-TA gave a contribution of 2, 3 counts per pixel over background. This value varies depending on the background intensity and on the presence or not of noisy areas on the frame. Moreover,

although the statistics is still low, it seems that it is easier to detect cosmic ray air shower moving towards the telescope, possibly due to the direct Cherenkov light, which propagates along the shower axis making it brighter and so better detectable. Looking to more technical aspects, the inclination of the event track on the frame is the projection of the cosmic ray air shower axis on the focal surface of the detector, combination of zenith and azimuth angles. The difference between the inclination of the tracks on the measured frames and the simulated ones, and the required shift of the shower core in the simulations, may be a direct consequence of the uncertainties of the TA reconstruction parameters. Finally, the efficiency of the detector has been estimated, but a direct measurement of it would be necessary to prove if the evaluation is correct.

Chapter 8

Study of the non-detected events

8.1 Simulation of the events in EUSO-TA FOV

The four detected events and the four candidate events discussed before are not the only cosmic ray air shower that crossed EUSO-TA FOV. The TA group supported the EUSO-TA data analysis looking for those events detected with TA and which crossed EUSO-TA FOV according to the EUSO-TA operation condition, i.e. if the acquisition was in external mode (triggered by TAFD) and considering the EUSO-TA elevation angle that may change from night to night. Table 4.1 in Section 4.3 summarizes these events, with a total of 110 events in EUSO-TA FOV in 55 days of data acquisition in the year 2015, four of which have been identified in the data and four are considered candidate events because they are too faint or with short tracks on the data frame to be classified as detected events.

Figure 4.3 shows with each marker an event on the plot R_p versus $\log_{10} E$, i.e. the distance of the shower axis to the telescope versus the energy of the primary cosmic ray. It is evident that there is a linear correlation of the TA detection limit with the increase of the logarithm of the energy and the distance. The same behavior of the detection limit is valid also for the six events detected by EUSO-TA, but given a fixed energy, the distance of an event has to be smaller than for TA.

To better understand the detection limit of EUSO-TA, simulation studies have been performed. Every event has been simulated, using the reconstruction parameters received from the TA group, i.e. energy of the primary cosmic ray, zenith and azimuth angle of the shower axis, coordinates of the impact point of the shower axis on ground. To each simulated event track, the background taken from the data at around the time when it was expected to be (corresponding to the time stamp given by the TA group), has been added. This choice comes from the fact that the average background varies over the months. Next to this factor, there are also some periodic noisy areas of the focal surface. The background frames added to the simulations are homogeneous, in order to evaluate the detector capability, excluding the noise sources due to electronics, several issues are still under study. This sort of "best condition" affects the number of events considered visible in the simulations,

because there is the possibility that an event hit the focal surface in a noisy area and in that case it would not be possible to see it. With "visible" is simply meant recognizable by eye. The look of the simulation results with background also helped in recognizing a few events in the data, not seen before, as mentioned in Section 4.3. Anyway, some events visible in the simulations still do not have a visible counterpart in the data and this is, at least in part, probably due to the variability of the background.

8.1.1   Candidate events

Simulating the cosmic ray air showers which crossed the EUSO-TA FOV but have not been not seen in the data in a first moment, helped to identify the so called candidate events and even a detected event (of the 18th September 2015). The candidate events are considered so because they are faint and their contribution to the frame brightness is of the same magnitude of some parasitic noise present on some areas of the frames, or because their tracks are not continuous and well defined. In the following, four candidate events are presented. As done for the detected events, for each case a table summarizes the characteristics of the event and the EUSO-TA elevation angle, almost all parameters necessary to run the simulations. Then, frames of data and simulations are shown, for comparison.

Candidate event of the 12th May 2015

This is a distant event with $R_p = 8.3$ km, going forward respect to the telescope, since the zenith angle is 56.9° and the azimuth angle is 74.3° (the azimuth angle of the telescope axis is −53°). In the simulation the event covers 4 GTUs.

Table 8.1 shows the event parameters from the TA event reconstruction and those calculated to perform the simulation. In this case, no shift of the shower core was needed to reproduce the position of the event track expected in the data.

The candidate event in the data and the simulated one are shown in Figure 8.1. In the simulation the first two frames show a segment of track which is not visible in the data, while the last two frames are more in agreement. Anyway, as seen in Figure 4.8, also TA did not detect signal in the top-right part of the EUSO-TA FOV, so this might be due to the presence of clouds in the FOV, for example.

Shower parameters	
* Zenith	56.9°
* Azimuth	74.3°
* Energy	$10^{18.69}$ eV
R_p	8.3 km
Ψ	44.8°
Core coord. w.r.t. CLF from TA rec.	(5.6 km, −8.7 km)
.... in UTM coord.	(341005 mE, 4342762 mN)
* .... in UTM coord. shifted	(- mE, - mN)
Core coord. shift	- km
Distance core to EUSO-TA	11.72 km
Number of GTUs	4
EUSO-TA configuration	
* Elevation	25°

Table 8.1: Candidate event possibly detected on the 12th May 2015. The parameters used to perform the simulation are marked with an asterisk.

The reason why it is considered a "candidate" event is that the presumed measured signal is faint and diffuse. Moreover, the PMT just below the single masked PMT is often noisy, so the structure at GTU 3 might be noise and the one at GTU 4 again noise, although on a PMT that is not usually noisy.

(a) Data, GTU 1

(b) Sim. plus bkg., GTU 1

(c) Data, GTU 2

(d) Sim. plus bkg., GTU 2

(e) Data, GTU 3

(f) Sim. plus bkg., GTU 3

(g) Data, GTU 4

(h) Sim. plus bkg., GTU 4
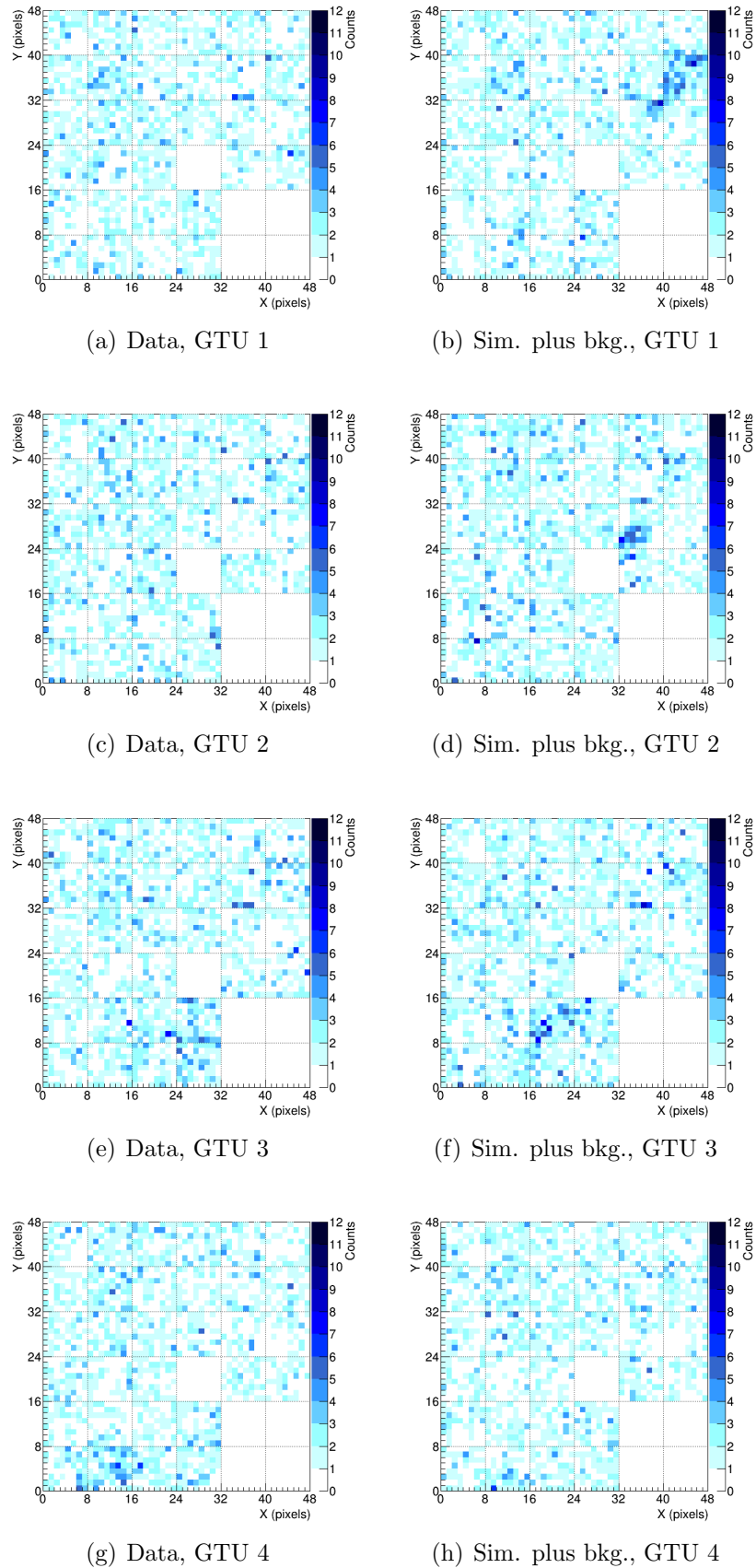
Figure 8.1: Candidate event possibly detected on the 12th May 2015. Comparison between frames of data (a,c,e,g) and simulation (b,d,f,h).

Candidate event of the 12th September 2015

This is a cosmic ray air shower of mid distance from the telescope, with $R_p = 5.0$ km, and its direction is going away from the telescope. The simulated event covers two GTUs. Table 8.2 shows the event parameters. As seen in Section 4.4, two candidate events are compatible as possible event regarding the sequence number of the GTU in the packet (Section 5.1.3). The candidate events in the data and the simulated one are shown in Figure 8.2. The first frame presents a segment of the event track on an often noisy PMT.

Shower parameters	
* Zenith	29.5°
* Azimuth	−164.9°
* Energy	$10^{18.05}$ eV
R_p	5.0 km
Ψ	74.7°
Core coord. w.r.t. CLF from TA rec.	(13.5 km, -8.1 km)
.... in UTM coord.	(348905 mE, 4343362 mN)
* .... in UTM coord. shifted	(348580 mE, 4343100 mN)
Core coord. shift	0.26 km (SW direction)
Distance core to EUSO-TA	5.36 km
Number of GTUs	2
EUSO-TA configuration	
* Elevation	21°

Table 8.2: Candidate event possibly detected on the 12th September 2015. The parameters used to perform the simulation are marked with an asterisk.

Because of the noisy PMT and the inactive PMTs (masked in the figures), none of the two candidate events has a defined track, so they cannot be classified as a detected event. Moreover, even more data frames than these selected and shown have structures similar to those of these presented at GTU 1, but just these two satisfies the requirements on the number of the GTU in the packet (Section 5.1.3). This means that the noise has to be the cause of one of the candidate events, but could be also the cause of both of them.

(a) Data, candidate I, GTU 1

(b) Data, candidate I, GTU 2

(c) Data, candidate II, GTU 1

(d) Data, candidate II, GTU 2

(e) Sim. plus bkg., GTU 1

(f) Sim. plus bkg., GTU 2
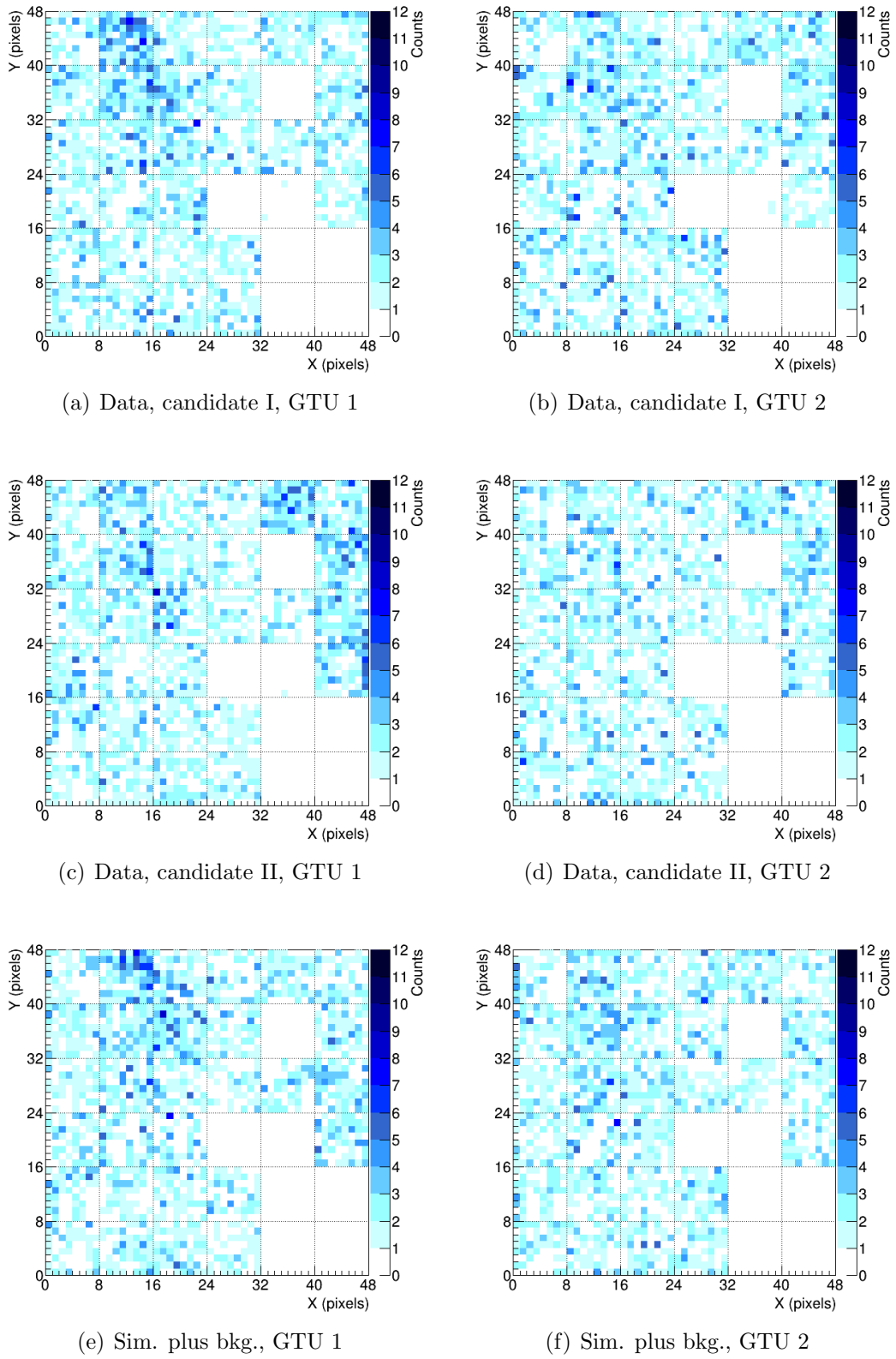
Figure 8.2: Candidate event possibly detected on the 12th September 2015. Comparison between frames of data for the candidate I (a,b), candidate II (c,d) and simulation (e,f).

Candidate event of the 15th October 2015

This is a distant cosmic ray air shower with $R_p = 9.0$ km, which goes slightly towards the telescope. The simulated event covers three GTUs. Table 8.3 shows the event parameters. The candidate event in the data and the simulated one are shown in Figure 8.3. In both the cases, just one frame, the second one, presents an evident event track, although irregular in the data, while in the other two, at least in the simulation, the counts are low and do not stand out against the background.

Shower parameters	
* Zenith	40.6°
* Azimuth	-120.5°
* Energy	$10^{18.52}$ eV
R_p	9.0 km
Ψ	99.5°
Core coord. w.r.t. CLF from TA rec.	(10.6 km, -5.6 km)
.... in UTM coord.	(346005 mE, 4345862 mN)
* .... in UTM coord. shifted	(345650 mE, 4345520 mN)
Core coord. shift	0.49 km (SW direction)
Distance core to EUSO-TA	9.14 km
Number of GTUs	3
EUSO-TA configuration	
* Elevation	15°

Table 8.3: Candidate event possibly detected on the 15th October 2015. The parameters used to perform the simulation are marked with an asterisk.

In this case, the event is considered a candidate event because in the data frame, the track in GTU 2 appears more like two bright spots than a continuous line. This would make an possible analysis difficult. However, the PMTs with possible event signals are usually not noisy, so there are good chances that the event is a real one.

(a) Data, GTU 1

(b) Sim. plus bkg., GTU 1

(c) Data, GTU 2

(d) Sim. plus bkg., GTU 2

(e) Data, GTU 3

(f) Sim. plus bkg., GTU 3
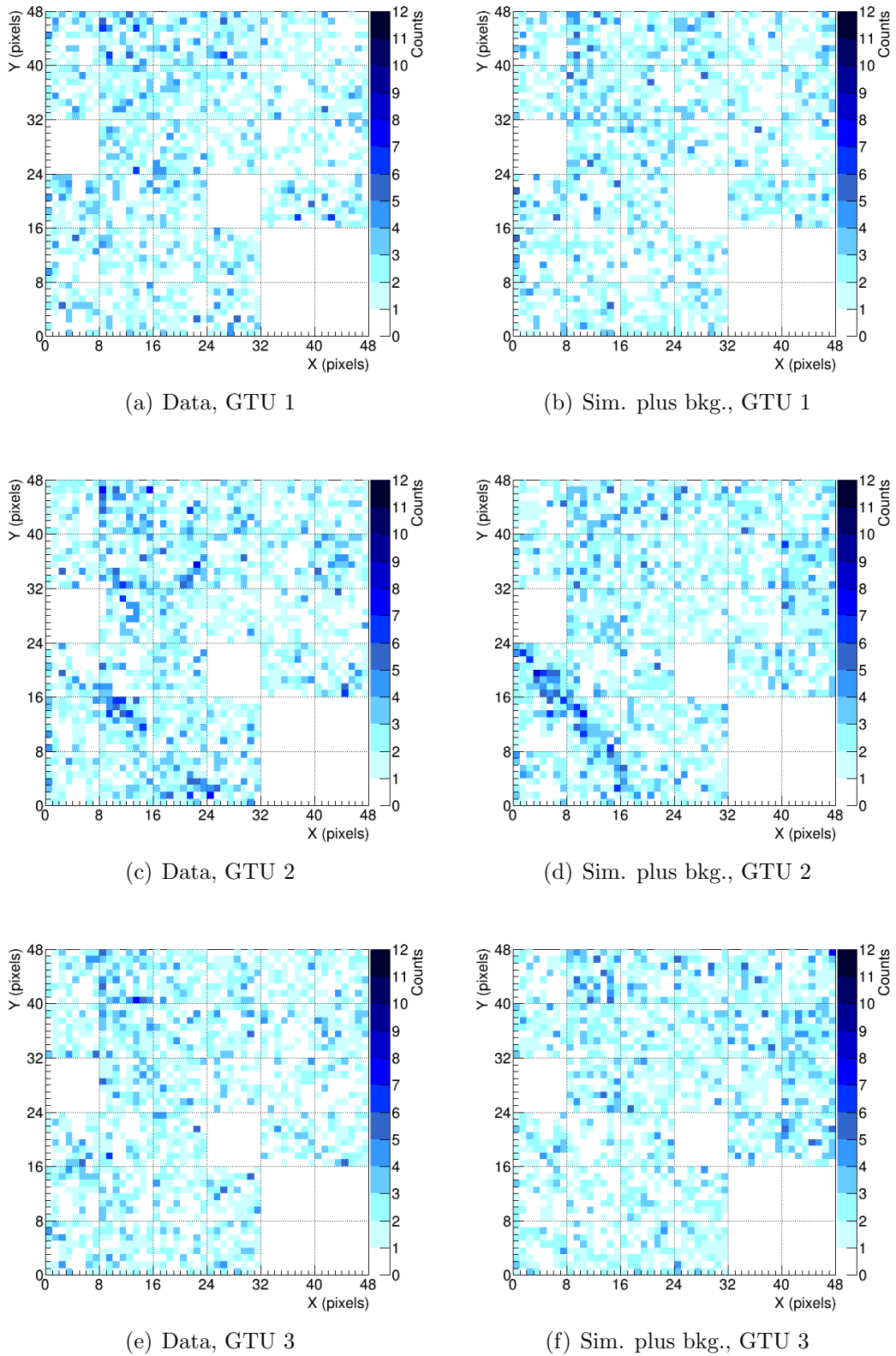
Figure 8.3: Candidate event possibly detected on the 15th October 2015. Comparison between frames of data (a,c,e) and simulation (b,d,f).

Candidate event of the 16th October 2015

This is a close shower with $R_p = 1.7$ km, going towards the telescope, but with a low zenith angle. The simulated event covers just one GTU. Table 8.4 shows the event parameters and Figure 8.4 shows the event in the data and the simulation.

Shower parameters	
* Zenith	10.6°
* Azimuth	−40.5°
* Energy	$10^{17.71}$ eV
R_p	1.7 km
Ψ	100.6°
Core coord. w.r.t. CLF from TA rec.	(15.6 km, −11.0 km)
.... in UTM coord.	(351005 mE, 4340462 mN)
* .... in UTM coord. shifted	(350730 mE, 4340180 mN)
Core coord. shift	0.39 km (SW direction)
Distance core to EUSO-TA	1.78 km
Number of GTUs	1
EUSO-TA configuration	
* Elevation	10°

Table 8.4: Candidate event possibly detected on the 16th October 2015. The parameters used to perform the simulation are marked with an asterisk.

This event is faint, crossing PMTs which are sometimes noisy and one which is inactive, but its geometry agrees with the simulated one. It could be the case of an unfortunate coincidence of noisy areas making a linear track.

(a) Data (b) Sim. plus bkg.
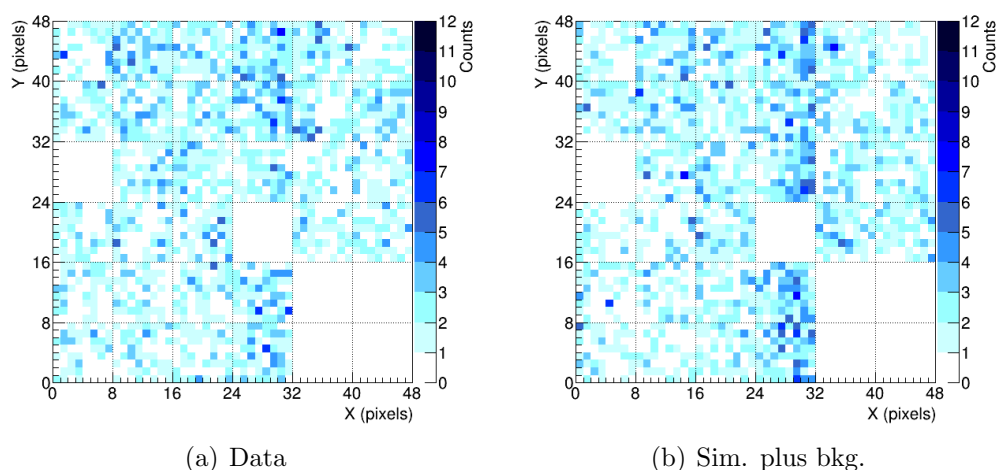
Figure 8.4: Candidate event possibly detected on the 16th October 2015. Comparison between frames of data (a) and simulation (b).

8.2   The EUSO-TA detection threshold

The detected events, together with the identified candidate events, as well as the not detected events, will be helpful in the evaluation of the EUSO-TA detection threshold. Figure 8.5 shows the impact parameter R_p versus $\log_{10} E$ plot updated with the simulation results. The green markers show the detected and the candidate events, in blue events that look visible in the simulation but have not been found in the data and in red events not detected and not visible in the simulation. The simulations have been performed for events with energy $E \geq 10^{17.4}$ eV, and from the trend observed, those with lower energy have been assumed as "not visible in the simulation".

The imaginary line which defines the detection limit for the events visible in the simulation looks almost parallel to the one for the detected events but shifted towards lower energies. Simulations of events with $R_p < 2$ km end with no output because of a not yet solved issue, so they cannot be studied. The fact that there are events visible in the simulations and not in the data might occur because of the variability of the background intensity, the noisy areas of the PDM, or simply because the real events were fainter than the simulated ones, for example because of the weather conditions that can influence the cosmic ray air shower development.
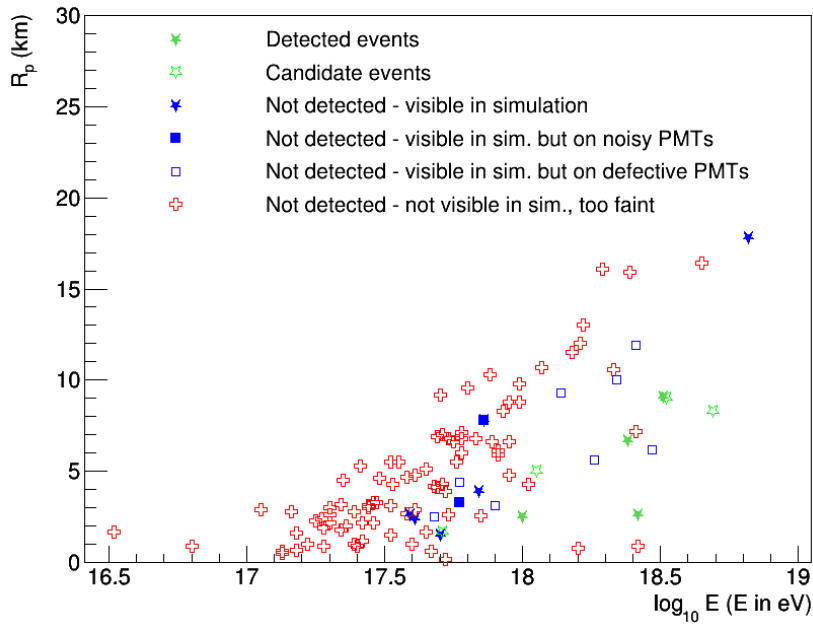
Figure 8.5: Detected, candidate and not detected events which crossed EUSO-TA FOV. Different markers show if an event has been detected and if it is visible in the simulations, once the background is added to the pure simulated event track.

To define some constraints on the detected and not detected events, the total number of counts in the simulated event tracks, without background, are considered. The result of this study is represented in Figure 8.6. The detected events, as well as a few
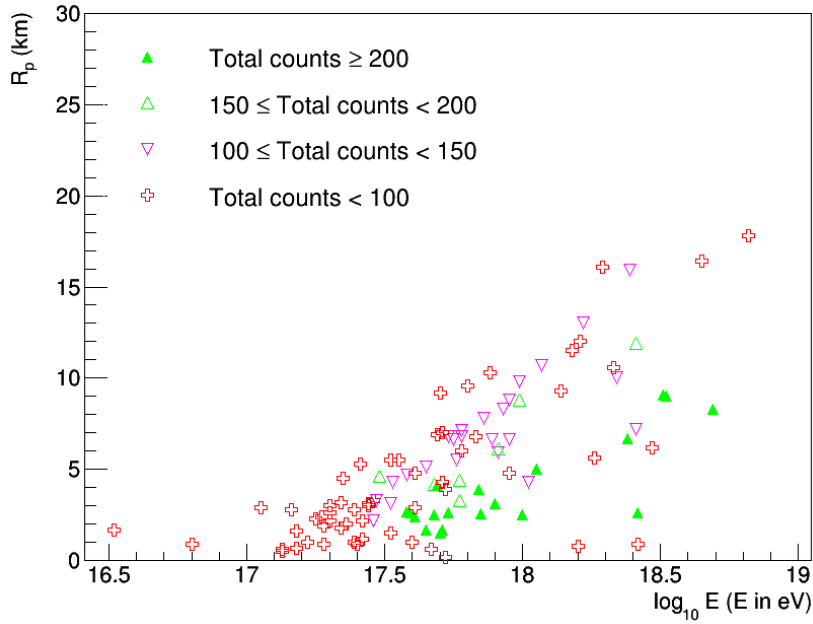
Figure 8.6: All the events which crossed the EUSO-TA FOV in 2015 are reported in the plot. The different markers show a different number of total counts making the event in the simulations.

other events, present ≥ 200 counts. Moreover, they are clustered in the same region of the R_p versus $\log_{10} E$ with a detection limit similar to the one of the detected events. Other categories of events has been considered, with total number of counts in the ranges 150-200, 100-150 and < 100 counts. With the decrease of the counts threshold, the detection limit moves towards lower energies. But almost all the events with 100-150 and < 100 counts correspond to not detected events and even not visible in the simulations.

From this, a rough evaluation of the average number of counts per PMT and pixel necessary to make an event visible over the background can be done. Assuming a vertical shower, the event track has a length of 48 pixels, between those of inclined showers traversing the FOV almost in the center and those of inclined showers crossing just a portion of FOV. Assuming the width of a shower track as 8 pixels, i.e. one PMT 8×8 pixels, almost all the track is taken into account. Indeed, since in Section 5.1.2 the FWHM of the Gaussian fitting the lateral distribution of the tracks of the detected events tracks have been evaluated between 3 and 5 pixels, with 8 also the tails of the Gaussian are taken into account. In this way, the "area" covered by the shower track can be considered as 6 PMTs or $8 \times 48 = 384$ pixels. The threshold of 200 counts for an event track means that each PDM should count about 33 counts above the background, corresponding to an average of 0.52 counts per pixel. This information can be used, for example, to confirm or improve the trigger algorithms used in the research of events in the EUSO-TA data.

8.2.1 Examples of non-detected events

In the R_p versus $\log_{10} E$ plot shown in Figure 8.5, an area where the detected and candidate events take place has been recognized. However, some non-detected events are non-visible in the simulations although they lie in the area of the detected and candidate events. On the other hand, some non-detected events are visible in the simulations, although they are in the area of the events non-detected and non-visible in the simulation. In the following, two examples of such events are reported.

Event non-detected on the 21st October 2015

This event is the one that in the R_p versus $\log_{10} E$ plot shown in Figure 8.5 is depicted with red cross marker at $R_p = 7.2$ km and $\log_{10} E = 18.41$, close to a green full star representing a detected event (20th September 2015). This case has been chosen as example of event non-detected and non-visible in the simulations, although in the area of plot of the potentially detectable events. Table 8.5 collects the shower parameters, reconstructed by TA. Figure 8.7 shows the event from pure simulation and with background added, over 3 GTUs.

The possible explanation is related to the showers geometry. In the case of the shower detected on the 20th September, the azimuth is $-24.8°$ and the shower goes slightly towards EUSO-TA, while for this one it is $-136.3°$ and the shower goes away from the telescope. Moreover, because of the zenith angle that is $41.2°$ for the event of the 20th September and $52.2°$ for this one, it is possible that $11°$ of difference make the shower developing faster through the atmosphere in the second case, and the corresponding signal arriving to the detector results to be weaker.

Shower parameters	
* Zenith	52.2°
* Azimuth	$-136.3°$
* Energy	$10^{18.41}$ eV
R_p	7.2 km
Ψ	85.1°
Core coord. w.r.t. CLF from TA rec.	(12.4 km, -6.5 km)
Number of GTUs	3
EUSO-TA configuration	
* Elevation	7°

Table 8.5: Non-detected and non-visible in the simulation event of the 21st October 2015. The parameters used to perform the simulation are marked with an asterisk.

(a) Simulation, GTU 1   (b) Sim. plus bkg., GTU 1

(c) Simulation, GTU 2   (d) Sim. plus bkg., GTU 2

(e) Simulation, GTU 3   (f) Sim. plus bkg., GTU 3
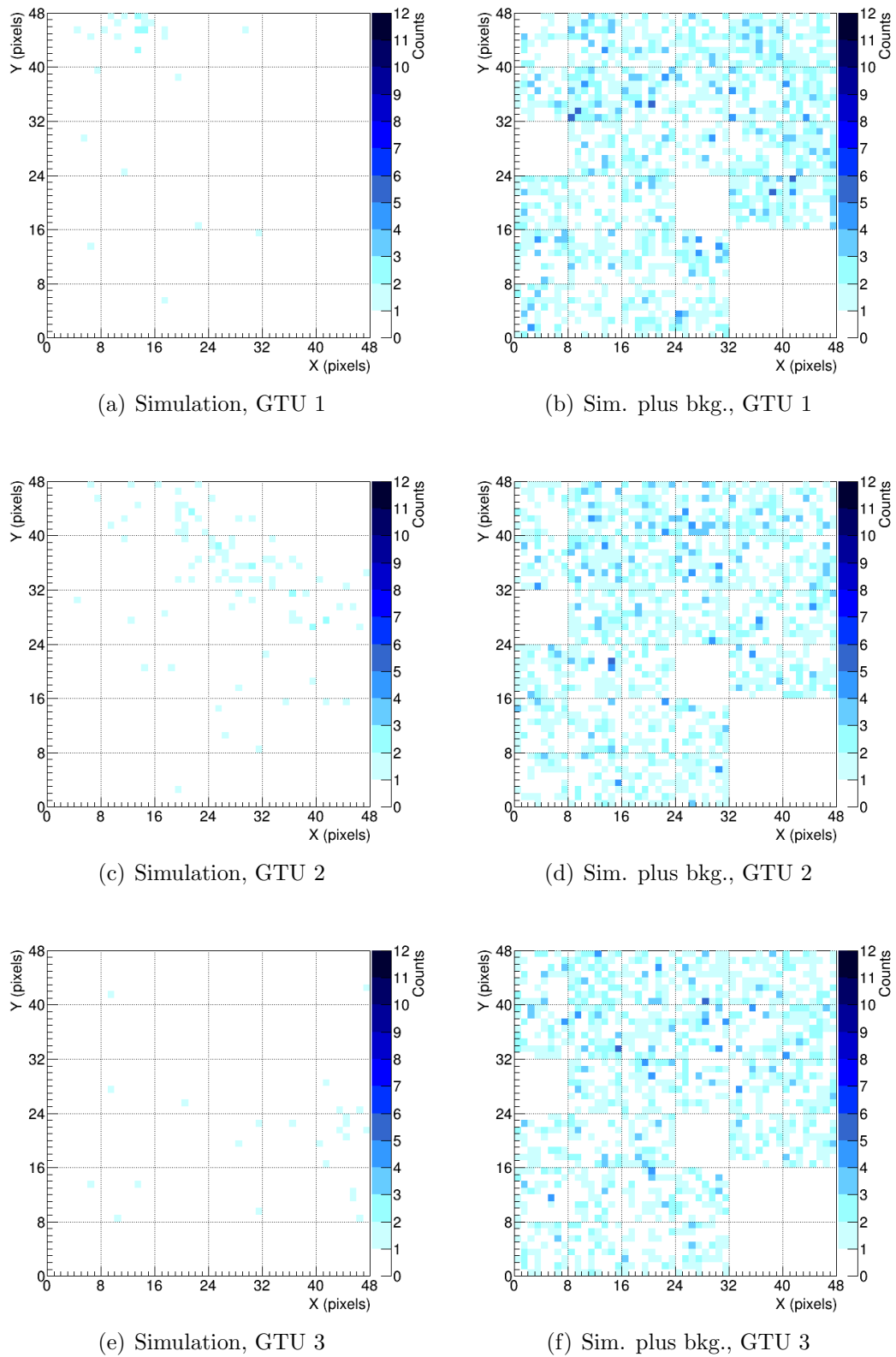
Figure 8.7: Event non-detected and not visible in the simulation, of the 21st October 2015. Frames of pure simulation (a,c,e) and simulation with background (b,d,f). The track is faint and diffuse, no signature of it in the frames with background.

Event non-detected on the 7th November 2015

This event is the most distant (R_p = 17.8 km) and most energetic ($10^{18.82}$ eV) that crossed EUSO-TA FOV during the data acquisition campaigns in 2015. Its parameters are listed in Table 8.6. From the combination of the zenith and the azimuth angles, the shower goes slightly away from the detector. In Figures 8.8 and 8.9 the development of the shower inside the FOV is shown, for pure simulation and simulation with background. Looking at the single frames, any segment of the track is visible. However, looking at the sequence, a tiny but relatively intense spot is moving. So, although it could be considered an extreme case, this event has been defined as "visible in the simulation".

Shower parameters	
* Zenith	37.9°
* Azimuth	112.1°
* Energy	$10^{18.82}$ eV
R_p	17.8 km
Ψ	53.0°
Core coord. w.r.t. CLF from TA rec.	(-1.9 km, -0.0 km)
Number of GTUs	8
EUSO-TA configuration	
* Elevation	10°

Table 8.6: Event non-detected but visible in the simulation, of the 7th November 2015. With a star are marked the parameters used to perform the simulation.

With respect to the event non-detected and non-visible in the simulation of 21st October 2015 discussed before, in this case the track is thinner (because of the long distance) but brighter (because of the high energy, although the distance is long). Indeed, it is the "density" of bright pixels due to an event track which makes it visible or non-visible.

(a) Simulation, GTU 1

(b) Sim. plus bkg., GTU 1

(c) Simulation, GTU 2

(d) Sim. plus bkg., GTU 2

(e) Simulation, GTU 3

(f) Sim. plus bkg., GTU 3

(g) Simulation, GTU 4

(h) Sim. plus bkg., GTU 4
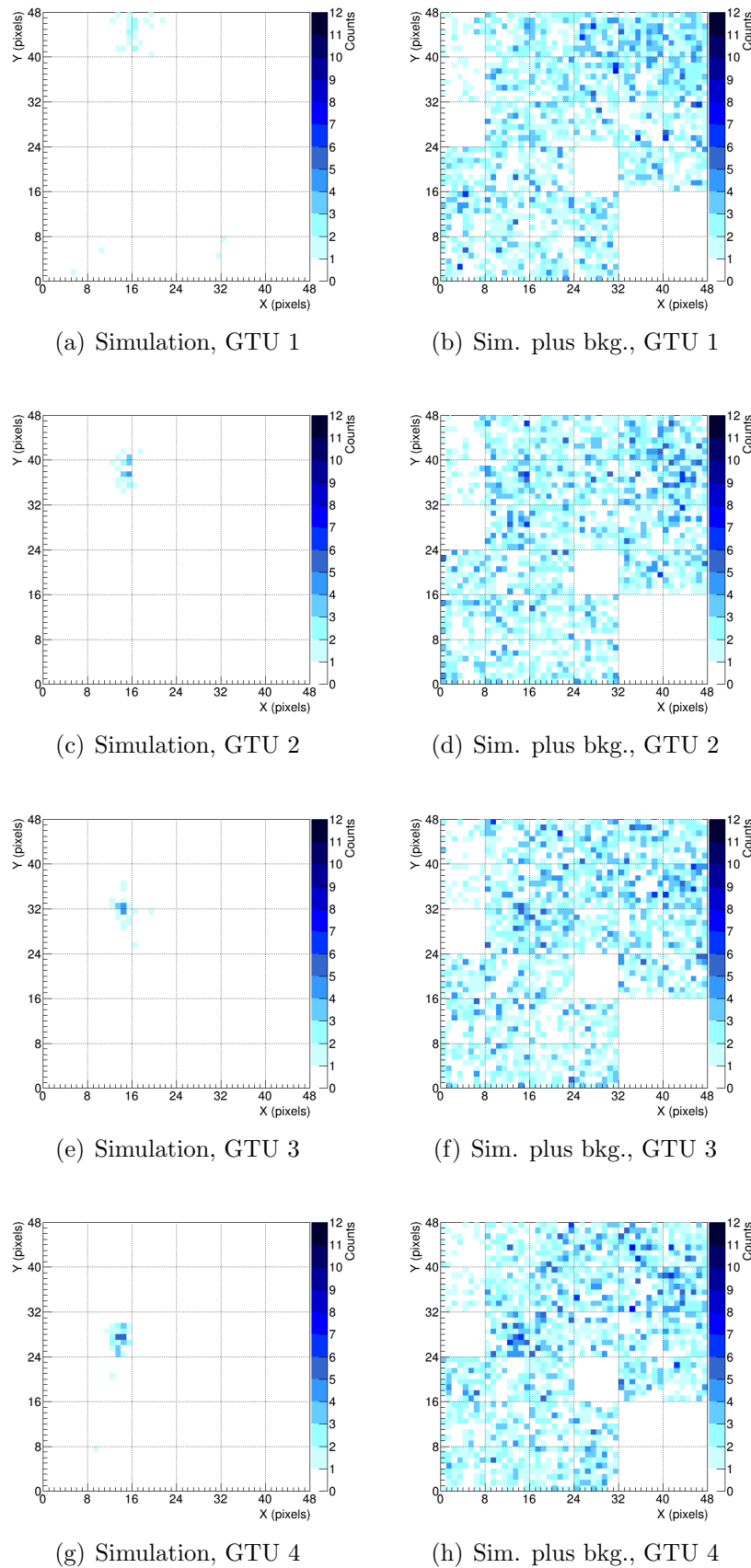
Figure 8.8: Event non-detected but visible in the simulation, of the 7th November 2015. Frames of pure simulation (a,c,e,g) and simulation with background (b,d,f,h). Although tiny, is is possible to see a spot moving through 8 frames (second part in Figure 8.9).

(a) Simulation, GTU 5

(b) Sim. plus bkg., GTU 5

(c) Simulation, GTU 6

(d) Sim. plus bkg., GTU 6

(e) Simulation, GTU 7

(f) Sim. plus bkg., GTU 7

(g) Simulation, GTU 8

(h) Sim. plus bkg., GTU 8
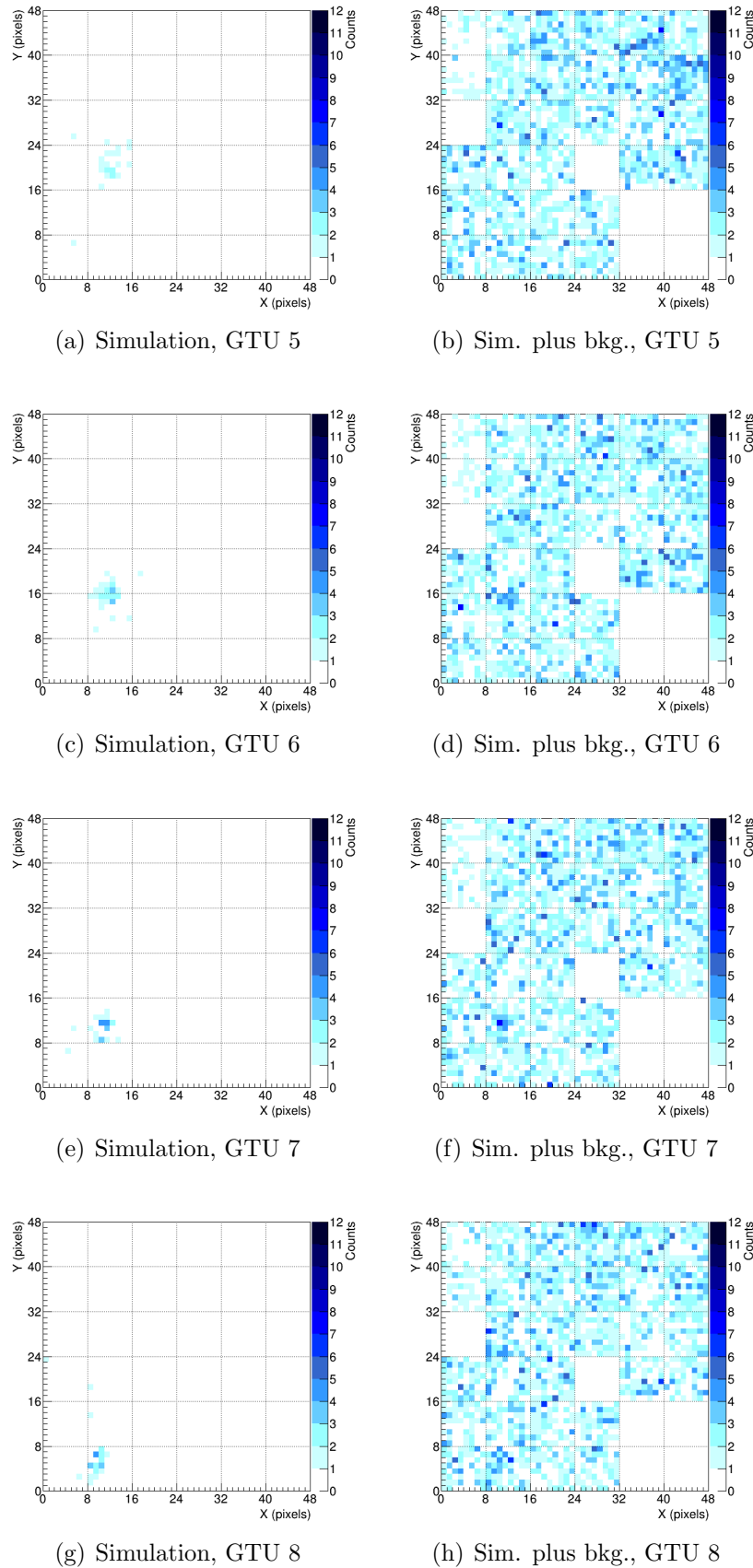
Figure 8.9: Event non-detected but visible in the simulation, of the 7th November 2015. Frames of pure simulation (a,c,e,g) and simulation with background (b,d,f,h). Although tiny, is is possible to see a spot moving through 8 frames (first part in Figure 8.8).

8.3 Estimation of expected number of events

8.3.1 First estimation

In 2011, before the beginning of EUSO-TA activity, a first analysis [64] has been done to estimate the flux of cosmic rays EUSO-TA would be able to detect in one year. This has been done under the assumptions:

- Cosmic ray spectrum measured by TA ($E > 10^{18}$ eV)

- Duty cycle of 10% (876 hours in one year)
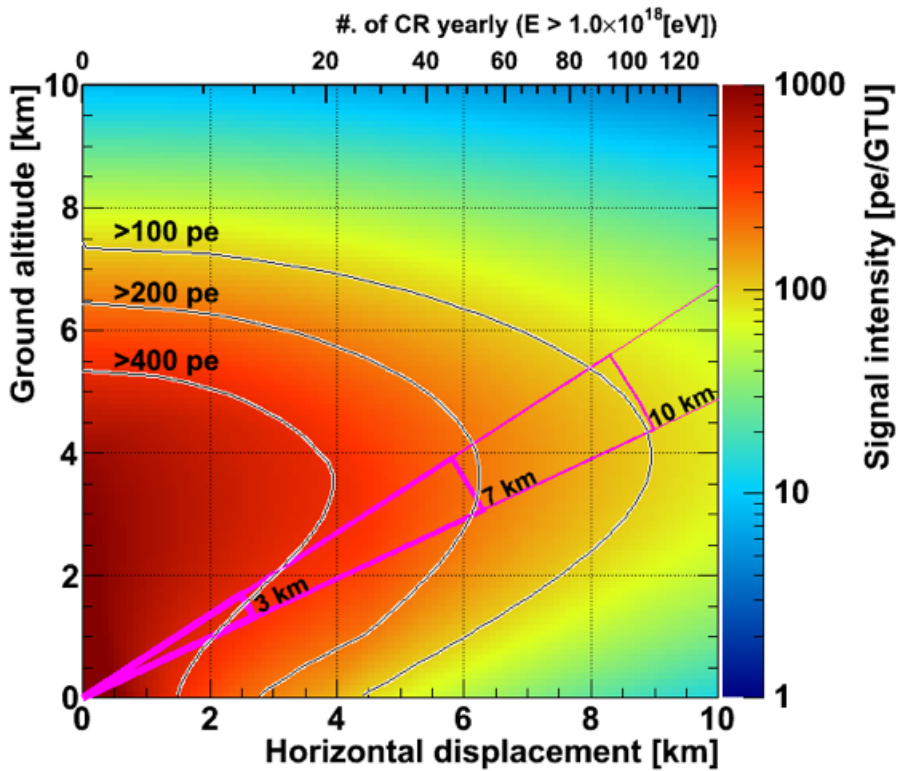
Figure 8.10: Analysis to estimate the number of detectable event with EUSO-TA [64].

Figure 8.10 shows the analysis result. On the X-axis there is the distance of the cosmic ray events from the telescope (horizontally), on the Y-axis there is the altitude from ground: it is as looking to one side of EUSO-TA. On the top axis, the number of cosmic rays expected per year is reported and the color scale defined the intensity of the signal. Two main classes of cosmic ray events can be defined, with the relative flux: about 10 events/year CLASS-I event (> 400 pe and $R < 3$ km) and about 100 events/year CLASS-II events (> 100 pe and $R \sim 10$ km). Scaling

for the actual data taking time in 2015 (123 hours, 112 effective hours taking into account about 10% internal dead time) one can expect about 1.3 CLASS-I events and 13 CLASS-II events, for a total of $14 - 15$ events. Actually, as seen before, the threshold of 100 pe/GTU seems to be too low to have a visible event track over background, so the number of expected CLASS-II events might be lower.

The plot also defines the most efficient elevation angle of the telescope in terms of expected events, which is 30°, drawn as a FOV in pink lines around this elevation. This value would be usable also because TA FOV extends in the range $3° - 33°$ in elevation, so it would be possible to be triggered by TA and crosscheck the detected events. Actually, the elevation angle of the telescope is up to 25°, because at higher values the telescope FOV would intersect the ceiling of the container hosting it.

8.3.2 Most recent estimation

Another estimation of the detectable events has been done recently[*]. In this analysis the following assumptions have been made:

- TA trigger efficiency of 100%

- Cosmic ray power spectrum E^{-1} ($10^{17} \leq E \leq 10^{19}$ eV). Such a power spectrum (different from the actual slope of about E^{-3}) allows to have higher statistics of UHECRs, with the purpose of calculating the trigger efficiency per every bin of energy, as described afterwards;

- Zenith angle in the range $[0, \pi/2]$ distributed as $\sin 2\theta$;

- Azimuth angle in the range $[0, 2\pi]$ uniformly distributed;

- Impact point on ground of the shower axis generated uniformly within a radius $R \leq 50$ km around the telescope;

- The number of cosmic ray air showers within EUSO-TA FOV with an impact parameter $1 \leq R_p \leq 10$ km have been estimated. Generating $N_{tot} = 10^8$ events, the fraction of such showers is:

$$f_{N_{FOV}} = N_{FOV}/N_{tot} \approx 1.578 \cdot 10^{-2}; \tag{8.1}$$

- Mean overall pixel efficiency of 10%;

- A trigger algorithm devised for this analysis, assures that a shower is detected if there are at least 2 PMTs with at least four pixels with a signal over 3σ, on 3 GTUs (which leads to a probability to be triggered by background of $\sim 5 \cdot 10^{-6}$, ~ 2 Hz);

---

[*]Work done by F. Catalano using the ESAF software, during an Erasmus Traineeship at KIT in Summer 2016, and presented at the JEM-EUSO Coll. meeting in Tokyo, December 2016
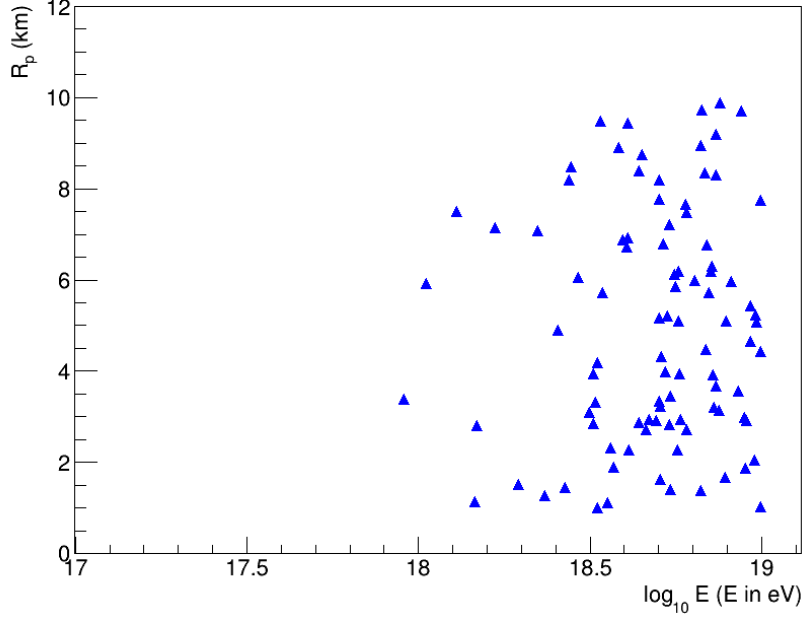
Figure 8.11: 94 events which passed the trigger selection out of 1000 simulated events.

- Simulation area A as

$$A = \pi r^2 \int_0^{2\pi} d\phi \int_0^{\pi/2} \sin\theta\cos\theta d\theta = \pi^2 r^2 \simeq 4.9 \cdot 10^{10}\,\mathrm{m}^2\mathrm{sr}; \qquad (8.2)$$

- Acquisition time $T = 100$ hours.

With these assumptions, 1000 events have been simulated. The trigger efficiency is a function of the energy, and is defined as $\epsilon_{trig}(E) = N_{trig}(E)/N_{sim}(E)$. Of the 1000 events, 94 passed the trigger selection, and are shown in Figure 8.11 in the R_p to $\log_{10} E$ plot. The energy range has been divided by 0.1 eV wide bins and the relative ϵ_{trig} per every bin has been calculate. The number of expected events N_{exp} is now obtained as:

$$N_{exp} = A \cdot f_{FOV} \cdot T \cdot \sum Flux^i(E) \cdot \epsilon_{trig}^i(E) \simeq 8 \qquad (8.3)$$

where the cosmic ray flux $Flux^i(E)$ in the range $10^{17} - 5 \cdot 10^{17}$ eV has been taken from IceTop measurements [87] and in the range $5 \cdot 10^{17} - 10^{19}$ eV has been taken from Auger measurements [88].

The first analysis resulted in an expected number of 14-15 events in the time corresponding to the actual data acquisition hours, and the second one gave 8 events. The four detected and the four candidate events are, in number, compatible with the expectations. In the simulations, five events resulted to be visible and on the active PMTs, but they do not have a counterpart in the data. This can be in part

understood imaging that at least some of the real events happened during a noisy GTU and they cannot be identified. However, also assuming the events visible in the simulations but not in the data, a number of 13 events would be reached. This value is within the expectation of the first analysis, so still reasonable, although probably too optimistic.

8.4 Summary and discussion

Thanks to the collaboration of the Telescope Array group, it has been possible to know how may and which cosmic ray air shower crossed EUSO-TA FOV, whether they have been detected by it or not. In 2015, 110 events crossed the EUSO-TA FOV, during the 123 hours of data acquisition, of which four have been detected and four are considered candidate events. Many showers crossed the EUSO-TA FOV but they have been not recognized in the data.

Simulations of these events classified them as visible or not visible in the simulations. They allowed to identify a detected event and four candidate events too. To the simulation result, background frames taken in the same packet of data (same day, almost same time) have been added. This choice comes from the fact that the background changed over the time, and in the same day, it may change over the time because of the stars or the Milky Way plane in the FOV. In some cases, although from the number of counts they should be visible, they hit non-working PMTs or noisy areas of the focal surface, so that could be the cause of the not detection. The detected and candidate events, the events visible in the simulations, the events not detected and not visible in the simulations lie in particular areas of the R_p versus $\log_{10} E$ plot. In particular, the detected and candidate events are below the imaginary line between $E \simeq 10^{17.7}$ eV, $Rp \simeq 2.5$ km, and $E \simeq 10^{18.7}$ eV, $R_p \simeq 10$ km.

Counting the counts corresponding to the events and showing them on the same R_p versus $\log_{10} E$ plot, events with total number of counts ≥ 200 lie on the same area of the detected and not detected events, and with the decrease of the counts, the areas of interest are those with events visible in the simulation but not in the data and finally those not visible in any way with total number of counts < 150. This means that the events, to be detected, should have at least 200 counts over background, with a rough estimation of about 30 counts per PMT.

A couple of estimations of the possible detected events have been performed. A first one has been performed before the activation of EUSO-TA, and gave a result of $14-15$ events in the time corresponding to the actual data acquisition hours and with a fully working PDM. But in this study, a threshold of 100 counts in one GTU have been considered, which might be too low, considering the results of the following analysis after the detector started to be operative. Another study made recently, gave a result of 8 events, considering the not working PMTs. The four detected and the four candidate events are, in number, compatible with the expectations. In the simulations, five events resulted to be visible and on the active PMTs, but they do not have a counterpart in the data. This can be in part understood imaging that at least some of the real events happened during a noisy GTU and they cannot be identified. However, also assuming the events visible in the simulations but not in the data, a number of 13 events would be reached. This value is within the expectation of the first analysis, so still reasonable, although probably too optimistic, al least for the current condition of the detector. Instead, considering the events visible in the simulations but on noisy or non-active PMTs, the number of events detectable would

be larger than any expectation. Probably while evaluating if an event is visible or not, in the simulation, the fact of knowing where to look for the track on the frame, makes the evaluation too easy, leading to a too optimistic evaluation.

Whether the non-active PMTs will be replaced and the periodic noise understood and possibly solved, the capability of the detector would certainly improve.

Chapter 9

SiPM sensors

In the last years semiconductor sensors for radiation detection have been developed and improved, and meanwhile they are attractive for scientific experiments, used in telescopes and in medical devices (PET-scanners) as well. Silicon Photomultipliers (SiPMs) offer the possibility to build large modular detector surfaces, since they are compact and light, they work with low power consumption, low voltage, and are not sensitive to magnetic fields [89, 90, 91]. These interesting properties include a very short response time (several hundreds of picoseconds), single photon detection capabilities, high photon detection efficiency, a high light damage resistance. Because of the semiconductor nature of this device, however, certain disadvantages are present, like a strong temperature dependence of dark counts, gain and the applied overvoltage as well as the presence of optical crosstalk and afterpulses.

SiPMs are considered for future cosmic ray space-missions, and the JEM-EUSO Collaboration, with particular contribution of KIT, already developed a first Silicon Elementary Cell Add-On (SiECA).

In this chapter, an overview of SiPMs in general will be given, and a comparison of the detector response considering SiPMs or MAPMTs as sensors for a EUSO-TA like detector will be discussed.

9.1   Working principle

Each channel of a SiPM is composed of an array of identical pixels or microcells, each one consisting of a Geiger-mode avalanche photodiode (G-APD) and a quenching resistor connected in series. The microcells are connected in parallel to a bias voltage V_{bias}. Indeed, SiPMs are also called multi-pixel photon counters (MPPCs). The SiPM pixel should not be confused with the MAPMT pixel: for an MAPMT every output channel gets the signal from one pixel; in a SiPM there can be several hundreds or even thousands of pixels per each output channel, with every pixel giving the same signal, when hit by a photon. The sum of the pixel responses gives the channel output. In the following, the term "microcell" or "G-APD" will be used, to not confuse between MAPMT and SiPM pixels.

The typical dimension of a SiPM sensor is between $1 \times 1\,\mathrm{mm}^2$ and $6 \times 6\,\mathrm{mm}^2$ and

the number of microcells per device ranges from several hundreds to several tens of thousands. The size of a microcell varies from $10 \times 10\,\mu\text{m}^2$ to $100 \times 100\,\mu\text{m}^2$. Spectral sensitivities range from UV to IR, peaking in the visible (400-500 nm). The required voltage varies between 20 V and 100 V, i. e. about 15 to 75 times lower than the one required by PMTs. In the following, a description of the G-APD working principle and then an overview of the SiPMs and SiPM arrays will be given. Most of the information is based on [92, 68].

9.1.1   Geiger-mode avalanche photodiodes

As mentioned, a SiPM channel consists of several hundreds of microcells, each one composed by a G-APD and a quenching resistor in series.

Figure 9.1 shows a schematic view of a G-APD together with the strength of the electric field along the G-APD length and the photon flux for shorter and longer wavelengths versus the depth of the structure. The bias voltage V_{bias} is in reverse
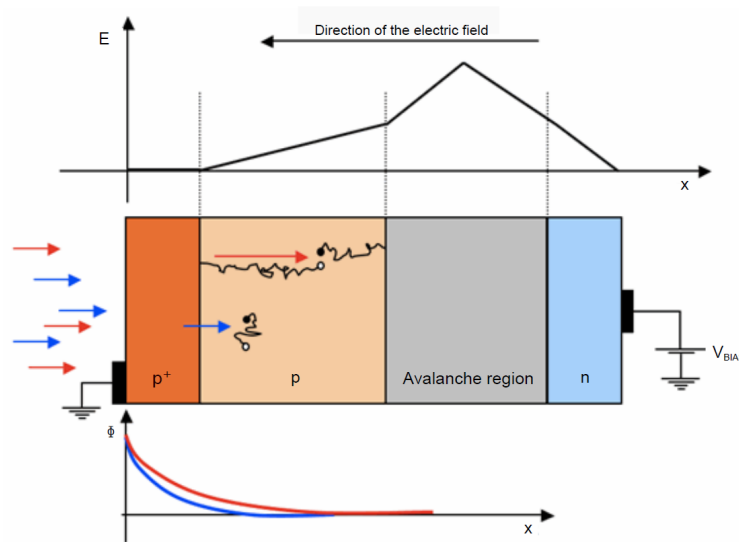
Figure 9.1: Sketch of the pn-junction of a G-APD. The upper diagram shows the strength of the electric field through the pn-junction, the scheme in the middle shows the layers of the pn-junction with a sketch of incident photons producing electron-hole pairs. The diagram below shows the photon flux depending on the depth of the pn-junction. Image taken from [92].

direction, resulting in the shown electric field directed from bottom to top of the device (right to left in figure). V_{bias} is also a few volts higher than the breakdown voltage V_{br} of the diode. The difference of these two voltages is called overvoltage $V_{over} = V_{bias} - V_{br}$ and is the main adjustable parameter controlling operation of the device, and defines the properties of an G-APD like gain, the photon-detection efficiency and the dark-count rate.

When a photon arrives onto a G-APD (left to right in figure), it can penetrate to different depths of the G-APD structure, depending on the wavelength of the photon and on the absorption coefficient of the material. When a photon penetrates into

the p$^+$-layer it can excite an electron into the conduction band if the photon energy is greater than the band gap of the layer. Since the photoelectron is not leaving the material, this process is called *internal photoelectric effect*. This can also be seen as the creation of a free electron-hole pair. The probability for the production of an electron-hole pair is given by the quantum efficiency QE_{SiPM}, defined as the ratio of the number of electron-hole pairs n_{e-h} generated by photons and the number of incident photons on the photosensitive area n_γ

$$QE_{SiPM} = \frac{n_{e-h}}{n_\gamma} \tag{9.1}$$

The probability for recombination in the p$^+$-layer is high, since the electric field is weak in this region. The recombination rate and the electron-hole pair lifetimes depend on the semiconductor material.

When a photon penetrates into the p-layer and produces an electron-hole pair, the pair is separated by the internal electric field. The hole is diffused into the p$^+$-layer and recombines. The electron is accelerated towards the pn-junction (grey area), through the remaining p-layer, where the probability for recombination is very low, since there are no free charge carriers (*depletion region*). When the energy of the accelerated electron becomes high enough, it can produce more electrons via ionization; secondary electrons are also accelerated by the electric field and can produce further electrons: in this way an electron avalanche starts. Due to the multiplication of the primary single electron in the *avalanche region* of the G-APD, an amplification of about a factor of 10^6 is reached. This amplification factor is the gain of the sensor.

Figure 9.2 shows the gain dependency regarding the bias voltage of a APD. For voltages below the breakdown voltage, the APD acts like a normal diode and the electric field in the avalanche region is too weak to accelerate electrons over the minimal energy threshold for impact ionization, and electrons are not multiplied. With increasing bias voltage the gain starts to rise linearly, with a stronger electric field and thus a positive gain. The energy threshold for impact ionization is reached, but the energy is not high enough to produce an ongoing avalanche. In the linear region the avalanche stops by itself without any quenching resistor. For voltages above the breakdown voltage, the gain increases very fast and the plot shows the Geiger-mode region. Here a strong electric field is present, leading to an ongoing avalanche. The required voltage depends on the sensor design and varies between 20 V and 100 V. The avalanche is stopped with a quenching resistor switched in series with the pn-junction which causes a voltage drop since the photoelectron current is flowing through the pn-junction. Since the voltage drop affects the electric field, the produced secondary electrons are no longer accelerated to energies large enough for further ionizations, the avalanche reaches its maximum, about 1 ns after the photon enters the G-APD, and then declines. After the maximum the photoelectron current drops and the voltage rises again to pre-avalanche levels. In this phase the G-APD is not sensitive to incident photons, this can take up to tens of nanoseconds.

The signal amplitude produced by the electron avalanche is a function of the over-
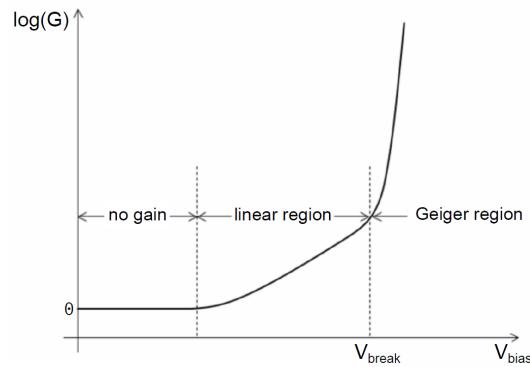
Figure 9.2: Sketch of the the working point of a G-APD showing the logarithm of the gain versus the reverse bias voltage. There are three operation regions: the photodiode region (no gain), the linear region, and the Geiger-region. Image taken from [92].

voltage V_{over} and the quenching resistor R_Q, proportional to V_{over}/R_Q. For every G-APD within a SiPM channel, the signal amplitude is the same. The signals generated by photons arriving at the same time on different G-APD, are superimposed onto each other and the total signal gives the output. On the other hand, if more photons arrive at the same time on the same G-APD, just one signal is given. In other words, the signal produced by a G-APD is of binary nature giving information about whether a photon was detected or not. Information about the number of photons entering a single G-APD and generating the electron avalanche is not available.

9.1.2   Silicon photomultiplier

Hundreds or thousands G-APDs make a basic SiPM. Figure 9.3 shows, from left to right, a cross section of three microcells, top view of the device on which light arrives, and an equivalent electrical circuit. The metal contacts, the quenching resistors (R_Q)
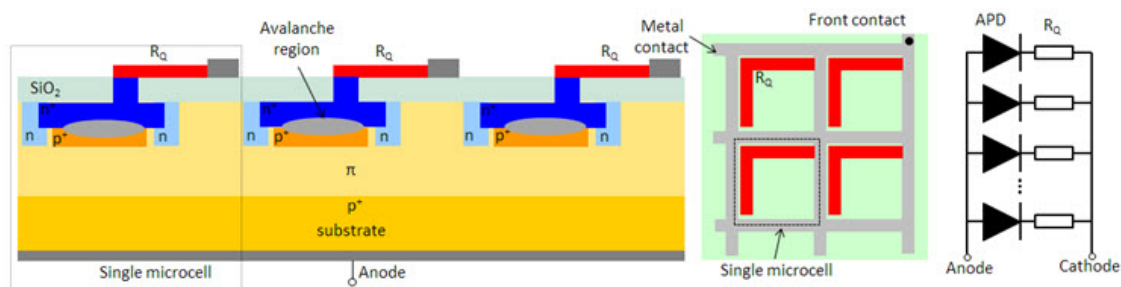
Figure 9.3: From left to right, cross section of three microcells, top view of the device on which light arrives, and an equivalent electrical circuit [93].

and the pn-junctions are clearly visible. The thickness of the whole structure is in the range of 310 μm. Photons have to pass an anti-reflection layer ($\sim$ 10 nm) and a silicon-oxide isolation layer ($\sim$ 150 nm), before passing the depletion region

(~ 1 μm). When the photon reaches the avalanche region at the boundary of the n^+-p^+-junction (a few μm), the electron avalanche can occur and generate a signal. The sum of the signals coming from all the G-APD in a SiPM channel gives its output signal. The metal contacts on top of the G-APDs are not transparent and therefore decrease the effective area. This is expressed via the fill factor F_g, which gives the ratio of the sensitive area and the geometrical area of a G-APD. The Photon Detection Efficiency (PDE) of a SiPM PDE_{SiPM} can be expressed via the quantum efficiency (Equation 9.1), multiplied by the fill factor F_g and the probability P_a to start an avalanche in the depletion region:

$$PDE_{SiPM} = QE_{SiPM} \cdot F_g \cdot P_a \qquad (9.2)$$

Noise sources

Due to their semi-conductive nature and the parallel distribution of many G-APDs in a small area, SiPM are highly noise afflicted. The three main noise sources are *dark noise*, *crosstalk* and *afterpulses*.

In general, due to their semi-conductive nature, the performance of G-APDs is dependent on the temperature of the junction. With temperature, several parameters like the breakdown voltage and the quench resistor change, mainly because of the temperature dependence of the band gap in semiconductors. Furthermore, temperature can generate noise. In a G-APD electrons can also be excited by thermal effects and generate an electron avalanche. The resulting signal is not distinguishable from a signal produced by a photon-excited electron. The resulting noise signal is called *dark noise*. As the name suggests, this noise is not correlated to any photons incident on the detector and therefore always present, as soon as an over voltage is applied. The dark current rate of a typical SiPM is in the MHz region and is one of the disadvantages compared to PMTs, which have a dark-count rate in the kHz range.

A second source of noise is given by *afterpulses*. They are secondary signal peaks occurring after the main signal, caused by trapped electrons in defects of the silicon in the depletion zone and released with some delay. Their absolute height is normally around the 1 photoelectron level. Since the probability of afterpulses rises with the number of electrons in the avalanche, the afterpulse probability increases with an increase in over-voltage and with the pixel size.

During an electron avalanche in a G-APD, photons can be produced by electrons passing the pn-junction. These photons can enter and trigger a neighboured G-APD resulting in a two photoelectrons signal induced by only one incident photon. This source of noise is called *crosstalk*. The crosstalk probability depends on the distance to neighbouring G-APDs: the longer it is, the lower is the crosstalk probability. Since a crosstalk event happens at the same time at which the original photon induced signal is produced, it is not distinguishable from that, and each signal with more than one photoelectron could contain a fake signal produced by crosstalk.

9.1.3   Silicon photomultiplier arrays

With the goal of building a large focal surface out of SiPMs, an important characteristic of the available SiPM is the photo sensitive area. The best choice for large sensitive areas is given by SiPM arrays, with the TSV (Through Silicon Via) technology. In single SiPMs the cathode is wired on the sides of the SiPM active surface and building an array of single SiPMs the dead space i.e. inactive surface, would be large. In the new SiPM arrays the cathode is etched through the silicon wafer in the middle of the SiPM (TSV), building an electrical interconnection from the surface to the back of the SiPM device. This allows to reduce the gap between two SiPM channels from 3 mm to 0.2 mm. Figure 9.4 shows the front and the back side of a SiPM array. On the front, the cathodes are visible as small white spots in the middle of each SiPM channel. On the back, the SiPM array is equipped with connectors. In the following, two different 64-channel SiPM arrays produced by Hamamatsu are considered: a former model *S12642-0808PA-50* and the newer *S13361-3050AS-08*. Further information about the SiPM arrays can be found in [94] and [95]. Beside a predicted better performance of the new series SiPM array, an important difference between the two arrays is the resin of the SiPM surface. The former series SiPM arrays have epoxy resin, the newer series ones have silicone resin. The different cover brings a different sensitivity of the SiPM to UV light with wavelengths lower then 400 nm, that causes a loss of photons in case of epoxy resin.

Figure 9.4: Pictures of the front and the back side of a 64-channel Hamamatsu SiPM array *S13361-3050NE*. Image taken from [92].

The newer model of SiPM array has been used to build the Silicon Elementary Cell Add-On (SiECA) at KIT. SiECA is an add-on camera to the JEM-EUSO pathfinder experiment EUSO-SPB, a scaled-down version of the JEM-EUSO detector that will be tested during a long duration super pressure balloon flight. For more details on SiECA, refer to [92].

The size of a SiPM array allows, with some adjustments, to substitute an MAPMT with a SiPM array in the focal surface: the side of a MAPMT is 2.62 cm (with active area side 2.3 cm) and that of a SiPM array 2.58 cm. The number of 8×8 channels per sensor would remain the same in both the cases, with pixel size of MAPMTs of 2.88 mm and a channel of SiPMs array of 3 mm.

9.2 SiPMs-MAPMTs comparison with simulations

As the photon absorption of radiation sensors is wavelength dependent, it follows that the resulting photo-detection efficiency is also wavelength dependent. Figure 9.5 shows the characteristic fluorescence spectrum of nitrogen molecules extended to the wavelength range 295-430 nm, with the main fluorescence line at 337.1 nm. Superimposed to the fluorescence spectrum are the PDE for a MAPMT prototype from 2009 (*R11265-00-M64*), for SiPM array with epoxy resin cover (*S12642-0808PA-50*, called from now on SiPM (epoxy)) and for SiPM array with silicone cover (*S13361-3050AS-08*, called from now on SiPM (silicone)), restricted to the same range of wavelengths of the fluorescence spectrum.
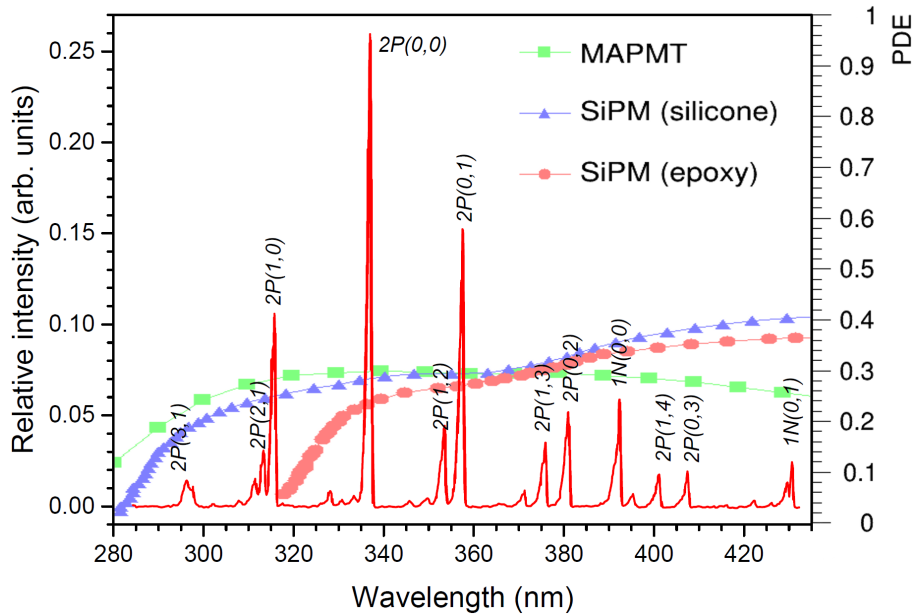
Figure 9.5: Air fluorescence spectrum of nitrogen relaxation in the UV band from 280 nm to 435 nm at 800 hPa (about 2 km) measured by the AIRFLY collaboration. The area is scaled to unity. This shows that 25% of the spectrum intensity is due to the main line at 337.1 nm. Plot taken from [32]. Superimposed, the PDE of MAPMTs [96] and PDEs of both the SiPM arrays, with epoxy and silicone covers [97].

The PDE for MAPMTs PDE_{MAPMT} is defined as the quantum efficiency QE_{MAPMT} multiplied by the collection efficiency CE. QE_{MAPMT} is the number of photoelectrons emitted by the photocathode n_{pe} divided by the number of incident photons n_γ, CE is the probability that photoelectrons will land on the effective area of the first dynode inside the MAPMT, assumed to be 80%. Data for the QE_{MAPMT} versus wavelength was provided by Hamamatsu to the JEM-EUSO collaboration and then provided to the research group by Naoto Sakaki [96] via the ESAF simulation framework. The PDE for SiPMs PDE_{SiPM} is the quantum efficiency QE_{SiPM}, multiplied by the fill factor F_g, which takes into account dead areas of the surface, and the probability P_a to start an avalanche in the depletion region. QE_{SiPM} is the

number of electron-hole pairs n_{e-h} generated by photons divided by the number of incident photons on the photosensitive area n_γ. PDEs of both SiPMs were taken from graphs available on the datasheets of the products provided by Hamamatsu, tested at a temperature of 25℃ [97].

$$QE_{MAPMT} = \frac{n_{pe}}{n_\gamma}, \qquad QE_{SiPM} = \frac{n_{e-h}}{n_\gamma} \qquad (9.3)$$

$$PDE_{MAPMT} = QE_{MAPMT} \cdot CE, \qquad PDE_{SiPM} = QE_{SiPM} \cdot F_g \cdot P_a \qquad (9.4)$$

It is evident that the SiPM (epoxy) is not sensitive to the first three lines of the fluorescence spectrum, and is even less sensitive than MAPMTs and SiPM (silicone) to the main line of the fluorescence spectrum at 337.1 nm.

Two simplified studies have been performed, using cosmic ray air showers with different geometry, to see the effects of changing sensors on the focal surface of EUSO-TA. In a simplified way, the focal surface has been considered as an array of MAPMTs, SiPMs (epoxy) or SiPMs (silicone). Just the PDE has been changed. The design of the EUSO-TA focal surface remains the same, as made of 6×6 MAPMTs. This means that also when simulating SiPM arrays, the side of each sensor is 2.6 cm instead of 2.58 cm, with 8×8 pixels of 2.88 mm side instead of 3 mm. Also the electronics considered is the same, with 30 ns dead time of the device after a photon hits a pixel and 200 ns dead times at the beginning of one GTU frame (see Sections 6.2 and 3.4).

Vertical shower

A vertical cosmic ray air shower with energy 10^{18} eV and core position on ground at 2 km from EUSO-TA, set with an elevation angle of 15°, has been simulated. Because of the short distance of the shower, the cosmic ray event lasts one GTU. The results will be discussed in the following.

Figure 9.6 shows the wavelength distribution of the photons arriving at the focal surface $Photons_{FS}$, that is independent of the kind of sensor considered (a), of photons generating photoelectrons PEs_{PDE} using MAPMTs (b), SiPMs (epoxy) (c) and SiPMs (silicone) (d). The plots clearly show the lines of the fluorescence spectrum, seen in Figure 9.5. SiPMs (epoxy) are the least efficient, as expected. Not just the main line at 337.1 nm is suppressed, but the overall integral over all the wavelengths is lower than in the other two cases. MAPMTs look still competitive with SiPMs (silicone), although the first ones look slightly more efficient at small wavelengths and the latter ones more efficient at the larger wavelengths.

As done for the events detected by EUSO-TA, with the simulations it is possible to discriminate between the different kinds of photons arriving at the aperture of the detector, in front of the first lens. Figure 9.7 shows the photons of different origin as a function of the GTU number, or elapsed time. As mentioned, being a close shower, the signal lasts just one GTU. Most of the contribution to the signal is due

to fluorescence light (85.8%). Because of the vertical orientation of the shower, just a tiny percentage of photons come directly from the Cherenkov cone (1%), while the rest is scattered Cherenkov light (13.2%). Also in this case, the plot is independent of the sensor used, but the total number of photons are of interest for the next step of the analysis.

With the total number of photons arriving at the aperture of EUSO-TA, estimations of the optics transmission efficiency (independent of the sensor used) and, most important, of the overall efficiency of the detector are possible. Figure 9.8 shows the number of photons at the aperture $Photons_{aperture}$ and at the focal surface $Photons_{FS}$, the number of photoelectrons considering just the PDE PEs_{PDE} and considering also the dead times PEs_{signal}. The optics transmission efficiency ($PEs_{PDE}/Photons_{aperture}$) and the overall efficiency ($PEs_{signal}/Photons_{aperture}$) are reported too. SiPMs (silicone) are the most efficient, although just about 0.3% more than MAPMTs.

The same result is given also in Figure 9.9. The average efficiency of the detector, given by $PEs_{signal}/Photons_{FS}$ is about 26.9% fot MAPMTs, 24.8% for SiPMs (epoxy) and 28.5% for SiPMs (silicone). So, the efficiency of the detector, not considering the optics, is for SiPMs (silicone) 6% higher than for MAPMTs and 15% higher than for SiPMs (epoxy).

(a) $Photons_{FS}$

(b) PEs_{PDE} - MAPMTs

(c) PEs_{PDE} - SiPMs (epoxy)

(d) PEs_{PDE} - SiPMs (silicone)
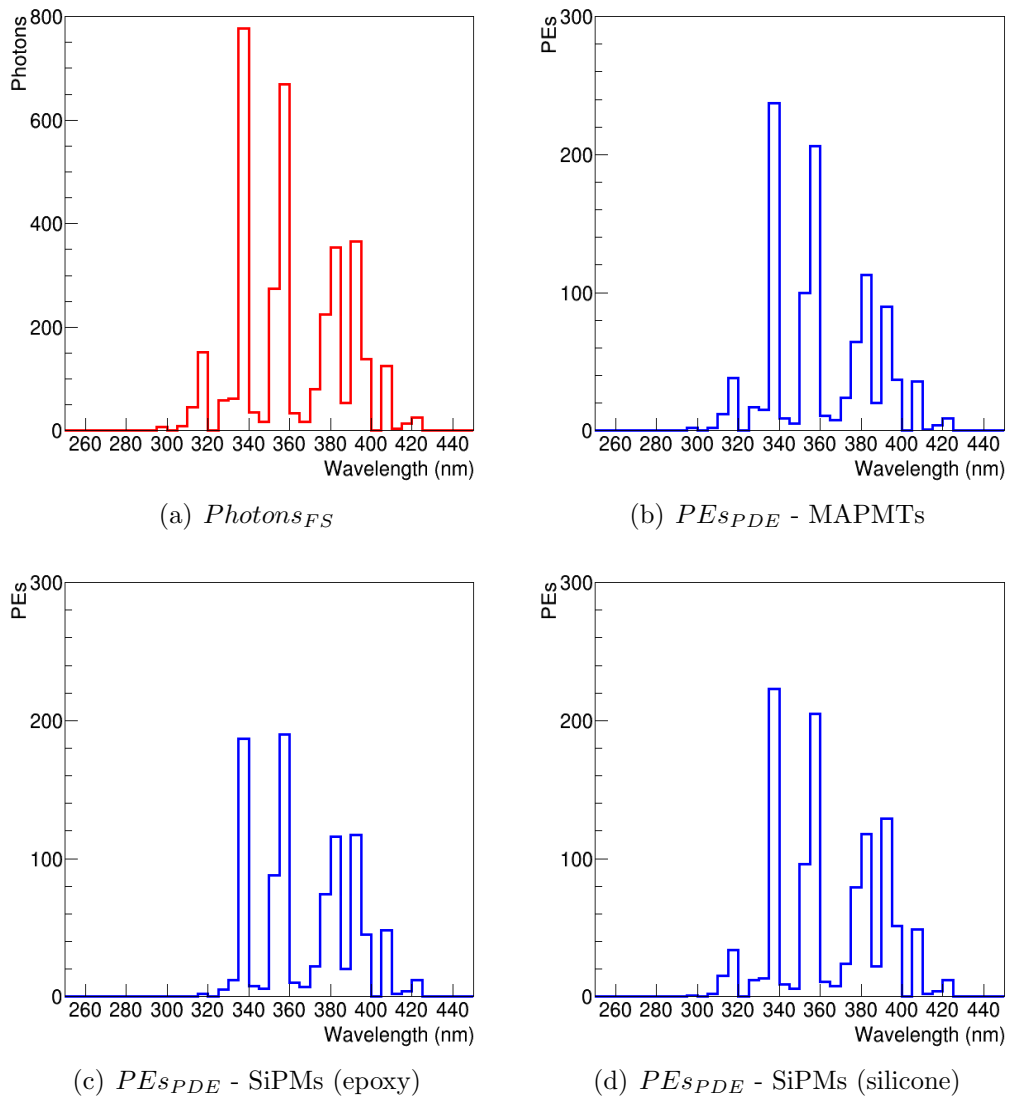
Figure 9.6: Vertical shower. Wavelength distribution of the photons arriving at the focal surface $Photons_{FS}$, independent of the kind of sensor considered (a), of photons generating photoelectrons PEs_{PDE} using MAPMTs (b), SiPMs (epoxy) (c) and SiPMs (silicone) (d).
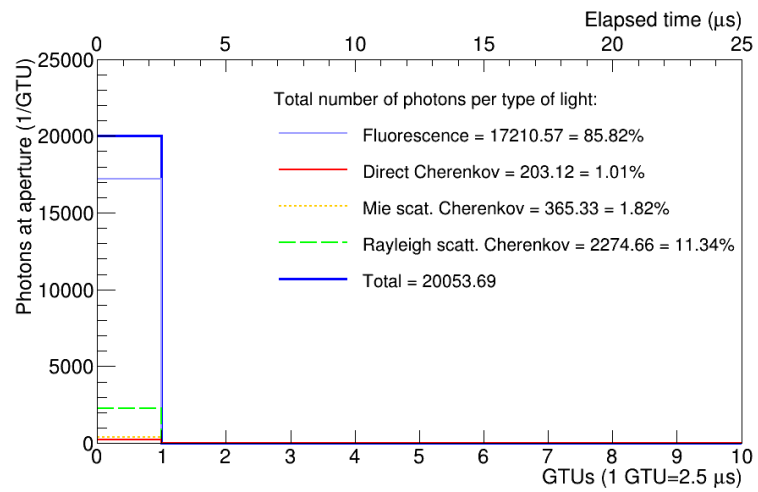
Figure 9.7: Vertical shower. Number of photons as a function of the GTU number. The simulated event is close to the telescope and therefore, lasts just one GTU. The contribution of the different kinds of light is reported in percentage.
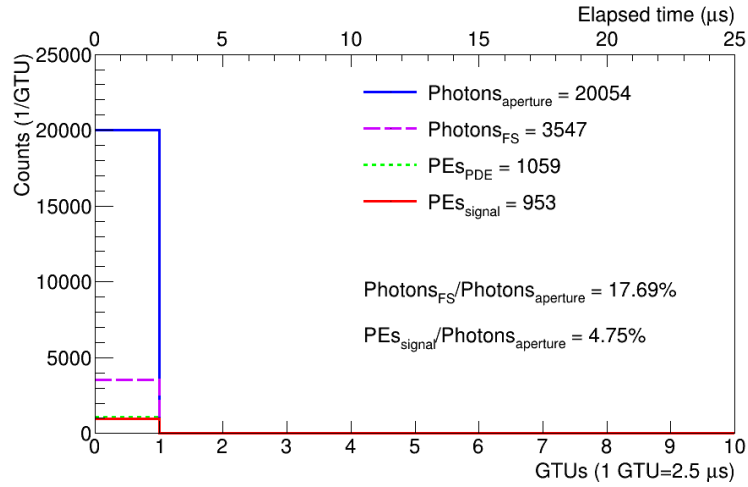
(a) MAPMTs
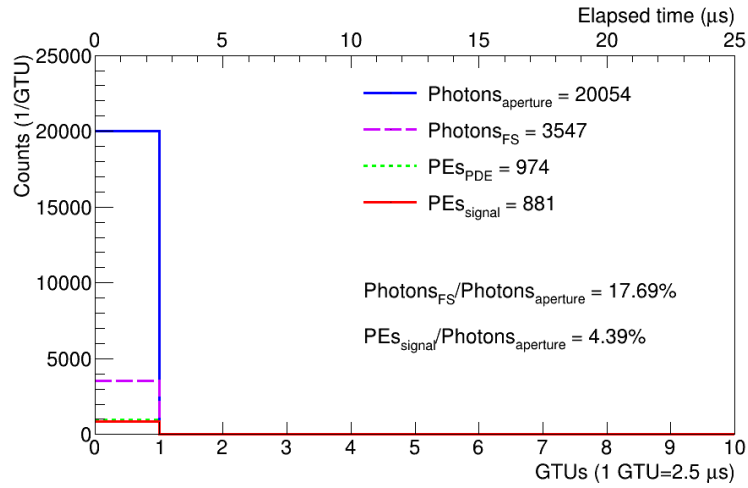
(b) SiPMs (epoxy)
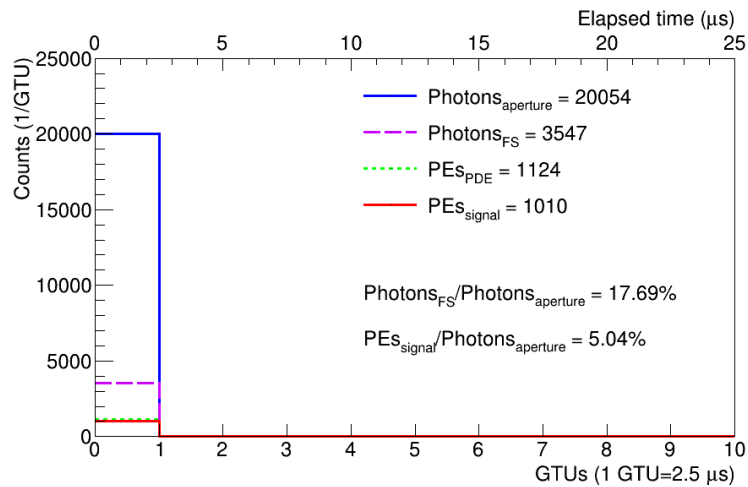
(c) SiPMs (silicone)

Figure 9.8: Vertical shower. Photons at the aperture $Photons_{aperture}$, photons at the focal surface $Photons_{FS}$, photoelectrons considering just the photo-detection efficiency PEs_{PDE} and considering also the dead times PEs_{signal}, as a function of the time. The optics transmission efficiency and the overall efficiency of the detector are reported too. Plots refer to MAPMTs (a), SiPMs (epoxy) (b) and SiPMs (silicone) (c).

(a) $Photons_{FS}$

(b) PEs_{PDE} - MAPMTs.

(c) PEs_{PDE} - SiPMs (epoxy)

(d) PEs_{PDE} - SiPMs (silicone)

(e) PEs_{signal} - MAPMTs

(f) PEs_{signal} - SiPMs (epoxy)

(g) PEs_{signal} - SiPMs (silicone)

(h) MAPMTs

(i) SiPMs (epoxy)

(j) SiPMs (silicone)
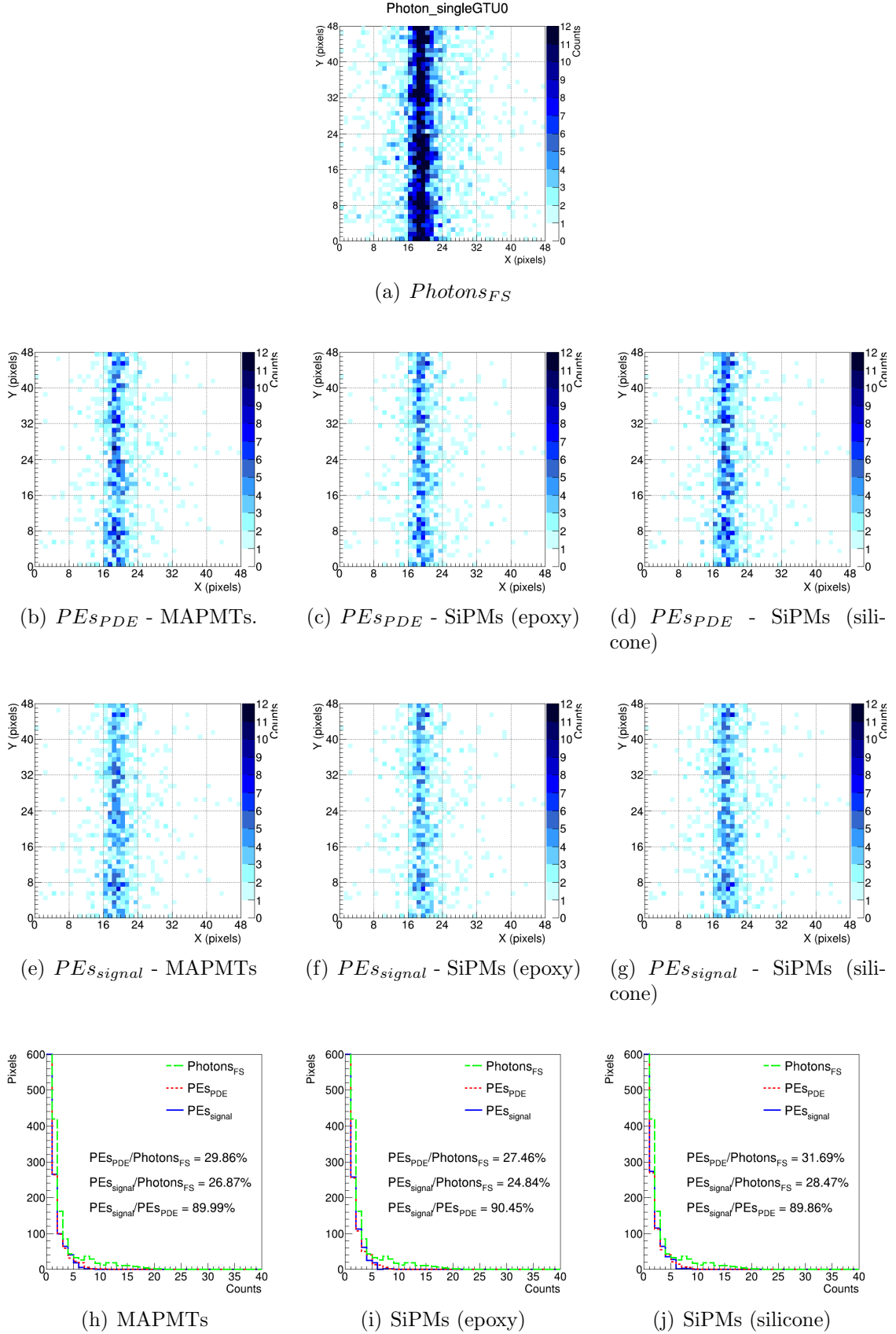
Figure 9.9: Vertical shower. Tracks of photons at the focal surface $Photons_{FS}$, photoelectrons considering just the photo-detection efficiency PEs_{PDE} and considering also the dead times PEs_{signal}, for the different kind of sensors: MAPMTs, SiPMs (epoxy) and SiPMs (silicone) (a-g). The count distributions for the different quantities are visible in (h-j), where their ratios are also reported.

Shower towards the telescope

A cosmic ray air shower with energy 10^{18} eV, zenith angle 40°, azimuth angle −53° (from North), core position on ground at 4 km from EUSO-TA, set with an elevation angle of 15°, has been simulated. The geometry of the shower makes it going towards the telescope. The cosmic ray event lasts one GTU. The results will be discussed, following the same procedure adopted for the vertical shower.

Figure 9.10 shows the wavelength distribution of the photons arriving at the focal surface $Photons_{FS}$ (a), of photons generating photoelectrons PEs_{PDE} using MAPMTs (b), SiPMs (epoxy) (c) and SiPMs (silicone) (d). Also in this case, in the comparison between MAPMTs and SiPMs (silicone), the firsts look slightly more efficient at low wavelengths and the latter more efficient at high wavelengths, while both detect more photons than the SiPMs (epoxy).

Figure 9.11 shows the photons of different origin as a function of the GTU number, or elapsed time. Most of the contribution to the signal is due to fluorescence light, but less than for the vertical shower (54%). Indeed, because of the orientation of the shower, a relatively high percentage of photons come directly from the Cherenkov cone (7.6%), as well as the scattered Cherenkov light (38.3%). Because of the longer distance from the telescope, the absolute number of photons arriving to the telescope is lower but, concerning this analysis, the interest is in the percentage of the different quantities.

Estimations of the optics transmission efficiency and of the overall efficiency of the detector have been done. Figure 9.12 shows the number of photons at the aperture $Photons_{aperture}$ and at the focal surface $Photons_{FS}$, the number of photoelectrons considering just the PDE PEs_{PDE} and of those considering also the dead times PEs_{signal}. The optics transmission efficiency ($Photons_{FS}/Photons_{aperture}$) and the overall efficiency ($PEs_{signal}/Photons_{aperture}$) are reported too. SiPMs (silicone) are the most efficient, although just about 0.13% more than MAPMTs.

Figure 9.13 shows in (a) the event track of $Photons_{FS}$, in (b, e) the event track using MAPMTs as PEs_{PDE} and PEs_{signal} respectively. The same is done for frames which are related to SiPM (epoxy) and SiPMs (silicone) (c, f) and (d, g) respectively. The last row of plots (h, i, j) shows the counts distributions for the different sensors and the rates between the different quantities. The average efficiency of the detector, given by $PEs_{signal}/Photons_{FS}$ is about 27.3% for MAPMTs, 25% for SiPMs (epoxy) and 28.2% for SiPMs (silicone). So, it is for SiPMs (silicone) 0.9% higher than for MAPMTs and 3.2% higher than for SiPMs (epoxy).

The difference in the photo-detection efficiency per each kind of sensors slightly varies changing the geometry of the shower. It results to be about 0.5% higher for the shower going towards the detector respect to the vertical one. But involved are also the total number of photons arriving at the telescope and the distance, which might introduce fluctuations. Therefore, from this first test, it can be concluded that the different amount of Cherenkov light, which is the main difference in the two showers, does not influence significantly the detector performances.

(a) $Photons_{FS}$

(b) PEs_{PDE} - MAPMTs

(c) PEs_{PDE} - SiPMs (epoxy)

(d) PEs_{PDE} - SiPMs (silicone)
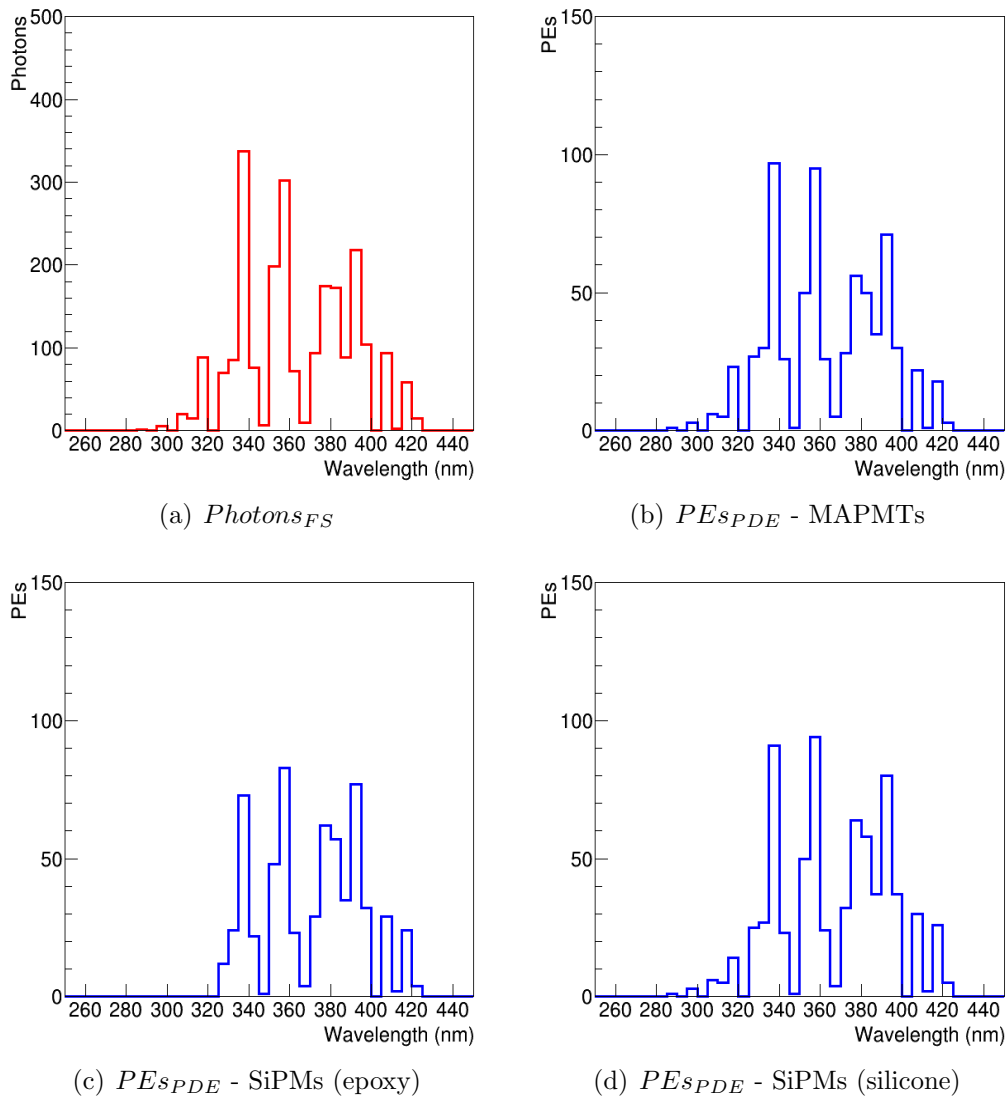
Figure 9.10: Wavelength distribution of the photons arriving at the focal surface $Photons_{FS}$, independent of the kind of sensor considered (a), of photons generating photoelectrons PEs_{PDE} using MAPMTs (b), SiPMs (epoxy) (c) and SiPMs (silicone) (d).
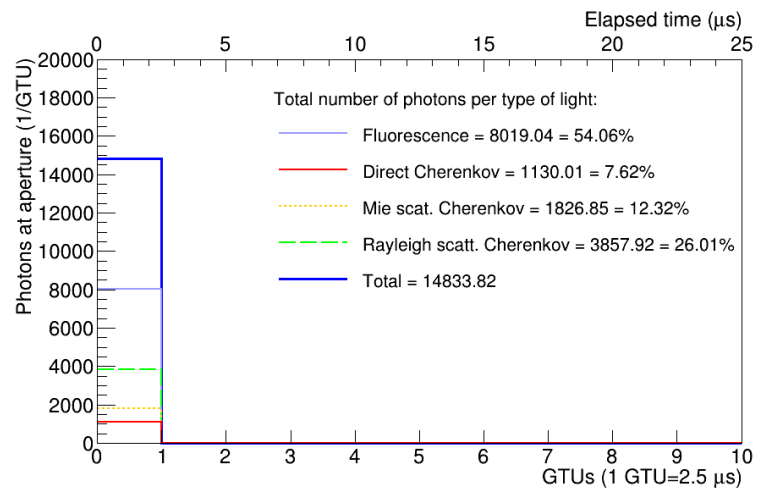
Figure 9.11: Shower towards the telescope. Number of photons as a function of the GTU number. The simulated event is close and for this, lasts just one GTU. The contribution of the different kinds of light is reported in percentage.
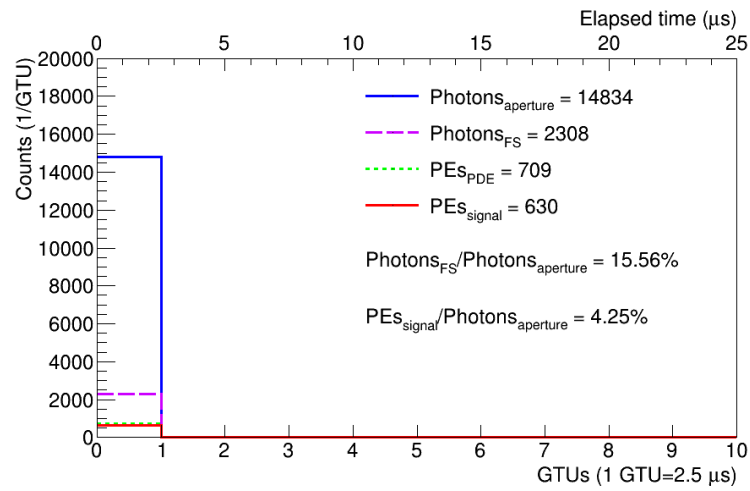
(a) MAPMTs
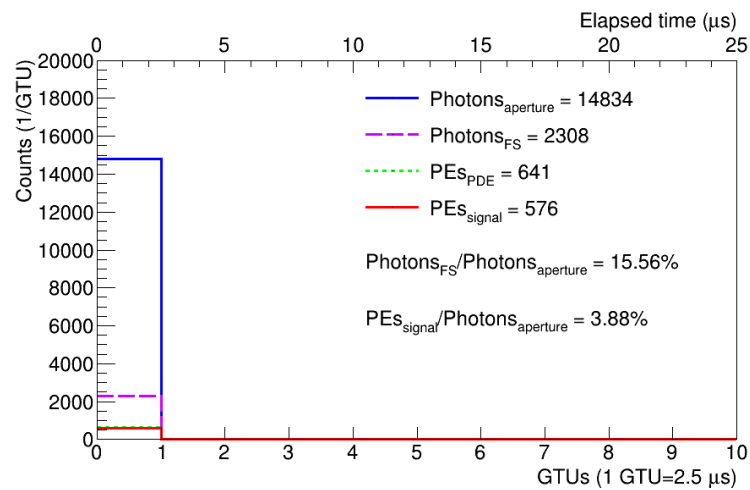
(b) SiPMs (epoxy)
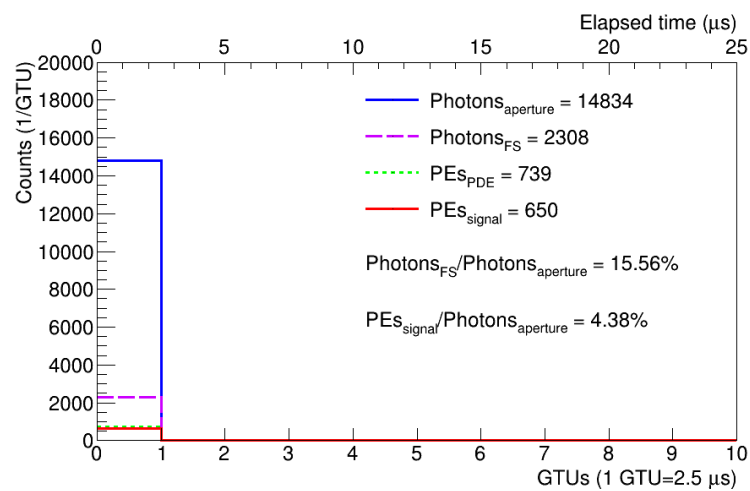
(c) SiPMs (silicone)

Figure 9.12: Shower towards the telescope. Photons at the aperture $Photons_{aperture}$, photons at the focal surface $Photons_{FS}$, photoelectrons considering just the photo-detection efficiency PEs_{PDE} and considering also the dead times PEs_{signal}, as a function of the time. The optics transmission efficiency and the overall efficiency of the detector are reported too. Plots refer to MAPMTs (a), SiPMs (epoxy) (b) and SiPMs (silicone) (c).

(a) $Photons_{FS}$

(b) PEs_{PDE} - MAPMTs.

(c) PEs_{PDE} - SiPMs (epoxy)

(d) PEs_{PDE} - SiPMs (silicone)

(e) PEs_{signal} - MAPMTs

(f) PEs_{signal} - SiPMs (epoxy)

(g) PEs_{signal} - SiPMs (silicone)

(h) MAPMTs

(i) SiPMs (epoxy)

(j) SiPMs (silicone)
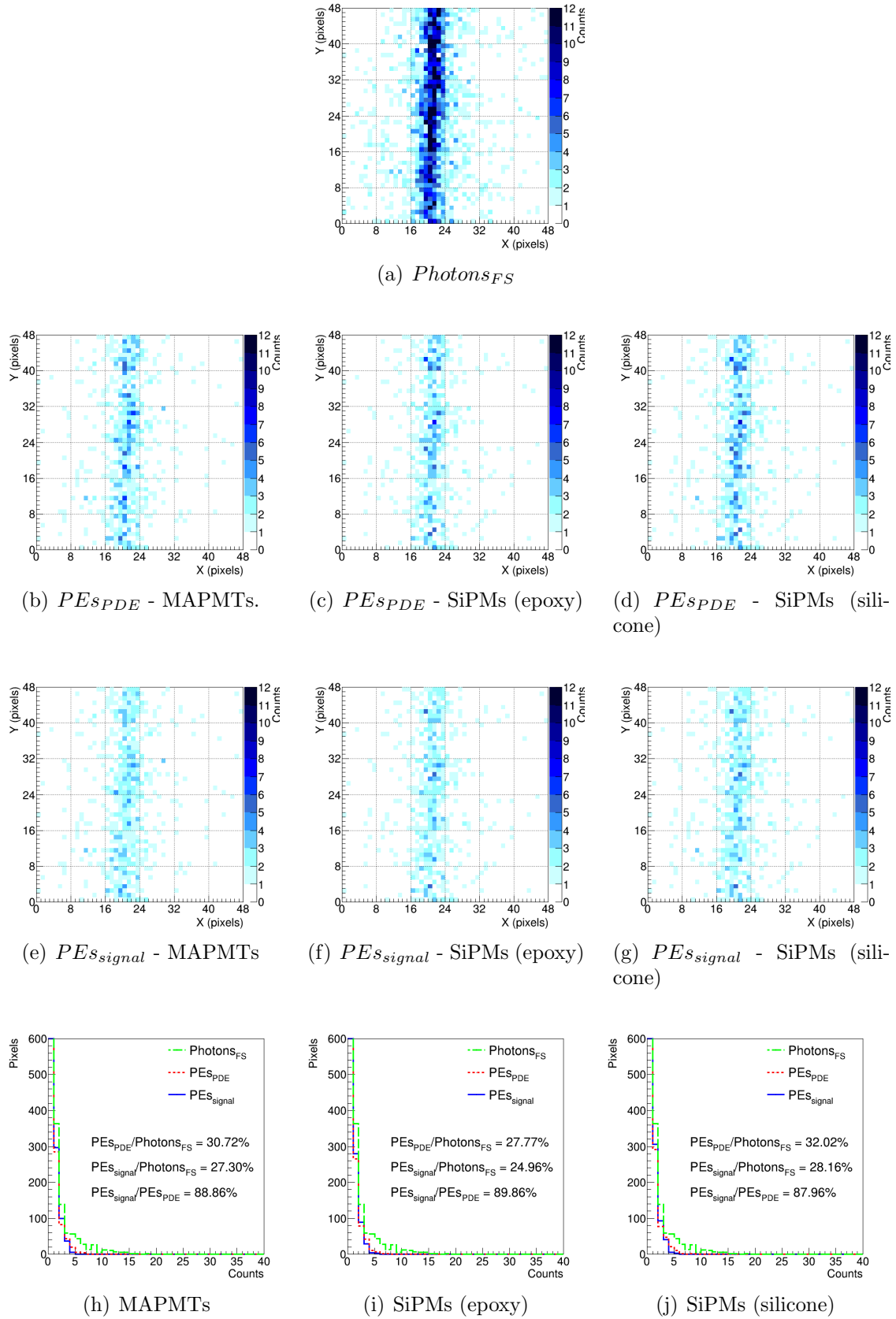
Figure 9.13: Shower towards the telescope. Tracks of photons at the focal surface $Photons_{FS}$, photoelectrons considering just the photo-detection efficiency PEs_{PDE} and considering also the dead times PEs_{signal}, for the different kinds of sensors: MAPMTs, SiPMs (epoxy) and SiPMs (silicone) (a-g). The count distributions for the different quantities are visible in (h-j), where their ratios are also reported.

9.3 Summary and discussion

A test of the detector efficiency using different kinds of photo sensors has been done. The test consists in simulating two cosmic ray air shower events applying, for the detector response, the PDE of MAPMTs (by default in the simulation framework), of SiPM arrays covered by epoxy resin, and of SiPM arrays with cover of silicone. The epoxy resin reduces the efficiency of the sensor at the lower wavelengths of the fluorescence spectrum of nitrogen. The two cosmic ray air shower differ for their geometry, since one is vertical and one oriented towards the telescope, leading to a higher percentage of Cherenkov light arriving to the telescope. As expected already from the comparison of the PDE curves as a function of the photon wavelengths (Figure 9.5), the SiPM arrays with silicone cover revealed to be more efficient than SiPM arrays with epoxy resin and MAPMTs, currently used for the EUSO detectors focal surface. Moreover, non significant effects of the Cherenkov light have been noticed, concerning the detector response.

However, the UV-background has not been considered in the analysis, since it was not available for SiPMs and it is known that SiPM are highly noise afflicted. For these reasons the signal to noise ratio has not been evaluated.

Because of the similar size of MAPMTs and SiPM arrays, with a higher filling factor for SiPMs, which allows to collect more light and increase the efficiency, focal surfaces made of silicon sensors are considered for a new generation of EUSO detectors. A first prototype of 2×2 SiPM arrays, SiECA, has been developed, and is going to be tested in the EUSO-SPB mission.

In the test presented, the electronics of the current EUSO-TA detector has been considered. However, new read out boards have been already created within the JEM-EUSO collaboration, and are installed on the newer detectors, i.e. EUSO-SPB and Mini-EUSO, which cause shorter dead times. This will improve already the performances of detectors with focal surface made of MAPMTs, and would make those with SiPM arrays even better.

Conclusion

The EUSO-TA detector is a down-scaled pathfinder experiment for JEM-EUSO, located at the Telescope Array (TA) site in Utah, USA. Its main goal is to test the observation principle and the detector design of JEM-EUSO on ground.
The work done for this thesis is centered on the analysis of the data collected by EUSO-TA and on simulation studies to evaluate the detector capabilities.

Several topics regarding the analysis of the data collected in 2015 have been studied. Because of the high spatial resolution of EUSO-TA with respect to the one of TA and other cosmic ray fluorescence detectors, it has been possible to evaluate the width of the tracks of the detected EAS projected on the focal surface, which gave an estimation of the shower lateral distributions. It resulted to be between 0.6° and 1°, depending on the energy and the distance of the EAS from the detector.
A study on the background has been done to evaluate if the presence of a cosmic ray event signal influences the intensity of a whole data frame in an evident manner. Some areas of the focal surface present parasitic noise, which increases the fluctuation of the background. The result was that, in the case of close EAS, for which the event is visible in just one frame, its contribution to the whole frame intensity is significant. For distant EAS, their tracks are split on more frames, and in this case the contribution of the cosmic ray event is of the same magnitude of the background fluctuations. Furthermore, the background fluctuations increased in intensity and in frequency with time, of up to 70% with respect to the first data acquisition campaign. The telescope is also sensitive to the diffuse light coming from the Galactic plane in the FOV, increasing the background by about 20%.

Most of the work of this thesis was related to analysis of events recorded with EUSO-TA through the simulation performed with the Offline analysis and simulation framework. Offline was initially developed for the Pierre Auger Observatory and then adapted for JEM-EUSO and its pathfinders. In the context of this thesis, the major contribution to the improvement of the software was to implement the detector response, including the Multi-Anode Photomultiplier Tubes (MAPMTs) efficiency and the dead times. In particular, it has been evaluated that the dead time due to the insensitivity of one pixel after being hit by a photon (pile-up effect), is more important for close and energetic showers (for which the photon flux is high), giving a loss of photons of up to 30%.
With the improvement of the simulation software, it has been possible to simulate

the four detected events and the results are in good agreement with the data, from a visual and quantitative point of view. Through the simulations, it has been possible to retrieve the origin of the photons arriving to the telescope, i.e. fluorescence, direct or scattered Cherenkov light. As expected, the light composition depends on the geometry of the shower. Most of the light was from fluorescence emission, between 65% and 80%, and direct Cherenkov light was more intense for EAS going towards the telescope.

Knowing the number of photons at the different steps of the simulation, i.e. at the aperture of EUSO-TA (in front of the front lens), at the focal surface, the photoelectrons just considering the photo-detection efficiency and the photoelectrons with the dead times applied (comparable with the data), the different ratios have been calculated. The transmission efficiency of the optical system was between 15% and 17%, while the overall efficiency of the telescope was between 4% and 5%. Unfortunately, no direct measurements of these efficiencies have been made, so the result of the simulations cannot be compared with measured values.

A fit algorithm has been developed to evaluate the track inclination and compare it for measured and for simulated events: a difference up to 4° has been found. This is possibly due to the uncertainty on the parameters of the EAS reconstructed by TA in monocular mode (using just the TA fluorescence detectors at Black Rock Mesa): the geometrical resolution of the opening angle is 7.4°, which may reconstruct a shower at a different angle with respect to the telescope axis.

The simulation of the events which crossed EUSO-TA following the reconstruction provided by TA but have not been detected, allowed the identification of four so called "candidate events" in the data, which are faint and in some cases with an irregular track, for which further analysis would be difficult.
This study allowed also to determine constraints of the detection capability of EUSO-TA. In the plot with the distance of the EAS axis to the detector R_p versus the logarithm of the primary cosmic ray reconstructed energy $\log_{10} E$, the detected and the candidate events lie in a particular area, below the line between $E \simeq 10^{17.7}$ eV, $R_p \simeq 2.5$ km, and $E \simeq 10^{18.7}$ eV, $R_p \simeq 10$ km. Above this line, lie first the events visible in the simulations but not found in the data, then the events non visible in the simulations and non detected. It has also been found that the detected and the candidate events have total number of counts higher than 200, or about 30 counts per PMT. Indeed, at least two counts over background have to be related to the event track, in order to notice it.

Finally, since Silicon PhotoMultipliers (SiPMs) have some advantages with respect to MAPMTs, which make them good candidates as radiation sensors in space (they are compact and light, they work with low power consumption, low voltage, and are not sensitive to magnetic fields), a test changing the photon detection efficiency of the MAPMTs with that of two models of SiPMs array has been performed. It revealed that the newest model of SiPMs will be indeed more efficient of than the MAPMTs, in the detection of fluorescence light. However, the UV-background has not been considered in the analysis, so the signal to noise ratio has not been evaluated.

The analysis of data and simulations for EUSO-TA are performed by a subgroup of the JEM-EUSO Collaboration, and the lack of person power due to other priorities (development of EUSO-SPB and Mini-EUSO) allowed to perform just a few data acquisition campaigns (five in 2015 and one in 2016). However, the detector is able to detect EAS, lasers, and stars. This thesis gives a contribution in understanding the detector capabilities, the limits and the issues concerning the identification of the events.

The results can be improved with the foreseen acquisition campaigns and the improvement of the focal surface conditions (replacement of the non-working PMTs, understanding and possibly solving the parasitic noise), which would lead to higher statistics of detected events.

Appendix A

ETOS software

ETOS (EUSO TO Screen) is the main quick-view and quick-analysis software developed by L. W. Piotrowski used for EUSO-TA data [98]. It operates on the ROOT files generated with the ETOT (EUSO TO Tree) software from the raw CPU data. Therefore it can be used with any other EUSO experiment that produces data in the same format, like EUSO-Balloon. ETOS is under development and different features are modified or added following the needs that might be highlighted while using the software itself and while increasing the experience with the data acquisition.

In Figure A.1 the graphic user interface of ETOS is shown. For each single GTU the pixel counts of the PDM are clearly visible on a 2D ROOT histogram that can be modified as usual for this kind of objects. It is possible to navigate the GTUs by simply pressing the backwards or forwards arrows. For CR events or laser shots, the single GTU visualization mode is the best option, that is set by default. One may also use the average of a defined number of GTUs. This might be helpful while analyzing slow objects like stars or meteorites. In a similar way as mentioned for the single GTUs mode, it is possible to navigate also through the average frames of GTUs. In the following, the most interesting features of ETOS are shortly described.

On the top right hand side of the ETOS window it is possible to select a mask to cover pixels not working properly. Masked pixels will not be used in further analysis. If requested, the pixel count values are corrected applying a dead time, with assumption of a 30 ns pixel dead time after one pixel is hit by a photon and 200 ns at the beginning of the GTU due to the analogue to digital conversion process. In Section 6.2.2 the dead times are explained more in detail. The options available to modify the pixel count values dividing o multiplying them by a value specified in an array are in principle working, but since an absolute calibration of the detector as well as its efficiency have not been evaluated yet, they are not used.

Stars are often detected by EUSO-TA. For this purpose, in ETOS it is possible to draw markers in correspondence of star position taken from the Hipparcos star catalogue. To retrieve the star position on the PDM, some information have to be set like the FOV angle, the orientation of EUSO-TA and its longitude, latitude and altitude.
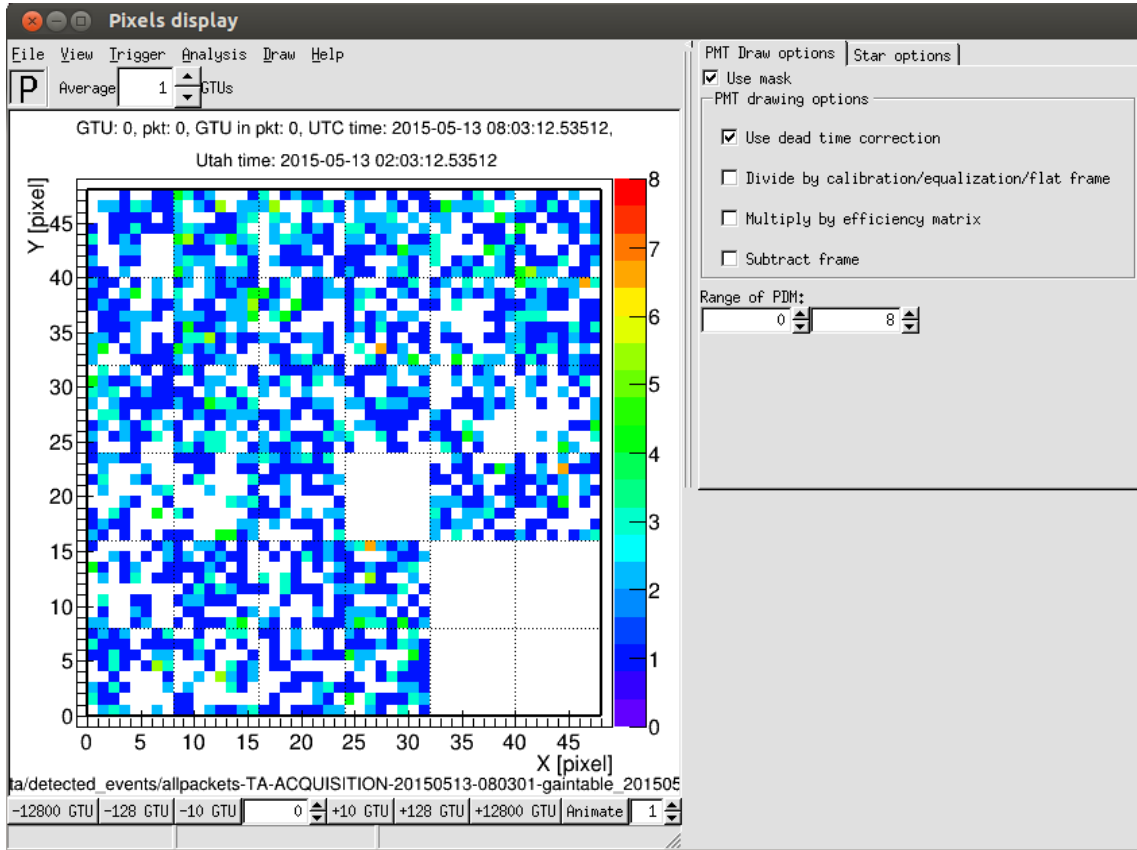
Figure A.1: Graphic user interface of ETOS.

In the top menu bar some actions like saving the visualized GTU as an image, ROOT or text file as well as animations of more than one GTU are present int the File menu. In the trigger menu, there is a couple of remarkable functions to search for triggers on the PDM. One method performs *multi-pixel triggering (time mean)*, appropriate for measurements with background brightness constant in time but immune to the brightness gradients on the frame. For each pixel it computes an average and standard deviation based on all frames, and finds frames where the number of counts is higher than threshold × standard_deviation + average. Then, for each frame it checks if the number of neighbouring pixels, triggered according to the first selection, is above the required number of pixels, and if the sum of counts in such a cluster is above required threshold. If yes, it adds the cluster to a list of triggers. The second method performs *multi-pixel triggering (frame mean)*, good for frames with uniform background. It is immune to background changes over time. It works similarly to the first method, but the average and standard deviation are computed for each frame separately, based on the (unmasked) pixels of all the frames. Both the triggering functions also display a graphical summary of events, where each point represents a trigger: its position shows the position of the event on the PDM and the color shows the time (blue means early, brown means late). This window should allow to find events that moved through the PDM. They should form a line

of relatively uniform color points (close in time). In Figure A.2 one can note lines originated by triggers found by the triggering functions. In (a) the line is formed by the overlap of triggers related to CLF events (every half an hour, 300 laser pulses are shot for 30 s with a frequency of 10 Hz). In (b) the cyan track is due to a aeroplane, with its characteristic blinking signal and the blue track is due to a star. In both plots some blobs are formed by background events.

(a) CLF

(b) Aeroplane and star
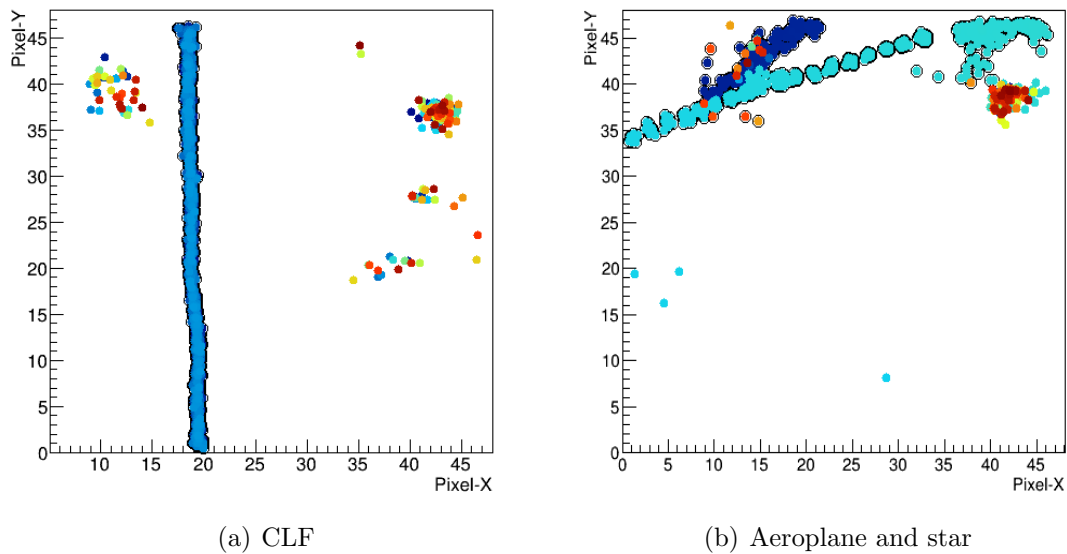
Figure A.2: ETOS triggering function display. It shows the events generating triggers, with its position on the PDM and time information (blue means early, brown means late). In (a) is the overlap of triggers from CLF events and in (b) triggers due to a aeroplane (blinking cyan track) and a star (blue track). In both the images, constantly triggering blobs formed by background events are also visible.

Appendix B

Calculation of the uncertainties

B.1   Uncertainties in the background analysis

In Section 5.3 the mean value of the pixel contents per frame, within packets of 128 frames containing the detected events, have been discussed and presented with their uncertainties.

Since the number of counts on each pixel per frame is low, the counts follow a Poisson distributions. Hence, the uncertainties on the content of each pixel p is:

$$\delta p = \sqrt{p} \tag{B.1}$$

The uncertainty on the sum s of the counts per frame is then:

$$\delta s = \sqrt{\sum_i (\delta p_i)^2} = \sqrt{\sum_i p_i}, \tag{B.2}$$

which finally gives the uncertainty of the mean value m of the pixel contents per frame:

$$\delta m = \frac{\sqrt{\sum_i p_i}}{N}, \tag{B.3}$$

where N is the number of (active) pixels in the frames or in the selected boxes, excluding the non-working pixels.

B.2   Uncertainties of the Gaussian fit

The track width (Section 5.1.2) and the star spot size (Section 5.2) are evaluated as the FWHM of the Gaussian used in the fit, from its relation with the standard deviation of the Gaussian:

$$\text{FWHM} = 2.355 \cdot \sigma. \tag{B.4}$$

Hence, the uncertainty of the track width depends on the uncertainty of σ, which is provided by the Gaussian fit, as:

$$\delta\text{FWHM} = 2.355 \cdot \delta\sigma. \tag{B.5}$$

B.3 Uncertainties in the inclination of the event track

From the linear fit with the method of least squares, used to evaluate the inclination of the event tracks in Section 7.2.2, the fitting straight line has the equation:

$$y = m \cdot x + q \tag{B.6}$$

where m and q are the line parameters and the uncertainties of these parameters are provided by the linear fit.

Finally, the uncertainty of the inclination angle $\alpha = \operatorname{arccot} m$ is

$$\delta\alpha = \left| \frac{d\alpha}{dm} \right| \cdot \delta m = \left| -\frac{1}{1 + m^2} \right| \cdot \delta m. \tag{B.7}$$

Appendix C

Stars crossing the EUSO-TA field of view

In this appendix, frames of the β Persei and the Vega stars crossing EUSO-TA FOV are shown. This frames have been used in Section 5.2 to estimate the star spot size on the focal surface.

C.1 β Persei

(a) Frame 1.

(b) Frame 2.
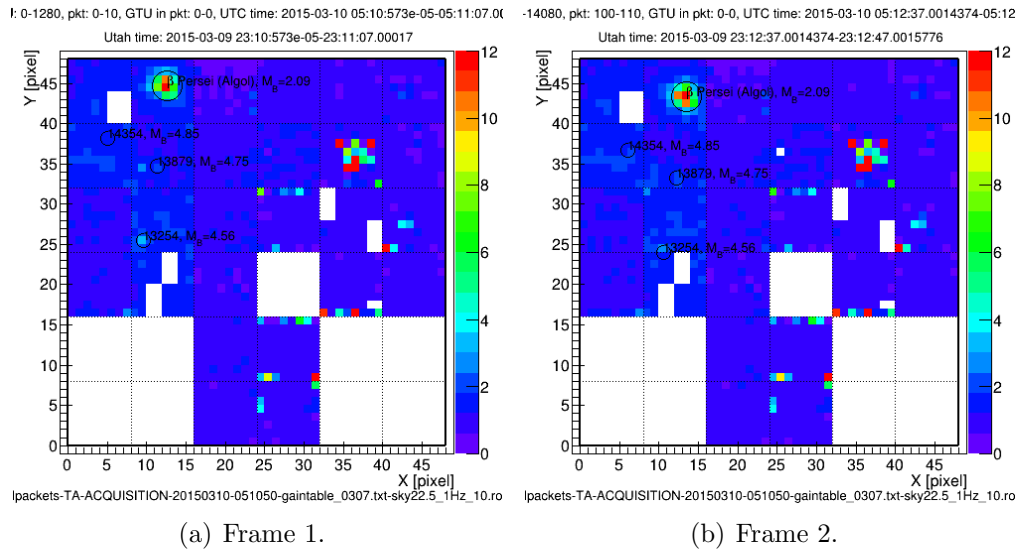
Figure C.1: Sequence (first part) of frames showing β Persei (Algol) and a few other fainter stars moving through EUSO-TA FOV. Every frame shows the average of 1280 GTUs and is separated from next frame by 12800 GTUs. Data taken on the 10th March 2015.

(a) Frame 3.

(b) Frame 4.

(c) Frame 5.

(d) Frame 6.

(e) Frame 7.
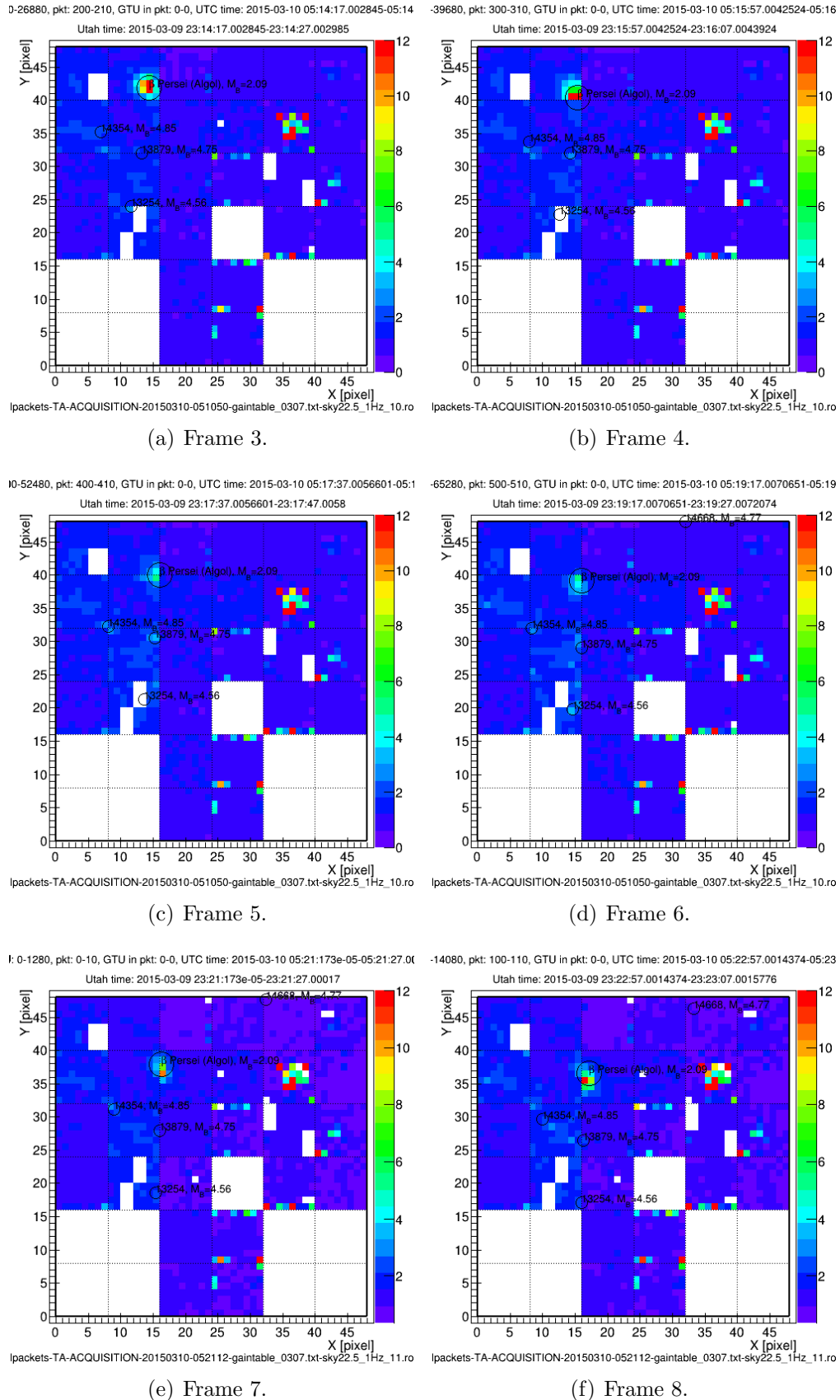
(f) Frame 8.

Figure C.2: Sequence (second part) of frames showing β Persei (Algol) and a few other fainter stars moving through EUSO-TA FOV. Every frame shows the average of 1280 GTUs and is separated from next frame by 12800 GTUs. Data taken on the 10th March 2015.

(a) Frame 9.

(b) Frame 10.

(c) Frame 11.

(d) Frame 12.

(e) Frame 13.
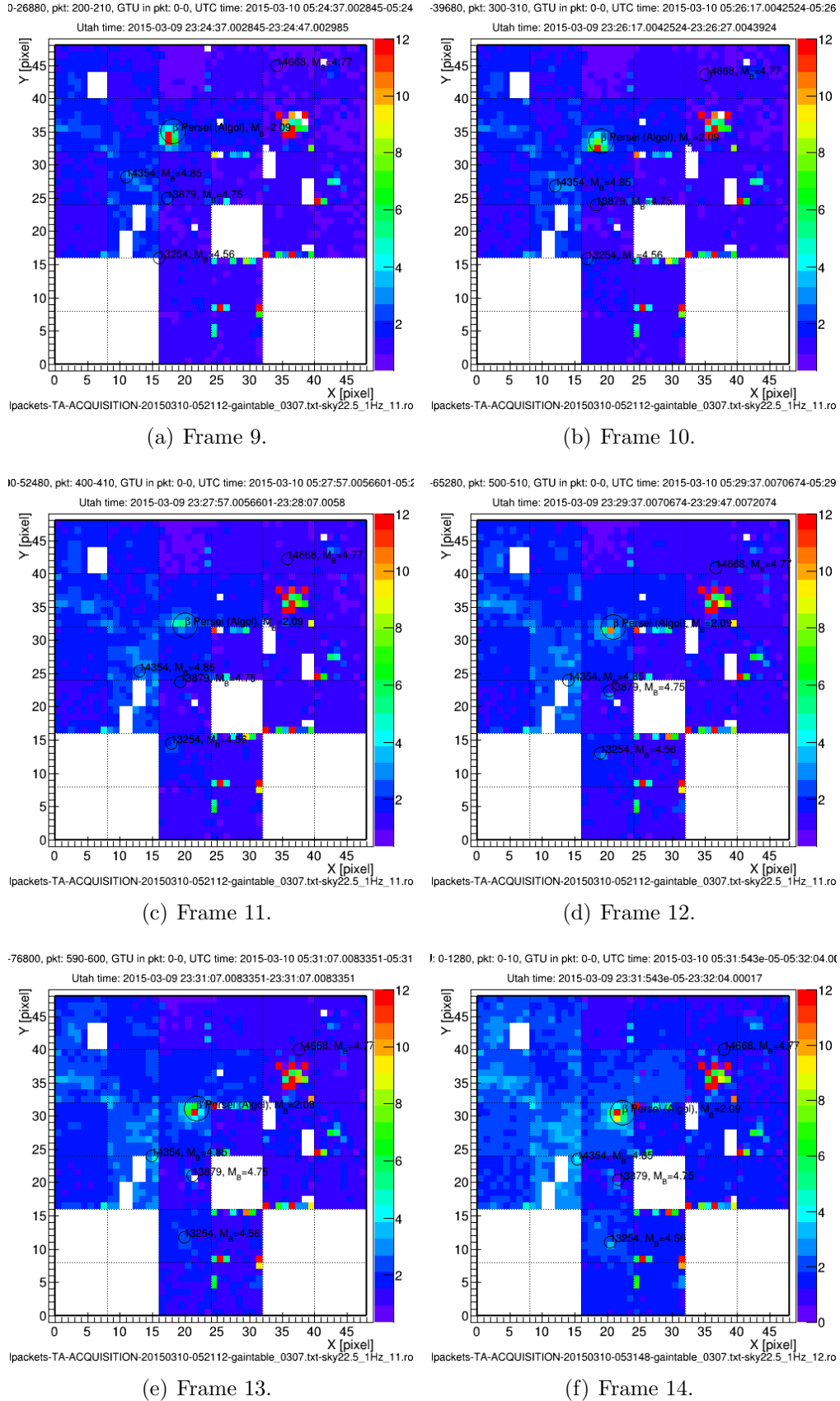
(f) Frame 14.

Figure C.3: Sequence (third part) of frames showing β Persei (Algol) and a few other fainter stars moving through EUSO-TA FOV. Every frame shows the average of 1280 GTUs and is separated from next frame by 12800 GTUs. Data taken on the 10th March 2015.

(a) Frame 15.

(b) Frame 16.

(c) Frame 17.

(d) Frame 18.
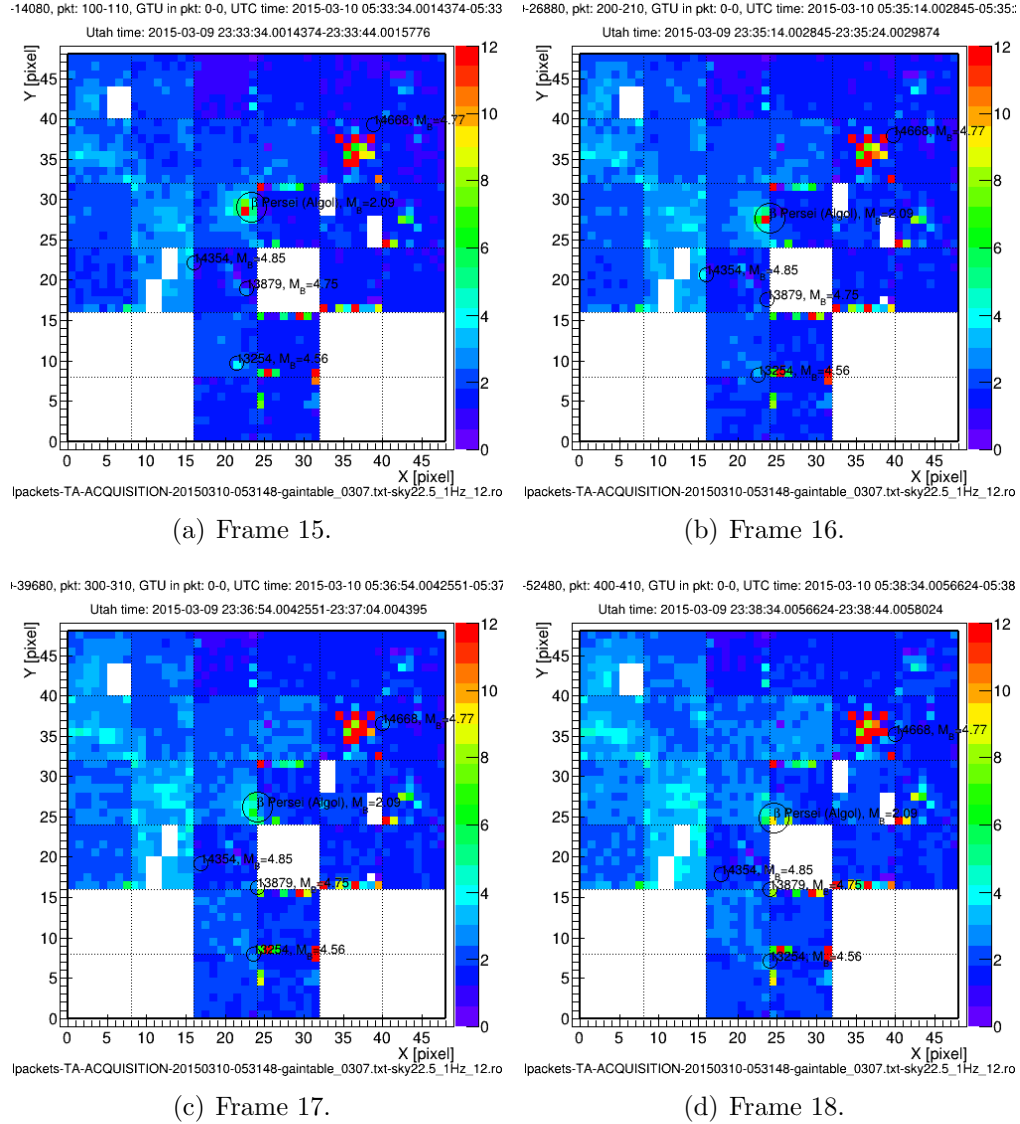
Figure C.4: Sequence (fourth part) of frames showing β Persei (Algol) and a few other fainter stars moving through EUSO-TA FOV. Every frame shows the average of 1280 GTUs and is separated from next frame by 12800 GTUs. Data taken on the 10th March 2015.

C.2   Vega

(a) Frame 1

(b) Frame 2

(c) Frame 3

(d) Frame 4
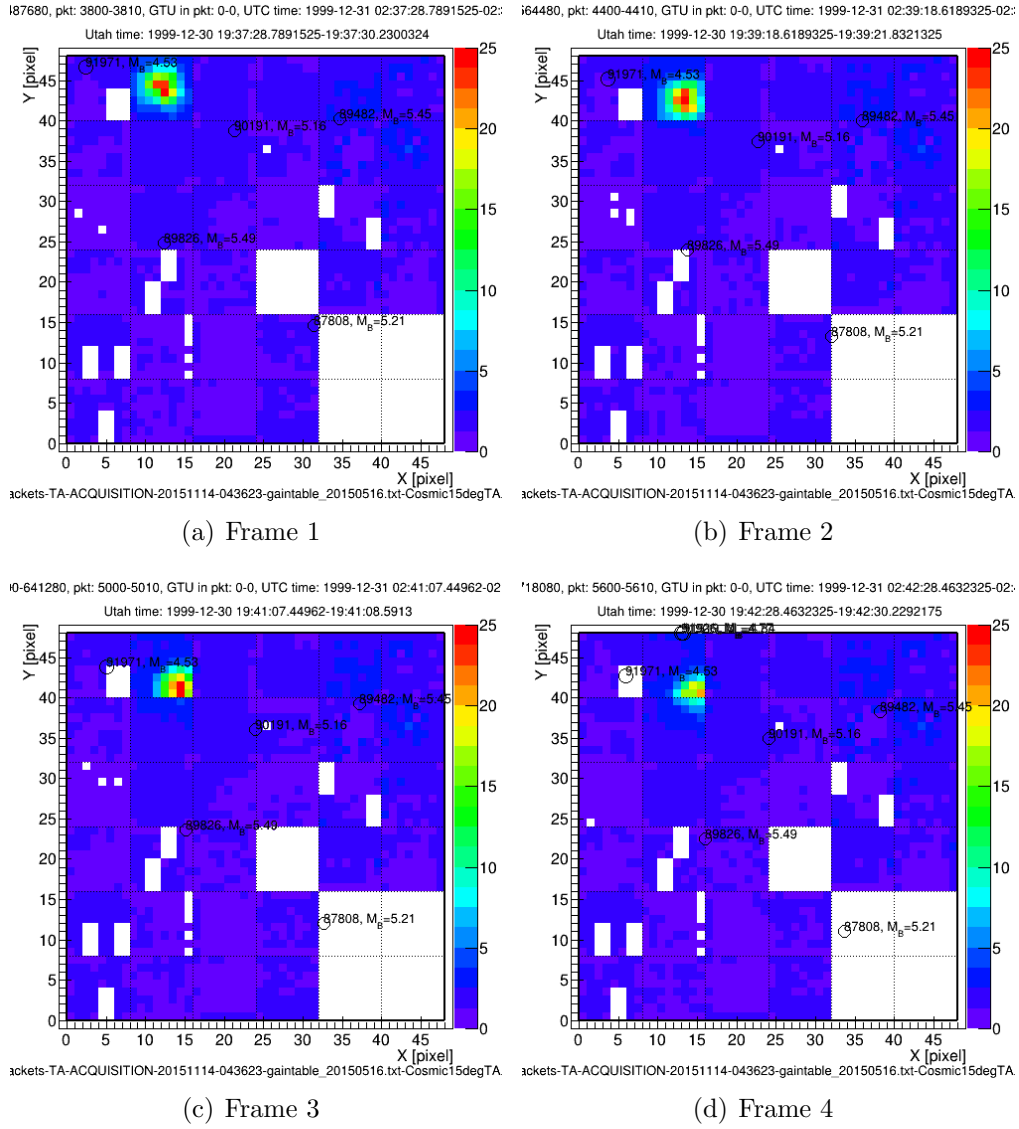
Figure C.5: Sequence (first part) of frames showing Vega and a few other fainter stars moving through EUSO-TA FOV. Every frame shows the average of 1280 GTUs and is separated from next frame by 76800 GTUs. Data taken on the 14th November 2015.

(a) Frame 5

(b) Frame 6

(c) Frame 7

(d) Frame 8

(e) Frame 9
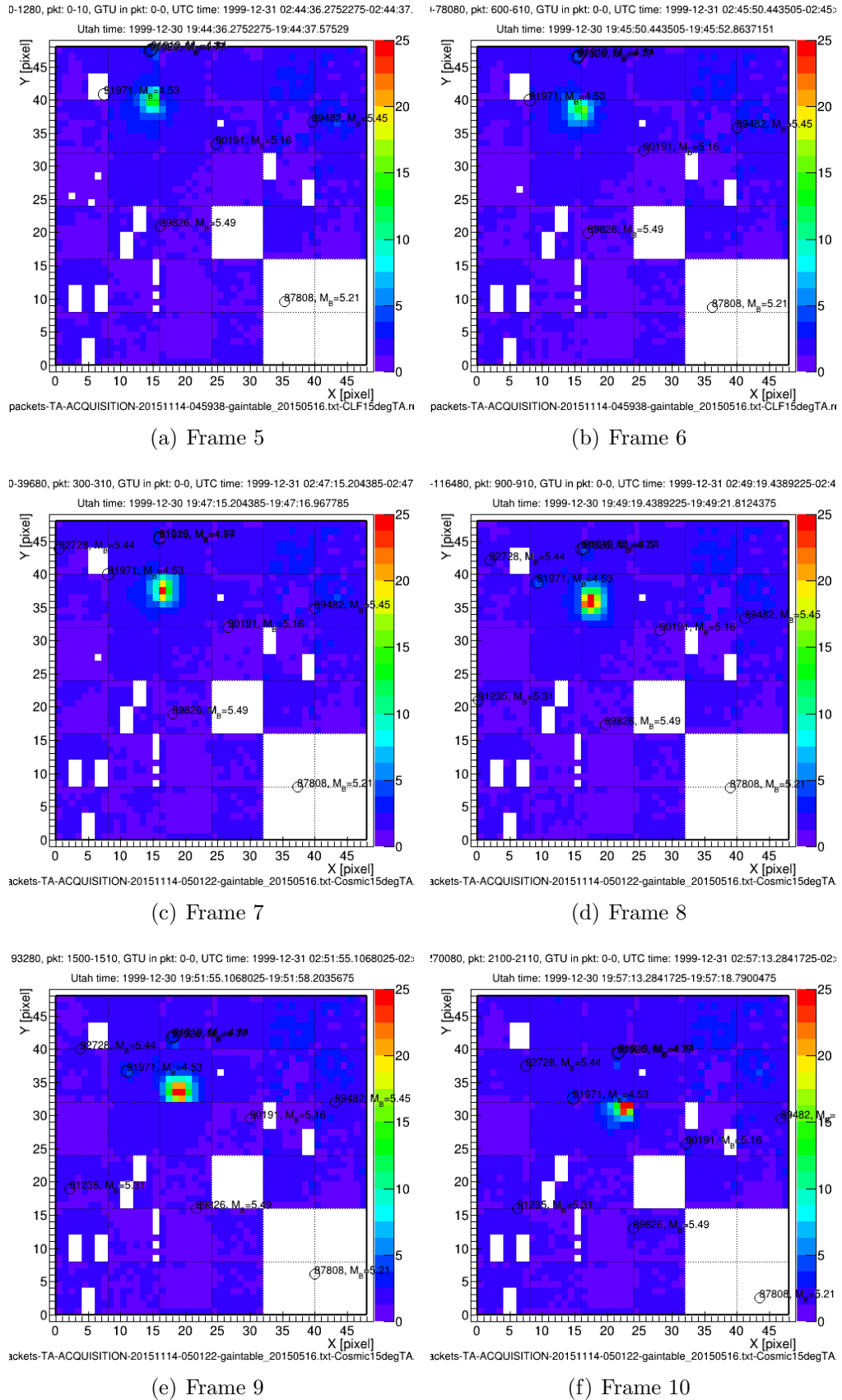
(f) Frame 10

Figure C.6: Sequence (second part) of frames showing Vega and a few other fainter stars moving through EUSO-TA FOV. Every frame shows the average of 1280 GTUs and is separated from next frame by 76800 GTUs. Data taken on the 14th November 2015.

(a) Frame 11   (b) Frame 12
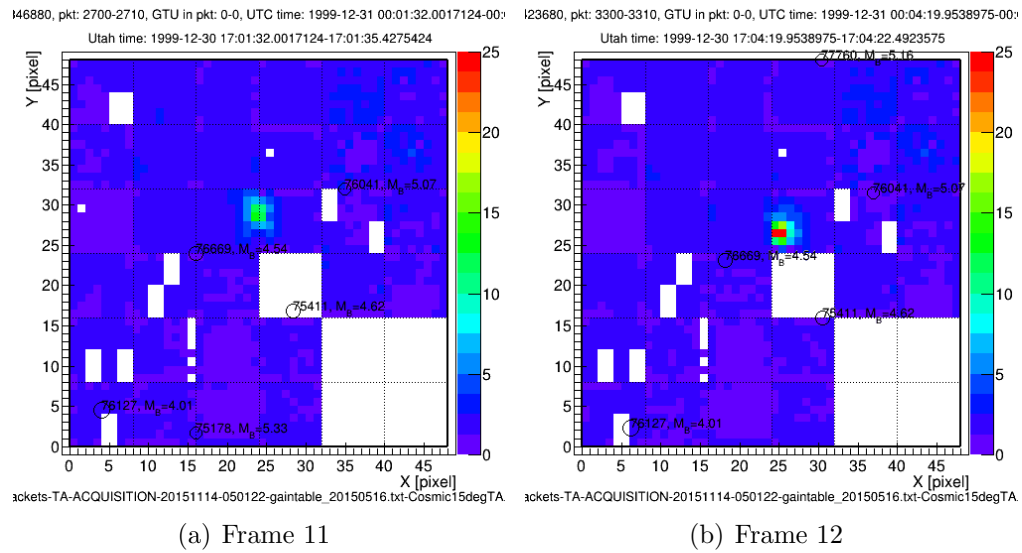
Figure C.7: Sequence (third part) of frames showing Vega and a few other fainter stars moving through EUSO-TA FOV. Every frame shows the average of 1280 GTUs and is separated from next frame by 76800 GTUs. Data taken on the 14th November 2015.

Appendix D

Figures of background "imitation"

In Section 7.1.2 the method to create background frames added the pure simulated events has been described, and the figure relative to the background for the event of 13th May 2015 has been shown there.
In this Appendix figures related to the creation of background frames for the detected events of 18th September, 20th September and 7th November 2015 are shown.

D.1   18th September 2015 background
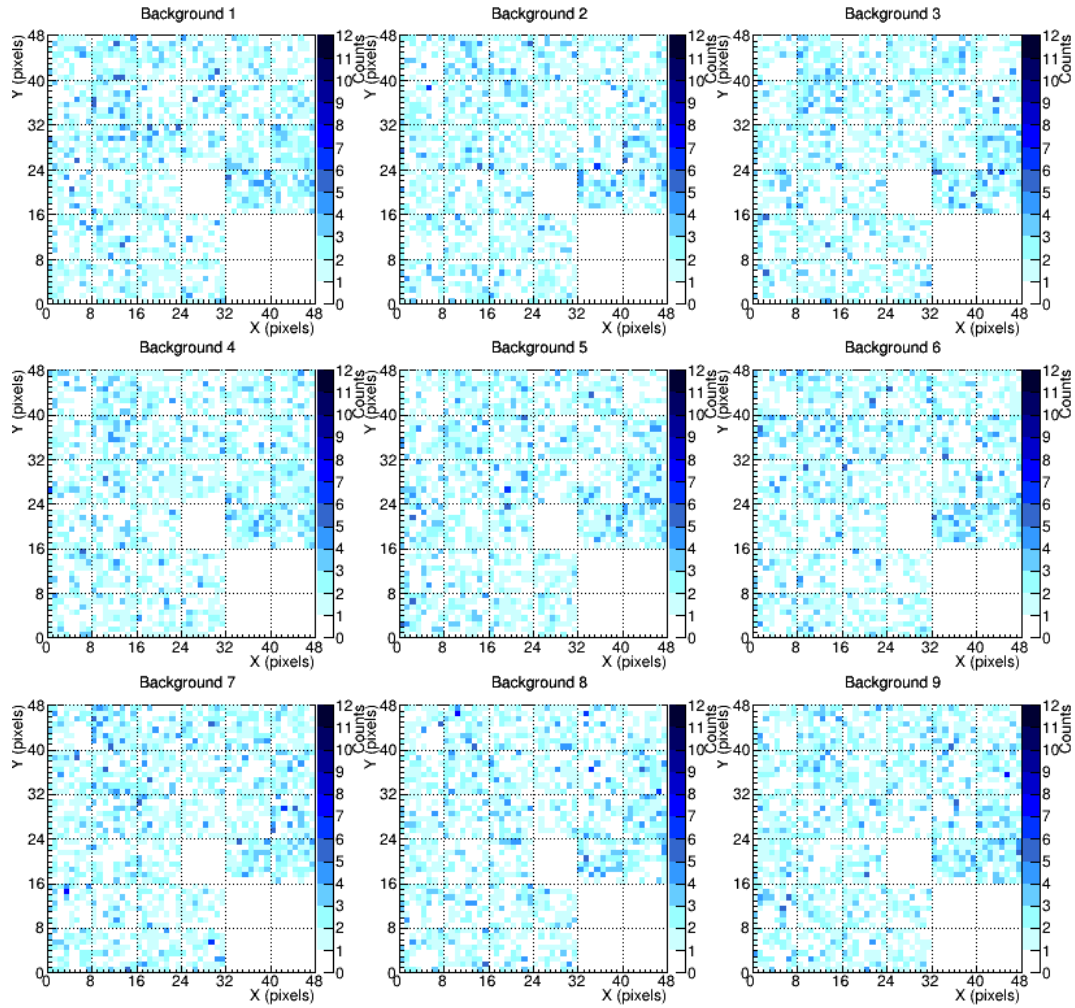
Figure D.1: Nine frames of background for the detected event on 18th September 2015, GTU 1.
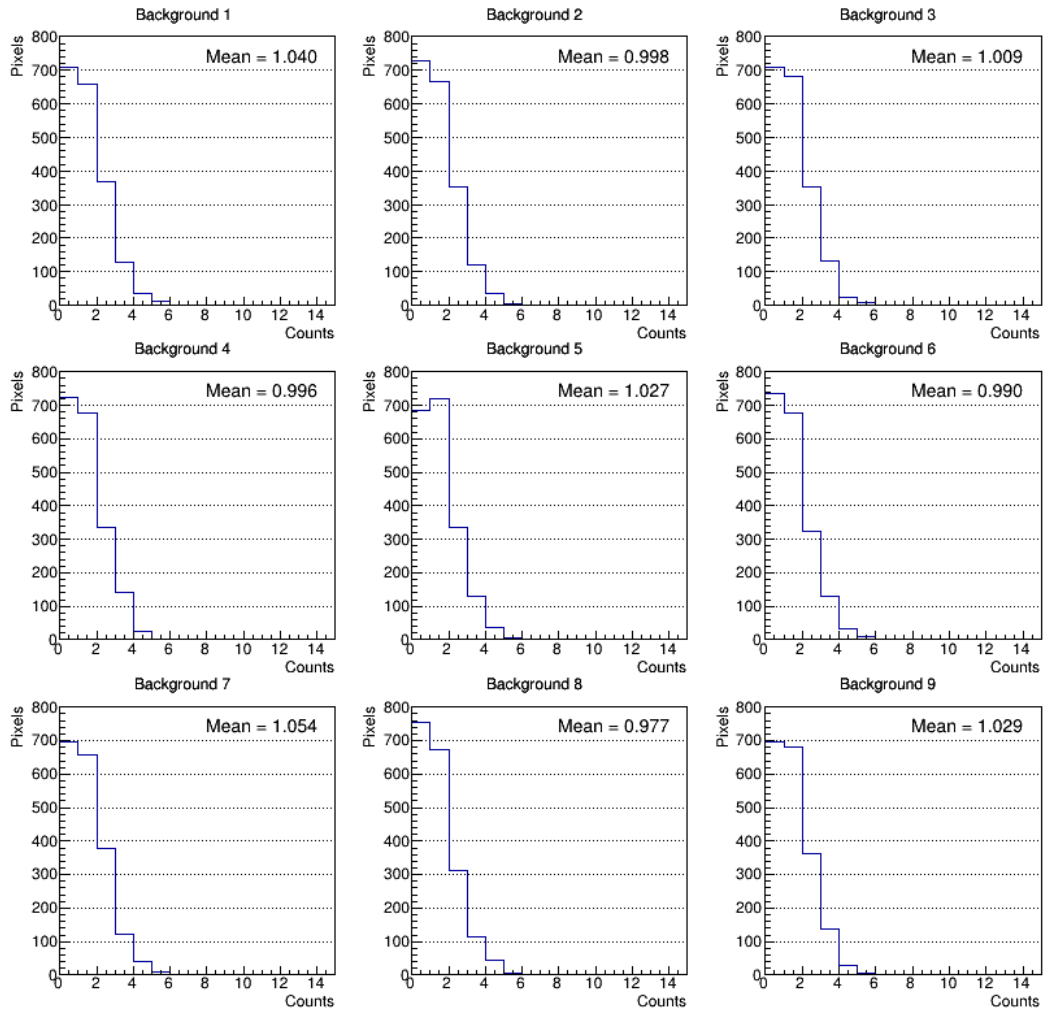
Figure D.2: Distribution of counts of the nine frames of background for the detected event on 18th September 2015, GTU 1.
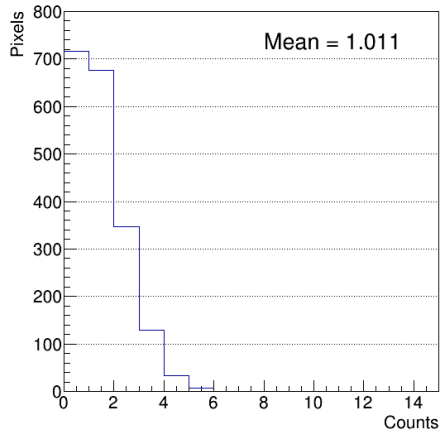
Figure D.3: Mean distribution of counts for the detected event on 18th September 2015, GTU 1.
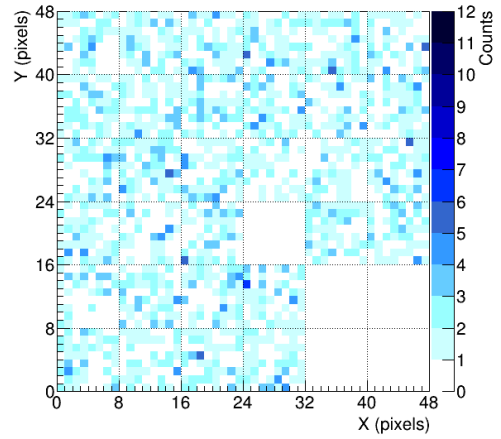
Figure D.4: Mean frame of background for the detected event on 18th September 2015, GTU 1.
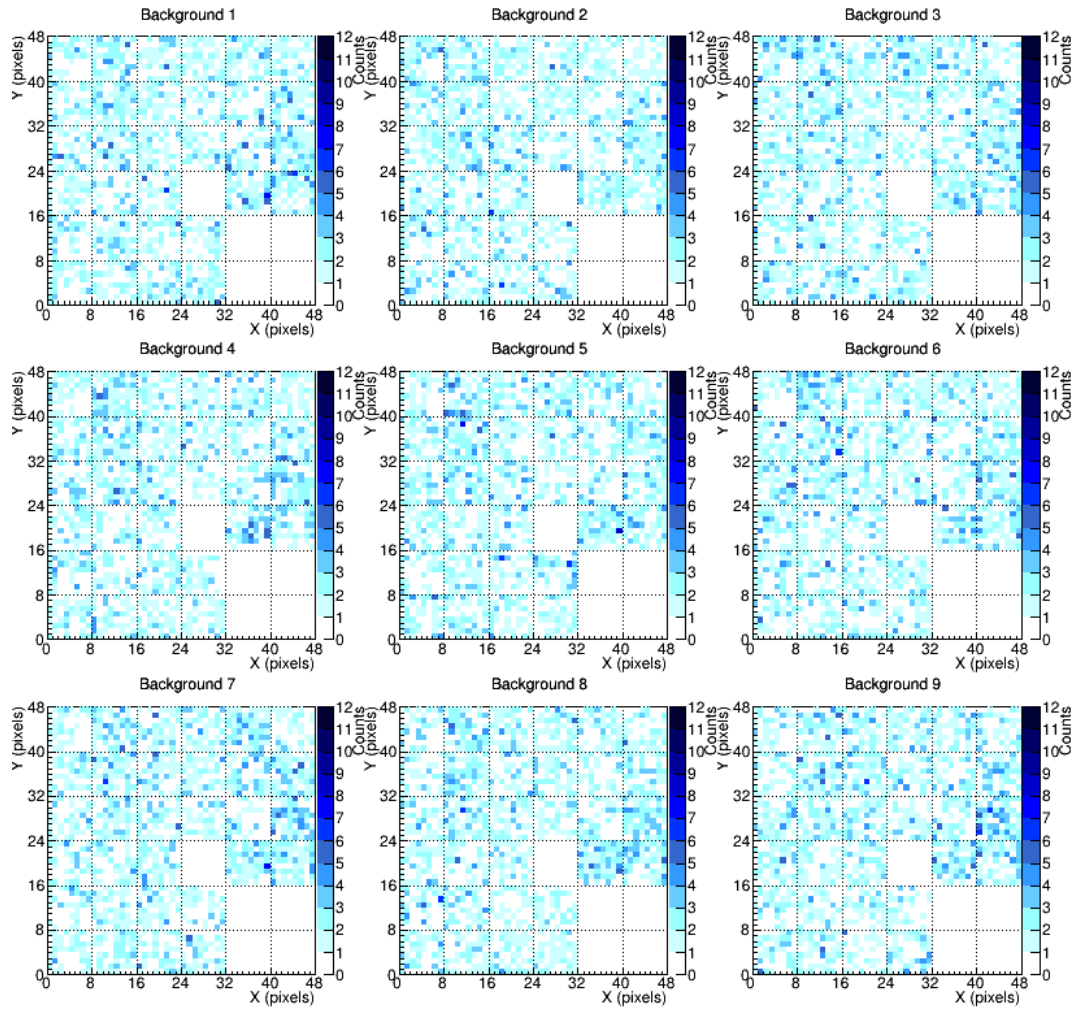
Figure D.5: Nine frames of background for the detected event on 18th September 2015, GTU 2.
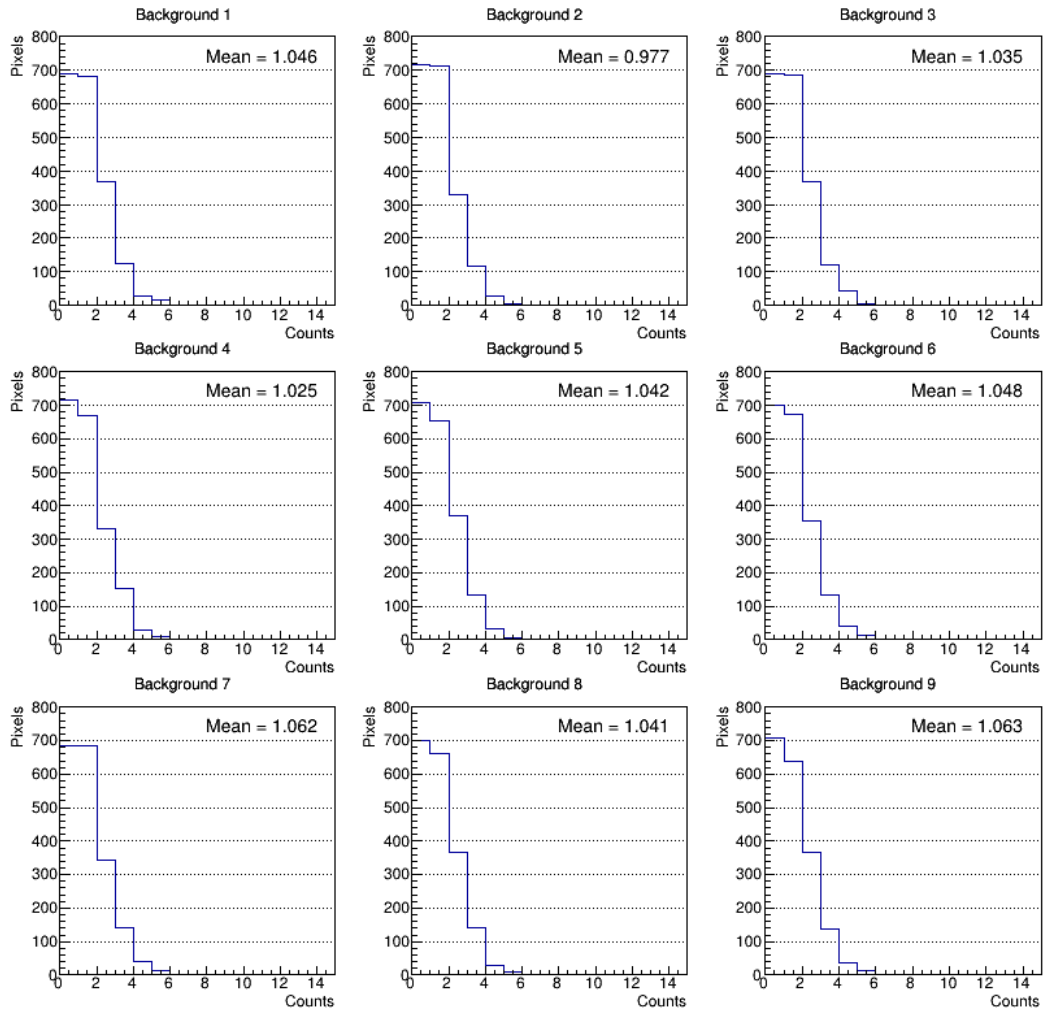
Figure D.6: Distribution of counts of the nine frames of background for the detected event on 18th September 2015, GTU 2.
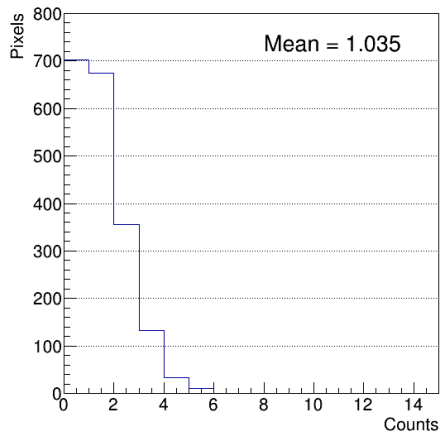
Figure D.7: Mean distribution of counts for the detected event on 18th September 2015, GTU 2.
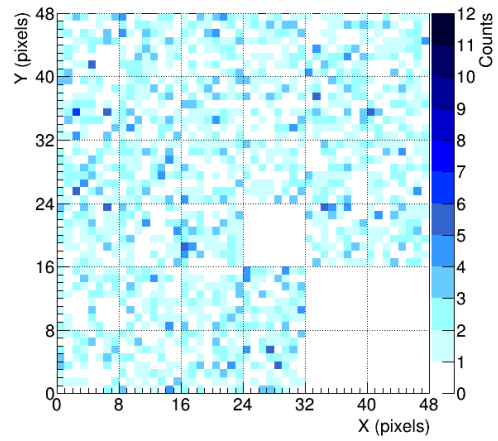
Figure D.8: Mean frame of background for the detected event on 18th September 2015, GTU 2.
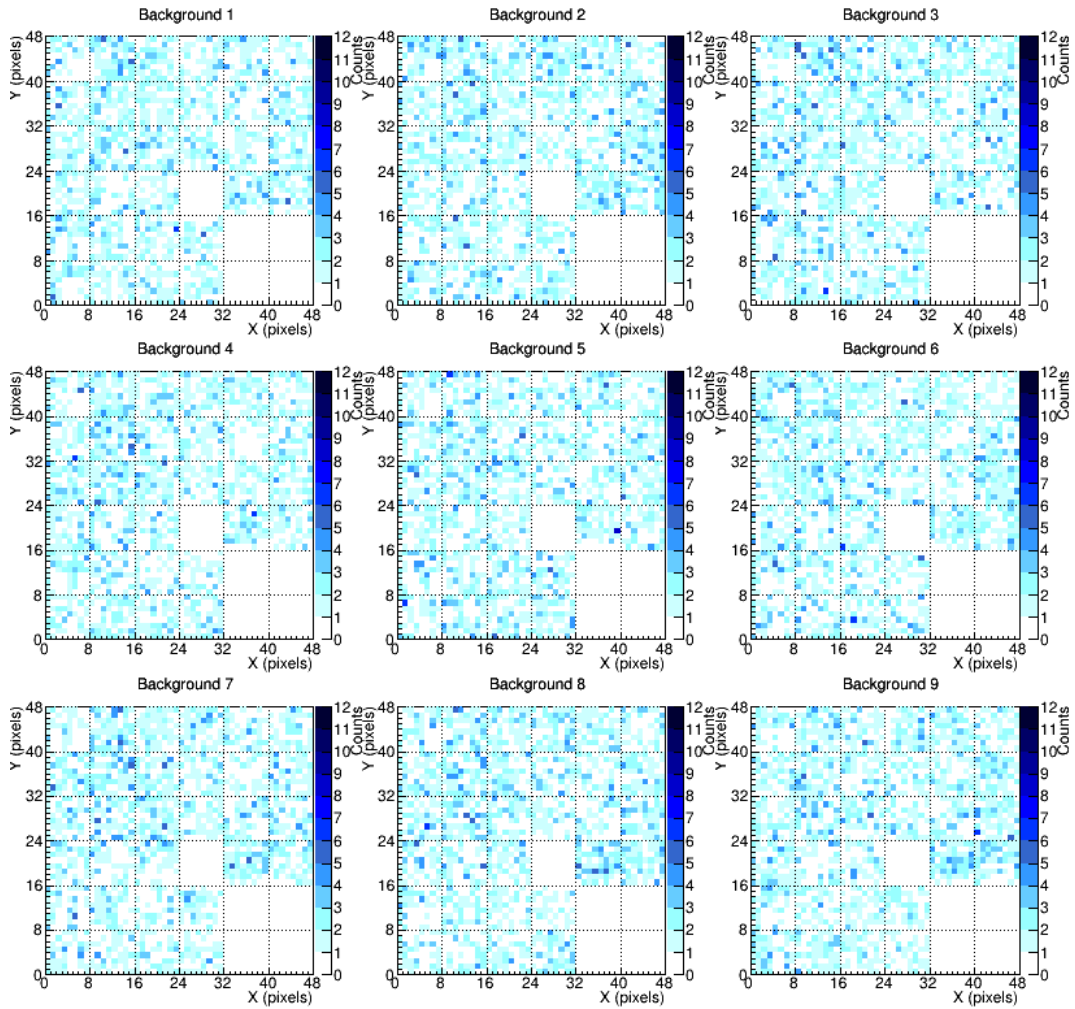
Figure D.9: Nine frames of background for the detected event on 18th September 2015, GTU 3.
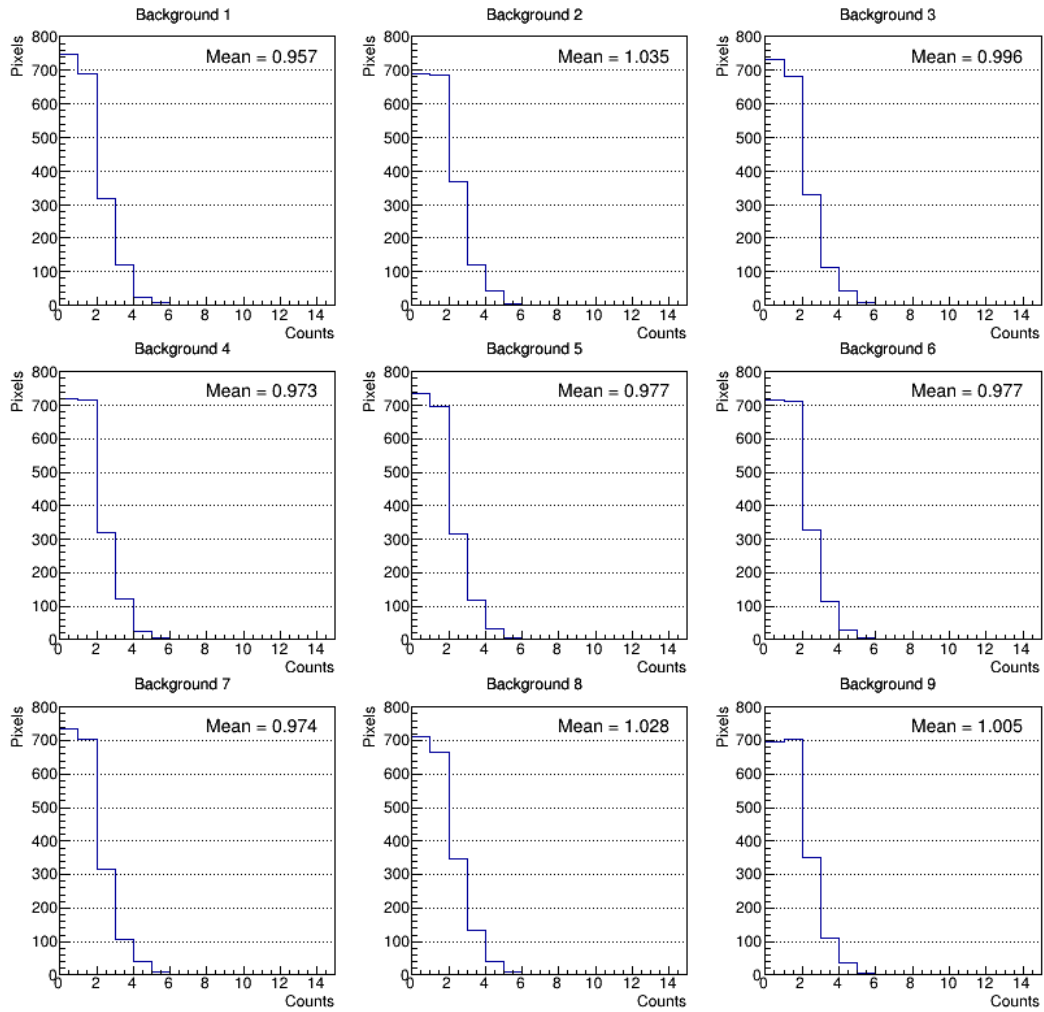
Figure D.10: Distribution of counts of the nine frames of background for the detected event on 18th September 2015, GTU 3.
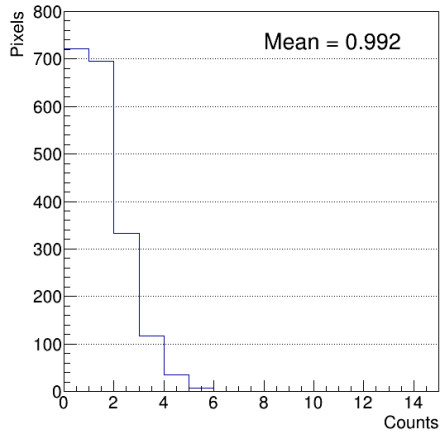
Figure D.11: Mean distribution of counts for the detected event on 18th September 2015, GTU 3.
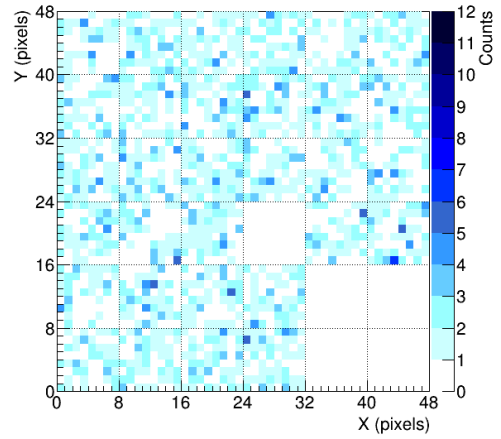
Figure D.12: Mean frame of background for the detected event on 18th September 2015, GTU 3.

D.2 20th September 2015 background
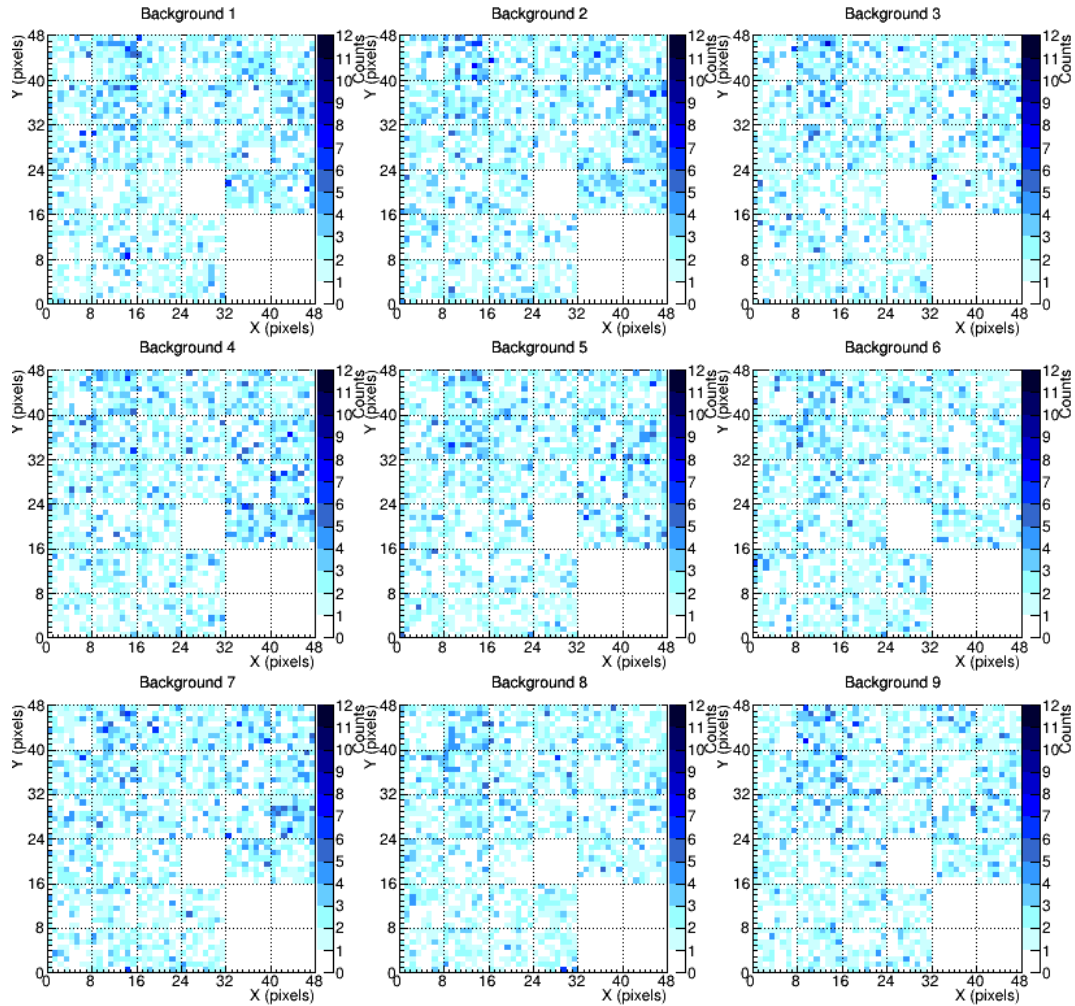
Figure D.13: Nine frames of background for the detected event on 20th September 2015, GTU 1.
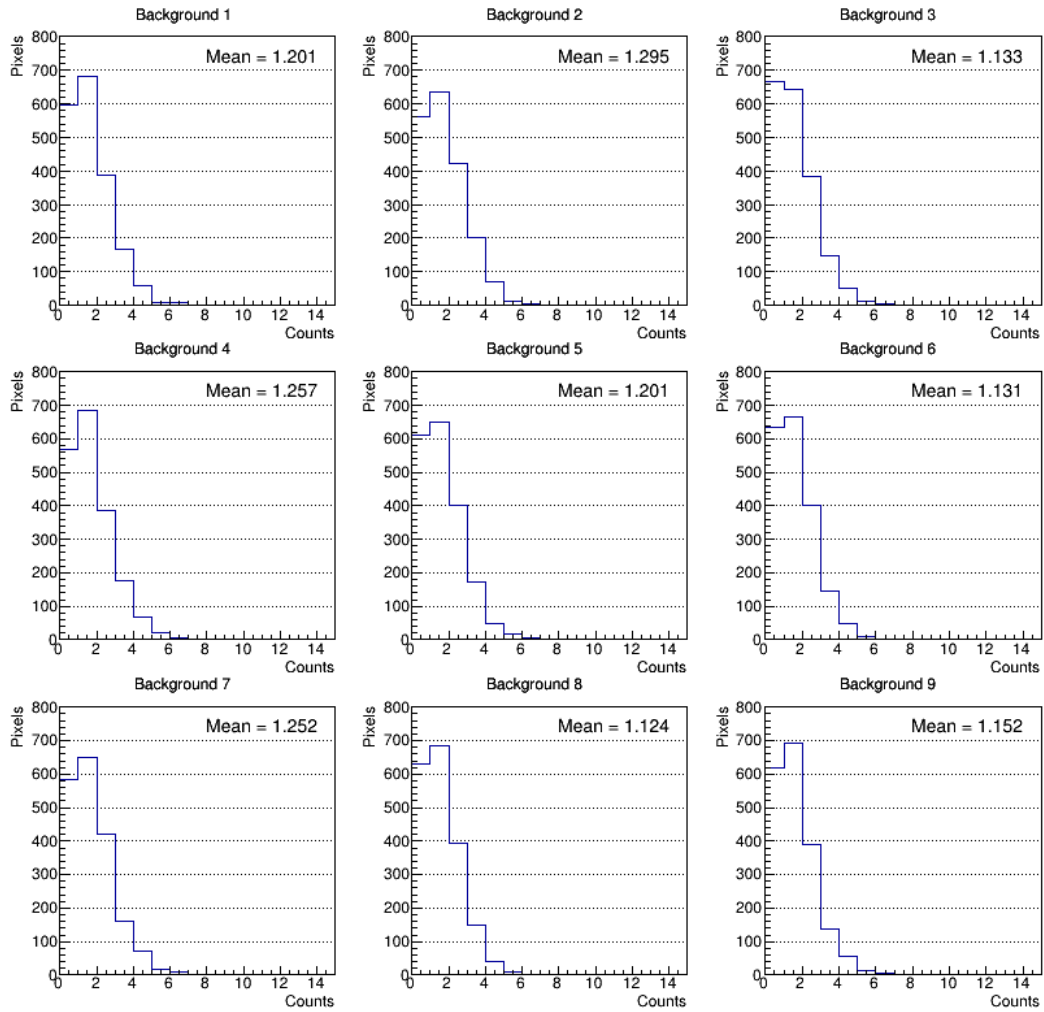
Figure D.14: Distribution of counts of the nine frames of background for the detected event on 20th September 2015, GTU 1.
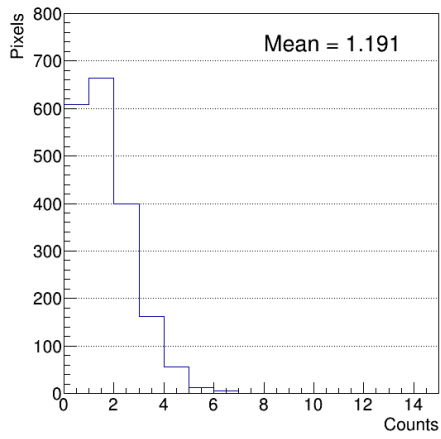
Figure D.15: Mean distribution of counts for the detected event on 20th September 2015, GTU 1.
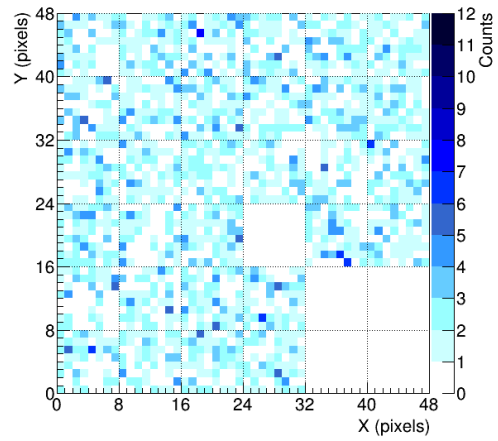
Figure D.16: Mean frame of background for the detected event on 20th September 2015, GTU 1.
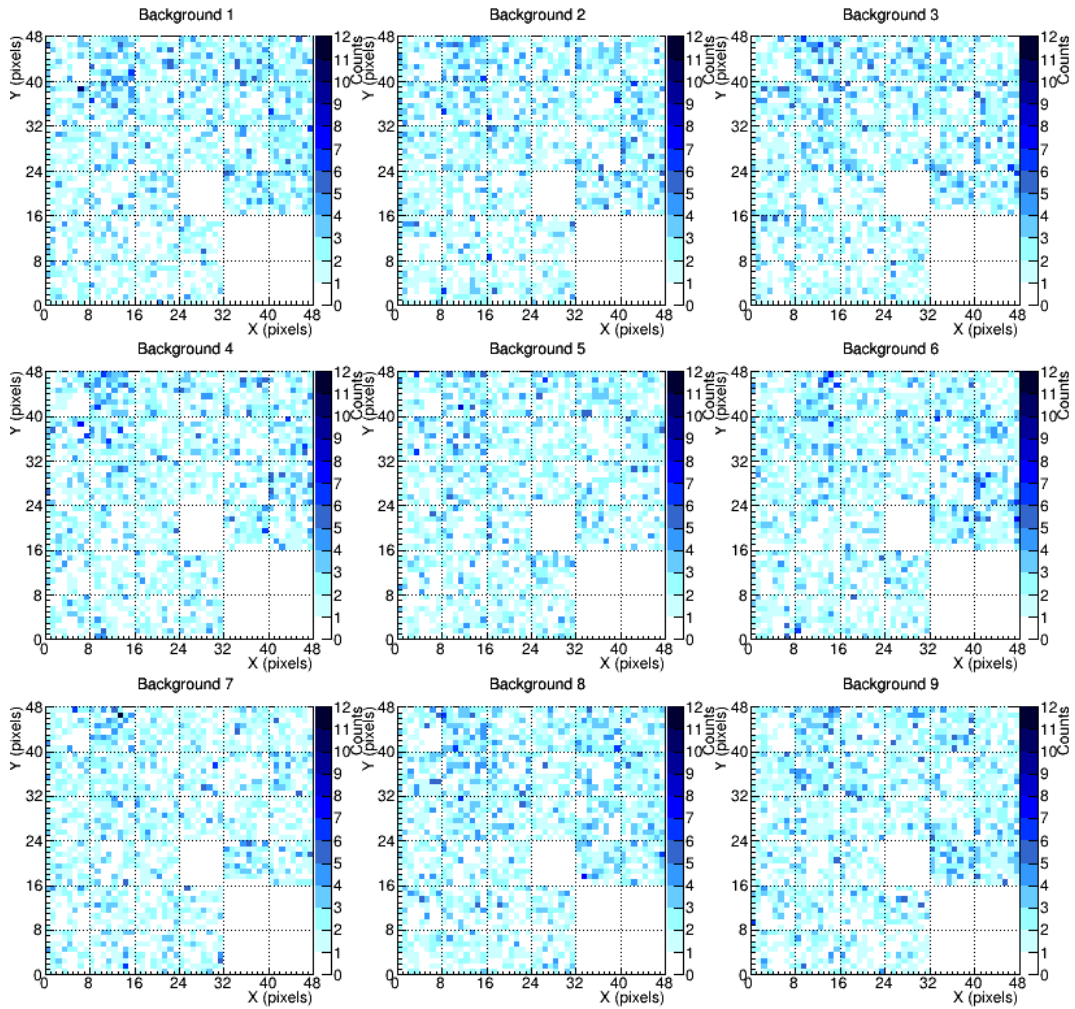
Figure D.17: Nine frames of background for the detected event on 20th September 2015, GTU 2.
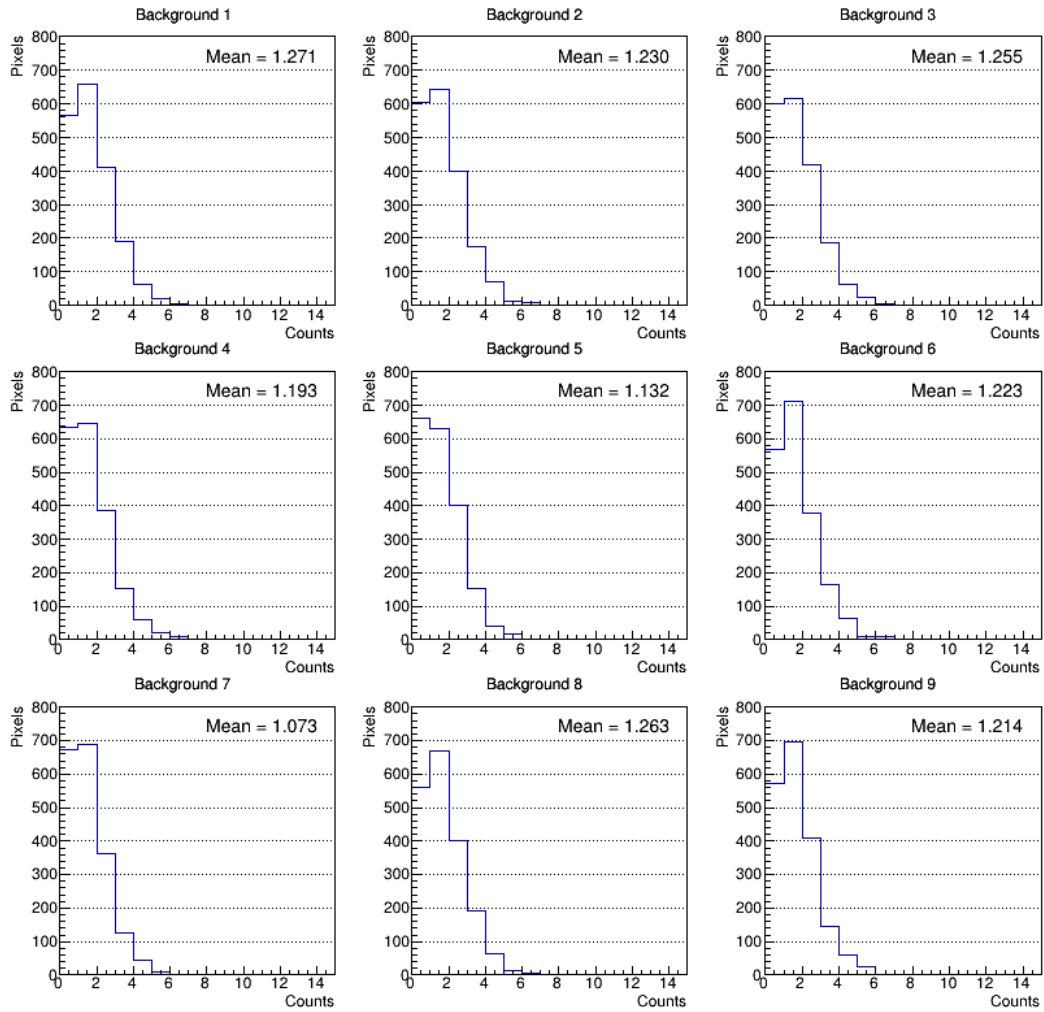
Figure D.18: Distribution of counts of the nine frames of background for the detected event on 20th September 2015, GTU 2.
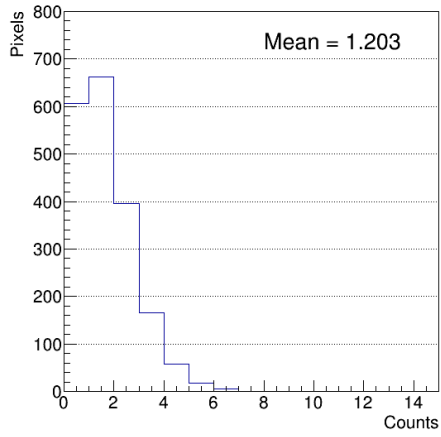
Figure D.19: Mean distribution of counts for the detected event on 20th September 2015, GTU 2.
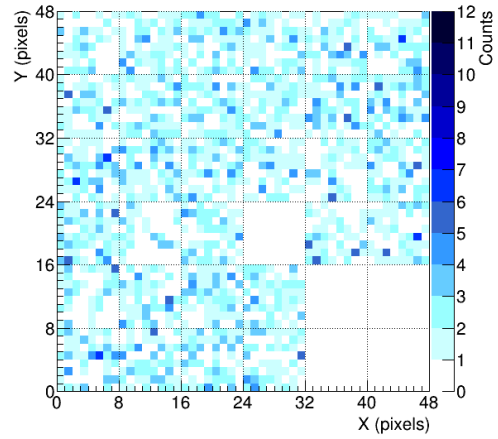
Figure D.20: Mean frame of background for the detected event on 20th September 2015, GTU 2.

D.3   7th November 2015 background
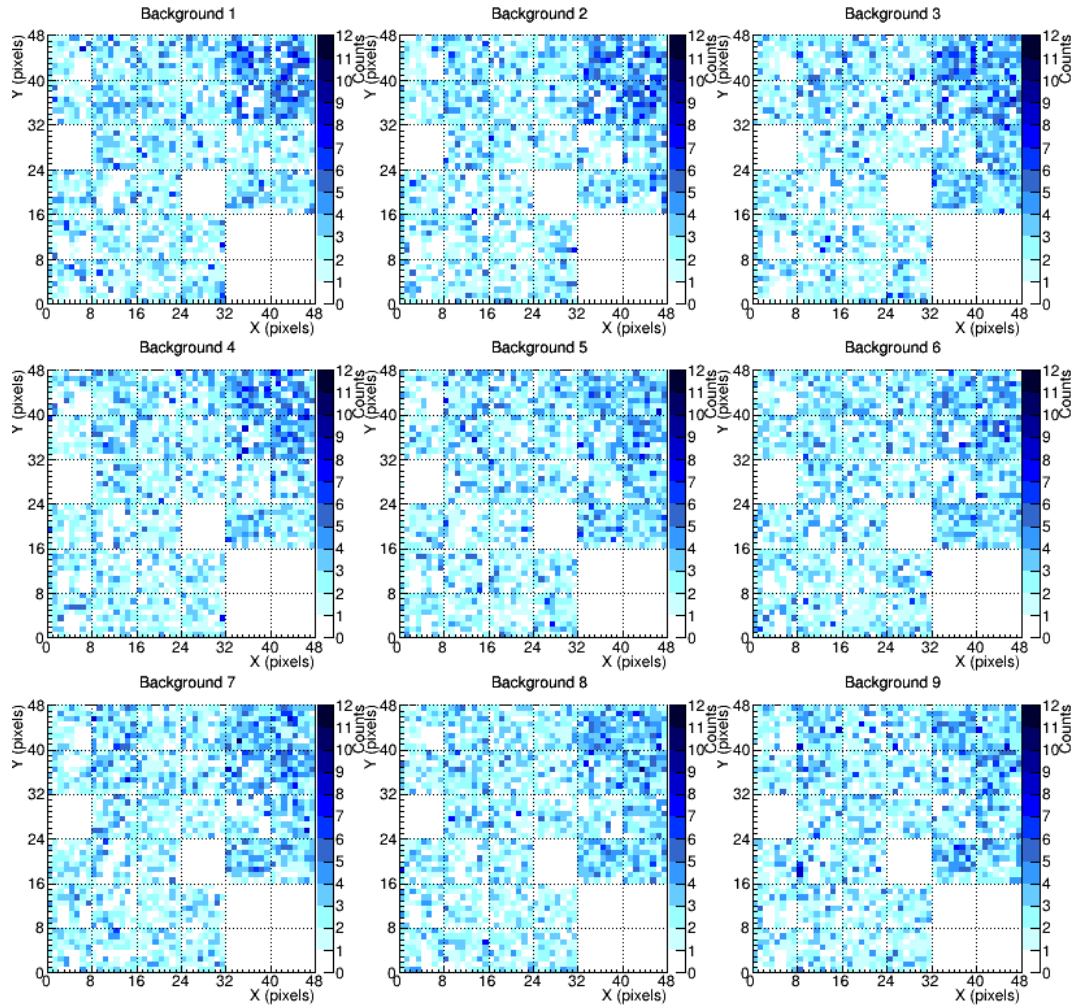
Figure D.21: Nine frames of background for the detected event on 7th November 2015.
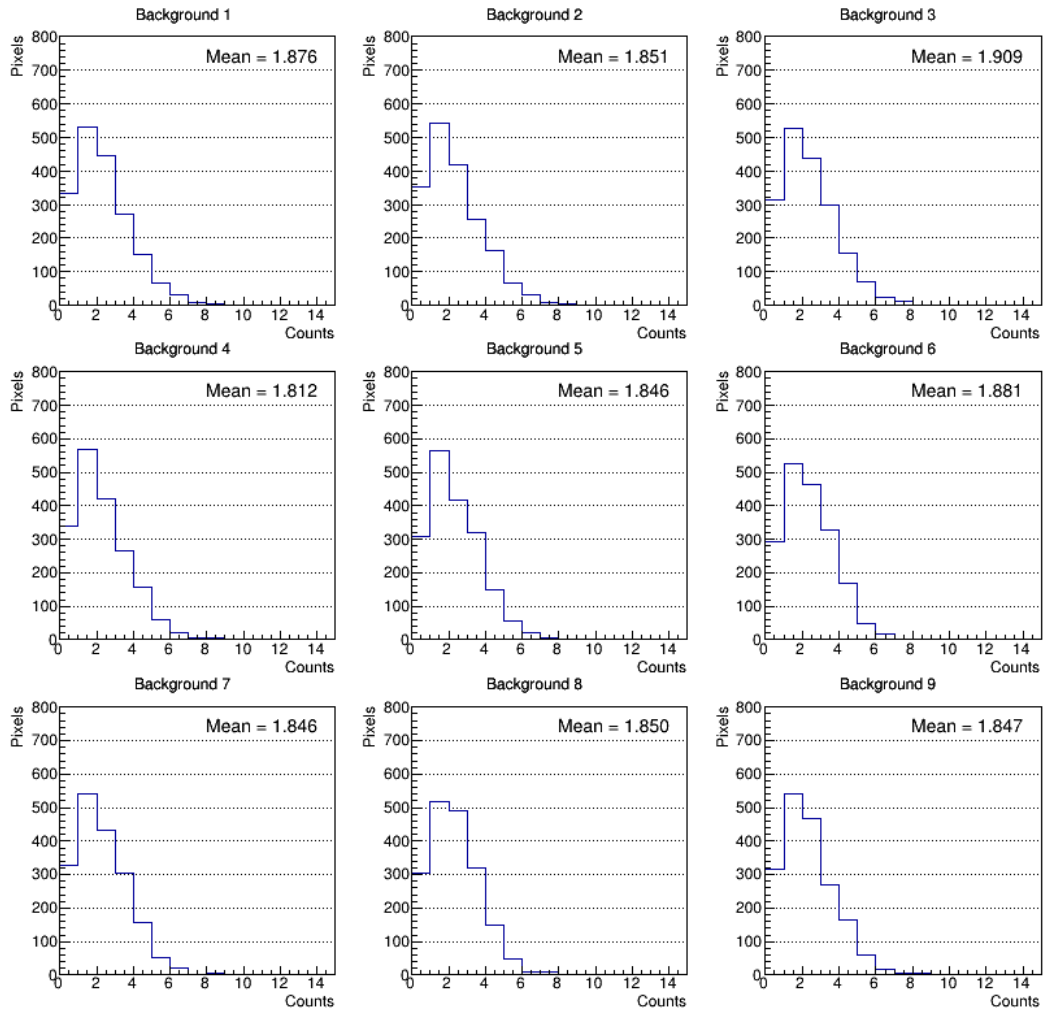
Figure D.22: Distribution of counts of the nine frames of background for the detected event on 7th November 2015.
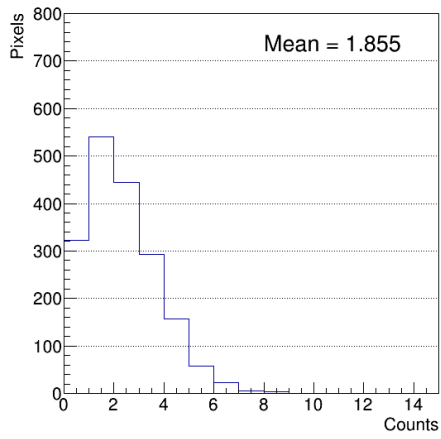
Figure D.23: Mean distribution of counts for the detected event on 7th November 2015.
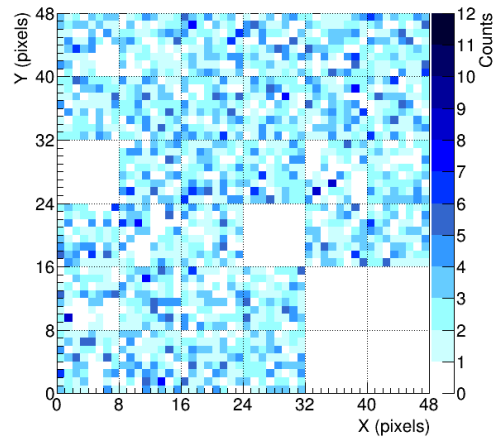
Figure D.24: Mean frame of background for the detected event on 7th November 2015.

Appendix E

Resolution of the TA reconstruction parameters

Here the resolutions of the geometrical reconstruction parameters of TA in monocular mode (using just the TAFD at Black Rock Mesa) are reported, estimated by comparing Monte Carlo simulated information with reconstructed one. The plots and their descriptions are taken from [86].

At first, an opening angle distribution, comparing arrival directions between simulated values and reconstructed ones, is shown in Figure E.1. The one sigma interval which includes 68% of the events data is from 0° to 7.4°. The geometrical resolution is determined as 7.4° in the monocular mode and it is worse than the resolution for stereo reconstruction (using more TAFD stations), which is about 1°.
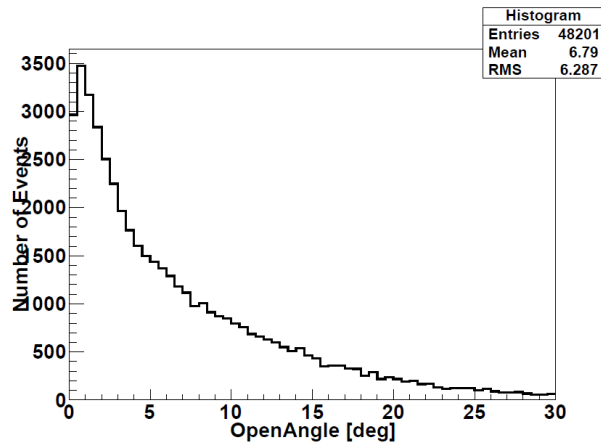
Figure E.1: The opening angle distribution comparing between simulated arrival directions and reconstructed ones.

Figure E.2 shows the resolution of the impact parameter. The mean of the reconstructed impact parameter is −110.4 m. As a result, the monocular analysis has a tendency to reconstruct cosmic ray air showers at a shorter distance than actual ones.

Figure E.3 shows the resolution of the angle of the cosmic ray air shower axis in
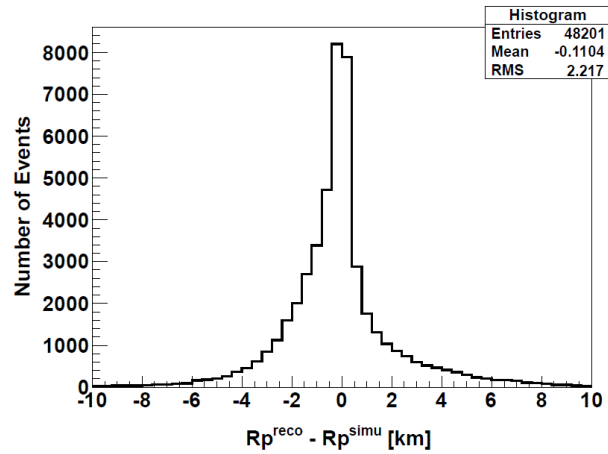
Figure E.2: The resolutions of the impact parameter estimation. It is a comparison between simulated and reconstructed values.

the Shower-Detector Plane (SDP) shown in Figure 4.1. The averaged difference of the angle is $-2.8°$, which means that the showers tends to be reconstructed more inclined than they are.
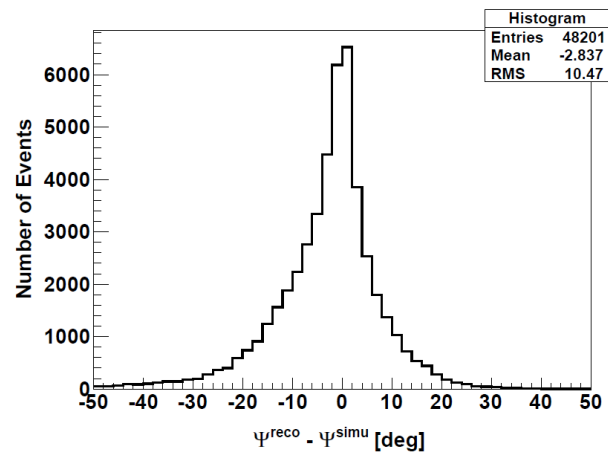
Figure E.3: The angle resolution on SDP compared between simulated and reconstructed.

The uncertainty on the shower geometrical parameters might cause the need to shift the shower core position on ground, using the Offline software (Section 7.1.1), to get results corresponding to the data. Also another geometrical difference has been observed using the fit algorithm to compare the detected and simulated events (Section 7.2.2), and such a difference can be connected to the uncertainty of the parameters.

Appendix F

Simulation studies of the detected events

F.1 Detected events parameters

In the following, tables report the reconstructed parameters of the detected events (provided by TA), used to perform the simulations of such events. They also show, for each events, the coordinates of the shower core on ground and the length of the shift, necessary to have the simulated event tracks in the same position on the focal surface as the detected ones.

Event of 13th May 2015

Shower parameters	
* Zenith	34.5°
* Azimuth	7.2°
* Energy	10^{18} eV
R_p	2.5 km
Core coord. w.r.t. CLF from TA rec.	(14.8 km, −10.9 km)
.... in UTM coord.	(350205 mE, 4340562 mN)
* .... in UTM coord. shifted	(349976 mE, 4340200 mN)
Core coord. shift	0.43 km (SW direction)
Distance core to EUSO-TA	2.43 km
Number of GTUs	1
EUSO-TA configuration	
* Elevation	15°

Table F.1: Event detected on the 13th May 2015. The parameters used to perform the simulation are marked with an asterisk.

Event of 18th September 2015

Shower parameters	
* Zenith	60.4°
* Azimuth	−79.3°
* Energy	$10^{18.51}$ eV
R_p	9.1 km
Core coord. w.r.t. CLF from TA rec.	(11.2 km, −2.5 km)
.... in UTM coord.	(346605 mE, 4348962 mN)
* .... in UTM coord. shifted	(346920 mE, 4349130 mN)
Core coord. shift	0.36 km (NE direction)
Distance core to EUSO-TA	11.32 km
Number of GTUs	3
EUSO-TA configuration	
* Elevation	20°

Table F.2: Event detected on the 18th September 2015. The parameters used to perform the simulation are marked with an asterisk.

Event of 20th September 2015

Shower parameters	
* Zenith	41.2°
* Azimuth	−24.8°
* Energy	$10^{18.42}$ eV
R_p	6.7 km
Core coord. w.r.t. CLF from TA rec.	(10 km, −8.4 km)
.... in UTM coord.	(345405 mE, 4343062 mN)
* .... in UTM coord. shifted	(345330 mE, 4342930 mN)
Core coord. shift	0.15 km (SW direction)
Distance core to EUSO-TA	7.82 km
Number of GTUs	2
EUSO-TA configuration	
* Elevation	10°

Table F.3: Event detected on the 20th September 2015. The parameters used to perform the simulation are marked with an asterisk.

Event of 7th November 2015

Shower parameters	
* Zenith	8.1°
* Azimuth	82°
* Energy	$10^{18.36}$ eV
R_p	2.6 km
Core coord. w.r.t. CLF from TA rec.	(14.8 km, −10.6 km)
.... in UTM coord.	(350205 mE, 4340862 mN)
* .... in UTM coord. shifted	(349950 mE, 4340533 mN)
Core coord. shift	0.42 km (SW direction)
Distance core to EUSO-TA	2.62 km
Number of GTUs	1
EUSO-TA configuration	
* Elevation	15°

Table F.4: Event detected on the 7th November 2015. The parameters used to perform the simulation are marked with an asterisk.

F.2   Qualitative and quantitative comparison

Event of 18th September 2015

The comparison between the counts distributions of data, simulation plus background and background itself shows again a common behavior of data and simulation with respect to the background, especially at GTU 2, where the signature of the event is visible for counts ≥ 3 (Figure F.1). At GTU 1 the segment of the track in the simulation is faint and in GTU 3 it is neither visible in the simulation nor in the data, so the comparison is almost just between background frames.

(a) GTU 1

(b) GTU 2

(c) GTU 3
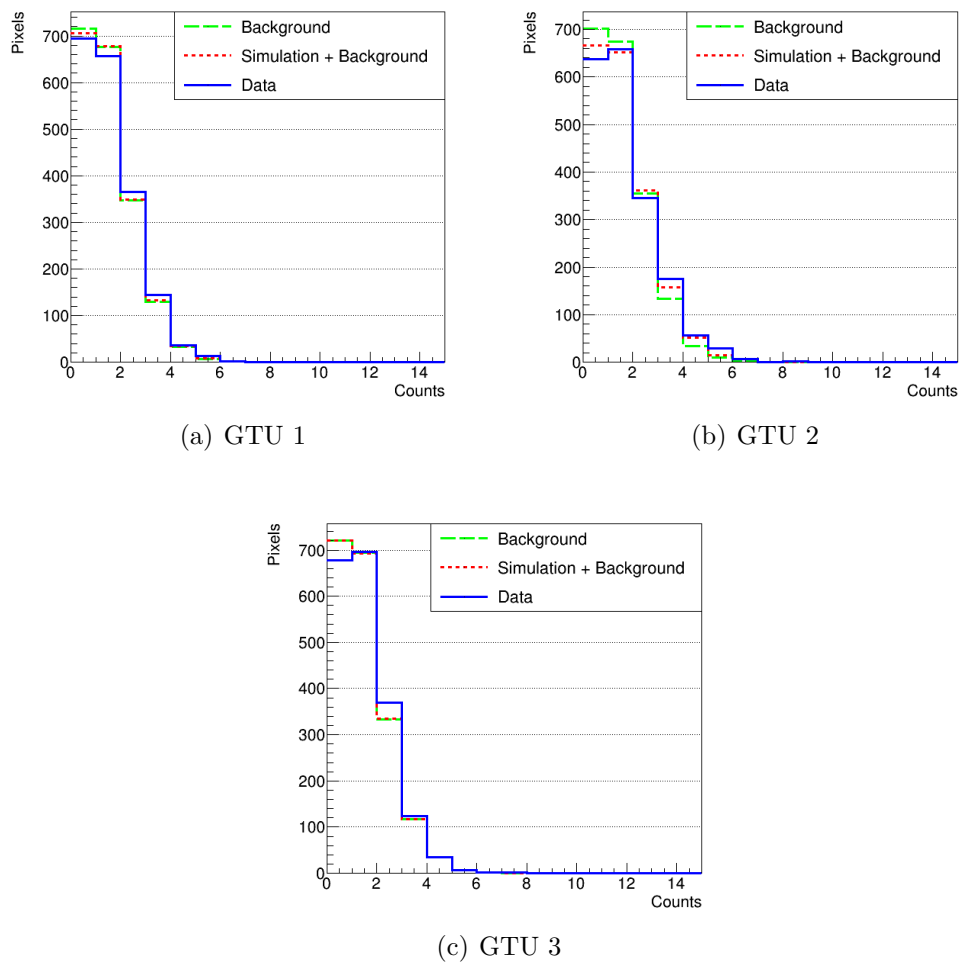
Figure F.1: Event detected on the 18th September 2015. Comparison between the counts distributions of data, sum of simulation and background and background itself for the three GTUs of the event.

Event of 20th September 2015

The comparison between the counts distributions of data, simulation plus background and background is done for single GTUs. In GTU 1 the excess of counts due to the presence of the event track appears for counts ≥ 2 in the simulation and counts ≥ 3 in the data, while in GTU 2 for counts ≥ 2 in both. The difference in the track segment length plays certainly a role, as well as a noisy PMT on the left side of the first segment of the track, which should not be related to the event, from a geometric point of view.
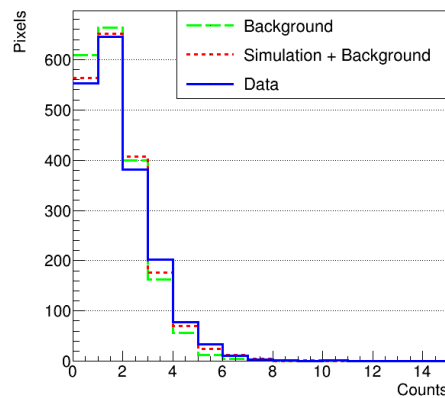
(a) GTU 1
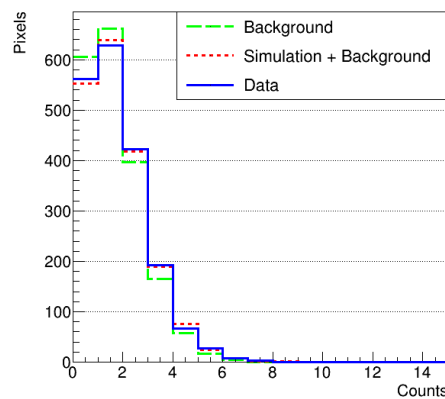
(b) GTU 2

Figure F.2: Event detected on the 20th September 2015. Comparison between the counts distributions of data, sum of simulation and background and background itself for the two GTUs.

Event of 7th November 2015

The excess of noisy pixels is visible in the counts distributions of data, simulation plus background and just background. Indeed, the bin for 0-counts presents much fewer entries than the previous distributions. The presence of the bright event is visible at counts ≥ 3 in both data and simulation. Anyway, both distributions have a long tail up to 12 counts.
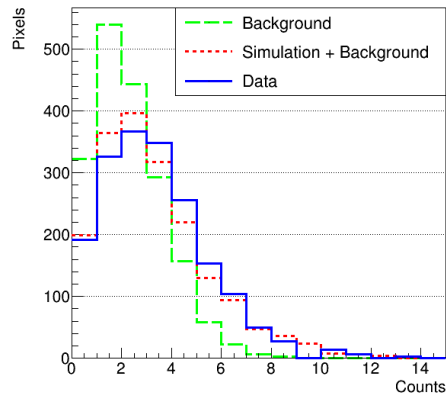
Figure F.3: Event detected on the 7th November 2015. Comparison between the counts distributions of data, sum of simulation and background and background itself.

F.3   Geometric comparison

Event of 18th September 2015

The inclination of the shower track on the PDM of the 18th September 2015 event is here evaluated with the fit algorithm, comparing the result for data, simulation with background and simulation alone. The results have been shown in Table 7.1. Figure F.4 displays the frames with the fitting line superposed, while in Figure F.5 the same line fits the means of the Gaussians (green markers) fitting every row of pixels.

(a) Data   (b) Sim. plus bkg.   (c) Simulation
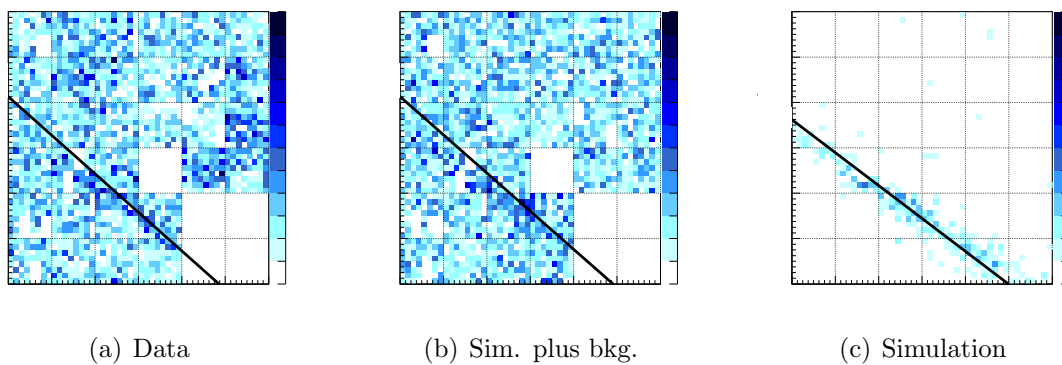
Figure F.4: Event detected on the 18th September 2015. Linear fit of the shower track for data (a), simulation plus background (b) and simulation (c). In both the cases, the sum of the three frames correspondent to the event is shown.

(a) Data   (b) Sim. plus bkg.   (c) Simulation
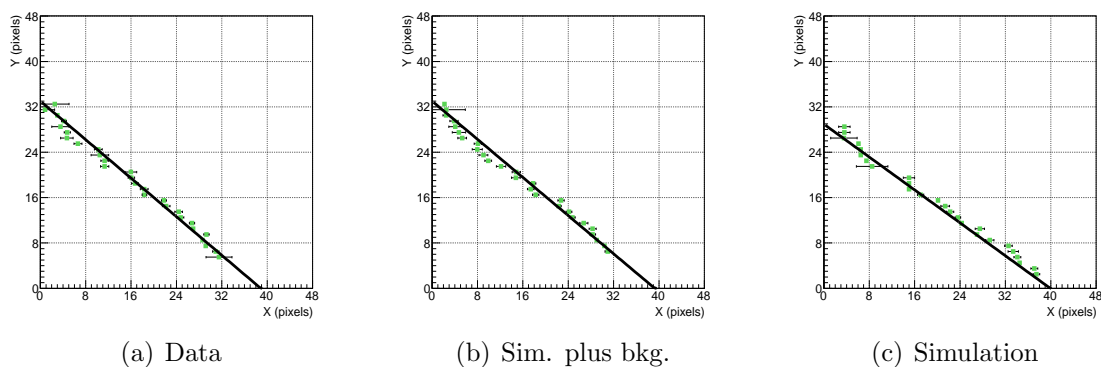
Figure F.5: Event detected on the 18th September 2015. Linear fit of the mean (green markers) of the Gaussian fits of every row of pixels for data (a), simulation plus background (b) and simulation (c). The means lie on the shower track.

Event of 20th September 2015

The inclination of the shower track on the PDM of the 20th September 2015 event is here evaluated with the fit algorithm, comparing the result for data, simulation with background and simulation alone. The results have been shown in Table 7.1. Figure 7.12 displays the frames with the fitting line superimposed, while in Figure F.7 the same line fits the means of the Gaussians (green markers) fitting every row of pixels.

(a) Data   (b) Sim. plus bkg.   (c) Simulation
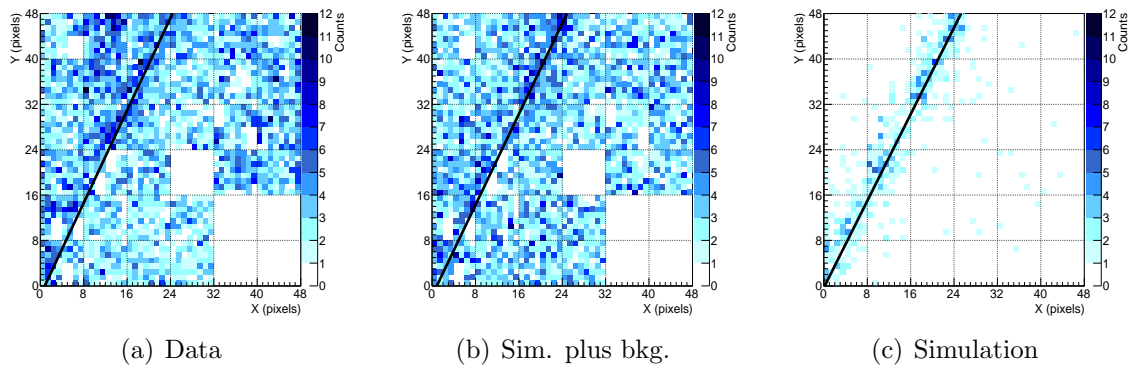
Figure F.6: Event detected on the 20th September 2015. Linear fit of the shower track for data (a), simulation plus background (b) and simulation (c). In both the cases, the sum of the two frames correspondent to the event is shown.

(a) Data   (b) Sim. plus bkg.   (c) Simulation
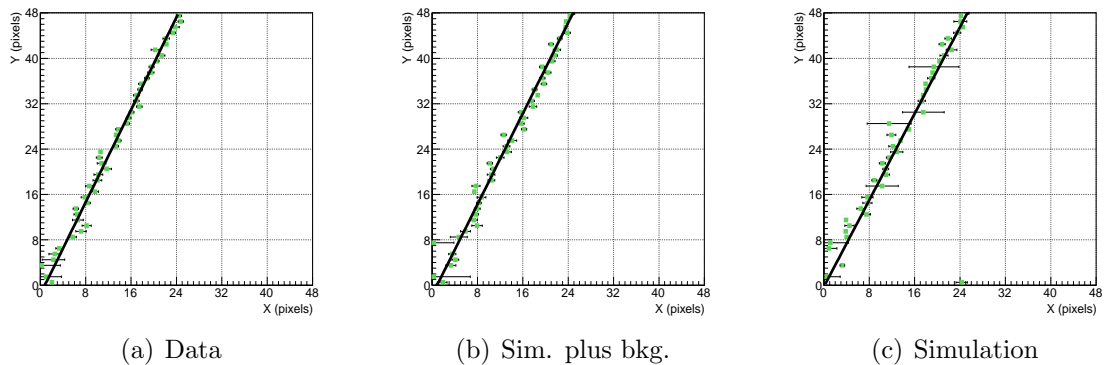
Figure F.7: Event detected on the 20th September 2015. Linear fit of the mean (green markers) of the Gaussian fits of every row of pixels for data (a), simulation plus background (b) and simulation (c). The means lie on the shower track.

Event of 7th November 2015

The inclination of the shower track on the PDM of the 7th November 2015 event is here evaluated with the fit algorithm, comparing the result for data, simulation with background and simulation alone. The results have been shown in Table 7.1. Figure F.8 displays the frames with the fitting line superimposed, while in Figure F.9 the same line fits the means of the Gaussians (green markers) fitting every row of pixels. The inclination of the tracks in data and simulation with background differ already from a visual point of view. This may rely on the uncertainty of the data event reconstruction parameters, used for the simulation in monocular mode of the TA stand alone reconstruction (using just the TAFD at Black Rock Mesa, as done for these events). The geometrical resolution of the open angle is 7.4°, which may reconstruct a shower at a different angle, i.e. position, respect to the telescope axis (Appendix E).

(a) Data	(b) Sim. plus bkg.	(c) Simulation
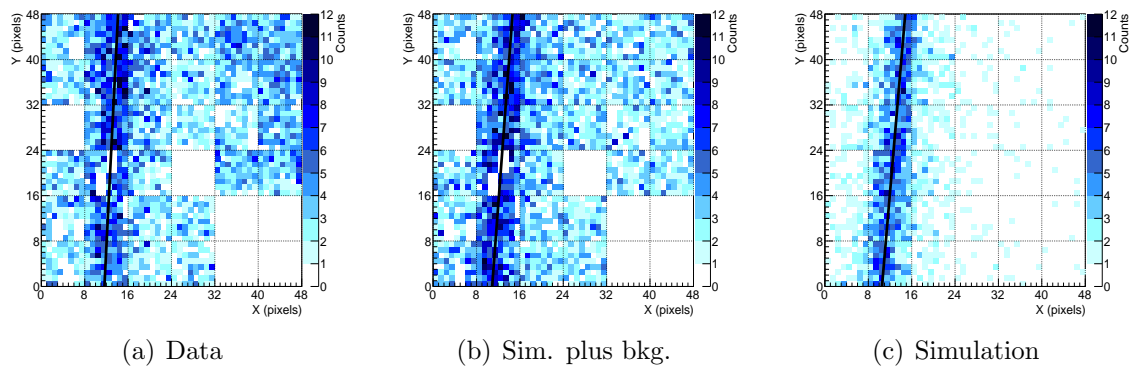
Figure F.8: Event detected on the 7th November 2015. Linear fit of the shower track for data (a), simulation plus background (b) and simulation (c).

(a) Data	(b) Sim. plus bkg.	(c) Simulation
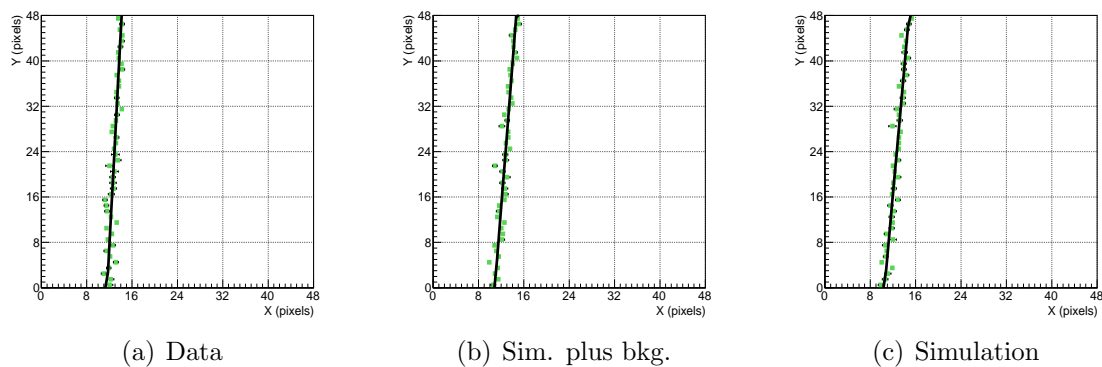
Figure F.9: Event detected on the 7th November 2015. Linear fit of the mean (green markers) of the Gaussian fits of every row of pixels for data (a), simulation plus background (b) and simulation (c). The means lie on the shower track.

F.4   Analysis of the simulation results

Event of 18th September 2015

In Figure F.10 the photons at the aperture of the telescope are plotted in function of the number of GTUs. Most of the light is fluorescence light and, because of the geometry of the cosmic ray air shower toward the telescope, the direct Cherenkov light is a bigger amount than in the 13 May event while the total amount of scattered Cherenkov light is about 13%. In Figure F.11 the photoelectrons considering just the photo-detection efficiency (PEs_{PDE}), those considering also the dead times (PEs_{signal}) and the photons at the focal surface ($Photons_{FS}$) are shown with respect to the total number of photons at the aperture of the telescope ($Photons_{aperture}$). About 17% of the photons arrive at the focal surface, and the overall efficiency is about 5%.

Figures F.12, F.13 and F.14 (a-c) show $Photons_{FS}$, PEs_{PDE} and PEs_{signal} per each of the three frames on which the signal is spread, for comparison. The ratios between the three quantities are reported in the plot in (d). In the first and third frames the segments of the event track are short, which means that a small number of photons is involved, and this might influence the rates. Anyway, there is evidence of the pile-up effect, related to dead time of the detector after a photon hits the sensor, which reduces the number of photoelectrons becoming signal. Since the effect of dead time is stronger at short distances (because more photons hit the same area in a short time, compared to distant showers), the fraction of PEs_{signal} with respect to PEs_{PDE} is much smaller in the third frame than in the first, since the shower approaches the telescope. In the second frame, with most of the signal component, about 30% of the photons at the focal surface contributes finally to the signal.
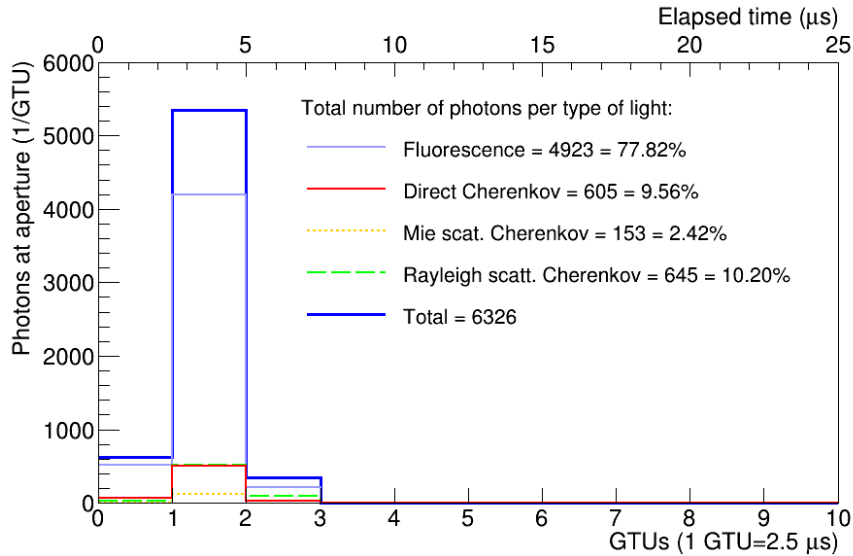
Figure F.10: Event detected on the 18th September 2015. Different types of photons at the aperture in function of the time.
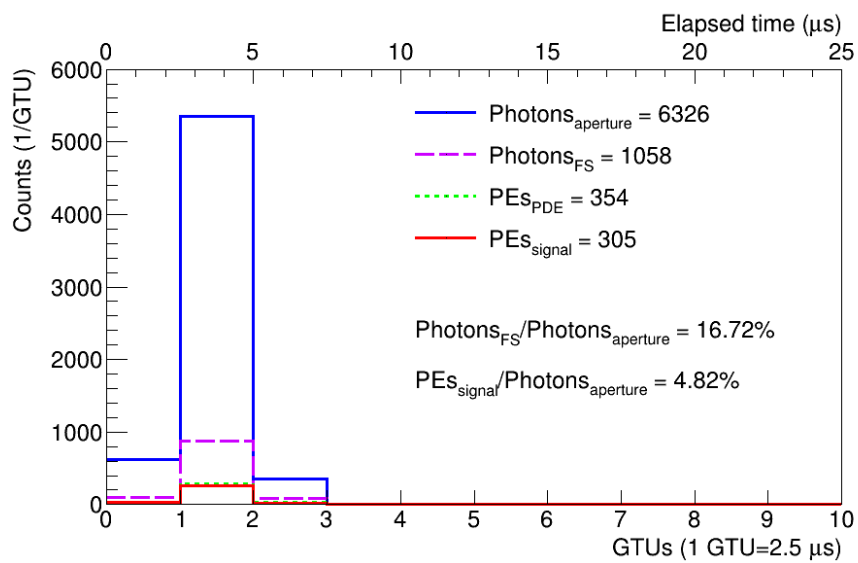
Figure F.11: Event detected on the 18th September 2015. Photons at the aperture $Photons_{aperture}$, photons at the focal surface $Photons_{FS}$, photoelectrons considering just the photo-detection efficiency PEs_{PDE} and those considering also the dead times PEs_{signal}, as a function of time. The ratio $Photons_{FS}/Photons_{aperture}$ represents the transmission efficiency of the optical system and the ratio $PEs_{signal}/Photons_{aperture}$ represents the overall efficiency of the detector.

(a) $Photons_{FS}$

(b) PEs_{PDE}

(c) PEs_{signal}

(d) Rates of the different quantities. The 0-counts bin has been cut to highlight the difference between the quantities.
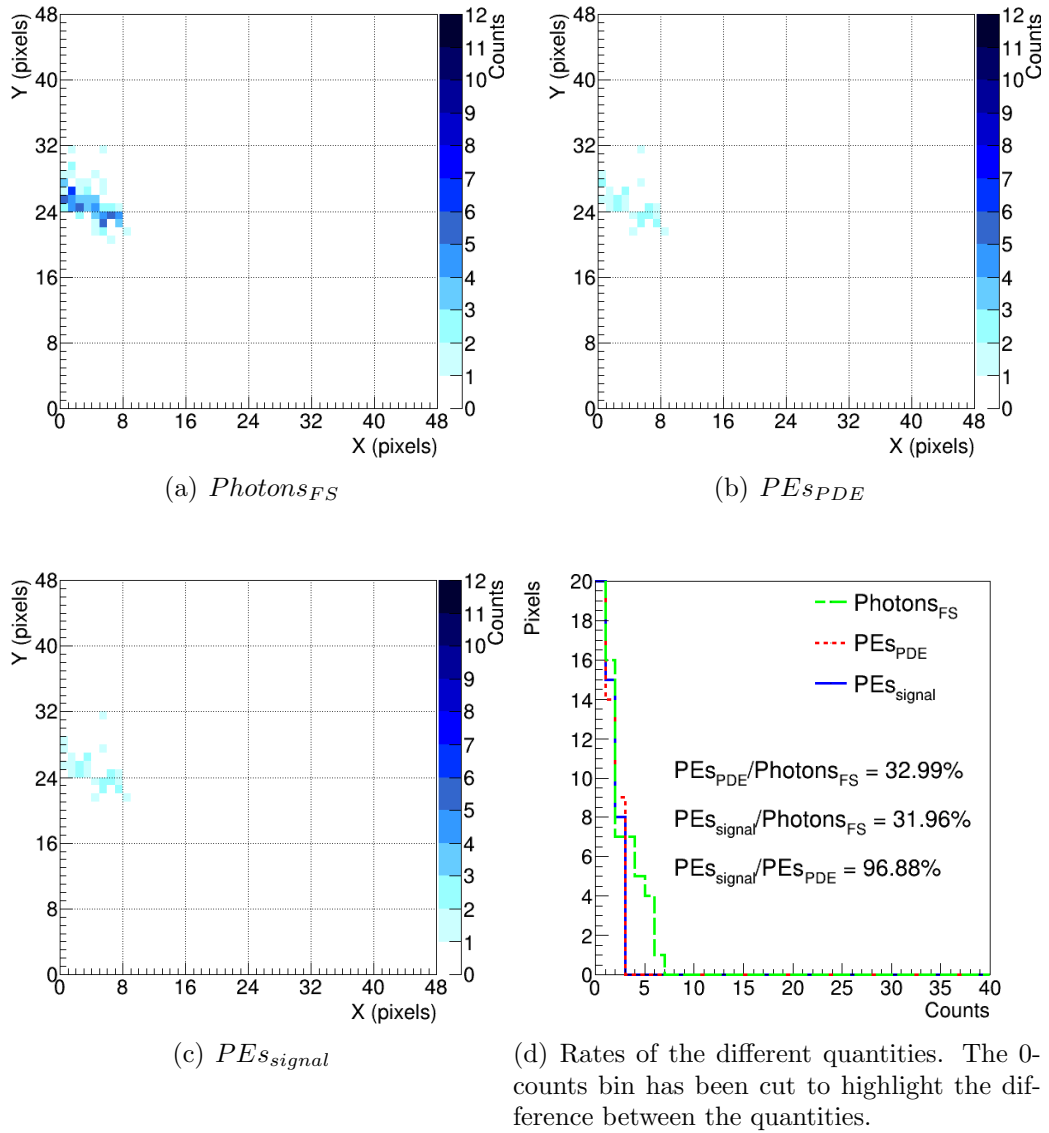
Figure F.12: Event detected on the 18th September 2015, GTU 1. Distributions of the photons at the focal surface $Photons_{FS}$, the photoelectrons considering just the photo-detection efficiency PEs_{PDE} and those considering also the dead times PEs_{signal}.

(a) $Photons_{FS}$

(b) PEs_{PDE}

(c) PEs_{signal}

(d) Rates of the different quantities. The 0-counts bin has been cut to highlight the difference between the quantities.
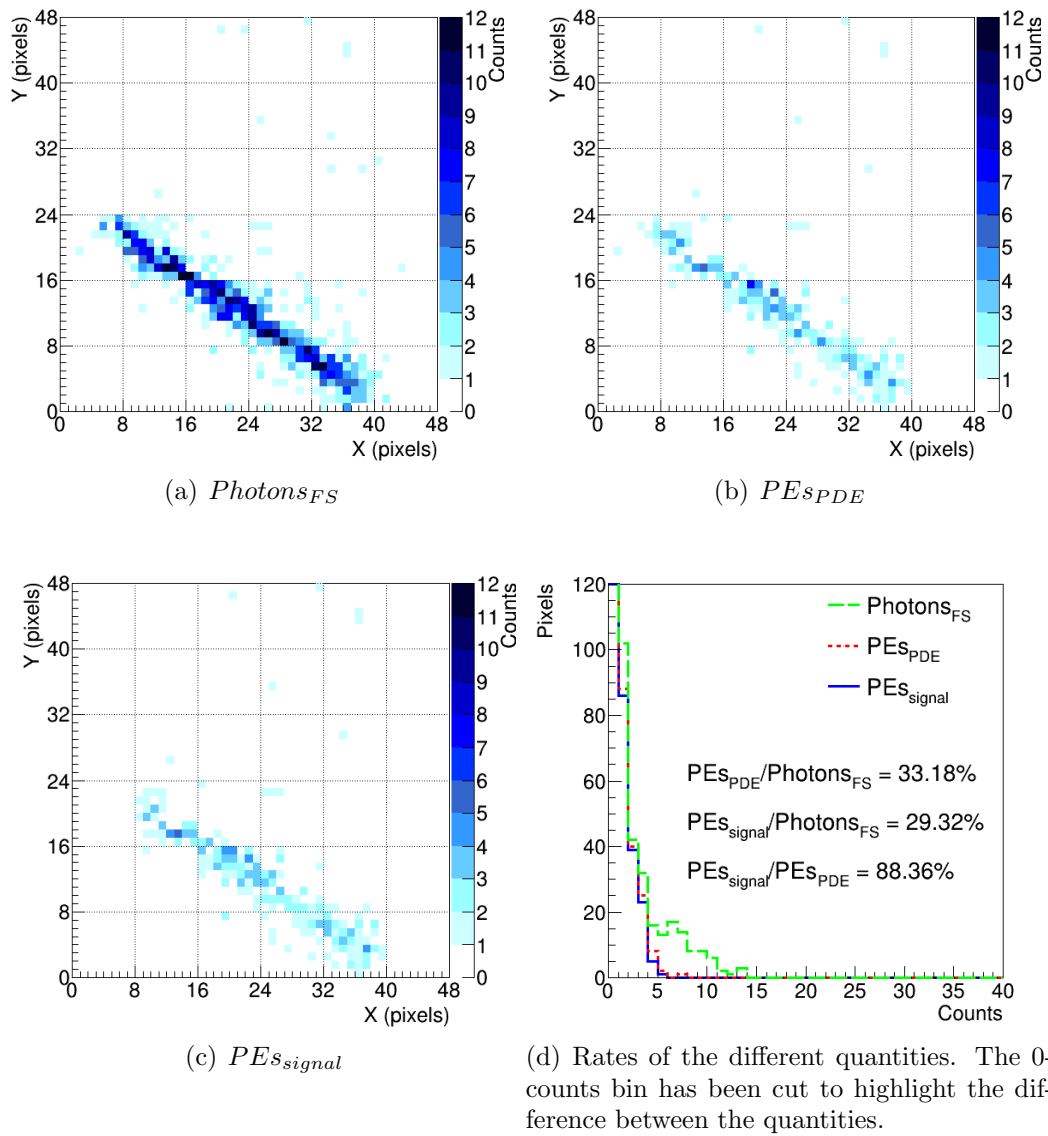
Figure F.13: Event detected on the 18th September 2015, GTU 2. Distributions of the photons at the focal surface $Photons_{FS}$, the photoelectrons considering just the photo-detection efficiency PEs_{PDE} and those considering also the dead times PEs_{signal}.

(a) $Photons_{FS}$

(b) PEs_{PDE}

(c) PEs_{signal}

(d) Rates of the different quantities. The 0-counts bin has been cut to highlight the difference between the quantities.
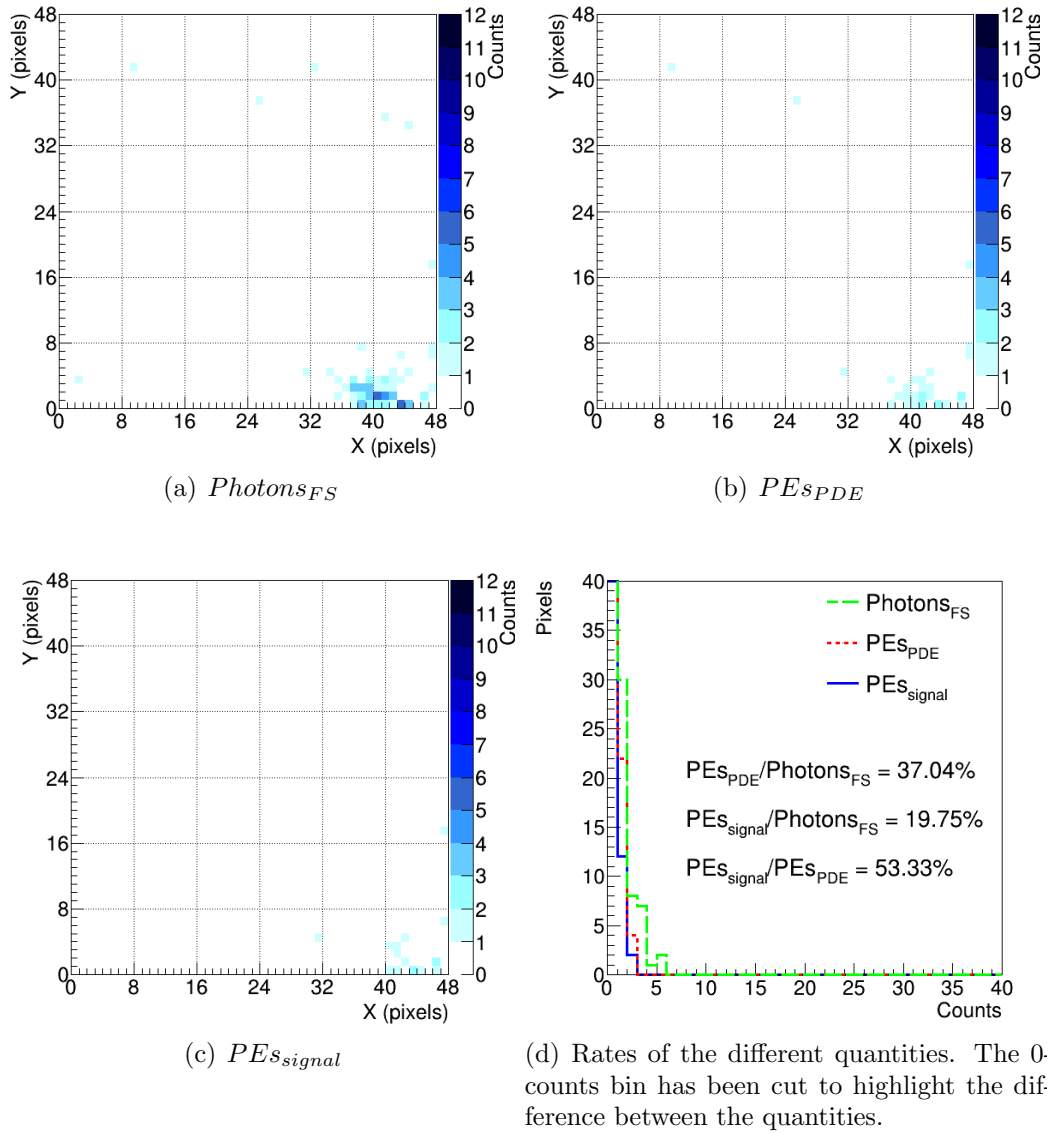
Figure F.14: Event detected on the 18th September 2015, GTU 3. Distributions of the photons at the focal surface $Photons_{FS}$, the photoelectrons considering just the photo-detection efficiency PEs_{PDE} and those considering also the dead times PEs_{signal}.

Event of 20th September 2015

In Figure F.15 the photons at the aperture of the telescope are plotted in function of the number of GTUs. Most of the light is fluorescence light and, because of the geometry of the cosmic ray air shower with azimuth angle in between those of the two previous events, the direct Cherenkov light is in between the previous two too, while the total amount of scattered Cherenkov light is about one third of the total. In Figure F.16 the photoelectrons considering just the photo-detection efficiency (PEs_{PDE}), those considering also the dead times (PEs_{signal}) and the photons at the focal surface ($Photons_{FS}$) are shown compared to the total number of photons at the aperture of the telescope ($Photons_{aperture}$). About 17% of the photons arrive at the focal surface, and the overall efficiency is about 4.6%.

Figures F.17 and F.18 (a-c) show the $Photons_{FS}$, PEs_{PDE} and PEs_{signal} for each of the two frames on which the signal is spread, for comparison. The ratios between the three quantities are reported in the plot in (d). Also in this case it seems that there is evidence of the pile-up effect, which has a stronger role at short distances. Indeed, the fraction of PEs_{signal} compared to the photoelectrons is much smaller in the second frame than in the first, since the shower slightly approaches the telescope. On average, about 27.5% of the photons at the focal surface finally contribute to the signal.
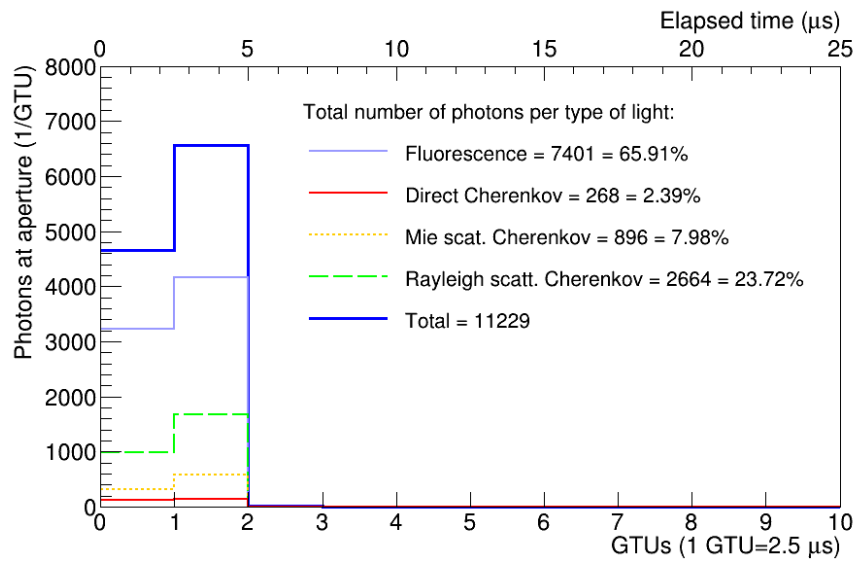
Figure F.15: Event detected on the 20th September 2015. Different types of photons at the aperture in function of the time.
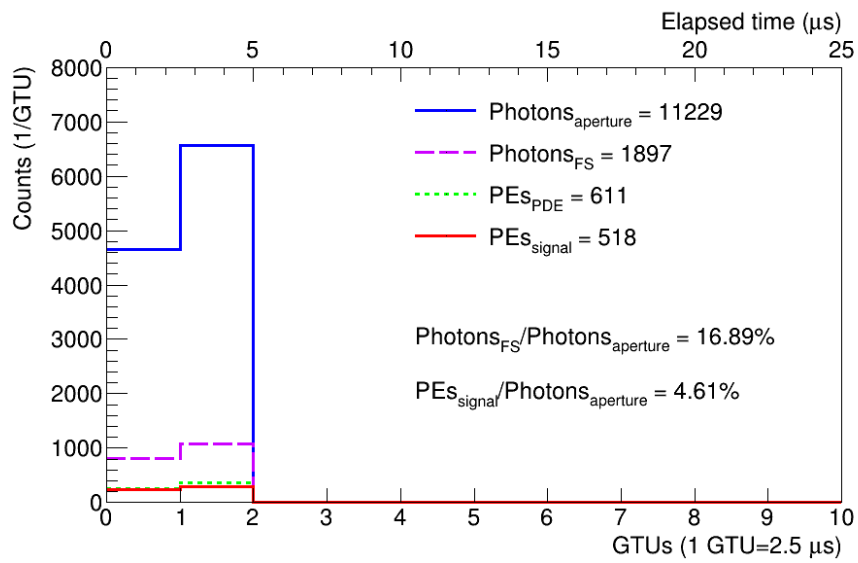
Figure F.16: Event detected on the 20th September 2015. Photons at the aperture $Photons_{aperture}$, photons at the focal surface $Photons_{FS}$, photoelectrons considering just the photo-detection efficiency PEs_{PDE} and those considering also the dead times PEs_{signal}, as a function of time. The ratio $Photons_{FS}/Photons_{aperture}$ represents the transmission efficiency of the optical system and the ratio $PEs_{signal}/Photons_{aperture}$ represents the overall efficiency of the detector.

(a) $Photons_{FS}$

(b) PEs_{PDE}

(c) PEs_{signal}

(d) Rates of the different quantities. The 0-counts bin has been cut to highlight the difference between the quantities.
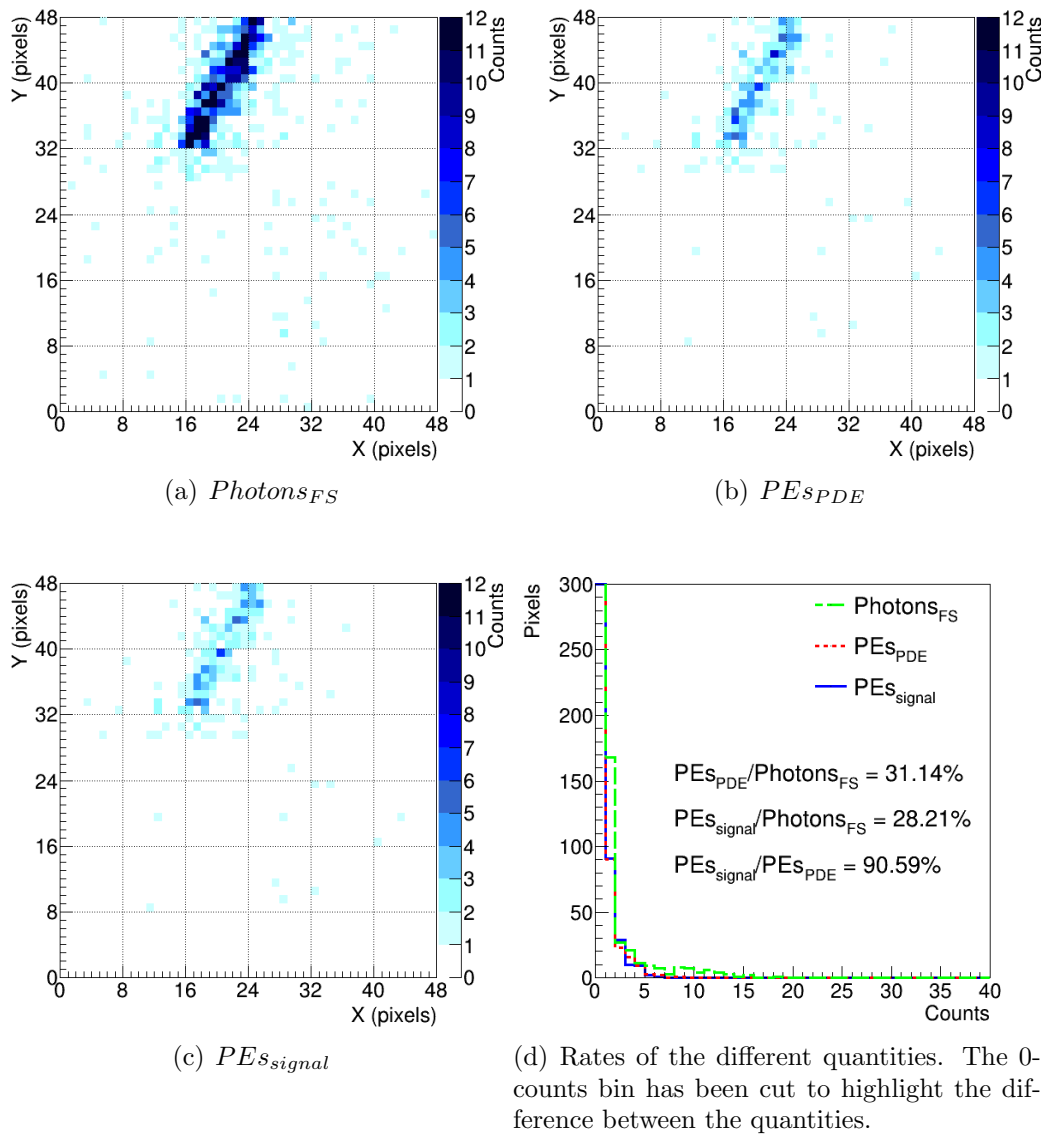
Figure F.17: Event detected on the 20th September 2015, GTU 1. Distributions of the photons at the focal surface $Photons_{FS}$, the photoelectrons considering just the photo-detection efficiency PEs_{PDE} and those considering also the dead times PEs_{signal}.

(a) $Photons_{FS}$

(b) PEs_{PDE}

(c) PEs_{signal}

(d) Rates of the different quantities. The 0-counts bin has been cut to highlight the difference between the quantities.
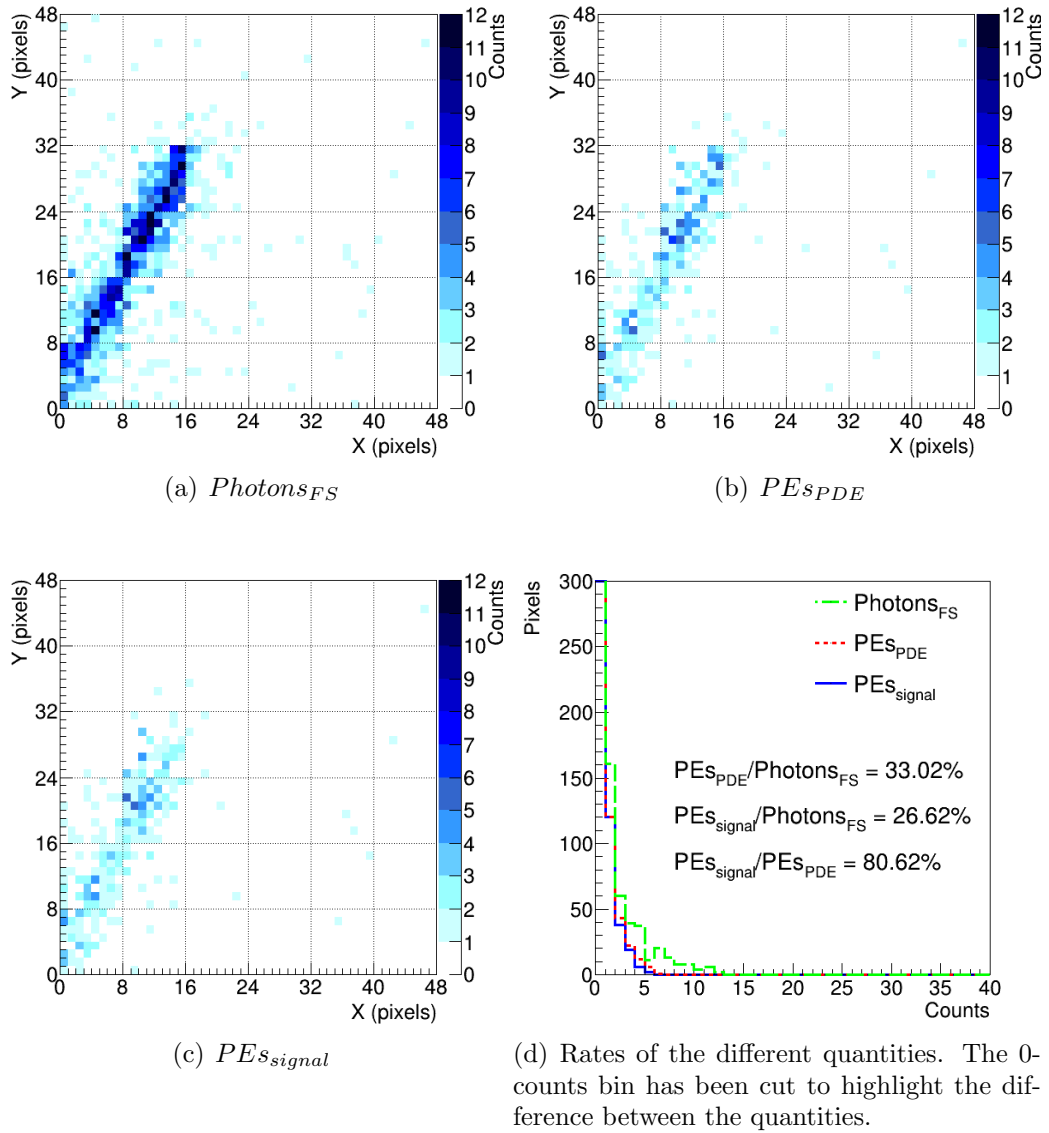
Figure F.18: Event detected on the 20th September 2015, GTU 2. Distributions of the photons at the focal surface $Photons_{FS}$, the photoelectrons considering just the photo-detection efficiency PEs_{PDE} and those considering also the dead times PEs_{signal}.

Event of 7th November 2015

In Figure F.19 the photons at the aperture of the telescope are plotted as a function of the number of GTUs. Most of the light is fluorescence light and, because of the geometry of the cosmic ray air shower, close to be vertical, the direct Cherenkov light is almost negligible, while the total amount of scattered Cherenkov light is about 20% of the total. In Figure F.20 the photons arriving at the focal surface ($Photons_{FS}$), photoelectrons considering just the photo-detection efficiency (PEs_{PDE}) and those including also the dead times (PEs_{signal}) are shown respect the total number of photons at the aperture of the telescope ($Photons_{aperture}$). About 16% of the photons arrive at the focal surface, and the overall efficiency is about 4%.

Figure F.21 (a-c) shows $Photons_{FS}$, PEs_{PDE} and PEs_{signal} for comparison. The ratios between the three quantities are reported in the plot in (d). About 25% of the photons at the focal surface contributes finally to the signal.
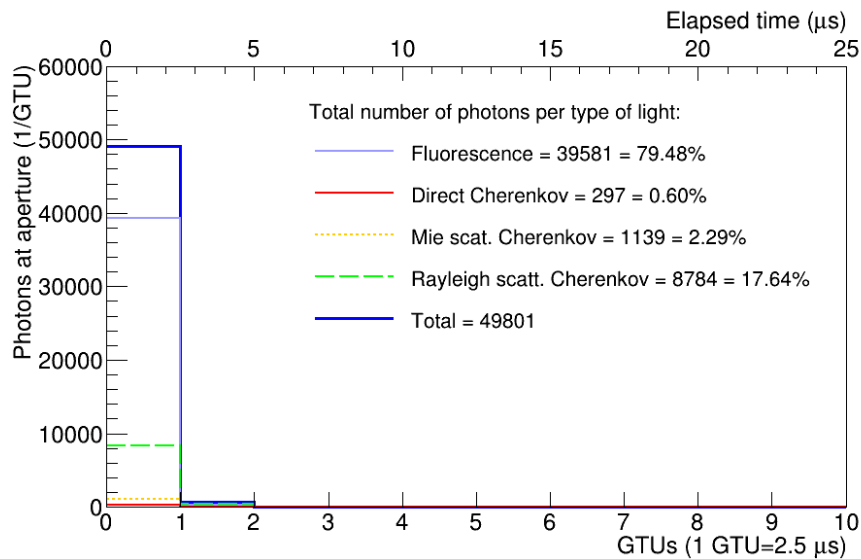
Figure F.19: Event detected on the 7th November 2015. Different types of photons at the aperture in function of the time.
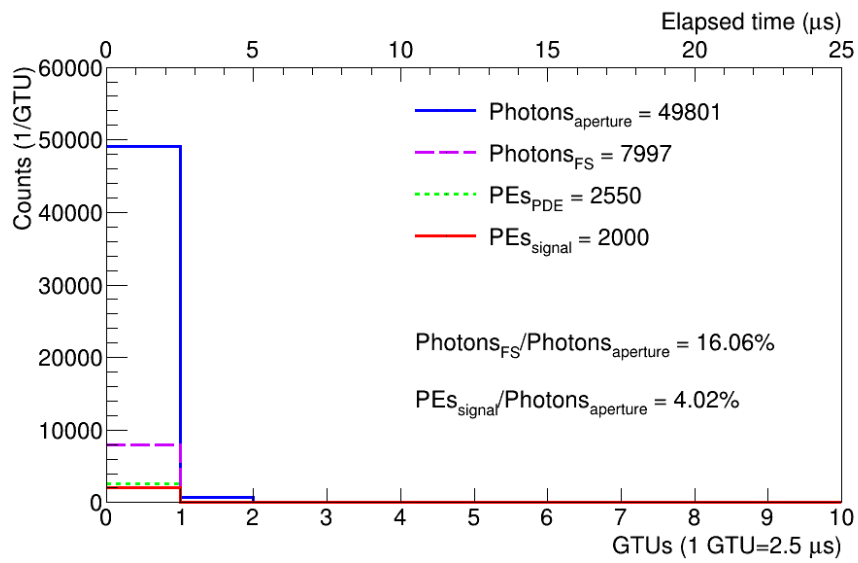
Figure F.20:   Event detected on the 7th November 2015.   Photons at the aperture $Photons_{aperture}$, photons at the focal surface $Photons_{FS}$, photoelectrons considering just the photo-detection efficiency PEs_{PDE} and those considering also the dead times PEs_{signal}, as a function of time. The ratio $Photons_{FS}/Photons_{aperture}$ represents the transmission efficiency of the optical system and the ratio $PEs_{signal}/Photons_{aperture}$ represents the overall efficiency of the detector.

(a) $Photons_{FS}$

(b) PEs_{PDE}

(c) PEs_{signal}

(d) Rates of the different quantities. The 0-counts bin has been cut to highlight the difference between the quantities.
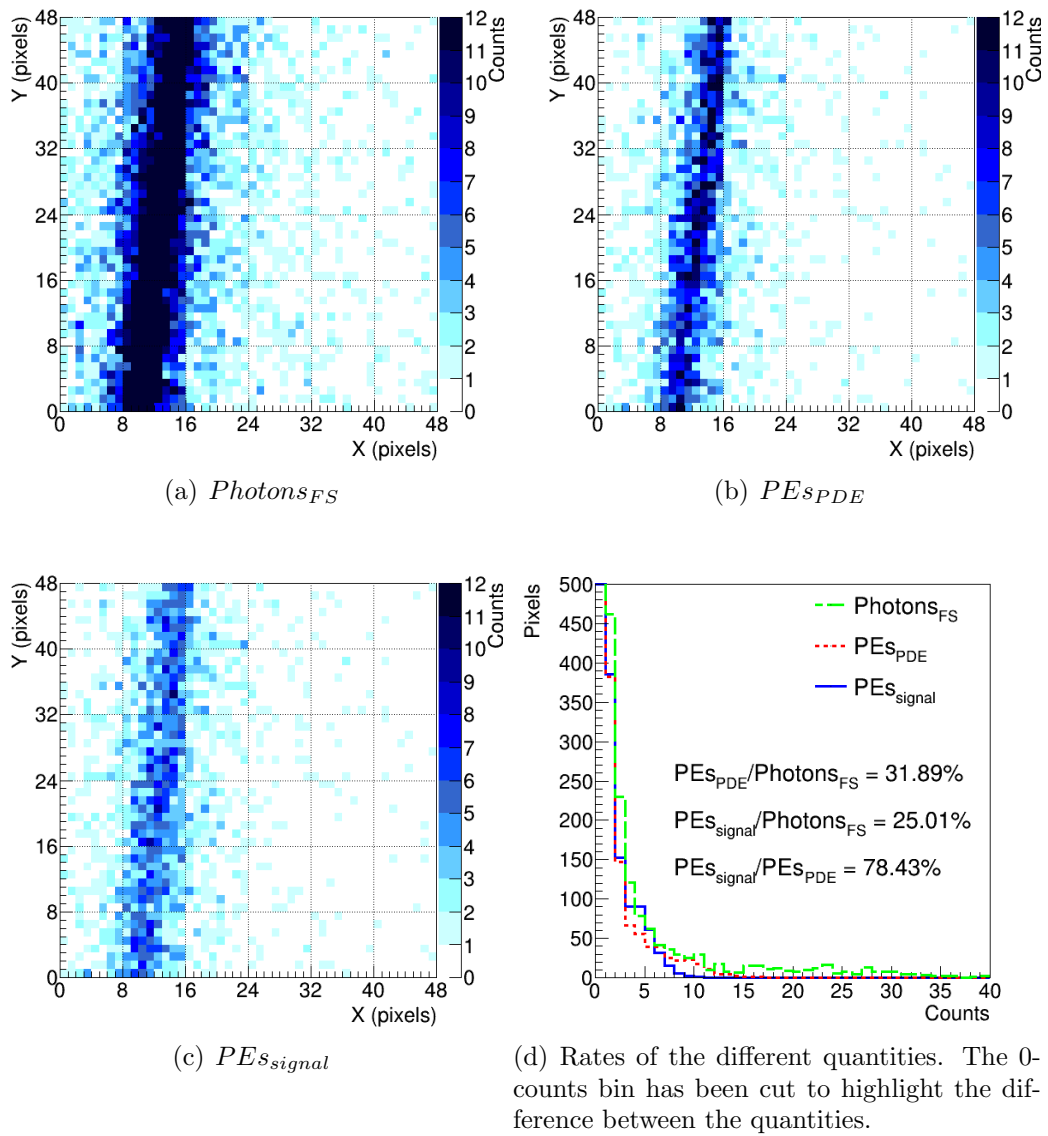
Figure F.21: Event detected on the 7th November 2015. Distributions of the photons at the focal surface $Photons_{FS}$, the photoelectrons considering just the photo-detection efficiency PEs_{PDE} and those considering also the dead times PEs_{signal}.

Acronyms

AGN	Active Galactic Nuclei
AMS	Atmospheric Monitoring System
APD	Avalanche PhotoDiode
ASIC	Application-Specific Integrated Circuit
BRM-TAFD	Telescope Array Fluorescence Detector at Black Rock Mesa
CCB	Cluster Control Board
CLF	Central Laser Facility (at the Telescope Array site)
CMB	Cosmic Microwave Background
CR	Cosmic Ray
DAQ	Data Acquisition
EAS	Extensive Air Shower
EC	Elementary Cell
EECR	Extreme Energy Cosmic Ray ($E \geq 5 \cdot 10^{19}$ eV)
ELS	Electron Light Source (compact electron linear accelerator at the Telescope Array site)
ESA	European Space Agency
ESAF	EUSO Simulation and Analysis Framework
ETOS	EUSO TO Screen
EUSO	Extreme Universe Space Observatory
EUSO-Balloon	EUSO experiment onboard a Balloon
EUSO-TA	EUSO experiment at the Telescope Array site
EUSO-SPB	EUSO experiment onboard a Super Pressure Balloon
FOV	Field Of View
FPGA	Field-Programmable Gate Array
FWHM	Full Width at Half Maximum
G-APD	Geiger-mode Avalanche PhotoDiode
GEANT4	Geometry And Tracking
GRB	Gamma Ray Burst
GTU	Gate Time Unit (time frame of 2.5 μs)
GZK	Greisen-Zatsepin-Kuzmin
HECR	High Energy Cosmic Ray ($E \geq 10^{15}$ eV)
IR	InfraRed
ISS	International Space Station

JAXA	Japan Aerospace Exploration Agency (Japanese federal space agency)
JEM-EUSO	Extreme Universe Space Observatory onboard the Japanese Experiment Module
K-EUSO	EUSO experiment onboard the ISS
KASCADE	Karlsruhe Shower Core and Array Detector
KIT	Karlsruhe Institute of Technology
LED	Light-Emitting Diode
LHC	Large Hadron Collider
LIDAR	Light Detection and Ranging
MAPMT	MultiAnode PhotoMultiplier Tube
Mini-EUSO	EUSO experiment onboard the ISS
NASA	(US) National Aeronautics and Space Administration
PDM	Photo-Detector Module
PSF	Point Spread Function
SDP	Shower Detector Plane
SPACIROC	Spatial Photomultiplier Array Counting and Integrating Chip
TA	Telescope Array
TAFD	Telescope Array Fluorescence Detector
UHECR	Ultra High Energy Cosmic Ray ($E \geq 10^{18}$ eV)

Bibliography

[1] D. Pacini. Penetrating radiation at the surface of and in water. *Nuovo Cimento*, VI/3:93, 1912.

[2] A. Gockel. Luftelektrische Beobachtungen bei einer Ballonfahrt. *Zeitschrift für Physik*, 11:280–282, 1910.

[3] V. F. Hess. Über die Absorption der γ-Strahlen in der Atmosphäre. *Zeitschrift für Physik*, 12:998–1001, 1911.

[4] V. F. Hess. Über Beobachtungen der durchdringenden Strahlung bei sieben Freiballonfahrten. *Zeitschrift für Physik*, 13:1084–1091, 1912.

[5] W. Kolhorster. Messungen der durchdringenden Strahlungen bis in Höhen von 9300 m. *Deutschen Physikalischen Gesellschaft*, 16:719–721, 1914.

[6] R. A. Millikan and I.S. Bowen. High frequency rays of cosmic origin I. Sounding balloon observations at extreme altitudes. *Physical Review*, 27:353–363, 1926.

[7] R. A. Millikan and G.H. Cameron. High frequency rays of cosmic origin III. Measurements in Snow-Fed lakes at high altitudes. *Physical Review*, 28:851–869, 1926.

[8] C. D. Anderson. The positive electron. *Physical Review*, 43:491–494, 1933.

[9] H. Yukawa et al. On the interaction of elementary particles IV. *Journal of the Mathematical Society of Japan*, 20:720–745, 1938.

[10] M. Gliozzi. Storia della fisica. *Bollati Boringhieri*, 2005.

[11] K. Greisen. End to the cosmic-ray spectrum? *Physical Review Letters*, 16:748, 1966.

[12] G. T. Zatsepin and V. A. Kuzmin. Upper limit of the spectrum of cosmic rays. *Soviet Journal of Experimental and Theoretical Physics Letters*, 4, 1966.

[13] R. Engel, D. Heck, and T. Pierog. Extensive air showers and hadronic interactions at high energy. *Annual Review of Nuclear and Particle Science*, 61:467–489, 2011.

[14] J. Blümer, R. Engel, and J. R. Hörandel. Cosmic rays from the knee to the highest energies. *Progress in Particle and Nuclear Physics*, 2:293–338, 2009.

[15] R. Aloisio, V. Berezinsky, and A. Gazizov. Transition from galactic to extragalactic cosmic rays. *Astroparticle Physics*, 39-40:129–143, 2012.

[16] G. Giacinti, M. Kachelriess, and D. V. Semikoz. The escape model for galactic cosmic rays. *Journal of Physics: Conference Series*, 632:012094, 2015.

[17] W. D. Apel et al. (KASCADE-Grande Collaboration). Kneelike structure in the spectrum of the heavy component of cosmic rays observed with KASCADE-Grande. *Physical Review Letters*, 107:171104, 2011.

[18] A. M. Hillas. The origin of ultra-high-energy cosmic rays. *Annual Review of Astronomy and Astrophysics*, 22:425–444, 1984.

[19] D. F. Torres and L. A. Anchordoqui. Astrophysical origins of ultrahigh energy cosmic rays. *Reports on Progress in Physics*, 67:1663–1730, 2004.

[20] P. Blasi, R. I. Epstein, and A. V. Olinto. Ultra-high-energy cosmic rays from young neutron star winds. *Astroparticle Physics*, 533(2):123–126, 2000.

[21] M. Kachelriess, E. Parizot, and V. Semikoz. The GZK horizon and constraints on the cosmic ray source spectrum from observations in the GZK regime. *Soviet Jounal of Experimental and Theoretical Physics Letters*, 88:553–557, 2009.

[22] A. Haungs, H. Rebel, and M. Roth. Energy spectrum and mass composition of high-energy cosmic rays. *Reports on Progress in Physics*, 66:1145, 2003.

[23] J. Matthewes. A Heitler model of extensive air showers. *Astroparticle Physics*, 22:287–297, 2005.

[24] P. F. G. G. Molière. Theory of the scattering of fast charged particles. 2. Repeated and multiple scattering. *Zeitschrift für Naturforschung A*, 3:78–97, 1948.

[25] I. Allekotte et al. (Pierre Auger Collaboration). The surface detector system of the Pierre Auger Observatory. *Nuclear Instruments and Methods in Physics Research Section A*, 586:409–420, 2007.

[26] T. Abu-Zayyad et al. The surface detector array of the Telescope Array experiment. *Nuclear Instrumentsand Methods in Physics Research Section A*, 689, 2012.

[27] The Pierre Auger Collaboration. The Fluorescence Detector of the Pierre Auger Observatory. *Instrumentation and Methods for Astrophysics Section A*, 620:227–251, 2010.

[28] H. Tokuno et al. New air fluorescence detectors employed in the Telescope Array experiment. *Nuclear Instruments and Methods in Physics Research, Section A*, 676:54–65, 2012.

[29] W. D. Apel et al. LOPES-3D: An antenna array for full signal detection of air-shower radio emission. *Nuclear Instruments and Methods in Physics Research Section A*, 696:100–109, 2012.

[30] D. Kostunin et al. The Tunka radio extension: reconstruction of energy and shower maximum of the first year data. *Proceedings of the ICRC2015*, 285, 2015.

[31] R. Smida et al. First experimental characterization of microwave emission from cosmic ray air showers. *Physical Review Letters*, 113:221101, 2014.

[32] M. Ave al. (AIRFLY Collaboration). Spectrally resolved pressure dependence measurements of air fluorescence emission with AIRFLY. *Nuclear Instruments and Methods in Physics Research Section A*, 597(1):41–45, 2008.

[33] A. Aab et al. The Pierre Auger Cosmic Ray Observatory. *Instrumentation and Methods for Astrophysics Section A*, 798:172–213, 2015.

[34] P. Tinyakov et al. Latest results from the Telescope Array. *Nuclear Instrumentsand Methods in Physics Research Section A*, 742:29–34, 2014.

[35] P. A. Cherenkov. Visible radiation produced by electrons moving in a medium with velocities exceeding that of light. *Physical Review*, 52:378–379, 1937.

[36] R. Benson and J. Linsley. Satellite observation of cosmic ray air showers. *Proceedings of the ICRC1981*, page 145–148, 1981.

[37] Y. Takahashi. Maximum-energy Auger (AIR)-shower satellite (MASS/AIRWATCH). *Proceedings of SPIE*, 2806:102–112, 1996.

[38] The JEM-EUSO Collaboration. Ultra high energy photons and neutrinos with JEM-EUSO. *Experimental Astronomy*, 40:215–233, 2013.

[39] The JEM-EUSO Collaboration. Erratum to: Ultra high energy photons and neutrinos with JEM-EUSO. *Experimental Astronomy*, 40:1–3, 2015.

[40] A. V. Olinto. Cosmic rays of extreme energies. *Nuclear Physics B - Proceedings Supplements*, 243-244:108–115, 2013.

[41] B. Rouillè D'Orfeuil et al. Anisotropy expectations for ultra-high-energy cosmic rays with future high-statistics experiments. *Astronomy and Astrophysics*, 567:A81, 2014.

[42] S. Falk. Atmospheric influences on space-based observations of extremely high-energy cosmic rays. *Ph.D. thesis Karlsruhe Institute of Technology (KIT)*, 2014.

[43] The JEM-EUSO Collaboration. The JEM-EUSO mission: status and prospects in 2011. *Instrumentation and Methods for Astrophysics*, 2011.

[44] A. Zuccaro Marchi et al. (for the JEM-EUSO Collaboration). The JEM-EUSO optics design. *Instrumentation and Methods for Astrophysics*, 3:180–183.

[45] The JEM-EUSO Collaboration. The JEM-EUSO Mission: Contributions to the ICRC 2013. *Proceedings of the ICRC2013*, 2013.

[46] Omega MICRO - SPACIROC Front-end Chip. 2015.

[47] The JEM-EUSO Collaboration. An evaluation of the exposure in nadir observation of the JEM-EUSO mission. *Astroparticle Physics*, 44:76–90, 2013.

[48] The JEM-EUSO Collaboration. The EUSO-Balloon mission. *Proceedings of the ICRC2015*, 322, 2015.

[49] L. Wiencke (for the JEM-EUSO Collaboration). EUSO-Balloon mission to record extensive air showers from near space. *Proceedings of the ICRC2015*, 631, 2015.

[50] NASA Super Pressure Balloon:
`http://www.nasa.gov/directorates/heo/scan/services/missions/earth/Balloons.html`.

[51] EUSO-SPB Project:
`http://astroserve.mines.edu/euso_spb/2017-spb.html`.

[52] M. Casolino et al. (for the JEM-EUSO Collaboration). EUSO-TA, a ground telescope at the Telescope Array to test JEM-EUSO detector performance. *Proceedings of the ICRC2015*, 636, 2015.

[53] F. Bisconti et al. (for the JEM-EUSO Collaboration). EUSO-TA fluorescence detector. *Proceedings of the ECRS2016*, 2017.

[54] M. Ricci et al. (for the JEM-EUSO Collaboration). Mini-EUSO: a pathfinder for JEM-EUSO to measure Earth's UV background from the ISS. *Proceedings of the ICRC2015*, 599, 2015.

[55] K-EUSO conceptual design: `http://jem-euso.roma2.infn.it`.

[56] M. Panasyuk et al. The current status of orbital experiments for UHECR studies. *Proceedings of the ECRS2015*, 2015.

[57] N. Sakaki et al. Expected acceptance of the KLYPVE/K-EUSO space-based mission for the observation of ultra-high energy cosmic rays. *Proceedings of the ICRC2015*, 939, 2015.

[58] M. Panasyuk et al. Ultra high energy cosmic ray detector KLYPVE on board the Russian Segment of the ISS. *Proceedings of the ICRC2015*, 669, 2015.

[59] M. Fukushima et al. Telescope Array project for extremely high energy cosmic rays. *Progress of Theoretical Physics Supplement*, 151:206–210, 2003.

[60] S. Udo, M. Allen, R. Cady, M. Fukushima, Y. Iida, J. N. Matthews, J. Thomas, S. B. Thomas, and L. R. Wiencke. The Central Laser Facility at the Telescope Array. *Proceedings of the ICRC2002*, 5:1021–1024, 2002.

[61] T. Shibata et al. (for the Telescope Array Collaboration). Absolute energy calibration of the Telescope Array fluorescence detector with an Electron Linear Accelerator. *Proceedings of the ICRC2011*, 3:309–312, 2011.

[62] J. Boyer, B. Knapp, E. Mannel, and M. Seman. FADC-based DAQ for HiRes fly's eye. *Nuclear Instruments and Methods in Physics Research Section A*, 482, 2002.

[63] T. Tomida et al. Atmospheric monitor for Telescope Array experiment. *Proceedings of the International Symposium on Future Directions in UHECR Physics*, 2012.

[64] K. Shinozaki. Estimation of number of events. *JEM-EUSO Collaboration meeting*, 2011.

[65] Fresnel concept: `http://academic.greensboroday.org/~regesterj/potl/Waves/ Refraction/RefractionA.htm`.

[66] Y. Hachisu et al. Manufacturing of the TA-EUSO and the EUSO-Balloon lenses. *Proceedings of the ICRC2013*, 2013.

[67] Y. Takizawa et al. The TA-EUSO and EUSO-Balloon optics designs. *Proceedings of the ICRC2013*, 2013.

[68] M. Karus. Development of a calibration stand for photosensors for extremely high-energy cosmic ray research. *Ph.D. thesis Karlsruhe Institute of Technology (KIT)*, 2016.

[69] H. Miyamoto et al. Performance of the SPACIROC front-end ASIC for JEM-EUSO. *Proceedings of the ICRC2013*, 2013.

[70] M. Bertaina et al. (for the JEM-EUSO Collaboration). Expected performance of the first level trigger logic of JEM-EUSO for cosmic ray detection. *Instrumentation and Methods for Astrophysics Section A*, 824:253, 2016.

[71] J. Bayer et al. Second level trigger and Cluster Control Board for the JEM-EUSO mission. *Proceedings of the ICRC2013*, 2013.

[72] L. W. Piotrowski et al. (for the JEM-EUSO Collaboration). Ground-based tests of JEM-EUSO components at the Telescope Array site, "EUSO-TA". *Experimental Astronomy*, 40:301, 2015.

[73] P. Gorodetzky et al. Absolute calibrations of the Focal Surface of the JEM-EUSO Telescope. *Proceedings of the ICRC2013*, 2013.

[74] L. W. Piotrowski et al. On-line and off-line data analysis for the EUSO-TA and EUSO-Balloon experiments. *Proceedings of the ICRC2013*, 2013.

[75] H. Nogima. Development and status of the Pierre Auger Observatory. *Brazilian Journal of Physics*, 32:895–900, 2002.

[76] H. Shin. Private communication. 2016.

[77] Y. Takahashi et al. (for the Telescope Array Collaboration). Central Laser Facility analysis at The Telescope Array experiment. *Conference Proceedings of the American Institute of Physics*, 157:1021–1024, 2011.

[78] M. A. C. Perryman et al. The HIPPARCOS Catalogue. *Astronomy and Astrophysics*, 323:49–52, 1997.

[79] T. C. Paul et al. (for the JEM-EUSO Collaboration). A new design for simulation and reconstruction software for the JEM-EUSO mission. *Proceedings of the ICRC2015*, 578, 2015.

[80] S. Argirò et al. The Offline Software Framework of the Pierre Auger Observatory. *Nuclear Instruments and Methods in Physics Research Section A*, 580:1485–1496, 2007.

[81] T. Bergmann et al. One-dimensional hybrid approach to extensive air shower simulation. *Astroparticle Physics*, 26:420–432, 2007.

[82] D. Heck et al. CORSIKA: A Monte Carlo code to simulate extensive air showers. *Wissenschaftliche Berichte FZKA-6019*, 1998.

[83] Shema: `http://www.w3.org/standards/xml/schema`.

[84] Hamamatsu Photonics. Photomultiplier tubes - basics and applications 3a.

[85] V. Verzi et al. (for the Pierre Auger Collaboration). The Energy Scale of the Pierre Auger Observatory. *Proceedings of the ICRC2013*, 2013.

[86] T. Fujii. Measurements of the Energy Spectrum and the Mass Composition of Ultra-High Energy Cosmic Rays with Telescope Array Fluorescence Detectors in Monocular Mode. *Ph.D. thesis*, 2012.

[87] B. Ruzybayev et al. (for the IceCube Collaboration). Measurement of the Cosmic Ray Energy Spectrum with IceTop 73. *Proceedings of the ICRC2013*, 2013.

[88] A. Schulz et al. (for the Pierre Auger Collaboration). The measurement of the energy spectrum of cosmic rays above $3 \cdot 10^{17}$ eV with the Pierre Auger Observatory. *Proceedings of the ICRC2013*, 2013.

[89] A. Haungs (for the JEM-EUSO Collaboration). Towards a SiPM based fluorescence camera for JEM-EUSO. *Proceedings of the ICRC2015*, 643, 2015.

[90] O. Catalano et al. (for the ASTRI Collaboration). The ASTRI SST-2M Prototype: Camera and Electronics. *Proceedings of the ICRC2013*, 2013.

[91] D. Mazin et al. Towards SiPM camera for current and future generations of Cherenkov telescopes. *Proceedings of the ICRC2013*, 2013.

[92] M. Renschler. Characterisation of 64 channel SiPM arrays for the Silicon Elementary Cell Add-on. *Master thesis at Karlsruhe Institute of Technology (KIT)*, 2016.

[93] Hamamatsu. A technical guide to silicon photomultipliers (SiPM).

[94] Hamamatsu. Datasheet 64-channel SiPM array S12642 series. 2014.

[95] Hamamatsu. Datasheet 64-channel SiPM array S13361 series. 2015.

[96] N. Sakaki. Private communication. 2014.

[97] C. Kramer (Hamamatsu Photonics Deutschland GmbH). Private communication. 2014.

[98] L. W. Piotrowski. ETOS (EUSO TO Screen) user's manual. 2015.

Acknowledgments

I would like to thank Prof. Johannes Blümer for giving me the opportunity to work at KIT for my Ph.D. thesis and Prof. Ulrich Husemann for his inputs to improve it. Further, I would like to thank Andreas Haungs for his supervision and support during these years.

Special thanks go also to all the people involved in the EUSO-TA data analysis and in the Offline development, whose contribution to my work has been really precious. In particular, I thank Mario Bertaina, Marco Casolino, Tom Paul, Lech Piotrowski and Hengsu Shin, who provided helpful information for the analysis of the EUSO-TA data, thanks to the collaboration with Telescope Array.

Then, I would like to thank the JEM-EUSO office mates, in order of appearance during my presence there, Stafanie, Naoto, Michael, Thomas, Max and William, with whom it was a pleasure to work and share space and time.

I also thank all the Erasmus students coming from Turin, who made the past summer times always a bit special.

Thanks also to Giuseppe, who has "sopportato e supportato" me during these years.

Last but not least, I thank my family, which supported me and was present despite the distance.